



728
2019

Berichte

zur Polar- und Meeresforschung

Reports on Polar and Marine Research

The Expedition PS115/2 of the Research Vessel POLARSTERN to the Arctic Ocean in 2018

Edited by

Ruediger Stein

with contributions of the participants

Die Berichte zur Polar- und Meeresforschung werden vom Alfred-Wegener-Institut, Helmholtz-Zentrum für Polar- und Meeresforschung (AWI) in Bremerhaven, Deutschland, in Fortsetzung der vormaligen Berichte zur Polarforschung herausgegeben. Sie erscheinen in unregelmäßiger Abfolge.

Die Berichte zur Polar- und Meeresforschung enthalten Darstellungen und Ergebnisse der vom AWI selbst oder mit seiner Unterstützung durchgeführten Forschungsarbeiten in den Polargebieten und in den Meeren.

Die Publikationen umfassen Expeditionsberichte der vom AWI betriebenen Schiffe, Flugzeuge und Stationen, Forschungsergebnisse (inkl. Dissertationen) des Instituts und des Archivs für deutsche Polarforschung, sowie Abstracts und Proceedings von nationalen und internationalen Tagungen und Workshops des AWI.

Die Beiträge geben nicht notwendigerweise die Auffassung des AWI wider.

Herausgeber

Dr. Horst Bornemann

Redaktionelle Bearbeitung und Layout

Birgit Reimann

Alfred-Wegener-Institut
Helmholtz-Zentrum für Polar- und Meeresforschung
Am Handelshafen 12
27570 Bremerhaven
Germany

www.awi.de

www.reports.awi.de

Der Erstautor bzw. herausgebende Autor eines Bandes der Berichte zur Polar- und Meeresforschung versichert, dass er über alle Rechte am Werk verfügt und überträgt sämtliche Rechte auch im Namen seiner Koautoren an das AWI. Ein einfaches Nutzungsrecht verbleibt, wenn nicht anders angegeben, beim Autor (bei den Autoren). Das AWI beansprucht die Publikation der eingereichten Manuskripte über sein Repositorium ePIC (electronic Publication Information Center, s. Innenseite am Rückdeckel) mit optionalem print-on-demand.

The Reports on Polar and Marine Research are issued by the Alfred Wegener Institute, Helmholtz Centre for Polar and Marine Research (AWI) in Bremerhaven, Germany, succeeding the former Reports on Polar Research. They are published at irregular intervals.

The Reports on Polar and Marine Research contain presentations and results of research activities in polar regions and in the seas either carried out by the AWI or with its support.

Publications comprise expedition reports of the ships, aircrafts, and stations operated by the AWI, research results (incl. dissertations) of the Institute and the Archiv für deutsche Polarforschung, as well as abstracts and proceedings of national and international conferences and workshops of the AWI.

The papers contained in the Reports do not necessarily reflect the opinion of the AWI.

Editor

Dr. Horst Bornemann

Editorial editing and layout

Birgit Reimann

Alfred-Wegener-Institut
Helmholtz-Zentrum für Polar- und Meeresforschung
Am Handelshafen 12
27570 Bremerhaven
Germany

www.awi.de

www.reports.awi.de

The first or editing author of an issue of Reports on Polar and Marine Research ensures that he possesses all rights of the opus, and transfers all rights to the AWI, including those associated with the co-authors. The non-exclusive right of use (einfaches Nutzungsrecht) remains with the author unless stated otherwise. The AWI reserves the right to publish the submitted articles in its repository ePIC (electronic Publication Information Center, see inside page of verso) with the option to "print-on-demand".

Titel: A-Galgen und Achterschiff von FS Polarstern mit Nordlichtern im Hintergrund, aufgenommen am 08.10.2018 in der westlichen Barents-See auf dem Rückweg nach Tromsø. (Foto: R. Love/MUN)

Cover: A-Frame and stern of RV Polarstern with Aurora borealis in the background, taken October 8th/09th 2018 in the western Barents Sea on the way to Tromsø. (Photo R. Love/MUN).

The Expedition PS115/2 of the Research Vessel POLARSTERN to the Arctic Ocean in 2018

Edited by

Ruediger Stein

with contributions of the participants

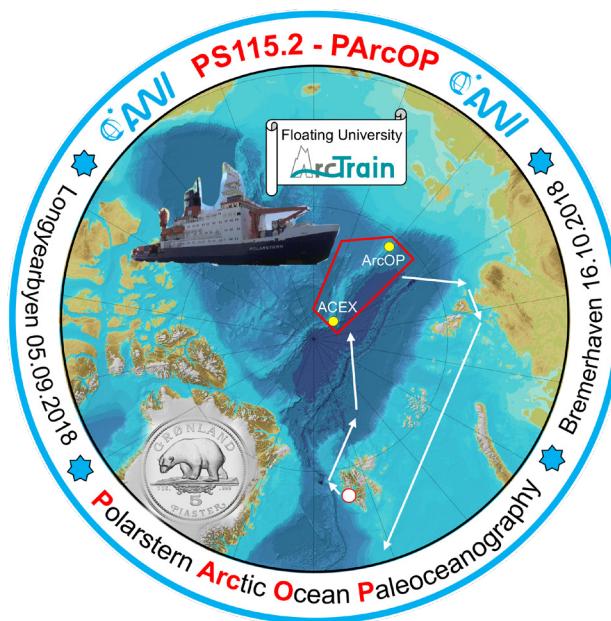
Please cite or link this publication using the identifiers

**<http://hdl.handle.net/10013/epic.e27f95dd-9b1d-4f76-b471-855c6f2edc49> and
https://doi.org/10.2312/BzPM_0728_2019**

ISSN 1866-3192

PS115/2

**05 September 2018 - 16 October 2018
Longyearbyen - Bremerhaven**



**Chief Scientist
Ruediger Stein**

**Coordinator
Rainer Knust**

Contents

1.	Zusammenfassung und Fahrtverlauf	3
	Summary and Itinerary	10
2.	Weather Conditions during Expedition PS115/2	14
3.	Meteorology & Radiosounding	18
4.	Sea Ice	24
4.1	Overview	24
4.2	Physical characteristics of melt ponds	25
4.3	Sea ice algae	28
4.4	Drifting buoys on sea ice	29
5.	Bathymetric Investigations during Expedition PS115/2	40
6.	Geophysics: Tectonic Evolution of the Arctic Ocean	45
6.1	Seismic Reflection	45
6.2	Passive seismology	52
6.3	Magnetic measurements	58
6.4	Gravity measurements	61
6.5.	Marine mammal observation (MMO)	69
7.	PS115/2 Marine Geology: Reconstruction of Past Climatic Conditions	71
7.1	Overview of the PS115/2 marine geology programme	71
7.2	PARASOUND sub-bottom profiling	82
7.3.	Physical-properties core logging	97
7.4	Sediment composition of selected sediment cores based on smear slide and coarse-fraction analyses	106
7.5	Sediment characteristics and lithostratigraphy of some PS115/2 cores	112
8.	The “ArcTrain Floating University”	134

Appendix

A.1	Teilnehmende Institute / Participating Institutions	139
A.2	Fahrtteilnehmer / Cruise Participants	142
A.3	Schiffsbesatzung / Ship's Crew	144
A.4	Stationsliste / Station List	147
A.5	PS115/2 Sampling and Publication Policy	161
A.6	PS115/2 Drift buoy deployment sheets	163
A.7	Reports of ArcTrain students	181

1. ZUSAMMENFASSUNG UND FAHRTVERLAUF

Ruediger Stein (AWI)

Grant-No. AWI-PS115/2_01

Zusammenfassung

Ziel der Expedition PS115/2 ("Polarstern Arctic Ocean Paleoceanography – PArcOP") war die Region des südlichen Lomonosov-Rückens und des südlichen Amundsen-Beckens in Angrenzung zum Laptev-See-Kontinentalrand, wo schwerpunktmäßig geowissenschaftliche Untersuchungen durchgeführt werden sollten (Abb. 1.1). Übergeordnete Fragestellungen bezogen sich dabei auf die detaillierte Rekonstruktion der kurz- und langfristigen Klimaänderungen und der tektonischen Entwicklung des Arktischen Ozeans. Das Hauptarbeitsgebiet als auch die wissenschaftlichen Schwerpunktthemen stehen in direktem Zusammenhang mit der IODP-Expedition 377 ("Arctic Ocean Paleoceanography - ArcOP"; siehe Stein 2017 für weitere Hintergrundinformationen). Die bewilligte und für Mitte August bis Mitte Oktober 2018 angesetzte IODP Expedition 377, ursprünglich als „Joint Venture“ zusammen mit dieser *Polarstern*-Expedition geplant, ist leider relativ kurzfristig gestrichen worden, da eine kostenneutrale Einwerbung eines zusätzlichen PS-starken Primäreisbrechers (z.B. eines russischen Atomeisbrechers) nicht garantiert werden konnte. Nun haben wir hier an den IODP-Lokationen in diesem Jahr – wie auch schon während *Polarstern*-Expedition PS87 in 2014 überhaupt kein Eis vorfinden können (Abb. 1.2), alles hätte also perfekt und ohne Eisbrecher laufen können. Wenn man das vorher gewusst hätte – schade, aber auch ein wenig frustrierend...! Auf jeden Fall konnten mit Expedition PS115/2 wichtige neue seismische und geologische Daten gewonnen werden, die für eine genauere und optimale Festlegung von Lokationen zukünftiger wissenschaftlicher Bohrungen auf dem Lomonosov-Rücken von größtem Wert sind. Diese Bohrungen können nun wahrscheinlich schon im Jahr 2021 realisiert werden, da in jüngster Vergangenheit der ECORD Council auf seinem letzten Meeting im November 2018 die IODP Expedition 377 wieder mit in das Expeditionsprogramm für Spätsommer/Frühherbst 2021 aufgenommen hat (ECORD's Headline #13, 11 November 2018, <http://www.ecord.org/outreach/headlines/> and <http://www.ecord.org/expedition377/>).

Die wichtigsten Fakten der *Polarstern*-Expedition PS115/2 lassen sich wie folgt zusammenfassen:

- Während Transitstrecken und der gesamten Arbeiten in den Untersuchungsgebieten wurden durchgehend vom 14.09. bis zum 04.10.18 (ca. 470 Stunden) PARASOUND-Daten aufgezeichnet. Insgesamt konnten ca. 3900 km neue Hydrosweep-Daten gewonnen und qualitativ hochwertige bathymetrische Detailvermessungen in Teilgebieten des Lomonosov-Rückens und des Amundsen-Beckens durchgeführt werden (Abb. 1.3). Im Amundsen-Becken konnte dabei ein ca. 600 m über die Tiefseeebene herausragender "Seamount" entdeckt werden (Abb. 1.3) (Auch wenn dieser "Seamount" nur weniger als 1000 m über die Tiefseeebene herausragt, nutzen wir hier die Klassifizierung "Seamount"; siehe Diskussion in Staudigel et al., 2010).
- Insgesamt wurden 1160 km seismische Profile aufgezeichnet, z.T. Mehrkanal-Seismik mit dem langen 3000 m Streamer, wobei hier insbesondere die neuen zusätzlichen

Kreuzungslinien über potentielle IODP-Bohrlokationen hervorzuheben sind. Diese Daten sind u. a. wichtige Grundlage für die weitere Optimierung der genauen Lokationen dieser IODP-Bohrpunkte, die wir in einem IODP-Proposal vorgeschlagen hatten (siehe Stein, 2017). Der neu entdeckte "Seamount" im Amundsen-Becken hat nach den seismischen Daten wahrscheinlich einen magmatischen Ursprung.

- Umfangreiche geologische Beprobungen (5 x Kastenlot, 31 x Schwerelet, 20 x Großkastengreifer, 10 x Multicorer, 2 x Dredge) wurden auf dem Lomonosov-Rücken und im Amundsen-Becken durchgeführt (Abb. 1.3). Die Beprobung von ungestörten oberflächennahen Sedimenten mittels Schwere- und Kastenlot an den Lokationen von potentiellen IODP-Bohrpunkten ist eine wichtige Ergänzung der späteren Bohrsequenzen. Das gewonnene Kernmaterial wird sicherlich genauere Rekonstruktionen der jüngeren und älteren Klimageschichte des Arktischen Ozeans erlauben. Zwei Dredge-Gänge über den "Seamount" haben zwar keine Basalte als Indiz für den magmatischen Ursprung ans Tageslicht gefördert, dafür aber eine Anhäufung von z.T. stark verwitterten und von dicken Mangankrusten überzogenen Sand-, Silt- und Tonsteinen an Deck gebracht. Diese wahrscheinlich direkt über der ozeanischen Kruste abgelagerten Sedimente können die einmalige Chance bieten, eine Altersdatierung und einen Einblick in die präglazialen (alttertiären?) arktischen Umweltbedingungen zu ermöglichen.
- Neben dem geowissenschaftlichen Schwerpunktprogramm wurden Eisuntersuchungen (Eiserkundungen auf Hubschrauberflügen, Eisdickenmessungen und Eisbohrungen und Beprobungen auf Eisschollen, Ausbringen von 17 Driftbojen zur Bestimmung der Eisdrift) und Untersuchungen zur Meteorologie (90 Radiosondenaufstiege im Rahmen des „Year Of Polar Prediction – YOPP“; Wolkenmessungen mittels Wolkenkamera) durchgeführt.
- Ein weiterer besonderer Aspekt war die „Floating University ArcTrain“, für die 13 Studenten/innen aus Canada und Deutschland zu Ausbildungszwecken mit an Bord waren. Die „ArcTrainler“, die aus ganz unterschiedlichen Fachrichtungen kamen (Geologie, Meereis, Satellitenbeobachtung, Ozeanographie, Modellierung), waren für alle unsere Arbeitsgruppen eine enorme Hilfe und Bereicherung. Mit großem Einsatz und Interesse und zu jeder Tag- und Nachtzeit waren sie einsatzbereit und voll in das Forschungsprogramm mit integriert.

Fahrtverlauf

„Anker hoch“! Am 05.09.18 gegen 16:00 verließen wir (d.h. 44 Besatzungsmitglieder sowie 49 Wissenschaftler, Hubschrauberpiloten und Techniker) Longyearbyen. Es folgten fünf Tage Transitfahrt, größtenteils durch die Nordost-Passage und somit innerhalb der Russischen „Ausschließlichen Wirtschaftszone“ („Exclusive Economic Zone - EEZ“), bis zum Erreichen unseres Forschungsgebiets (Abb. 1.4). Am 10.09.18, kurz nach Mitternacht und nur wenige Stunden vor Forschungsbeginn mussten wir wegen eines akuten medizinischen Notfalls umdrehen und in Richtung Longyearbyen zurückdampfen. Am 11.09.18 gegen 22:45 fand dann ein Rendezvous mit einem Rettungshubschrauber NE von Svalbard bei 81°N/40°E statt (Abb. 1.4), der zwei Patienten aufgenommen und in Richtung Krankenhaus bzw. Heimat transportiert hat.

Am 14.09.18 um 12:27 verließen wir die Russische EEZ, und die Forschungsaktivitäten konnten beginnen. Ein erster Meereismess- und Beobachtungsflug mit dem Helikopter wurde von der Meereisgruppe durchgeführt. Die erste Geostation, auf der Großkastengreifer und Kastenlot erfolgreich eingesetzt wurden, folgte dann gegen 18:00. Am 15.09.18 wurden vier

Meeresbodenseismometer („OSB“) an der Nordflanke des Gakkel-Tiefs in einer Wassertiefe von ca. 4.000 m ausgesetzt. Diese OBS-Systeme sollen nun in den folgenden 12 Monaten Erdbebenaktivitäten im Bereich des Gakkel-Rückens aufzeichnen und dann hoffentlich im Herbst 2019 wieder von *Polarstern* aufgenommen werden. Parallel zu den OBS arbeiten wurden Eisarbeiten durchgeführt (Messungen von Eisdicken, Eisbeprobungen, Aussetzen von Driftbojen). Am 16.09.18 wurde eine weitere geologische Beprobung im Gakkel-Tief in 5.000 m Wassertiefe angesetzt, auf der Schwerelot und Kastengreifer zum Einsatz kamen. Nach Abschluss dieser Arbeiten wurde mit einer dreitägigen seismischen Profilfahrt vom Gakkel-Tief durch das gesamte Amundsen-Becken bis hin zum Lomonosov-Rücken begonnen, auf der Kreuzungsprofile über drei der vorgeschlagenen Lokationen für mögliche IODP-Bohrungen (LR-06A, LR-05A and LR-03A) eingefahren wurden (Abbs. 1.2 and 1.3).

Am 19.09.18 erfolgten im direkten Anschluss an die seismische Profilfahrt weitere geologische Beprobungen an vier Stationen. An der letzten dieser Stationen, die der vorgeschlagenen Lokation von IODP Site LR-06A entsprach, kam in der Nacht 19./20.09.18 das Kastenlot zum Einsatz. Am 20.09.18 wurde dann eine Geostation aufgesucht, auf der nach Daten der *Polarstern*-Expedition PS51 (Jokat, 1999) wahrscheinlich präquartäre Sedimente oberflächennah ausstreichen. Nach einer Hydrosweep- und PARASOUND-Vermessung wurde dort so eine intensive geologische Beprobung durchgeführt, auf der an sechs nah bei einander gelegenen Lokationen das Schwerelot sechsmal eingesetzt wurde. An den dann folgenden zwei Tagen (21.-22.09.18) wurden dann weitere geologische vier Stationen auf dem Lomonosov-Rücken abgearbeitet.

Für den 23.09.18 wurde eine längere „Multi-Station“ angesetzt, auf der parallel geologische Sedimentbeprobungen und umfangreiche Eisarbeiten auf einer größeren Eisscholle durchgeführt werden sollten. Trotz intensiver Bemühungen konnte keine Eisscholle von geeigneter Größe und Dicke gefunden werden, so dass diese Station leider getrichen werden musste. Es erfolgte so eine geologische Beprobungsaktion mit Großkastengreifer und Kastenlot an der Lokation der vorgeschlagenen IODP-Bohrung LR-09A (Abbs. 1.2 und 1.3). Nach Abschluss dieser Arbeiten wurde am selben Tag gegen 19:00 mit einer weiteren seismischen Profilfahrt begonnen. Wegen der guten Eisbedingungen konnte hier der 3000 m-Streamer ausgebracht werden.

Wegen zu schlechter Wetterbedingungen - Windstärken von 8-9 Bft mit Wellenhöhen von 3 bis 4 m - musste dann am 27.09.18 nachmittags die Seismik abgebrochen werden. Unter diesen Bedingungen war schließlich auch keine Geostation möglich, so dass entschieden wurde, weiter nach Norden Richtung Eisrand zu dampfen. Als die Wetter- und Eisbedingungen und auch die Sichtverhältnisse schließlich gut genug waren, wurden am 28.09.18 auf 82°N/148°45'E (Abb. 1.3; PS115/2_30, die östlichste Position der gesamten Expedition) zeitgleich geologische Sedimentbeprobungen (inkl. Kastenloteinsatz) und zwei Helikopterflüge für Eisbeobachtungen und Aussetzen einer Driftboje durchgeführt. In den drei folgenden Tagen (29.09.-01.10.18) erfolgte dann ein intensives geologisches Beprobungsprogramm mittels Schwerelot auf dem südlichen Lomonosov-Rücken (Abb. 1.3).

Am 02.10.18 wurden die vorgeschlagenen Lokationen der IODP Sites LR-02A and LORI-16A (Abb. 1.3) angefahren und Großkastengreifer, Schwerelot und Kastenlot für die Sedimentbeprobungen eingesetzt. Am 03.10.18 erreichten wir wieder das Gebiet des neu entdeckten „Seamount“ im Amundsen-Becken, wo zweimal erfolgreich die Gesteinsdredge eingesetzt wurde und zahlreiche verfestigte Sand-, Silt- und Tonsteine an Bord gebracht wurden. Am 04.10.18 fand dann eine letzte geologische Beprobung mittels Schwerelot sowie ein letztes Aussetzen einer Driftboje auf einer Eisscholle statt. Am selben Tag wurde dann um 10:00 Bordszeit das Forschungsprogramm der Expedition PS115/2 beendet, Geräte und Registriereinrichtungen abgeschaltet und mit der Rückfahrt Richtung Bremerhaven begonnen.

Auf unserem Rückweg Richtung Bremerhaven hatten wir einen kurzen Zwischenstop in Tromsø (Abb. 1.4). Dort wurden neun Ingenieure und Techniker eingeschifft, die bereits während der letzten Tage unserer Expedition mit vorbereitenden Maßnahmen für die in Bremerhaven anstehenden umfangreichen Werftarbeiten beginnen sollten. Im „Austausch“ gingen die vierköpfige HeliService-Gruppe sowie je eine Person aus Besatzung und Wissenschaft von Bord. Am 16.10.18 gegen 08:30 erreichte *Polarstern* dann Bremerhaven.

Obwohl wegen eines medizinischen Notfalls am Anfang der Expedition eine sofortige Umkehr und Rückfahrt Richtung Longyearbyen erforderlich war und damit fünf Expeditionstage wegfielen, sind am Ende die Hauptziele der Expedition alle erreicht worden. Dies geht zum einen auf die Hin- und Rückfahrt durch die jeweils eisfreie Russische EEZ zurück (was kalkulierbarer war und Zeit gespart hat), zum anderen aber auch insbesondere auf die exzellente Zusammenarbeit zwischen Mannschaft und Wissenschaft. Wir möchten uns so abschließend ganz herzlich bei Kapitän Wunderlich und seiner Besatzung für die große Unterstützung und Hilfsbereitschaft in allen Situationen bedanken.

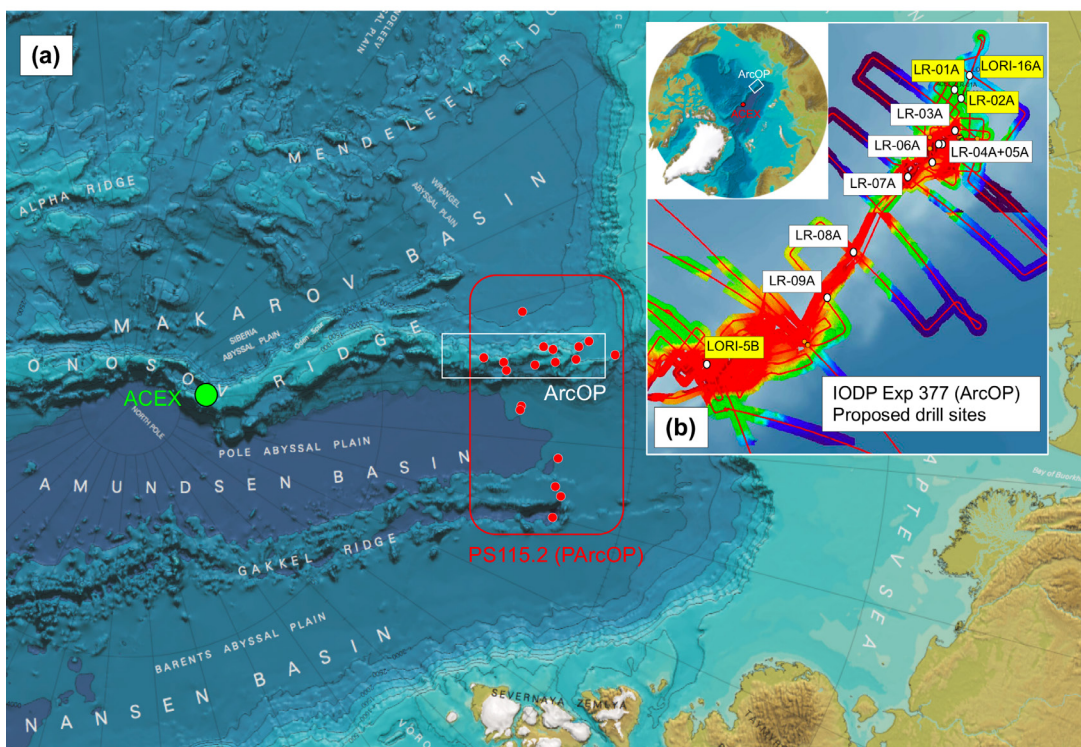


Abb. 1.1: (a) Hauptarbeitsgebiet der Expedition PS115/2 (rote Box) mit Lokationen der Geostationen (rote Kreise); das Arbeitsgebiet der geplanten IODP Expedition 377 (ArcOP) zeigt die weiße Box. (b) Karte rechts oben zeigt mögliche Lokationen für IODP-Bohrungen im Rahmen der IODP Expedition 377 (ArcOP; Stein et al., 2015; Stein, 2017; <http://www.ecord.org/expedition377/>) und Profillinien der Hydrosweep-Vermessungen während Expedition PS87 (Stein, 2015).

Fig. 1.1: (a) Main working area of Expedition PS115/2 (red box) with locations of geological stations (red circles); working area IODP Expedition 377 (ArcOP) is shown as white box. Map in the right upper corner (b) display locations proposed drill sites for IODP Expedition 377 (ArcOP; details in Stein et al., 2015; Stein, 2017; <http://www.ecord.org/expedition377/>) and tracks of PS87 Hydrosweep survey (Stein, 2015).

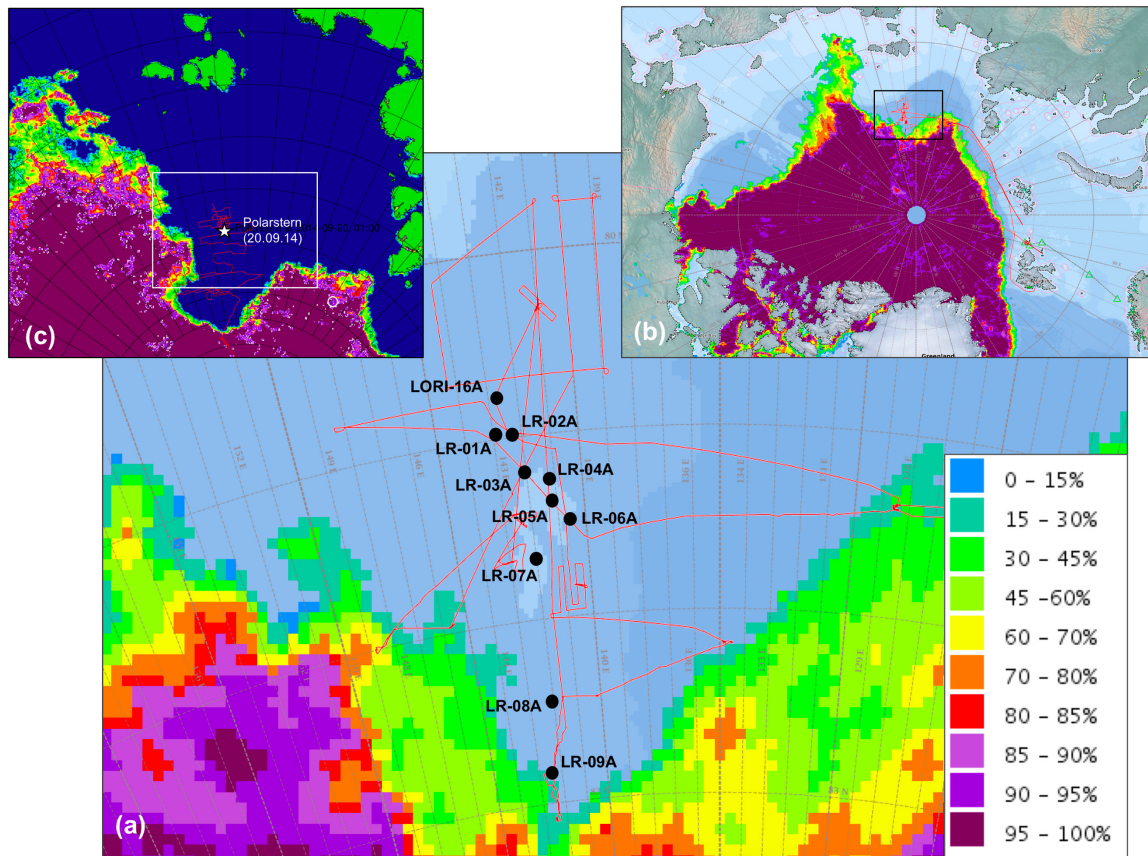


Abb. 1.2: Arktische Meereiskonzentrationen Mitte September 2018 (<http://mapserver.fs-polarstern.de:8081/mapviewer>). Rote Linie zeigt die Fahrtroute unserer Expedition. (a) Detailkarte für das Umfeld des PS115/2-Arbeitsgebiets, (b) Übersichtskarte mit den Meereiskonzentrationen für den gesamten Arktischen Ozean. Die Lokationen potentieller IODP-Sites der geplanten und dann leider abgesagten IODP Expedition 377 sind angegeben. Alle Lokationen wären in diesem Jahr im eisfreien Wasser gewesen!! (c) Arktische Meereiskonzentrationen Mitte September 2014, d.h., während der Polarstern-Expedition PS87 (Stein, 2015). Der gelbe Stern zeigt die Polarstern-Position am 20.09.14. Auch während dieser Expedition waren alle vorgeschlagenen IODP-Bohrlokationen in mehr oder weniger eisfreien Wasser.

Fig. 1.2: Arctic sea-ice concentration in mid-September 2018 (<http://mapserver.fs-polarstern.de:8081/mapviewer>). Red line indicates cruise track. (a) Detailed map of the PS115/2 working area, (b) Overview mapping showing the sea ice concentration of the entire Arctic Ocean. The locations of potential IODP drill sites of the scheduled and unfortunately later cancelled IODP Expedition 377 are shown in (b). Note: all of the locations are in ice-free waters! (c) Arctic sea-ice concentration in mid-September 2014, i.e., during Polarstern Expedition PS87, one of the main sites survey expeditions for IODP Expedition 377 (Stein, 2015). The yellow star shows the Polarstern position on 20 September 2014. Also in 2014, the locations of the proposed IODP sites were in more or less ice-free waters.

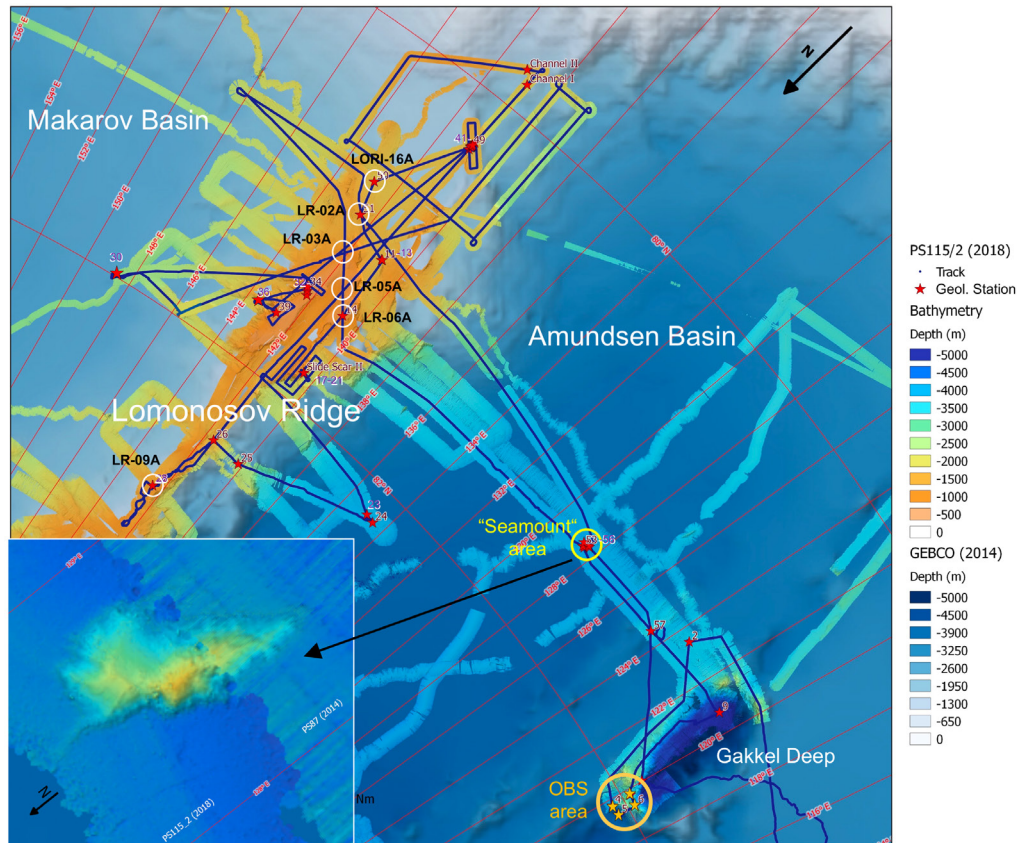


Abb. 1.3: Bathymetrische Karte mit Fahrtroute und Hydrosweep-Tracks der Expedition PS115/2. Zusätzlich sind ausgewählte Hydrosweep-Tracks älterer Polarstern-Expeditionen eingetragen (siehe Bathymetrie-Kapitel für weitere Details). Die geologischen Stationen der Expedition PS115/2 sind als rote Sterne eingetragen, die Lokationen der möglichen IODP-Bohrlokationen LR-09A, LR-06A, LR-05A, LR-03A, LR-02A und LORI-16A als weiße Kreise hervorgehoben. Das Gebiet um den neu entdeckten "Seamount" und das OBS-Gebiet sind als gelber bzw. oranger Kreis markiert.

Fig. 1.3: Bathymetry map with cruise and hydrosweep track of expedition PS115/2 and selected tracks from earlier Polarstern expeditions (map by courtesy of M. Steffen and S. Andree, AWI Bathymetry; see Bathymetry Chapter for further details). In addition, the PS115/2 geological stations (red stars) are shown. Locations of potential future IODP drill holes LR-09A, LR-06A, LR-05A, LR-03A, LR-02A and LORI-16A are marked by white circles. The areas of the discovered "Seamount" (yellow circle and enlargement in the lower left corner) and of the deployment of the OBS system (orange circle) are shown as well.

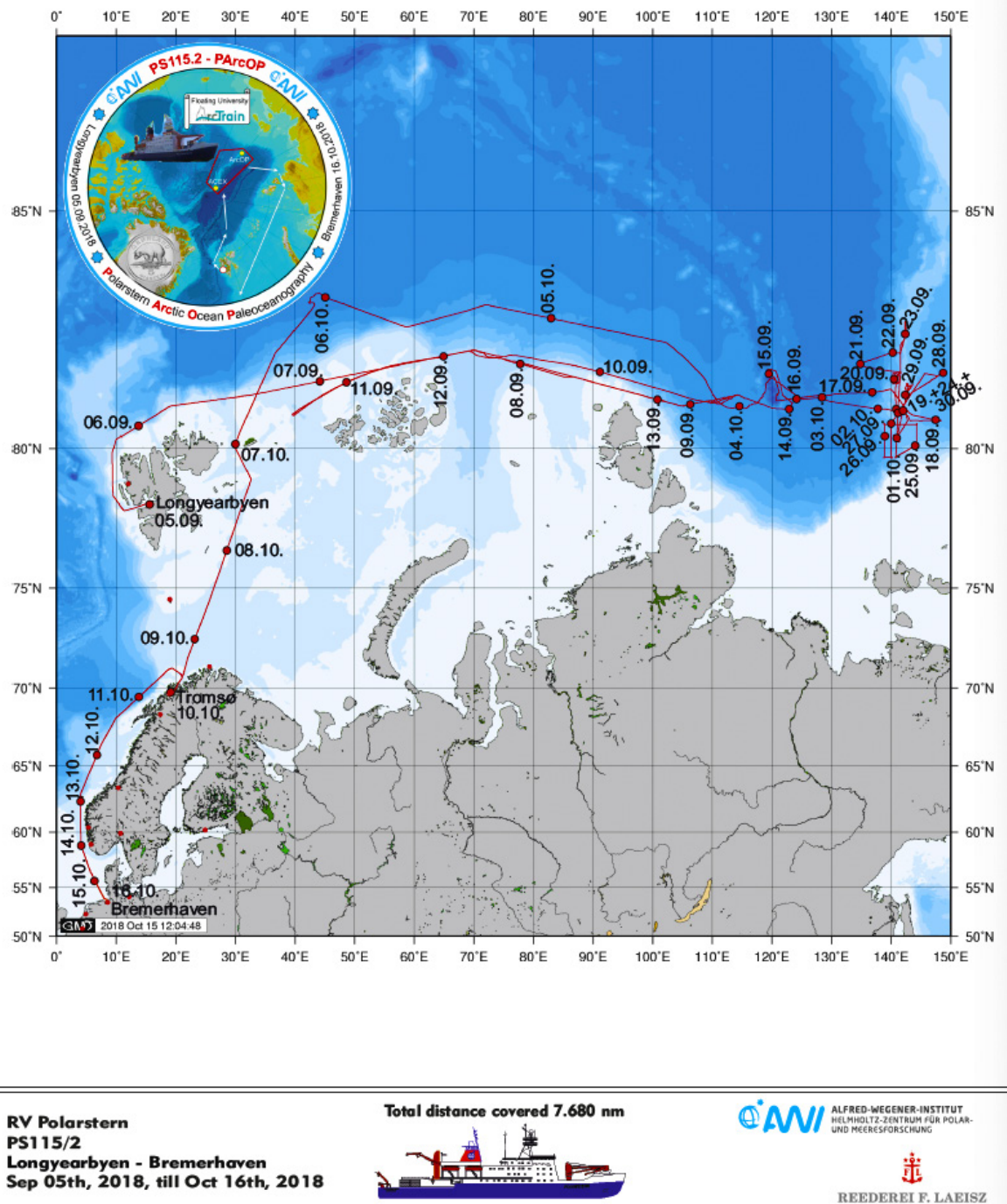


Abb. 1.4: Fahrtroute der PS115/2-Expedition. Siehe <https://doi.pangaea.de/10.1594/PANGAEA.895773> für eine Darstellung des master tracks in Verbindung mit der Stationsliste für PS115/1.

Fig. 1.4: Cruise track of PS115/2-Expedition. See <https://doi.pangaea.de/10.1594/PANGAEA.895773> to display the master track in conjunction with the list of stations for PS115/1.

SUMMARY AND ITINERARY

Summary

Expedition PS115/2 (“**P**olarstern **A**rctic **O**cean **P**aleoceanography – PArcOP”) was mainly related to geoscientific investigations in the area of the southern Lomonosov Ridge and the Amundsen Basin towards the Laptev Sea continental margin (Fig. 1.1). The overall goal of the research programme was the detailed reconstruction of the short- and long-term climate history as well as the tectonic evolution of the Arctic Ocean, based on seismic reflection and marine-geological data. The main research area as well as the key objectives of Expedition PS115/2 are closely related to those of IODP Expedition 377 (“**A**rctic **O**cean **P**aleoceanography - ArcOP”; see Stein 2017 for background and references) (Fig. 1.1). This IODP expedition already scheduled for mid-August to mid-October that year and originally planned as joint venture together with our *Polarstern* Expedition 115/2, was cancelled because the availability of an additional powerful primary icebreaker (e.g., one of the Russian nuclear icebreakers) could not be guaranteed as in-kind contribution (= no additional costs for IODP) in time. However, this year – similar to the ice conditions during *Polarstern* Expedition PS87 in 2014 – we did not find any ice at all the potential drill sites (Fig. 1.2), i.e., the drilling campaign could have been carried out without any additional icebreaker support. What a pity (but also somehow frustrating) that we had not known this in advance! In any case, with Expedition PS115/2 new seismic and geological site survey data became available that is of major importance for selecting the optimum site locations for future scientific drilling on Lomonosov Ridge. Most recently, i.e., in November 2018, the ECORD Council approved the re-scheduling of IODP Expedition 377 for late summer/early autumn 2021 (see ECORD’s Headline #13, 11 November 2018, <http://www.ecord.org/outreach/headlines/>). Let’s hope and fingers crossed that this IODP drilling campaign will become reality and will be carried out successfully.

Some key facts of the Expedition PS115/2 can be summarized as follows:

- During transit and within the main working areas, PARASOUND was running continuously between 14 September and 04 October (ca. 470 hours). In total ca. 3,900 km of new Hydrosweep profiles were collected and detailed high-quality bathymetry surveys were carried out in selected areas of the Lomonosov Ridge and the Amundsen Basin (Fig. 1.3). In the Amundsen Basin, an unknown isolated “seamount” elevating about 600 m above the abyssal plain, was discovered (Fig. 1.3) (even if the elevation height is <1,000 m above the abyssal plain and thus only might be classified as “knoll”, we use the classification “seamount”; see discussion about definition in Staudigel et al., 2010).

- In total, 1,160 km of high-quality seismic profiles were recorded, part of which are multichannel seismic lines with the 3,000 m long streamer. These data are important to optimize the locations of potential drill site we have proposed for a future IODP drilling campaign in the Lomonosov Ridge area. Based on our new seismic data, the newly discovered seamount in the Amundsen Basin has most probably a magmatic origin.
- A detailed geological coring programme (5 x Kastenlot corer, 31 x Gravity corer, 20 x Giant box corer, 10 x Multicorer, 2 x Dredge) was carried out on Lomonosov Ridge and in the Amundsen Basin (Fig. 1.3). The coring of undisturbed near-surface sediment sections from potential IODP drill sites is an important supplement to the long deep sedimentary sections hopefully to be drilled during a future IODP drilling campaign. Furthermore, the recovered high-quality sediment cores will certainly allow detailed reconstructions of the Quaternary climate and paleoenvironmental history. The rocks dredged from the seamount unfortunately did not contain any magmatic/basaltic material. However, they are composed of sand-, silt- and claystones, partly covered by manganese crusts. These rocks are probably more or less directly overlying the oceanic basement and thus may allow to get some information about the age of the basement as well as some insight into the “old” (early Cenozoic?) climate and environmental history of the preglacial warm & ice-free Arctic Ocean.
- The geoscientific programme was supplemented by additional activities related to sea ice studies (i.e., ice observations during helicopter flights, measurements of sea ice thickness, ice coring and the deployment of 17 drift buoys) and meteorological studies (i.e., the launching of 90 radiosondes attached to a weather balloon as part of the special observing period of the “Year Of Polar Prediction – YOPP”, and measurements of the cloud base height using a cloud camera system).
- As major part of Expedition PS115/2, a “Floating University” was held onboard *Polarstern* under the umbrella of the International Research Training Group “Processes and impacts of climate change in the North Atlantic Ocean and the Canadian Arctic - ArcTrain”. Within this programme, 13 Canadian and German PhD and master students with very different scientific backgrounds (i.e., geosciences, sea ice, glaciers, oceanography, remote sensing, and modelling) were introduced to all technical aspects of field work in marine sciences as well as to the concepts of teamwork and interdisciplinary and international collaboration. All the ArcTrain students did an excellent job and contributed significantly to the success of this expedition.

Itinerary

Polarstern left Longyearbyen/Svalbard (Fig. 1.4) on September 05 around 16:00, onboard 44 crew members and 49 scientists, helicopter pilots, and technicians from a large number of different institutions in Germany, Canada and Russia. Five days of transit ahead of us, most of this transit through the Northeast Passage, the Russian Exclusive Economic Zone (EEZ), before reaching our main working area. On September 10, shortly after midnight, bad news: a serious case of medical emergency, the expedition’s program had to be stopped, and we had to steam back towards Longyearbyen. On September 11 at about 22:45 we had a rendezvous with a long-range rescue helicopter NE of Svalbard at 81°N/41°E (Fig. 1.4) where a rescue team took-over our two patients.

On September 14 at 12:27 we left the Russian EEZ and could start with our PS115/2 research activities. The *enroute* profiling systems Hydrosweep and PARASOUND were switched-on and recording started. A first sea ice observation and measurement flight was carried out by the sea ice group. The first geological station was reached at 18:00, and the giant box

corer and the kastenlot corer were run successfully. On September 15, four “Ocean Bottom Seismometer” (OBS) systems were deployed at the northern flank of the Gakkel Deep in a water depth of about 4,000 m (Fig. 1.3). These OBS system will now stay at the seafloor for 12 months, monitoring the earthquake activities in the Gakkel Ridge area. In autumn 2019, they hopefully will be recovered again. Contemporaneously to the OBS activities, some ice station work (measurements of ice thickness, deployment on drift buoys) could be done. On September 16, a second geological station was scheduled with coring activities in the Gakkel Deep at about 5,000 m water depth. On the same day, after having finished the geological station work, we started with a three-days seismic survey from the Gakkel Deep through the entire Amundsen Basin towards Lomonosov Ridge, crossing the locations of three proposed IODP drill sites (LR-06A, LR-05A and LR-03A) (Figs. 1.2 and 3).

On September 19, after having finished the seismic survey, we directly continued with a geological sampling programme at four stations, including a kastenlot coring at the location of the proposed IODP drill site LR-06a during the night of September 19/20 (Fig. 1.3). On September 20, we revisited a coring location from *Polarstern* Expedition PS51 (Jokat, 1999) where probably old (pre-Quaternary?) sediments are cropping out, and carried out a Hydrosweep and PARASOUND survey, followed by detailed coring activities by means of the gravity corer at six close-by stations. During the following two days (September 21 and 22), the geological coring programme on Lomonosov Ridge continued.

For September 23, a major multi-station with contemporaneous geological and sea ice work was planned. As no ice floe big and thick enough for intensive sea ice work by a larger group of people was found, we had to cancel this program. Instead, a geological station with multicorer, giant box corer and kastenlot corer was scheduled at the location of the proposed IODP Site LR-09A (Figs. 1.2 and 1.3). After having finished the coring activity, the second seismic survey started at 19:00. As ice conditions allowed, the long 3,000 m long streamer was used for the survey.

In the afternoon of September 27, we had to stop the seismic profiling as weather conditions became worse, i.e., we got very strong winds (8-9 Bft) with 3 to 4 m high waves. As the weather was even not good enough for a geological station we steamed towards the north back into the ice. As the ice, weather and visibility conditions became then good enough, contemporaneously geo-station work (including a kastenlot run) and two helicopter flights for sea ice observations and the deployment of a drift buoy were scheduled and carried out on September 28 at 82°N/148°45'E (Fig. 1.3; PS115/2_30, the easternmost station of the entire expedition). A further intensive geological coring program with several runs of the gravity corer followed between September 29 and October 01 on southern Lomonosov Ridge (Fig. 1.3).

On October 02, we visited the locations of the proposed IODP drill sites LR-02A and LORI-16A (Fig. 1.3), where near-surface sediments were recovered by means of the giant box corer, gravity corer and kastenlot corer. At the seamount discovered during our expedition, the stone dredge was used successfully two times on October 03, and a large number of sand-, silt- and claystones were recovered. On October 04, we had a final geostation with one further gravity corer run and an ultimate ice station for deployment of a drift buoy. The same day at 10:00, we stopped all scientific research instruments and registration systems – this was the end of our research program, and we started our return journey to Bremerhaven.

During our way back to Bremerhaven, we had a short stop in Tromsø on October 10 (Fig. 1.4) to embark nine engineers and technicians who directly started onboard *Polarstern* with some prework to prepare the large-scale and time-consuming reparation work to be done during the coming shipyard stay in Bremerhaven. In “exchange” the four HeliService persons as well as two persons from the crew and science party left the ship in Tromsø. On October 16 at about 08:30 am, *Polarstern* arrived in Bremerhaven (Fig. 1.4).

Although we had to steam back towards Longyearbyen due to a serious case of medical emergency and thus lost about five days of research time, we could achieve all our main research goals at the very end. This was mainly possible for two reasons. First, we could use the Northern Sea Route through the Russian EEZ twice, i.e., during the transit towards the main study area as well as for the way back. Dominantly ice-free conditions allowed a much more precise expedition's planning and also saved time. Second and not less important, was the excellent cooperation between crew and scientists during the entire expedition, in all situations and during day and night. For this strong support throughout the entire expedition, we cordially thank our Captain Thomas Wunderlich and his entire crew.

References

- Jokat W (Ed) (1999) Arctic '98: The Expedition of the Research Vessel *Polarstern* to the Arctic in 2008, Rep. Pol. Res. 597, 221 pp.
- Staudigel H, Koppers AAP, Lavelle JW, Pitcher TJ, Shank TM (2010) Defining the Word "Seamount". *Oceanography* 23, 20-21.
- Stein R (Ed) (2015) The Expedition PS87 of the Research Vessel *Polarstern* to the Arctic Ocean in 2014, Reports on Polar and Marine Research 688, Bremerhaven, Alfred Wegener Institute for Polar and Marine Research 688, 273 pp (http://epic.awi.de/37728/1/BzPM_0688_2015.pdf).
- Stein R (2017) From Greenhouse to Icehouse: The late Mesozoic-Cenozoic Arctic Ocean sea-ice and climate history. *Polarforschung* 87, 61-78.
- Stein R, Jokat W, Niessen F and Weigelt E (2015) Exploring the long-term Cenozoic Arctic Ocean Climate History – A challenge within the International Ocean Discovery Program (IODP). *Arktos* 1, doi: 10.1007/s41063-015-012-x.

2. WEATHER CONDITIONS DURING EXPEDITION PS115/2

Max Miller, Christian Rohleder

DWD

Weather conditions during Expedition PS115/2 (05 September – 15 October 2018) are summarized in Figs 2.1 and 2.2.

On Wednesday afternoon, September 05 2018, 16:15 pm, *Polarstern* left Longyearbyen for the campaign PS115/2. Light to moderate south-easterly winds, 6° C and light rain were observed.

Leaving the fjord (and its shelter) winds veered rapidly southwest and increased up to 6 Bft at a sea state of 2 m. Soon winds veered northwest and abated on Thursday (Sep. 06) off the north coast of Svalbard.

On our way east we got at the southwest side of a low over Laptev Sea heading north. During the night to Friday north-westerly winds freshened up to 7 Bft and abated again on Saturday (Sep. 08). Due to steaming close to the ice the sea state could not exceed 2 m.

From the New Siberian Islands a high spread northeast. We got at its south side and light winds veered southwest on Sunday (Sep. 09). A medical emergency forced *Polarstern* to turn back. Late Tuesday evening (Sep. 11) a SAR-helicopter from Longyearbyen took over the patient between Franz-Josef-Land and Svalbard at light winds but some snow showers.

Northeast of Severnaya Zemlya a low had formed and headed towards Franz-Josef-Land. Steaming east towards the research area again we passed its southern end on Wednesday (Sep. 12). South-westerly winds increased up to 6 Bft for short times. Snowfall was temporarily observed, too.

Northwest of Banks Island a high formed and became stationary for several days. On Thursday (Sep. 13) it built a ridge towards Laptev Sea. *Polarstern* got into the ridge at light southerly winds. On Friday breaking clouds enabled helicopter flights, but soon fog patches approached again.

A low over eastern Siberia built a trough towards Severnaya Zemlya. Therefore on Sunday (Sep. 16) winds veered east and freshened up to 6 Bft. At first it was snowing, later rain was mixed in. On Monday winds abated but rain, snow and fog patches did not allow any flight operation. On Wednesday (Sep. 19) a small low formed near the New Siberian Islands and moved northeast. Soon winds veered north and freshened up to 5 Bft. Precipitation changed into snow and decreased. Finally on Saturday (Sep. 22) clouds broke temporarily and helicopter operations became possible.

On Sunday (Sep. 23) a storm (Ex-“Helene”) had reached North Cape and headed further north. On Monday it split near Svalbard. One part moved towards the Queen-Elizabeth-Islands and the other slowly northeast. On Wednesday (Sep. 26) *Polarstern* got at the east side of this system. Winds veered southwest and increased up to 7 Bft. Close to the Taymyr Peninsula an additional secondary low formed and moved northeast. On Friday winds veered south, peaked at 8 Bft and forced a sea state up to 4 m off the ice.

Weather enroute PS115/2

from 05.09.2018 00 UTC to 15.10.2018 06 UTC

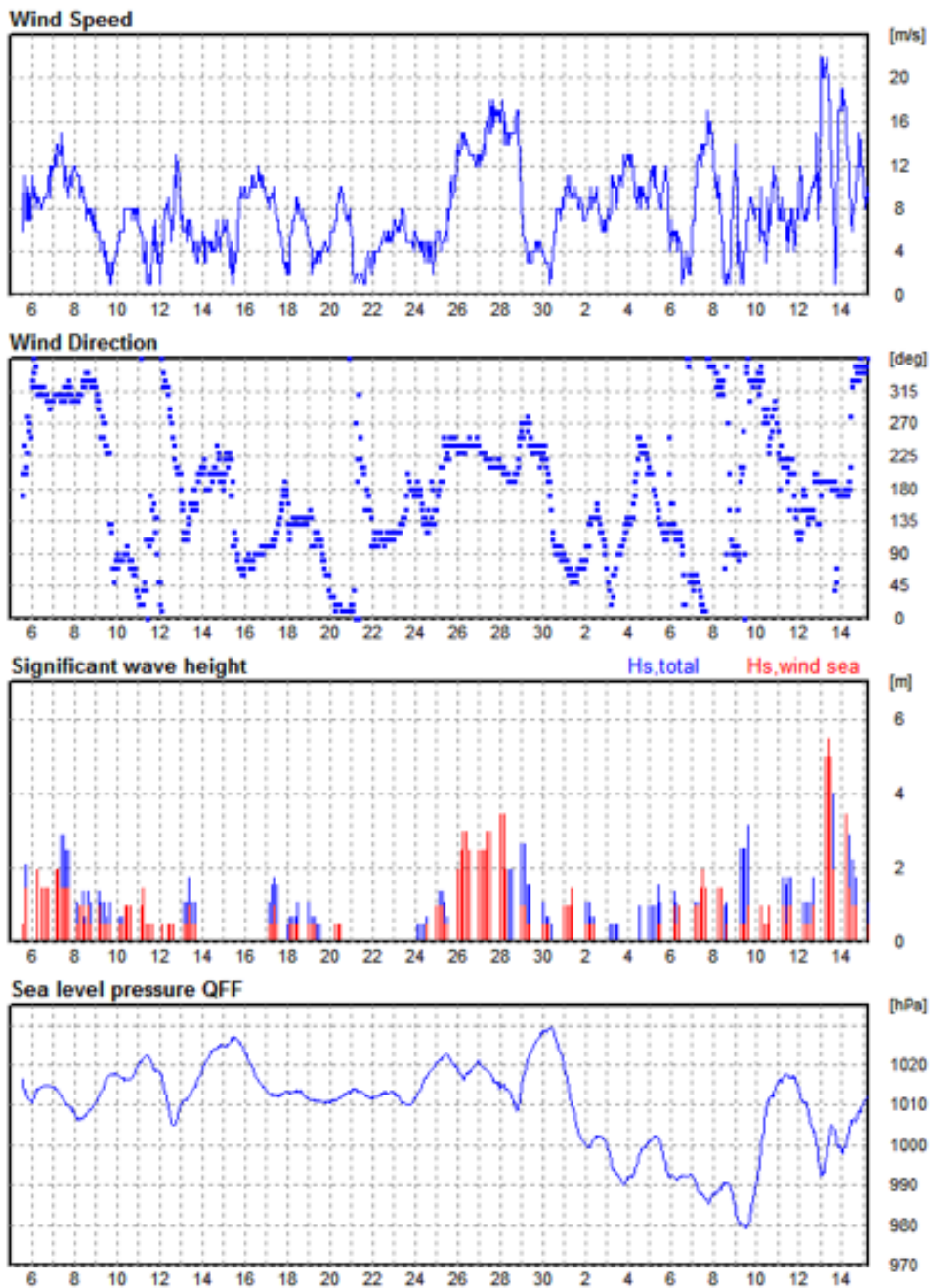


Fig. 2.1: Weather conditions during Expedition PS115/2 (05 September – 15 October 2018), Part 1: Wind speed, wind direction, significant wave height, and sea level pressure

Weather enroute PS115/2
from 05.09.2018 00 UTC to 15.10.2018 06 UTC

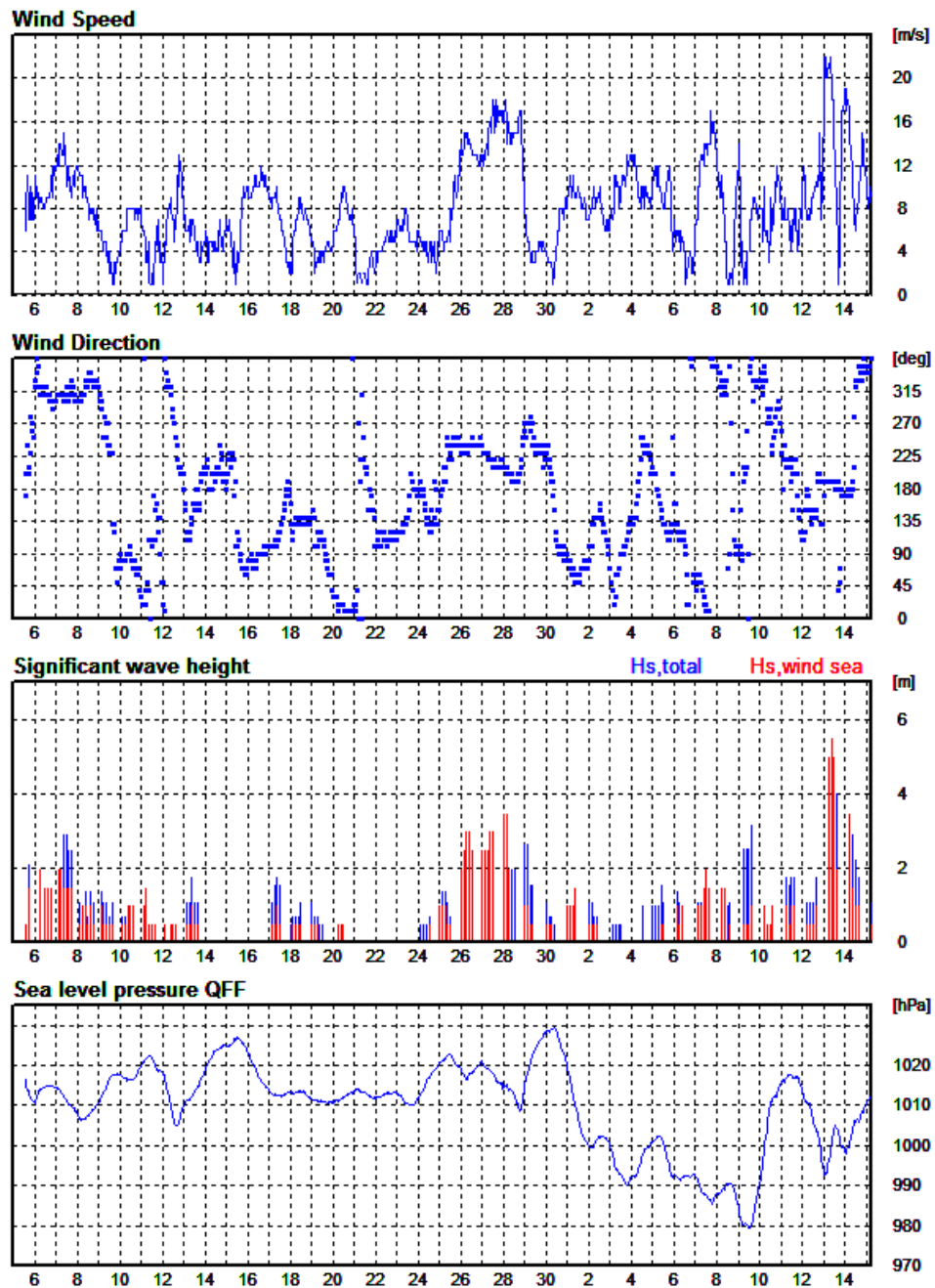


Fig. 2.2: Weather conditions during Expedition PS115/2 (05 September – 15 October 2018), Part 2: Visibility, cloud cover, ceiling, and temperature

From Beaufort Sea a ridge spread towards Laptev Sea. Already during the night to Saturday (Sep. 29) winds abated clearly. On Sunday the calm high pressure influence persisted and enabled a helicopter flight.

Over eastern Siberia a new low had formed. On Monday (Oct. 01) *Polarstern* got at its edge at south-easterly winds 5 to 6 Bft. On Wednesday (Oct. 03) the low crossed the New Siberian Islands and headed towards Severnaya Zemlya. Winds veered south and peaked at 7 Bft but the sea state was dampened by ice.

Noon on Thursday (Oct. 04) we started our return journey (first towards Tromsø) and followed the low at abating winds. But the low became stationary between Svalbard and Franz-Josef-Land. Therefore on Sunday (Oct. 07) northerly winds increased up to 7 Bft while steaming the east side of Svalbard. The parallel coastline accelerated the northerly winds, too.

A low near Iceland headed towards Barents Sea. On Tuesday (Oct. 09) *Polarstern* crossed the low at light and variable winds. During the night to Wednesday north-westerly winds freshened up to 6 Bft at its west side.

Noon on Wednesday (Oct. 10) *Polarstern* tied up in Tromsø for short times at moderate westerly winds and some showers. A high over Eastern Europe built a ridge towards Scandinavia. Therefore during the first part of the remaining return journey southerly winds didn't exceed 5 Bft at a sea state up to 2 m.

On Thursday (Oct. 11) a low developed north of the Azores. It deepened rapidly to a storm and moved north. Friday evening (Oct. 12) southerly winds increased up to 8 and after midnight to 9 Bft forcing a sea state of 6 m. On Saturday the storm abated temporarily but increased again up to 8 to 9 Bft during the night to Sunday (Oct. 14) while steaming off Bergen. The parallel coastline contributed an additional push to the southerly winds. On Sunday winds abated finally and veered northwest.

On Tuesday morning, October 16, 2018, *Polarstern* reached Bremerhaven at light to moderate south-westerly winds.

3. METEOROLOGY & RADIOSOUNDING

Dirk Olonscheck¹,
not on board:
Holger Schmithüsen², Stefan Kinne¹

¹MPI-M
²AWI

Grant-No. AWI_PS115/2_02

Objectives

The objectives of the meteorological activities during PS115/2 are twofold: First, we collect radiosounding data at high temporal resolution to substantially improve the understanding of the state of the Arctic atmosphere. This should contribute to significantly improve our weather forecast abilities in the northern high latitudes. Second, we collect high-frequency data of clouds, aerosols and water vapor, which in conjunction with meteorological data on the ship, will provide valuable insights into the spatio-temporal variability and the small-scale processes of water and aerosols in the Arctic atmosphere. Clouds and aerosols substantially affect the Earth's climate (i.e., small changes in cloud/aerosol parameters can lead to large impacts on many aspects of the simulated climate), but the understanding of cloud processes, and the representation of clouds, aerosols and their radiative effects in climate models still remain challenging. For a better understanding of clouds and their interactions with radiation, and to evaluate and improve the representation of clouds in climate models, observations of the spatio-temporal variability of clouds are required. Both objectives contribute to a better understanding of the variability and relevant processes of the Arctic atmosphere, as well as improved weather forecasts in the rarely sampled northern high latitudes.

Work at sea

The work at sea consists of three activities: First, the extra launches of radiosondes at every six hours (6 pm, 12 pm and 6 am UTC) in addition to the launch at 12 am UTC. Second, the running of a cloud camera system that automatically records optical and thermal images of the ceiling every ten seconds. And third, the sampling of aerosol properties and water vapour content based on sun-photometer measurements.

The additional radiosoundings are performed as part of the Year Of Polar Prediction (YOPP), a two-year project of the World Meteorological Organisation that aims to improve the weather forecasts in the Arctic by a coordinated network of observations. We performed these additional radiosoundings whenever we were outside the Russian Exclusive Economical Zone (EEZ) and 70 nm away from Norwegian land. Overall, we launched 90 radiosondes during PS115/2 mainly under sufficiently calm conditions and without major failures. The launching procedure includes the calibration of the radiosonde, filling and launching of the weather balloon and the recording of the station data at the time of the launch. The collected data of temperature, relative humidity, air pressure and winds from the sea surface up to about 35 km provides a rich data base of Arctic weather conditions. The collected data are also used directly to judge the safety of the helicopter flight activities during the cruise.

The 'Pinocchio' cloud camera system from MPI-M was installed on the pile deck at the starboard side railing and operated continuously from 6 September 2018 until 14 October 2018. It contains two cameras, one for visible and one for near-infrared radiation. Pointed towards the sky, it automatically records images of the ceiling every 10 seconds. While the images from the hemispheric visible camera are only used for comparison purposes during daytime, the images from the thermal camera (sensitive in the near IR-range 8.5-11.0 μm) can be used for the whole 24 hours. Before the cruise, the thermal camera was calibrated in laboratory in order to determine the brightness temperature for every pixel of each infrared image. With a field of view of 45°, the calibrated thermal camera provides temperature images of the ceiling. Thus, it cannot only sample cloud cover but also cloud field organization and cloud base altitudes. In contrast to a ceilometer that was running on board as well, the cloud camera does not only provide a point measurement of the cloud base altitude above the ship, but allows for a comprehensive picture of the spatio-temporal variability of the cloud base altitude. We started on board with the postprocessing of the infrared images to derive and analyze the spatio-temporal variability of the cloud cover and the cloud base altitude. To do so, we used the temperature profiles from the 6-hourly radiosoundings to infer an effective lapse rate for each time window. The derivation of the cloud properties and their spatio-temporal variability will be subject of ongoing research at MPI-M.

Finally, aerosol properties and water vapor content are sampled using a MICROTOPS sun-photometer that was provided by NASA. The MICROTOPS measurements are a contribution to the very sparse network of measurements over the remote waters of the Central Arctic. The small hand-held instrument measures the direct solar radiation during daylight when the solar disk is not obscured by clouds. It is combined with a GPS to estimate the intensity of the solar radiation at the top of the atmosphere. Incoming solar radiation measured on the ship is reduced by absorption and scattering. Based on associated differences in radiation, the properties of atmospheric aerosols and the water vapor content are derived. Unfortunately, the weather conditions during PS115/2 did not allow for many MICROTOPS measurements. Because of only four days with an unobscured view on the solar disk, I only had very few possibilities to measure the atmospheric aerosols and the water vapor content. Furthermore, the low angle of the sun that did not become larger than 7 degrees above the horizon limited the windows of useful measurements and likely requires to apply a correction to the few measurements. The data was submitted to and quality checked by the Marine Aerosol Network (MAN) as part of the Aerosol Robotic Network (AeroNet, Smirnov et al., 2009). The measurements might be used to update the present-day aerosol climatology of MPI-M (MAC, Kinne et al., 2013). This climatology is the basis for the simple plumes parameterization MACv2.0-SP1.0 for aerosol optical properties for usage in CMIP6 models (Stevens et al., 2016; Fiedler et al., 2017).

Preliminary (expected) results

1. Radiosoundings

The launch of additional radiosondes in the framework of YOPP was successful and only limited by the restrictions within the Russian EEZ and along the Norwegian coastlines. Together with the regular radiosoundings once a day, we collected atmospheric profiles of air temperature, relative humidity and air pressure from 90 radiosoundings (see Fig. 3.1 as an example) that sampled different atmospheric conditions both during day and night. A first quality check shows that all radiosoundings launched during PS115/2 provide reasonable data. The analyses of the data will be done at AWI collectively with the YOPP data collected during PS114 and PS115/1.

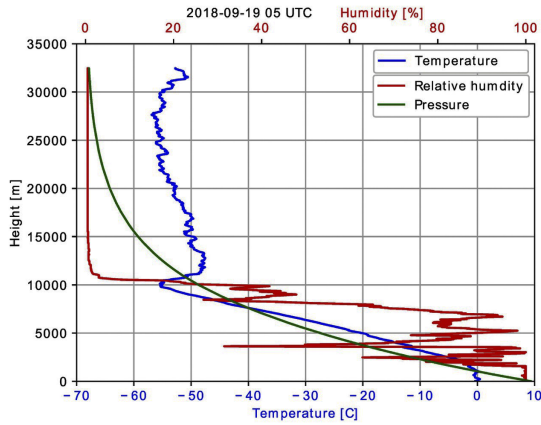


Fig. 3.1: Radiosounding profile from the launch at 5:00 UTC on 19 September 2018. For illustrative purposes, the pressure is divided by 10 and uses the humidity axis.

Together with the radiosoundings launched at previous cruises, the big data base on Arctic atmospheric conditions is expected to provide valuable insights into Arctic weather conditions and to substantially improve the ability of weather forecasts in the Arctic.

2. Cloud camera system

During the whole cruise, we ran a cloud camera system to determine the spatio-temporal variability of the cloud cover and the cloud base altitudes along the ships track. The cloud camera system was for the first time used in the Arctic and performed very well without any failures. The started post-processing of the huge amount of taken images allows for first preliminary results: During the cruise, the ceiling was most of the time fully cloud covered (Fig. 3.2). At times without full cloud coverage, the coverage was highly variable, and clear-sky conditions usually did not persist for long. Such conditions are typical for the Arctic, which allows us to analyse very representative cloud conditions.

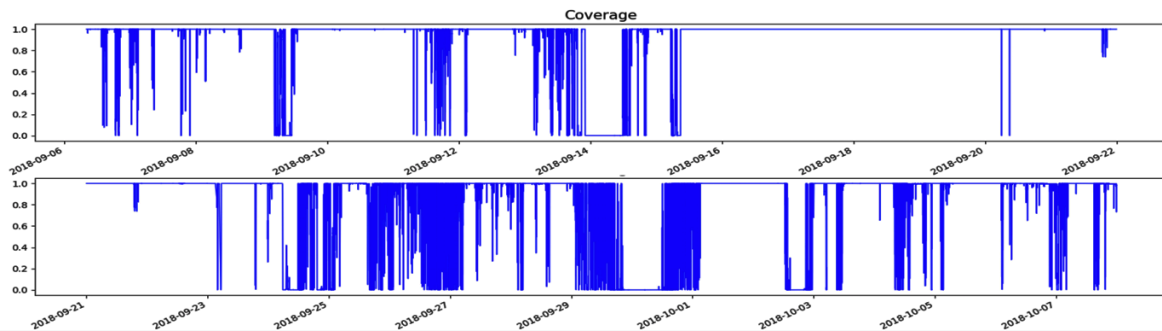


Fig. 3.2: Evolution of the cloud coverage of the ceiling above Polarstern from 06 September 2018 to 07 October 2018 at 10 seconds resolution

In addition to the evolution of the cloud coverage, the images of the brightness temperatures of the clouds will allow us to determine the spatio-temporal variability of the cloud base altitudes. From computing for individual days which proportion of the cloud cover is at pre-defined altitudes, we find that the cloud base altitude can be highly variable. To infer the relationship between the measured brightness temperatures of the clouds and the corresponding cloud heights, we use the temperature profiles from the 6-hourly radiosoundings. As expected beforehand, we find that the frequently occurring Arctic temperature inversion limits the exact determination of the cloud base altitude for low-level clouds, since we cannot directly distinguish

between clouds at different altitudes that have the same brightness temperatures. However, combining the information from the cloud camera with similar cloud statistics derived from the ship's ceilometer might allow us to distinguish the cloud base altitude also during times of temperature inversions. The preliminary findings from the cloud camera system provide valuable insights into the variability of cloud properties in the Arctic. The collected data allow us to further analyse the variability of the cloud base altitudes in detail, and to infer information on the cloud structure from an inhomogeneity parameter. The analysis will be continued at MPI-M.

3. MICROTOPS sun-photometer measurements

Despite the cloudy conditions during the cruise and the low altitude angle of the sun above the horizon, few measurements of the aerosol properties and the water vapor content were possible (Table 3.1).

Tab. 3.1: Raw data from the MICROTOPS sun-photometer showing the first measurement of each measurement series collected during a day.

DATE	TIME	LATI-TUDE	LONGI-TUDE	ALTI-TUDE	PRESS-URE	SZA	AM	SDCORR	TEMP	AOT380	AOT440	AOT675	AOT870	AOT936	WATER
2018-09-14	07:45:47	81.122	119.852	18	1020	81.86	6.752	1.009	17.6	0.063	0.045	0.037	0.017	0.015	0.61
2018-09-24	06:20:45	81.093	121.373	18	1011	83.50	8.253	1.003	20.2	0.319	0.204	0.103	0.066	0.060	0.92
2018-09-29	23:08:53	81.678	143.176	18	1026	87.02	15.21	1.000	19.7	0.025	0.022	0.033	0.022	0.020	0.56
2018-10-12	11:18:17	65.905	6.888	10	1006	73.37	3.458	0.993	20.0	0.410	0.374	0.336	0.306	0.278	1.71

The MICROTOPS sun-photometer measure at five solar wavelengths: 380, 440, 675, 870 and 936 nm (columns 11-15 in Table 3.1). The last two wavelengths are used to extract the water vapor content in the atmosphere, because water vapor absorbs at 936 nm but not at 870 nm. The first four wavelengths are used to extract the AOD for aerosol amount. The AOD at 500 nm (AOD500), a value commonly used in global modeling and satellite remote sensing, is not directly measured but interpolated based on the spectral dependence of the AOD.

The post-processed data on the AOD500 (Fig. 3.3) show that the aerosol amount is very low (<0.1) in the research area of PS115/2. This confirms our expectations since there are no relevant air pollution sources present. It further agrees with the results from the very few previous measurement taken in other parts of the central Arctic and provides valuable reference data in this unsampled region of the Arctic (compare Fig. 3.4). Further measurements would have been desired, but were not possible primarily because of persistent cloudy conditions during most of the cruise.

Further analysis can be done based on the Angstrom parameter and the water vapor content to infer information about the aerosol size and the atmospheric water vapor content.

Overall, the collection of meteorological data during PS115/2 was very successful and provides valuable insights into the variability of the Arctic atmosphere.



Fig. 3.3: Post-processed data of AOD500 showing the measurements from four days during PS115/2 (Source: https://aeronet.gsfc.nasa.gov/new_web/cruises_new/Polarstern_18_1.html)

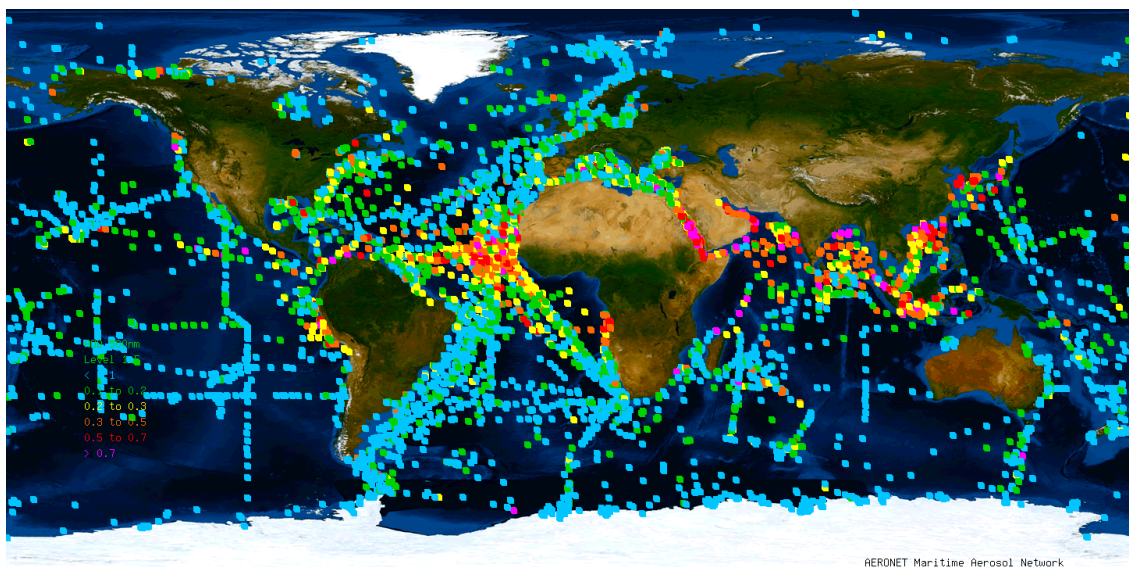


Fig. 3.4: Post-processed data of AOD500 showing the network of measurements from all cruises and the data gaps in the Arctic. Note that the map already contains the measurements taken during PS115/2. (Source: https://aeronet.gsfc.nasa.gov/new_web/maritime_aerosol_network.html)

Data management

The radiosounding data is directly stored in the AWI PANGAEA database and will be made available according to the PANGAEA regulations. Please contact Holger Schmithüsen (AWI) for further information.

The data from the cloud camera system will be made available on request by contacting Stefan Kinne (MPI-M) or Dirk Olonscheck (MPI-M).

The MICROTOPS measurements are already transmitted to the publicly accessible MAN database: http://aeronet.gsfc.nasa.gov/new_web/maritime_aerosol_network.html. For further information, please contact Alexander Smirnov (NASA).

References

- Fiedler S, Stevens B, and Mauritsen T (2017) On the sensitivity of anthropogenic aerosol forcing to atmospheric variability and parameterizing a Twomey effect. *Journal of Advances in Modeling Earth Systems*, 9, 1325–1341, doi:10.1002/2017MS000932.R.
- Kinne S, O'Donnel D, Stier P, Kloster S, Zhang K, Schmidt H, Rast S, Giorgetta M, Eck TF, Stevens B (2013) MAC-v1: A new global aerosol climatology for climate studies. *Journal of Advances in Modeling Earth Systems*, 5 (4), 704–740, doi: 10.1002/jame.20035.
- Smirnov et al. (2009) Maritime Aerosol Network as a component of Aerosol Robotic Network. *J. Geophys. Res.*, 114, D06204, doi:10.1029/2008JD011257.
- Stevens B, Fiedler S, Kinne S, Peters K, Rast S, Müsse J, Smith S J, Mauritsen T (2016) Simple Plumes: A parameterization of anthropogenic aerosol optical properties and an associated Twomey effect for climate studies. *Geosci. Model Dev. Disc.*, 2016, 1–34, doi:10.5194/gmd-2016-189.

4. SEA ICE

4.1 Overview

Gerit Birnbaum¹, Gunnar Spreen²,
Niels Fuchs¹, Marcel König³,
Heike Zimmermann⁴

¹AWI
²UoB-IEP
³CAU
⁴AWI-P

Grant-No. AWI_PS115/2_02

Sea ice work on PS115/2 was performed by three groups with different foci described in the following subsections: (4.2) Physical characteristics of melt ponds, (4.3) Sea ice algae, and (4.4) Drifting buoys on sea ice, in addition (4.5) a Sea Ice Watch from the bridge was carried out by the *ArcTrain Floating University*. Due to a change in the intended cruise track shortly before the start of the expedition away from the central Eurasian Basin to the ice margins, there was only limited access to second year ice, i.e. ice that had not melted during the summer season. We mostly operated in open water and in the marginal ice zone, which was dominated by newly formed ice and broken-up second year ice (see Subsection 4.5). Therefore, some key goals of the sea ice groups could not be reached. The work plan, however, was adapted as far as possible and the actual work done at sea and expected results are given below. A list of all “ice stations”, which include all sea ice related activities, is shown in Table 4.1.1.

Tab. 4.1.1: Summary of all PS115/2 ice stations

Number	Date	Time (UTC)	Action	Number of scientists involved
PS115/2_ICE-1	14.09.2018	08:16-09:42	Helicopter (AIRRGBCAM, AIRHYPCAM)	4
PS115/2_ICE-2	15.09.2018	08:00-08:45	Ice station from the ship (access via Mummy Chair): buoy deployment, ice thickness measurements	4
PS115/2_ICE-3	15.09.2018	12:45-13:15	Ice station from the ship (access via Mummy Chair): work had to be stopped due to a polar bear	4
PS115/2_ICE-4	18.09.2018	12:00-12:30	Buoy deployment from the ship in open water	2
PS115/2_ICE-5	21.09.2018	03:30-04:00	Buoy deployment from the ship in open water/ new ice	2
PS115/2_ICE-6	21.09.2018	22:15-23:15	Ice station from the ship (access via Mummy Chair): buoy deployment, ice thickness measurements, ice core drilling	4

Number	Date	Time (UTC)	Action	Number of scientists involved
PS115/2_ICE-7	22.09.2018	03:25-04:58	Helicopter (AIRRGBCAM, AIRHYPCAM)	2
PS115/2_ICE-8	22.09.2018	05:51-07:50	Ice station via helicopter: buoy deployment, ice thickness measurements, EMP transect, hyperspectral camera	4
PS115/2_ICE-9	23.09.2018	04:00-06:00	Ice station from the ship (access via Mummy Chair): buoy deployment, melt pond survey, ice thickness measurements, ice core drilling	5
PS115/2_ICE-10	24.09.2018	03:45-05:26	Helicopter (Deployment of 8 buoys)	1
PS115/2_ICE-11	24.09.2018	06:25-08:05	Helicopter (AIRRGBCAM)	2
PS115/2_ICE-12	28.09.2018	04:52-05:49	Helicopter (AIRRGBCAM, AIRHYPCAM, deployment of buoy)	2
PS115/2_ICE-13	28.09.2018	15:00-16:00	Ice fishing with metal cage	1
PS115/2_ICE-14	30.09.2018	03:36-05:23	Helicopter (AIRRGBCAM, AIRHYPCAM)	2
PS115/2_ICE-15	03.10.2018	07:30-08:00	Buoy deployment from the ship on pancake ice by means of Mummy Chair	2
PS115/2_ICE-16	04.10.2018	03:00-03:30	Buoy deployment from the ship on an ice floe by means of Mummy Chair	2

4.2 Physical characteristics of melt ponds

Gerit Birnbaum¹, Niels Fuchs¹,
 Marcel König²,
 not on board: N. Oppelt²

¹AWI
²CAU

Grant-No. AWI_PS115/2_02

Objectives

Improving the predictive capabilities for the development of Arctic sea ice cover strongly depends on a better understanding of the ice-albedo feedback mechanism. There is still a lack of knowledge about the temporal and spatial dynamics of melt ponds and their role in the Arctic climate and ecosystem. During the cruise PS115/2 we aimed to investigate melt pond characteristics in the period of refreezing in September/October, to complement earlier measurements during PS106 in June/July 2017 (Oppelt et al., 2018), when melt ponds formed and evolved. Using a combination of multi- and hyperspectral airborne imagery, field spectroscopy and bio-optical modelling, we aim to quantify melt pond fraction, pond size distribution and surface albedo in different ice regimes, and additionally, in case of open ponds, melt pond depth, thickness of underlying ice and pond water constituents (chlorophyll, total

suspended matter and coloured dissolved organic matter). The main objective is to develop a semi-automated method for melt pond analysis for air- and space-borne multi- and hyperspectral instruments. A further objective is to use the collected data for validation and improvement of melt pond parameterizations in regional and global climate models. The intended ground-based measurements are essential for the parameterization of bio-optical models as well as for the validation of surface classification and melt pond characteristics derived from air- and spaceborne measurements.

Work at sea

a) Airborne acquisition of sea ice and melt pond characteristics

Airborne measurements were carried out by use of the BK117C1 helicopter D-HARK. Two instruments, a Canon DSLR camera (AIRRGBCAM) and an AISA_{eagle} hyperspectral camera (AIRHYPCAM), were mounted at the helicopter. The limited accessibility of appropriate second year ice by helicopter and the weather situation allowed for only five measurement flights in total. Measurements were conducted mostly under overcast conditions, but few times also under clear sky conditions. The flight altitude varied between 450 ft and 3,000 ft. The flight time for measurements amounted to approximately seven hours. We took aerial RGB images of more than 500 km² surface area (5,359 images in total) and, in some cases, recorded combined hyperspectral data with the AISA_{eagle}. We did not reach our main goal to perform flights over ice floes, which were sampled *in-situ* at the same time. Hence, there are no ground-based *in-situ* data of melt pond characteristics that can be used for validation of airborne data. For this reason, we adjusted the focus of our measurement flights to three other major goals. Firstly, covering the typical ice surface in the measurement area for statistical analysis. Secondly, flying above the same ice area in different altitudes to evaluate the height dependence of our measurements. And finally, performing extensive measurements including the AIRHYPCAM above floes with a considerable number of ponds.

b) Ground-based measurements of melt pond characteristics

The great majority of melt ponds observed from the vessel was already refrozen. Field measurements could only be carried out on 23.09.2018 during an ice station (PS115/2_ICE-9, access via mummy chair) between 4:00 and 6:00 UTC. Because of the limited time frame only one melt pond could be sampled. Ground-based measurements simultaneous to helicopter overflights and satellite overpasses could not be carried out at all due to limited ice and/or weather conditions.

Preliminary (expected) results

Optical properties of the refrozen surface of the melt pond sampled during the ice station were determined using a setup consisting of two hyperspectral mini-spectrometers (Ocean Optics STS-VIS, 350 – 850 nm, ~2 nm spectral resolution). One spectrometer pointing nadir is equipped with a one degree fore optic, the second spectrometer directed upwards is equipped with a cosine collector. This double-spectrometer setup enables the correction of changes in illumination during a measurement cycle, increasing the quality of the reflectance measurements (see Fig. 4.2.1 and Fig. 4.2.2). In total, 13 spectral measurements were acquired at different locations on the pond in the period between 04:56 and 05:26 UTC.

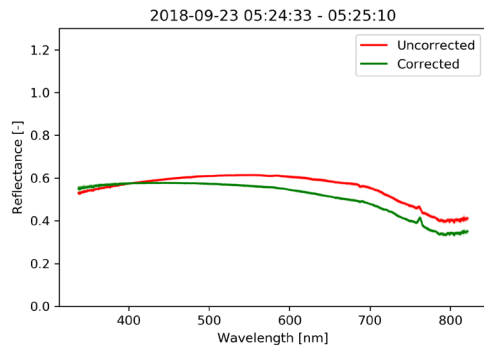


Fig. 4.2.1: Melt pond surface reflectance

In addition, images of the pond surface were taken at every measurement site for characterization. Ice thickness of the pond ice cover was determined after spectral measurements at five locations, indicating that the pond had melted through the ice before refreezing. For further characterization of the pond and to verify that it had melted through, videos with an underwater camera were taken at three drilling sites. The new ice layer on top of the pond was already 5.0-7.5 cm thick and had a bulk salinity of 9.5 g/kg, i.e., it grew from sea water. Only the shape of the sampled area confirmed the pond history. Due to the limited time frame of the ice station, sampling of pond water and measurements of the pond geometry could not be carried out.

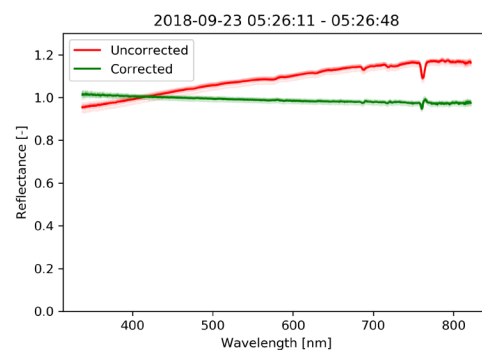


Fig. 4.2.2: White reference measurement at the end of measurement section indicating the change in illumination

The recorded airborne measurements are expected to provide maps and spatial statistics of different sea ice surface classes in the expedition area. An inertial motion and GPS unit in the helicopter will be used to geo-locate the data and correct the image geometry. The main focus of the surface classification is the separation of melt ponds, both open and refrozen, from bare and snow-covered ice as well as open water. As a spectral separation of refrozen melt ponds that had melted through and new ice is challenging without ground-based investigations, a spatial classification approach that considers adjacent image pixels will be tested.

Data management

All sea ice data collected during PS115/2 will be delivered to the PANGAEA database and to the appropriate national data centres after post-cruise calibration and processing.

References

Oppelt N, Birnbaum G, Gege P, König M, Fuchs N (2018) Physical Characteristics of Melt Ponds. In: The Expeditions PS106/1 and 2 of the Research Vessel POLARSTERN to the Arctic Ocean in 2017, Macke A and Flores H, (eds). Reports on Polar and Marine Research, 719, 45 – 56, <http://hdl.handle.net/10013/epic.4ff2b0cd-1b2f-4444-a97f-0cd9f1d917ab>, doi:10.2312/BzPM_0719_2018, ISSN 1866-3192 .

4.3 Sea ice algae

Heike Zimmermann, not board: AWI-P
Kathleen Stoof-Leichsenring, Ulrike
Herzschuh

Grant-No. AWI_PS115/2_02

Objectives

Sea ice is the habitat of single-celled microalgae such as diatoms, a highly diverse taxonomic group that is often used for paleoenvironmental reconstructions from ancient sediments. Our main objective is to analyze spatial and temporal changes of species composition and diversity among sea ice diatoms using DNA metabarcoding in surface sediments and along marine sediment cores, respectively. Therefore, it is of particular importance to characterize the DNA signal of sea ice diatoms from ice cores. To distinguish the sea ice diatom composition from communities of other habitats, we aimed at taking additional samples from snow and sea water.

Work at sea

The change of the cruise track and weather conditions restricted the possibilities to access the sea ice, resulting in only four ice stations (see Table 4.1.1). The ice floes were reached from the ship by mummy chair. To find a suitable coring location on the ice floe, we first measured ice thickness using the Kovacs ice thickness kit. The ice cores were then drilled with the Kovacs Mark II coring system. The first cores drilled on the ice floes (PS115/2_ICE-6-Temp, PS115/2_ICE-9-Temp) were designated for temperature (Fig. 4.3.1) and salinity measurements in 10 cm intervals. The second and third cores (PS115/2_ICE-9-Genetics1, PS115/2_ICE-9-Genetics2) were designated for DNA analyses and therefore handled with nitrile gloves and packed in sterile bags. Additionally, one snow sample (PS115/2_ICE-9-snow) was taken next to the coring site. A further attempt of retrieving ice containing algae, was carried out with a metal cage (PS115/2_ICE-13), which was lowered down through the slush ice between smaller ice floes to fish out floating pieces of ice that were inspected on board for visible algae inclusions. A small piece of an ice floe bottom broke out and was recovered, melted in the dark over 38 hours and filtrated through a cellulose nitrate filter (0.45 µm pore size).

Sea water samples (18 samples) were taken and a volume of 2 L filtered through sterile cellulose nitrate filters (0.45 µm pore size) on-board immediately after collection.

Surface sediments were collected from the giant box corer (14 samples) as well as from the multi-corer (5 samples). Additionally, from two MUC cores (PS115/2_11-2-MUC and PS115/2_28-1-MUC) every second centimeter was sampled for paleogenetic analyses.

Preliminary (expected) results

The sea ice station PS115/2_ICE-6 allowed for the drilling of a temperature core, but as the core did not have any algae inclusions and time was running out, we could not drill a core for DNA analysis. At the sea ice station PS115/2_ICE-9 we were drilling one core to measure a temperature profile (Fig. 4.3.1) and two cores for DNA analyses, even though no algae inclusions were visible in the bottom ice.

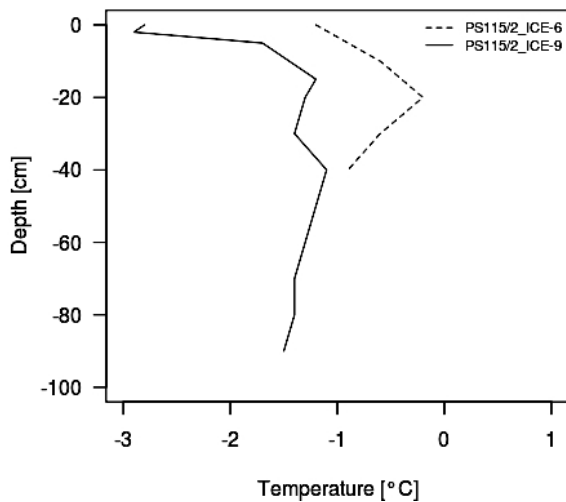


Fig. 4.3.1: Ice core temperature profiles at stations PS115/2_ICE-6 and PS115/2_ICE-9

Data management

The collected samples have to be processed with molecular genetics methods and analysed bioinformatically. The resulting data will be made available in the PANGAEA Data Publisher for Earth & Environmental Science database and unrestricted access to the data will be granted after about three years, pending analysis and publication.

4.4 Drifting buoys on sea ice

Gunnar Spreen¹

¹UoB-IEP

the ArcTrain Team

not on board: M. Hoppmann (AWI), V. Ludwig (UoB-IEP), S. Dolk (NOAA), Wendy S Ermold (APL-UW), H. Goessling (AWI), M. Janout (AWI), T. Krumpfen (AWI), M. Nicolaus (AWI), B. Rabe (AWI), I. Rigor (APL-UW)

Grant-No. AWI_PS115/2_02

Objectives

Seventeen buoys drifting with the sea ice (“sea ice drifters”) were brought out during this expedition. There are two main objectives for the buoy deployment programme: (a) collect data from the buoys as a contribution to the *Year of Polar Prediction* (YOPP) and (b) a pre-study for the *Multidisciplinary drifting Observatory for the Study of Arctic Climate* (MOSAiC) in 2019/20.

The mission of YOPP is to enable breakthroughs in environmental prediction capabilities for the Polar Regions and beyond. The core period of YOPP, which takes place between mid-2017 to the beginning of 2020, will entail periods of enhanced observational and modelling campaigns in both the Arctic and the Antarctic. This will allow carrying out subsequent forecasting system experiments aimed at optimizing observing systems in the polar regions and providing insight into the impact of better polar observations on forecast skills in lower latitudes.

One particular component that needs to be better predicted, and hence analyzed, is the general atmospheric circulation in the Polar Regions. A lot of activities like satellite remote sensing,

4.4 Drifting buoys on sea ice

core modelling & prediction, field campaigns, and Special Observing Periods (SOPs) are being conducted during the YOPP core phase to fill this gap.

One of the biggest challenges for weather forecasts and numerical weather simulations is the scarcity of *in-situ* observations of two of the most critical parameters, surface pressure and air temperature, in remote areas and especially in winter months (Fig. 4.4.1). Indeed, in spite of many satellite systems, measuring surface parameters remains a challenging task in the polar regions, as cloud cover and the background sea ice pose specific issues to most satellite instruments (infrared or microwave-based), as compared to other regions of the globe. One important aim of YOPP is to enhance the routine *in-situ* observations in an attempt to demonstrate that closing the data gaps in the conventional Arctic and Antarctic observing systems may bring significant value for global applications.

Motivated by the Arctic SOPs in Jul/Aug/Sep 2018 and Feb/Mar 2020, we support the efforts of YOPP by deploying nine buoys for YOPP during *Polarstern* cruise PS115/2. These deployments should cover an as large as possible area in the Nansen and Amundsen Basins, where currently no single observation is being made. Our buoys complement deployments from other vessels in other regions of the Arctic Ocean in 2018 to form a comprehensive Arctic buoy network during the YOPP Jul/Aug/Sep 2018 SOP and beyond.

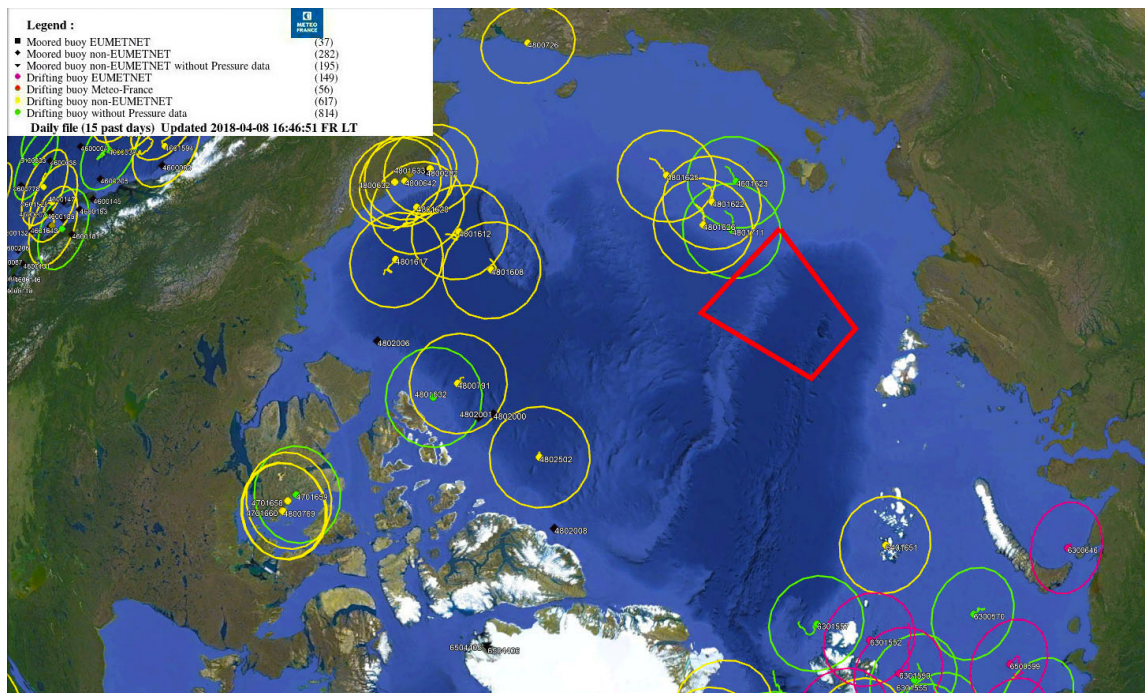


Fig. 4.4.1: The (sparse) March/April 2018 network of moored and drifting buoys in the Arctic that report meteorological data into the Global Telecommunications System (GTS). The circles indicate a radius of 250 km around a buoy. The red box marks the PS115/2 working area, where no buoys were operational before our deployments. (Fig. created using Google Earth with help from Paul Poli and data from ESurfmar/EUMETNET)

The second objective for the buoy deployments is a pre-study for the upcoming *Multidisciplinary drifting Observatory for the Study of Arctic Climate* (MOSAIC), which is a major, year-round expedition into the central Arctic Ocean (<http://www.mosaic-expedition.org>). The MOSAIC Observatory will be deployed in the Arctic sea-ice pack in fall 2019, and drift with it for a full annual cycle (Fig. 4.4.2). The deployment location north of the Laptev Sea is critical to ensure that the vessel follows the Transpolar Drift towards the North Pole, and then drifts further to the Fram Strait, where it will finally leave the Arctic Ocean.

In order to better understand the sea-ice drift patterns in, or adjacent to, the potential MOSAiC deployment region, eight GPS drifters are deployed on sea ice in the main work area of PS115/2 along the southern Lomonosov Ridge. MOSAiC consists of a Central Observatory (*Polarstern* attached to the main sea ice floe) and a distributed network of autonomous observation platforms, which are installed in a radius of approximately 15 and 40 km away from the Central Observatory. The eight buoys during this expedition are aimed to be deployed in an array with similar dimensions and spatial scales. The deployed MOSAiC buoy array will measure the typical sea ice drift velocities during the winter one year prior to the actual experiment. With an array of buoys, however, not only drift velocities but also sea ice deformation can be measured. From triangles

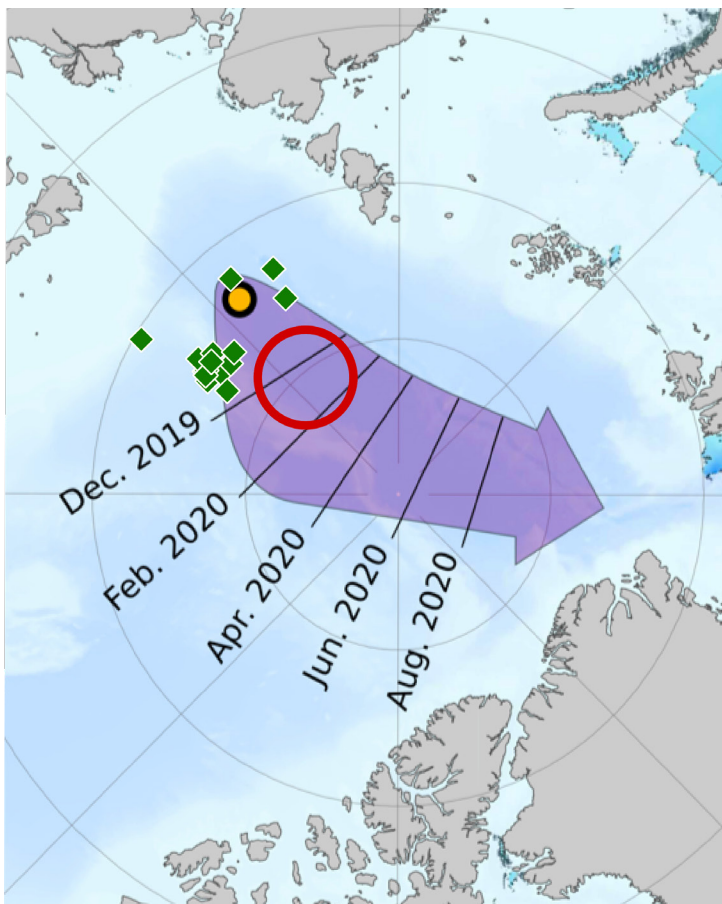


Fig. 4.4.2: The purple arrow marks the potential drift corridor for the MOSAiC experiment in 2019–2020 based on ice drift trajectories of the last ten years. The yellow dot marks the starting point of the drift trajectories. The currently envisioned starting position of the MOSAiC drift between 115° – 145° E, 84.5° – 86.5° N is indicated by the red circle. The positions on 5th October 2018 of sea ice drift buoys deployed during PS115/2 are shown as green diamond.

(Drift simulations and Fig.background:
T. Krumpfen; buoy position overlay: G. Spreen)

between at minimum three buoys divergence, shear, and vorticity can be calculated based on the buoy velocities and the line integral around the triangle boundary (e.g. Hutchings et al., 2012; Itkin et al., 2017). Time series of sea ice deformation will be calculated throughout the winter until next summer to give an indication of how frequent and of what magnitude sea ice deformation events can be expected during MOSAiC. Previous sea ice station experiments mostly took place on thick multiyear ice. MOSAiC, however, will start on thinner second-year ice, which just has survived the summer melt, and thus will be more susceptible to ice break-up. It can be expected that the main floe will break-up during autumn storms, when the MOSAiC experiment is still close to the ice margins. The buoy array deployed during PS115/2 will shed more light on these issues.

All buoys are also part of the *International Arctic Buoy Programme* (IABP). IABP is a framework of numerous collaborators, who maintain a network of ice-tethered buoys in the Arctic Ocean since several decades. Depending on the availability of funding and, more importantly, the logistical

challenges, the coverage of this network varies a lot between the years. Due to several YOPP related activities in 2018 one of the largest buoy networks will be operational.

4.4 Drifting buoys on sea ice

Work at sea

A total of nine *Surface Velocity Profilers* (SVP-B manufactured by PacificGyre) with sea surface temperature and barometric pressure sensors were deployed in the PS115/2 working area. Table 4.4.1 gives the deployment dates and positions, Fig. 4.4.3 shows a map of the deployments and drift trajectories of the buoys. The Appendix A.6 contains deployment sheets for all buoys. The SVP were spread out as far as possible within the PS115/2 working area (indicated as red box in Fig. 4.4.1). The buoy deployments cover an area from 80.8°N to 83.1°N and 119.3°E to 148.7°E. Initial plans to deploy the YOPP buoys in the central Nansen and Amundsen Basins could not be achieved because the transfer to and back from the PS115/2 main working area was going through the Russian *Exclusive Economic Zone* (EEZ), where no buoy deployments could be made.

Tab. 4.4.1: Overview of the 17 buoy deployments during PS115/2 (for further details see Appendix A6). The SVP-B models are related to the YOPP project, the Microstar drifters were deployed on 24.09.2018 in an array as pre-study for MOSAiC. Pacific Gyre, Oceanside, CA, USA is the manufacturer and data provider for the buoys, buoys are owned by AWI, NOAA, and University of Washington. Buoy data can be accessed via <https://www.meereisportal.de> or the [IABP website](#).

Ice Station No.	Model	IMEI	Name	Date	Time [UTC]	Lat [°]	Lon [°]	Notes
PS115/2_ICE-2	SVP-B	300234065802030	2018P73	15.09.2018	08:22	82.06	119.27	Mummy Chair
PS115/2_ICE-4	SVP-B	300234065709990	2018P66	18.09.2018	12:26	80.79	147.71	in open water
PS115/2_ICE-5	SVP-B	300234065802000	2018P72	21.09.2018	03:49	82.06	138.06	in open water/ new ice
PS115/2_ICE-6	SVP-B	300234065800000	2018P67	21.09.2018	22:35	82.18	134.50	Mummy Chair
PS115/2_ICE-8	SVP-B	300234065801040	2018P71	22.09.2018	07:17	82.42	140.08	helicopter station
PS115/2_ICE-9	SVP-B	300234065800030	2018P68	23.09.2018	05:00	83.09	142.51	Mummy Chair
PS115/2_ICE-10	Microstar	300234011880340	2018P75	24.09.2018	04:00	81.70	141.49	helicopter flight
PS115/2_ICE-10	Microstar	300234011882340	2018P77	24.09.2018	04:30	81.62	142.08	helicopter flight
PS115/2_ICE-10	Microstar	300234011885340	2018P79	24.09.2018	04:30	81.42	142.58	helicopter flight
PS115/2_ICE-10	Microstar	300234011882350	2018P78	24.09.2018	04:46	81.94	141.40	helicopter flight
PS115/2_ICE-10	Microstar	300234011888330	2018P83	24.09.2018	05:00	82.15	141.13	helicopter flight
PS115/2_ICE-10	Microstar	300234011889340	2018P65	24.09.2018	05:00	81.74	140.82	helicopter flight
PS115/2_ICE-10	Microstar	300234011881340	2018P76	24.09.2018	05:30	81.80	141.99	helicopter flight
PS115/2_ICE-10	Microstar	300234011883240	2018P82	24.09.2018	06:00	81.94	142.19	helicopter flight
PS115/2_ICE-12	SVP-B	300234061872720	2018P74	28.09.2018	05:03	82.13	148.73	helicopter flight
PS115/2_ICE-15	SVP-B	300234065800040	2018P69	03.10.2018	07:50	81.39	128.52	Mummy Chair on pancake ice
PS115/2_ICE-16	SVP-B	300234065801030	2018P70	04.10.2018	03:14	81.82	119.61	Mummy Chair

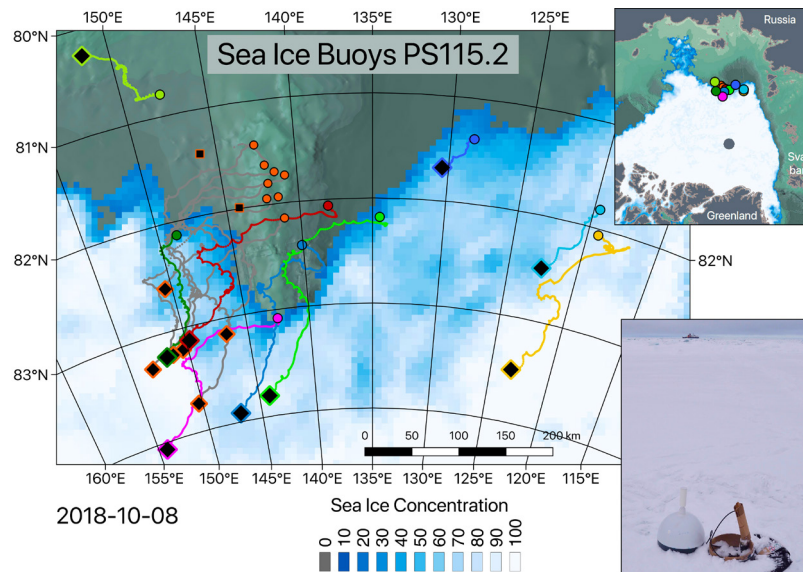


Fig. 4.4.3: The circles indicate the starting positions of the 17 buoys deployed during PS115/2 (two in water, the rest on ice floes). As an example, the lower right image shows the buoy deployment on 22.9.2018 with *Polarstern* in the background. Forced by wind and ocean currents the buoys drift with the ice, which is shown by the colored lines. The positions of the buoys on 8 October 2018 are indicated by the black diamonds; two of the Microstar buoys were not sending their position since the week before and are likely dead (black squares). The background shows the sea ice cover on 8 October; the topography of the ocean floor can be seen in areas without ice. (Maps and photo: G. Spreen)

Different means of deployment were used. Two SVP buoys were deployed by helicopter (22. & 28.9.), five were deployed by Mummy Chair on ice floes next to *Polarstern* (15., 21., 23.9., 2., 4.10.; Fig. 4.4.4 left), and two were dropped from the working deck of *Polarstern* in open water (18. & 21.9.). The preferred way of deployment was by helicopter or Mummy Chair with an additional sea ice station next to the buoy. To interpret the sea ice drift data of the buoys, knowledge of the physical ice conditions they are deployed on are of importance. One factor influencing the deformation of an ice floe is its thickness (Tab. 4.4.2). For four out of the nine SVP buoys the ice and now thickness was measured:

Tab. 4.4.2: Physical ice conditions at buoy deployment sites

Station No.	Date	Snow Thickness	Ice Thickness	Ice Freeboard
PS115/2_ICE-2	15.09.2018	8 cm	192 cm	13 cm
PS115/2_ICE-6	21.09.2018	9 cm	78 cm	6 cm
PS115/2_ICE-8	22.09.2018	7 cm	358 cm	63 cm
PS115/2_ICE-9	23.09.2018	12 cm	74 cm	2 cm

The sea ice for the three other buoys deployed on ice was either too thin (02.10.2018) or the floes were too small to work on them (28.09. & 4.10.2018). To extend the region covered by the buoys two of them were dropped into the sea. The region they were deployed in will freeze during the coming weeks and it is expected that they also will become ice-fastened buoys. For the buoy deployment on 21.09.2018 this already happened: New ice formation was already observed during deployment and by October the buoy became incorporated into the sea ice (see trajectory of dark red buoy in Fig. 4.4.3). It is preferred to deploy the SVP buoys on sea ice to obtain information about sea ice drift and dynamics. In addition, only on sea ice the SVPs

4.4 Drifting buoys on sea ice

measure air temperature (or the temperature of the upper snow layer). If deployed in water they measure sea surface temperature (SST), which is what they are built for.

For the pre-study for MOSAiC a total of 8 Microstar GPS drifters (manufactured by PacificGyre) were deployed by helicopter on 24.09.2018. They were dropped on mainly small ice floes in the marginal ice zone between 81.42°N to 82.15°N and 140.82°E to 142.19°E (see orange circles in Fig. 4.4.3). Floes in this area were small in the order of 10 m, broken up and had open water areas in between them (Fig. 4.4.4 right). New ice formation, however, had already started. The distributed network of autonomous measurement stations and buoys planned for MOSAiC covers the two main spatial scales of 15 km from the ship (30 km diameter) and 40 km from the ship (80 km diameter). The buoy array brought out during this expedition covers the same scales. The planned two triangles with 40 km side length and buoys at 15 km between could not be completely realized because of open water areas at some locations. However, a good spatial distribution could be achieved during this 2-hour flight. The helicopter could not land on all floes due to the small size and swell. Then the Microstar drifter buoy was dropped from about 2 m height out of the helicopter door. On three floes we could land and the buoy was deployed by hand in the snow. The mean buoy array position at 81.8°N/141.7°E is further south than the envisioned starting location north of 84°N for MOSAiC in October 2019 (see Fig. 4.4.2). During our short trip north of 82°N between 21st and 23rd September closer to the MOSAiC starting position, weather conditions did not allow helicopter flights to bring out a buoy array of that extend. The buoy array together with the SVP buoys, however, is within the expected drift corridor of the MOSAiC expedition. They likely in the coming weeks will reach the expected MOSAiC starting area (red circle in Fig. 4.4.2) and will precede the MOSAiC drift by approximately one year. Thereby important information for planning the MOSAiC experiment is collected and the buoy array will help to later set the MOSAiC drift into context with other years.

The SVP buoys wake up every hour, do their measurements, and transmit the data back to land via Iridium satellite connection. The Microstar drifters of the buoy array do the same but every 30 minutes (exception: Microstar drifter 2018P82, IMEI 300234011883240 is only sending every hour). All buoys were put out on the observation deck of *Polarstern* for several days before deployment to test that the measurements and Iridium transmission are working.

The help of the helicopter crew and ArcTrain team (Chapter 8) for bringing out the buoys is gratefully acknowledged. It would not have been possible to deploy 17 buoys in the short time frames we had in the ice without their dedicated support.



Fig. 4.4.4: Left: Deployment of SVP buoy by Mummy Chair on 15.09.2018. Right: Ice situation on 24.09.2018 during the deployment of the pre-MOSAiC buoy array. (Photos: G. Spreen)

Preliminary (expected) results

In the context of YOPP the buoys are expected to fill a critical observational gap of temperature and barometric pressure data in the central Arctic Ocean buoy network, which is particularly pronounced in the under-observed Eurasian Basin (see Fig. 4.4.1). The cruise track allowed to cover the south-eastern part of the Nansen and Amundsen Basins. An area of approximately 550 km diameter is now covered with atmospheric but also sea ice dynamics observations, where otherwise no single observation would exist.

The data will contribute to an improvement of weather forecasts even down to mid-latitudes, and serve as validation for numerical simulations of the atmosphere, ice and ocean, as well as for remote sensing products. These aspects are of particular importance for the efforts currently undertaken within the framework of the Year of Polar Prediction and its Special Observing Periods in Jul/Aug/Sep 2018 and Feb/Mar 2020. In addition to operational forecasting centers, academic university and government researchers will potentially use the observations, not only to assess forecast impacts to guide the future polar observing system, but also to better understand the polar weather and climate system with its unique physical environment, e.g., to improve polar model parameterizations (Jung et al., 2016).

On 8 October one SVP buoy already drifted north of 84°N (Fig. 4.4.3) and is now very close to the expected starting position of MOSAiC (red circle in Fig. 4.4.2). Also, the MOSAiC array of Microstar drifters and most of the other SVPs have drifted north-eastward by about 230 km and are getting closer to the MOSAiC starting position. The grid of all sea ice drifters will allow to analyze a potential drift trajectory of the MOSAiC distributed network and how the network will deform during the one-year long drift. The MOSAiC trajectory and behavior of the distributed network (e.g., divergence and shear of the grid) can later be compared to the buoy grid deployed during PS115/2 to evaluate inter-annual differences. The grid of Microstar drifters has already deformed significantly during the two weeks of drift shown in Fig. 4.4.3 (compare the distribution of orange circles on 24.09. with orange diamonds on 08.10.). Two of the Microstar drifters have likely died by now, they stopped sending data on 26. and 27.09.18, respectively (likely due to battery failures; the voltage of both dropped below 9V from initially 12V).

Some of the buoy deployment positions lie now in open water because the general ice drift direction was towards Northeast since deployment and the ice edge moved northward, too. While refreezing started between the ice floes when we were in the ice, the newly created water areas created by southerly winds have not yet been refrozen. Thus, many of the deployment positions lie now in open water. The region was mainly dominated by low pressure systems in the area. This can also be seen from the buoy measurements. The mean pressure measured by all SVP buoys on sea ice since their deployment until 08.10.2018 was 1012 hPa. However, the histogram of surface pressure in Fig. 4.4.5, left shows that there were also phases of higher pressure of 1025 hPa and a second low pressure mode at 1005 hPa. The low-pressure systems were accompanied by comparable warm air of on average -2.2°C and a mode at -1.7°C , which is just the freezing temperature of sea ice (see Fig. 4.4.5, right). At such air temperatures no strong sea ice formation can be expected. The southerly winds pushed the ice edge northward and the air temperatures were not cold enough to start a fast refreezing of these opened-up ocean areas. The three buoys in water, however, that measure SST show mean and modal SST temperature of -1.5°C , which is close to the freezing point of sea water. This means that the upper ocean is already cooled down and preconditioned for sea ice formation if air temperatures start to drop. From *Polarstern* sea ice formation already was observed at several different locations during PS115/2 (see also Subsection 4.5 and Appendix A.7.4.1).

4.4 Drifting buoys on sea ice

More preliminary analysis of the buoy data can be found in Section A.7.4.5 in the Appendix, where Natasha Ridenour provides more insight into the atmospheric buoy measurements and correspondence of ice drift and wind speed.

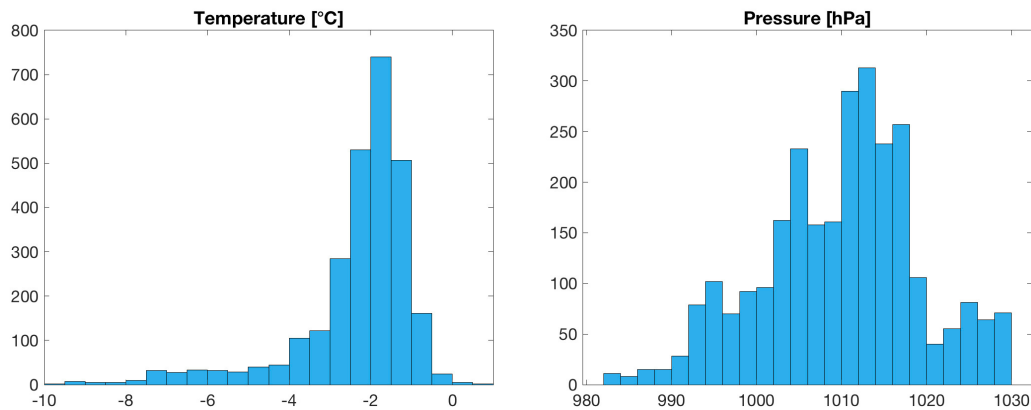


Fig.4.4.5: Histograms of surface temperature (left) and pressure (right) for all SVP buoy measurements between deployment and 08.10.2018. Buoys in the water and thus measuring SST are excluded

Data management

Immediately upon measurement, the buoy data is transmitted to the buoy programme manager via the iridium satellite network. The data is then delivered into the Global Telecommunications System (GTS) in near-real time, and is freely available in the public GTS database approximately 10 minutes after the measurement time. The buoys also contribute to the public database hosted by the International Arctic Buoy Programme (IABP) and are also available under www.meereisportal.de. Note that all buoy data are publicly available: WMO (1995) Resolution 40 Annex I considers such data among those “to be exchanged without charge and with no conditions on use”.

References

- Hutchings JK, Heil P, Steer A, and Hibler III WD (2012) Subsynoptic scale spatial variability of sea ice deformation in the western Weddell Sea during early summer. *J. Geophys. Res.*, 117, C01002. [doi:10.1029/2011JC006961](https://doi.org/10.1029/2011JC006961).
- Itkin P, Spreen G, Cheng B, Doble M, Girard-Arduin F, Haapala J, Hughes N, Kaleschke L, Nicolaus M, and Wilkinson J (2017) Thin ice and storms: Sea ice deformation from buoy arrays deployed during N-ICE2015. *J. Geophys. Res. Oceans*, 122, 4661–4674. [doi:10.1002/2016JC012403](https://doi.org/10.1002/2016JC012403).
- Jung T, Gordon ND, Bauer P, Bromwich DH, Chevallier M, Day JJ, Dawson J, Doblus-Reyes F, Fairall C, Goessling HF, Holland M, Inoue J, Iversen T, Klebe S, Lemke P, Losch M, Makshtas A, Mills B, Nurmi P, Perovich D, Reid P, Renfrew IA, Smith G, Svensson G, Tolstykh M, and Yang Q (2016) Advancing Polar Prediction Capabilities on Daily to Seasonal Time Scales. *Bull. Amer. Meteor. Soc.*, 97, 1631–1647, [doi:10.1175/BAMS-D-14-00246.1A.1](https://doi.org/10.1175/BAMS-D-14-00246.1A.1).
- WMO (1995) Cg-XII Resolution 40. Available on-line http://www.wmo.int/pages/prog/hwrrp/documents/wmo_827_enCG-XII-Res40.pdf (last accessed 9 April 2018).

4.5 Ice watch – visual sea ice observations from the bridge

Gunnar Spreen ¹ , Charles Brunette ² ,	¹ UoB-IEP
Anouk Vlug ³ , Pascal Bourgault ² ,	² McGill
Camille Brice ⁴ , Myriam Caron ⁵ , Amelie	³ UoB-MARUM
Desmarais ² , Rémi Lenny ³ , Aliaksandra	⁴ UQAM
Kazlova ¹ , Ryan Love ⁶ , Dimitri	⁵ UQAR
Murashkin ¹ , Natasha Ridenour ⁷ , Damien	⁶ MUoN
Ringeisen ⁸ , Samira Samimi ⁹	⁷ UoAE
	⁸ AWI
	⁹ UoC

Grant-No. AWI_PS115/2_02

Objectives

Visual observations of sea ice from the bridge of ice-going vessels is an integral part of sea ice monitoring since the beginning of Arctic exploration.

Visual observations are the only possibility to regularly obtain a broad range of sea ice parameters extended with photographs and comments about distinctive features. Starting with explorers and whalers, visual observations from ships represent the longest time series about the Arctic sea ice state (Divine & Dick, 2006). Today still all ice-going research vessels are asked to carry out such standardized *Ice Watch* observations to enlarge the existing database. The *Ice Watch* programme for the Arctic (Hutchings et al., 2018) is based on and is compatible with the ASPeCt protocol developed for the Antarctic (Worby & Allison, 1999). Besides being a valuable dataset on its own, these observations can be used as *in-situ* comparison to otherwise obtained measurements like remote sensing data. They have the advantage of discriminating different ice types and specific features like ridge distribution and stages of surface melt, which are hard to obtain by other methods. Also, ancillary information like biological content and sediments in the ice are recorded. In addition, the *Ice Watch* observations serve as a reference record for the cruise. They provide an easy way to revisit the specific sea ice and meteorological condition at hourly frequency throughout the cruise.

Nevertheless, it has to be considered that all observations strongly depend on the personal view and estimation of each individual observer and such the absolute accuracy is low. Additionally, *Polarstern* favors open water and thin ice areas for steaming, which may bias ice thickness observations.

Work at sea

To obtain a continuous record of the sea ice state, standardized visual observations were performed from the ship's bridge every hour during day time (07:00 – 00:00) and three more times during night time (02:00, 04:00, 05:00 or 06:00). Observations were started when *Polarstern* approached the ice or was operating close to the ice margins and continued to well after the ice was left again. In total 329 observations from the bridge were taken.

The observations were conducted following the standardized protocol of the *Ice Watch* programme (<http://icewatch.gina.alaska.edu/>). *Ice Watch* provides the ASSIST software tool, which is a Java application that was installed on a notebook on the bridge. ASSIST version 4.1 was used for recording the data, a Panasonic Lumix DMC-ZS7 camera was used for the three photographs per observation (see example in Fig. 4.5.1). The *Ice Watch* Manual (Hutchings et al., 2018) and WMO sea ice nomenclature (WMO, 1989) helped conducting the observations. ASSIST can record 110 different parameters per observation. Only a small subset, however,

4.5 Ice watch – Visual sea ice observations from the bridge

is recorded always: time, location, and ship movement, total ice concentration and ice types, ice thickness, and meteorological conditions. Snow, ice topography, melt state and other parameters were added if observed.

The observations were carried out by the 14 members of the ArcTrain Floating University (see Section 8), i.e., the authors of this section. Every observer had one or two fixed hours during the day for taking ice observations, the duty for the three observations during night were rotated within the team.



Fig. 4.5.1: Typical photographs taken from the bridge to port side (left), forward (middle), and starboard side (right) on September 23, 20:11. (Photo's by Remi Lenny)

Preliminary (expected) results

The first sea ice observation was taken on 7 September 2018, 12:00 and the last on 6 October 2018, 17:30 UTC. Fig. 4.5.2 shows the time series of total sea ice concentration observed during the cruise and the histogram of all observations. Most observations were taken in open water and a large fraction of intermediate ice concentrations were observed. This reflects that the PS115/2 expedition was mainly located in the marginal ice zone and open water areas. The ocean north of the Laptev Sea was not refrozen after the sea ice minimum was reached in mid-September. The total ice concentration observations are split up in different ice types and thicknesses, which can be analyzed separately. In Appendix A.7.4.1 a more detailed analysis and comparison to AMSR2 satellite data is presented by A. Vlug and C. Brunette.

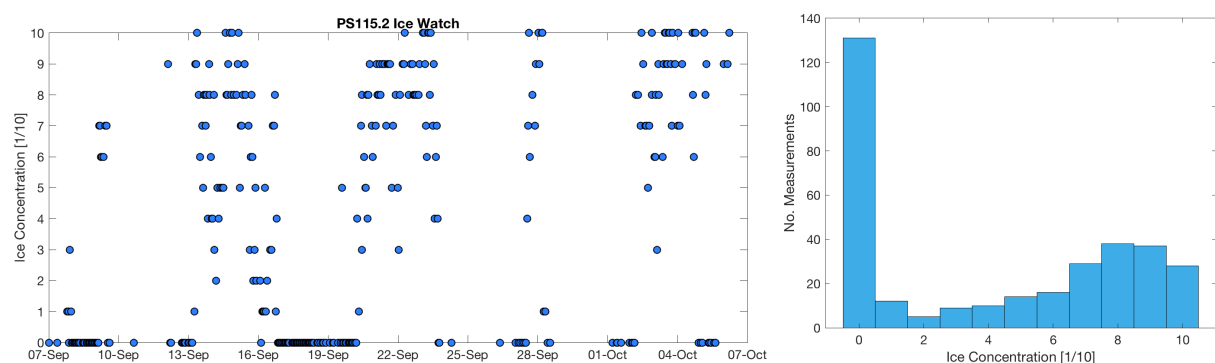


Fig. 4.5.2: Time series of total sea ice concentration during the PS115/2 cruise (left) and the accordant histogram of sea ice concentrations (right).

Data management

Directly after the cruise all data will be made openly available via the *Ice Watch* website hosted by the University of Alaska Fairbanks (<http://icewatch.gina.alaska.edu/>). The *Ice Watch* database contains ship-based sea ice observations from all major Arctic research vessels. The provision of the ASSIST software and the database by the *Ice Watch* programme is gratefully acknowledged.

Within six months after the cruise it will be assessed if an additional copy of the sea ice observation dataset will be submitted to PANGAEA database to secure long-term storage.

References

- Divine DV, Dick C (2006) Historical variability of sea ice edge position in the Nordic Seas. *J. Geophys. Res.*, 111, C01001. doi:10.1029/2004JC002851.
- Hutchings JK, Delamere J, Heil P (2018) The Ice Watch Manual, Draft 2018/06/30 for ASSIST v4.1. Draft Technical Report, University of Alaska Fairbanks, USA. <http://icewatch.gina.alaska.edu/>.
- WMO (1989) WMO sea ice nomenclature. World Meteorological Organization, Geneva, Switzerland, WMO/OMM/BMO 259-TP-145, suppl. 5.
- Worby A, Allison I (1999) A technique for making ship-based observations of Antarctic sea ice thickness and characteristics, Part 1 Observational technique and results. Cooperative research centre for the Antarctic and Southern Ocean environment. Hobart, Tasmania, Australia, 14.

5. BATHYMETRIC INVESTIGATIONS DURING EXPEDITION PS115/2

Melanie Steffen, Sophie Andree,
not on board: Simon Dreutter, Boris
Dorschel

AWI

Grant-No. AWI_PS115/2_01

Objectives

One of the main objectives of the bathymetric investigations was to support the geological work by mapping the seafloor. The data had to be processed, and the output are 2D and 3D maps of specific key study areas as well as overview maps of the whole area. These maps were the basis for the planning of further PARASOUND surveys in areas with specific characteristics of the seafloor (e.g. steep slopes where old sedimentary rocks might crop out).

Work at sea

The bathymetric data obtained during Expedition PS115/2 were acquired by using the Hydrosweep DS 3 of Teledyne Atlas. The Hydrosweep is supposed to measure depth in a range of 6 m – 12, 000 m using an average frequency of 15 kHz. The desired number of beams is 345 beams per ping. The opening angle can be set manually to a maximum of 150°, which is useful to cover a large area, but in less fine resolution. Especially in regions with a high amount of ice and ice floes, it is necessary to adjust the angle in a good balance to cover a large area, but to not open the angle too much, that the outer beams become useless due to the noise caused by the ice. It appears that the real swath width was significantly narrower (up to 5 km less) than the calculated swath width (Fig. 5.1).

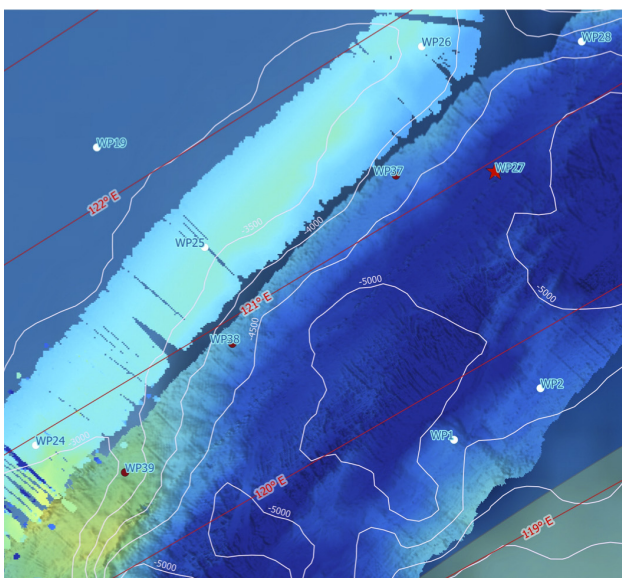


Fig. 5.1: A gap between two Hydrosweep tracks. That means, the swath width is narrower than calculated. The reason for this might be noisy outer beams, whose reflections were filtered by the system because of the bad quality.

The mapping started after leaving the Russian EEZ and ended before entering it again. In the Russian Exclusive Economic Zone (EEZ) no measurements were done. The survey lines mostly were defined by transits to the working areas and the seismic surveys. Depending on the ice conditions, the ship steamed with ~ 6 – 10 kts and the Hydrosweep was operated with an opening angle of about 130°. The partly slow speed of the ship resulted in a higher accuracy.

The system onboard *Polarstern* is connected to a motion sensor (Hydrins INS by IxBlue), which gives information about the ship's movement (heave, pitch and roll), a GPS receiver (Trimble SPS 855) for the orientation of the data and to C-Keel-Sonde (SVP 70 by RESON), which is mounted in the hydrographic funnel of the vessel and provides continuous information about the sound velocity characteristics of the water.

The Hydrosweep system is paired with several software packages by Teledyne e.g., Atlas HYDROMAP Control, which enables the user to control the Echo sounder by adjusting

- (1) the swath angle, the ping mode (used: single swath for good coverage),
- (2) the pulse type (depending on the water depth: continuous wave or frequency modulated (chirp) wave were chosen. The Chirp mode puts more energy into the water column, so it is preferred in the deeper areas), and
- (3) the spacing of the soundings (which is chosen to be equidistant during this cruise).

Along with this, the acquisition software PARASTORE has been used. Furthermore, PDS acquisition software is used for the online visualisation of the incoming data. It enables the user to choose between various views of the data and also adjust some settings, for example, the swath angle. For the sound velocity corrections sound velocity profiles (SVP) were obtained from SVP casts. As the ship's SVP sonde was tied to the wire during gravity corer or giant box corer casts no additional ship's time was needed for the operation. The Atlas Sensor Manager feeds in the SVP data into the Hydrosweep system. This also had to be done in the PDS acquisition software to ensure the same depth values in all the different windows. The water's sound velocity is measured by a sound velocity profiler (Valeport MIDAS) and the C-Keel-Sonde.

Preliminary (expected) results

The mapped Hydrosweep track has an overall length of about 2093 nm. The water depth of the stations varied between 779 m as minimum depth and 5002 m as maximum depth. Some statistics of the PS115/2 Hydrosweep survey are summarized in Table 5.1, an overview map with the Hydrosweep tracks is shown in Fig. 5.2.

Tab. 5.1: Statistics of the PS115/2 Hydrosweep survey

Parameter	Effort
Hrs of testing	~1.5 hrs
Hrs of operation	307 hrs
(operating distance in nm/km)	~2093 nm/ 3876 km
Numbers of people	2 (+ several helpers)

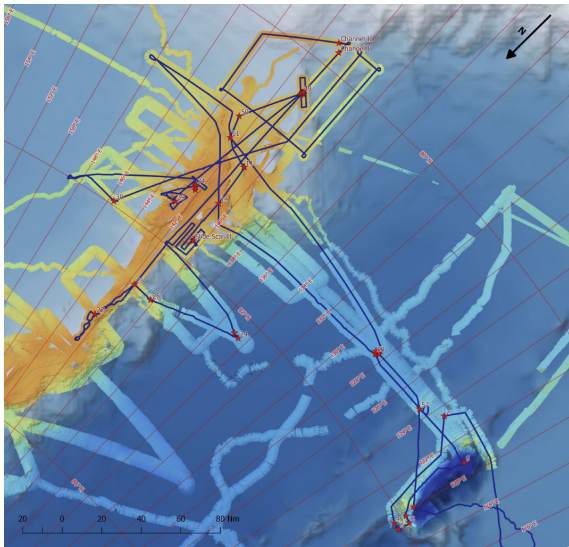


Fig. 5.2: Overview map of the main PS115/2 working area, with the key elements southern Lomonosov Ridge and Gakkel Deep, both identifiable from the GEBCO and Hydrosweep data

The grid size varies between ~160 m (6 kts) and ~280 m (10 kts) at an average ping rate of 0.1 Hz and was interpolated to 100 – 150 m during the post-processing. Thus, the bathymetry of the echosounder is much more precise than the GEBCO data which is mostly based on satellite altimetry. The part of the Lomonosov Ridge belonging to our working area, stretches from north to the south (~80°N – 85°N, 120°E – 150°E) and has a minimum depth of ~650 m. It consists of several plateaus and terraces (Fig. 5.3) as well as some steep slopes/slide scars (Fig. 5.4 and 5.5) that had been mapped more precisely for further studies such as geological coring.

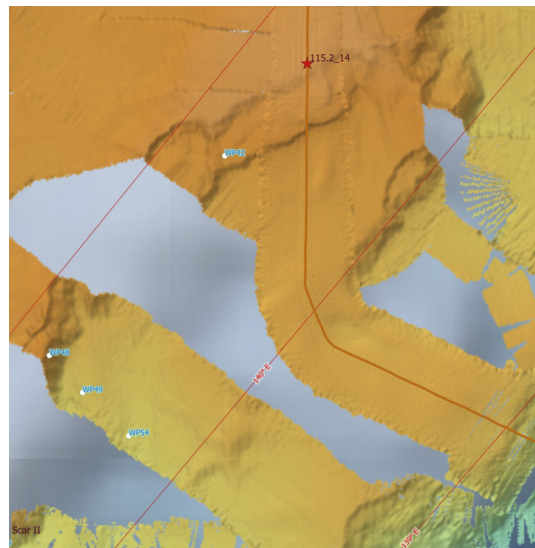


Fig. 5.3: Terraces at the flanks of the Lomonosov Ridge

In the Amundsen Basin, an unknown “seamount-like” structure elevating about 600 m above the abyssal plain, was discovered (Fig. 5.5). A part of this structure had already been mapped during *Polarstern* Expedition PS87 in 2014 (Stein 2015). The quality of the new hydrosweep data, however, is much better than that of the 2014 survey (Fig. 5.5), which was obtained at high ship speed of about 14 kn.

The Gakkel Deep has been mapped in more detail as survey before starting the OBS deployments (see Chapter 6.2). Maximum water depth of the Gakkel Deep is approximately 5200 m. Part of its western flank is within the Russian EEZ; thus, in this cruise only the central and eastern area could be explored (Fig. 5.6).

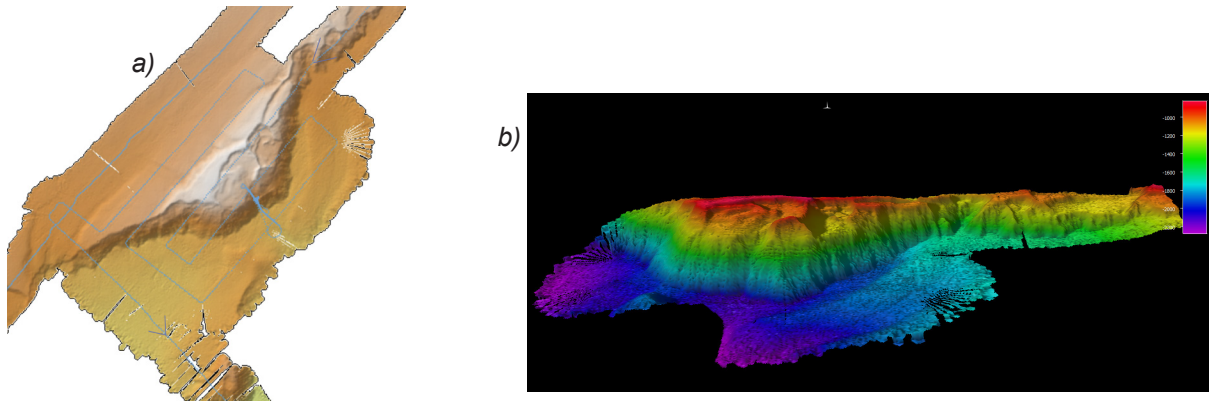


Fig. 5.4: (a) and (b) Detailed mapping of a slide scar area that allows 3D models for a better visualization.

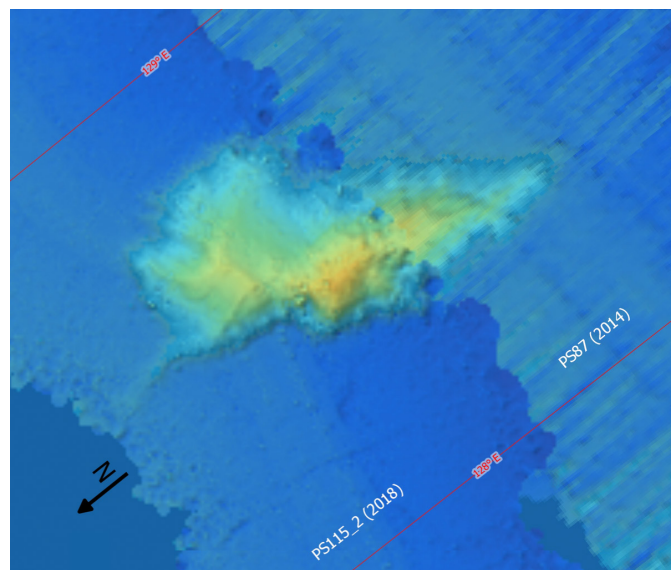


Fig. 5.5: A "seamount-like feature" mapped in several steps for a better resolution

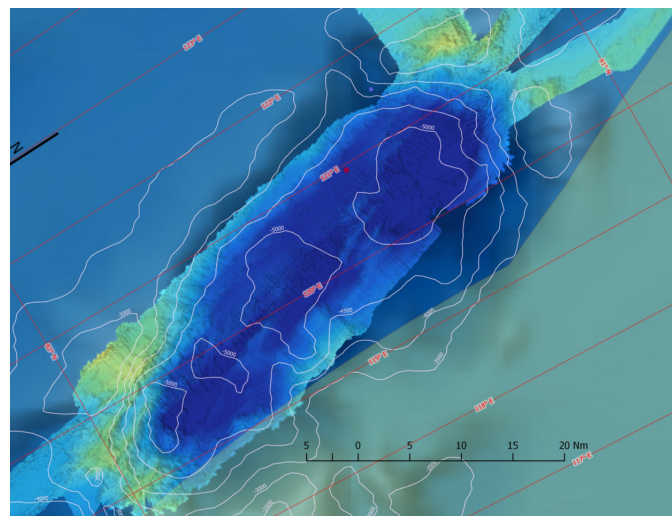


Fig. 5.6: Detailed map of the Gakkel Deep

Data management

The acquired Hydrosweep raw data will be stored in the long-term archive PANGAEA and will be available on request. The processed data will be archived in the bathymetric archive of the AWI bathymetry group. Furthermore, the data will contribute to global datasets such as IBCAO (International Bathymetric Chart of the Arctic Ocean) and GEBCO (General Bathymetric Chart of the Oceans).

The obtained hydrosweep data of PARASTORE is stored as PHF (Primary High Frequency) raw data (*.asd), which can be used in several post-processing software packages.

Caris HIPS was used to check the data and reject outliers. During Expedition PS115/2 this mainly occurred due to systematic errors and ice conditions. The post-processing was done in multiple steps using the Swath, Navigation and Subset Editor. After processing the data, the GeoTiff (*.tif) format was used for exporting the data for subsequent map-making purposes in the Geo-Information System (GIS) software QGIS. In the GIS Project GEBCO data were used as base map. Some sites and features as well as the cruise track were integrated as ASCII files, while stations and waypoints were defined as separate vector layers, which were kept updated continuously during the cruise.

References

Stein R (2015) The Expedition PS87 of the Research Vessel *Polarstern* to the Arctic Ocean in 2014, Reports on Polar and Marine Research 688, Bremerhaven, Alfred Wegener Institute for Polar and Marine Research 688, 273 pp (http://epic.awi.de/37728/1/BzPM_0688_2015.pdf).

6. GEOPHYSICS: TECTONIC EVOLUTION OF THE ARCTIC OCEAN

6.1 Seismic Reflection

Estella Weigelt¹, Kai Berglar², Timo Ebert²,
Thorsten Eggers¹, Cristoph Gaedicke², Sergei
Freiman³, Norbert Lensch¹, Adalber Pfeiffer¹,
John Scholz¹, Nikolai Wöhljtjen¹, not on board:
Wilfried Jokat¹

¹AWI
²BGR
³MSU

Grant-No. AWI_PS115/2_01

Objectives

The Lomonosov Ridge is one of the most prominent topographic features in the Arctic Ocean. It stretches from the northern Greenland Shelf to the Laptev Sea Shelf separating the Cenozoic Eurasia Basin from the Mesozoic Amerasia Basin. As a sliver of continental crust it rifted from the Siberian margin in early Palaeocene at about 58 Ma (Chron 25) (e.g. Heezen and Ewing, 1961; Vogt et al., 1979; Kristoffersen, 1990) and subsided below sea level in the early Eocene (e.g. Jokat et al., 1995; Moran et al., 2006). Its tectonic evolution influenced ocean currents, which in turn influenced climate, sedimentation conditions, and even the setting of ecosystems in the adjacent Amundsen and Makarov basins (e.g. Jakobsson et al., 2007; Björk et al., 2018). Most of these processes left an imprint on sedimentary layers and crust, which can be imaged with geophysical methods. The geophysical research topic aims to record a set of seismic reflection data, which will enhance insights into the tectonic evolution, sedimentation history, and paleoceanography of the Central Arctic Ocean. As well, these new data contribute to a better understanding of the link between tectonics and climate changes in the Arctic, one of the overall goals of the proposed IODP drilling campaign 377 (Stein et al., 2015).

The main scientific targets of the seismic programme originally were to:

- Perform high-resolution multichannel seismic reflection profiling across the central and the southern part of the Lomonosov Ridge (Fig. 6.1.1) for imaging of sedimentary structures and crustal surface to reconstruct depositional systems and ocean circulations. The minor sea ice coverage around 81°N enabled to perform a complete transect across the Amundsen Basin from the Gakkel Deep towards the Lomonosov Ridge, and further into the Makarov Basin.
- Supplementing the profiles obtained during *Polarstern* Expedition PS 87 in 2014 in the surroundings of future IODP-drilling locations (Stein, 2015, 2017). To improve the pre-site survey, cross-lines to existing profiles shall enhance the imaging of sedimentary strata and the depth calculation of target reflectors. The minor sea ice cover south of 82.5° N made this survey successfully.

6.1 Seismic Reflection

- Acquire a seismic line to connect the seismic network at ACEX drilling location on the central Lomonosov Ridge and the seismic lines recorded on the southeastern ridge for a spatial extrapolation of findings. Dense sea ice north of 83° and the time constraints prevented this plan.

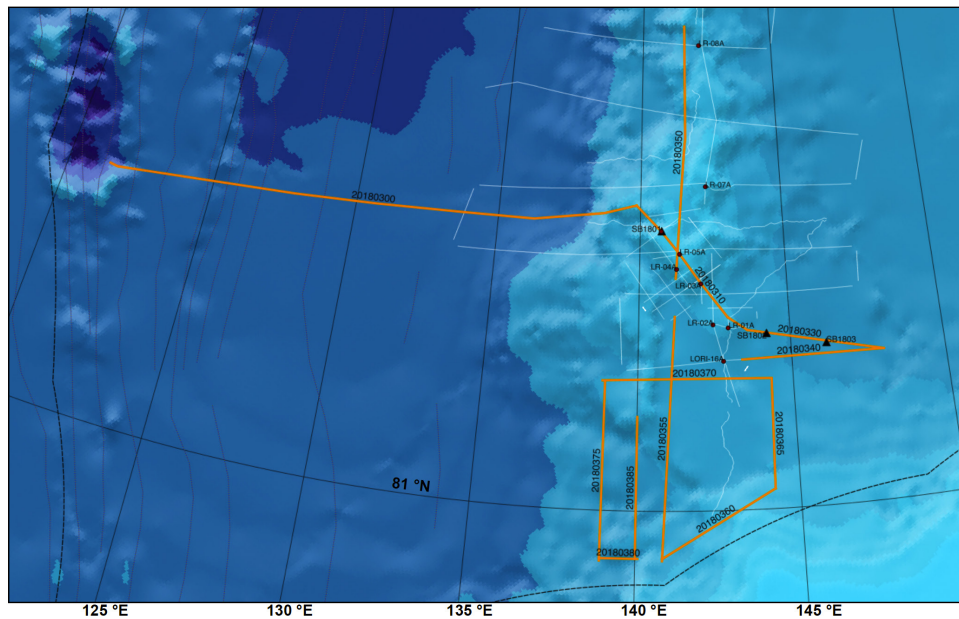


Fig. 6.1.1: Siberian part of the Lomonosov Ridge. Orange lines indicate the seismic reflection lines gathered during this cruise, black numbers the profile names, respectively. White lines: Seismic profiles acquired in 1998, 2008 and 2014; red dots: proposed IODP drill sites; black triangles: location of sonobuoys. Black, dashed lines mark the border of the Exclusive Economic Zone versus Russia, thin grey dashed-lines magnetic anomalies after Chernykh & Krylov (2011).

Work at sea

During the multichannel seismic-reflection survey (Tables 6.1.1 and 6.1.2; Fig. 6.1.1) we operated with a combination of the seismic equipment of the AWI and BGR, as streamers, airguns and recording system. We did not use any tail buoys with the streamer in order to avoid entanglements with drifting sea ice, although in the southern part of our research area no major drifting ice fields were sighted.

The seismic source was an array of 4 x 4.1 ltr. (~4 x 250 in³) G-Guns operated at 140 bar. The array is assembled compactly on a bar and was towed close behind the stern of the vessel in a constant depth of 12 m in order to protect the array from collisions with sea ice.

Seismic investigations started at Sept.16th, 04:50 UTC at the eastern rim of the Gakkel Deep. This first survey was continuously recorded and ended Sept. 18th, 23:51 UTC at the eastern slope of the Lomonosov Ridge (LR) (Fig. 6.1.1, Table 6.1.1). Since the first set of lines (20180300/310/320/330/340) were located close to the ice rim, the digital Sentinel-Streamer of the BGR with an active length of 600 m and 96 channels was used (Table 6.1.2). To make sure to depict the acoustic basement in the Amundsen Basin (AB) these lines were recorded with a shot point distance of 37.5 m (~15s), 14 s record length, and 2 ms sample rate.

The second set of seismic lines started at Sept. 23th, 15:45 UTC in a thin sea-ice coverage of 70 %. Consequently, for line 20180350 still the digital Sentinel-Streamer of the BGR with an active length of 600 m and 96 channels was used (Table 6.1.2). Further south, where sea ice was not encountered, a combination of the 2,400 m long digital Sentinel-streamer of the AWI (192 channels) and the 600 m long digital Sentinel-Streamer of the BGR (96 channels) was deployed.

This combination, resulting into a total active length of 3000 m and 288 channels, was operated for the remaining profiles (20180355/360/365/370/375/380) (Table 6.1.2). Lines of this second set were recorded with a shot interval of 25 m (~10s), 9.5 s record length and 2 ms sample rate. Due to bad weather conditions and heavy sea state the seismic survey had to be aborted at Sept. 27th, 9:00 UTC.

Tab. 6.1.1: Profile statistics for the seismic lines gathered during expedition PS115/2

Profile	Start of Profile				End of Profile				Length [m] (with gmt)	Time [h]	FFID/ Shot Start	FFID/ Shot End	Shots	Sono- buoy	
	Date	Jul. Day	Time UTC	Lon°E	Lat°N	Date	Jul. Day	Time UTC							Lon°E
20180300	16.09.2018	259	05:07:22	121°23'48.5"E 121°23'8.033"E 121°39'68"E 175773.35	81°19'04.8"N 81°19'08"N 81°13'18.0"N 9084095.44	17.09.18	260	17:23:43	139°51'07.9"E 139°51'13.17"E 139°51'13.17"E 481257.92	81°35'21.1"N 81°35'35.17"N 81°58'9.2"N 9059159.12	84	8313	8230	-	
20180310	17.09.2018	260	17:23:52	139°51'13.1"E 139°51'21.83"E 139°55'36"E 481281.17	81°35'21.0"N 81°35'35.00"N 81°58'9.2"E 9059155.02	18.09.2018	261	02:43:15	142°57'23.6"E 142°57'39.93"E 142°56'55"E 554146.04	81°00'27.83"N 81°00'46.6"N 8994296.64	8315	10559	2245	1801	
20180320	17.09.2018	261	02:43:30	142°57'28.5"E 142°57'47.50"E 142°95'7"E 534170.87	81°00'15.7"N 81°00'26.12"N 81°00'43"N 8994268.92	17.09.2018	261	04:12:32	143°35'08.6"E 143°35'14.33"E 143°58'57"E 545470.02	80°56'03.6"N 80°56'06.00"N 80°93'43"N 8986888.73	10560	10920	361	-	
20180330	18.09.2018	261	04:12:47	143°35'15.8"E 143°35'26.33"E 143°58'7"E 545505.90	80°56'03.7"N 80°56'05.17"N 80°93'42"N 8986875.17	18.09.2018	261	13:02:06	147°59'59.7"E 147°59'59.95"E 147°99'9"E 624888.49	80°46'55.4"N 80°46'9.233"N 80°78'21"N 8976417.96	10921	13056	2136	1802 1803	
20180340	18.09.2018	261	14:54:46	147°59'00.0"E 147°59'00.00"E 147°98'33"E 624889.2	80°46'55.5"N 80°46'9.25"N 80°78'21"N 8976419.66	18.09.2018	261	23:51:43	143°23'20.40"E 143°23'14.0"E 143°38'56"E 542654.54	80°46'53.9"N 80°46'8.983"N 80°78'16"N 8969708.87	13057	15257	2201	-	
20180350	23.09.2018	266	16:56:36	141°36'36.5"E 141°36'6.083"E 141°6'01"E	82°31'18.2"N 82°31'3.033"N 82°52'17"N	24.09.2018	267	09:17:38	141°13'47.9"E 141°13'7.983"E 141°23'00"E	81°12'36.1"N 81°12'6.017"N 81°21'00"N	351	6213	5862	-	
20180355	24.09.2018	267	11:43:34	141°11'43.9"E 141°11'7.317"E 141°19'55"E	81°00'40.9"N 81°00'68.17"N 81°01'14"N	25.09.2018	268	03:17:59	140°47'48.9"E 140°47'8.15"E 140°79'69"E	79°44'19.7"N 79°44'3.283"N 79°73'88"N	261	5950	5689	-	
20180360	25.09.2018	268	04:02:05	140°48'09.1"E 140°48'15.17"E 140°80'25"E	79°45'02.0"N 79°45'03.33"N 79°75'06"N	25.09.2018	268	12:31:10	144°13'57.9"E 144°13'9.650"E 144°23'27"E	80°06'11.3"N 80°06'1.883"N 80°103'1"N	4	3111	3107	-	
20180365	25.09.2018	268	12:31:20	144°14'01.9"E 144°14'03.17"E 144°23'39"E	80°06'11.7"N 80°06'1.95"N 80°103'2"N	25.09.2018	268	19:28:41	144°18'03.7"E 144°18'06.17"E 144°30'10"E	80°40'29.2"N 80°40'4.667"N 80°6'748"N	3112	5699	2587	-	
Run out profile??															
20180370	25.09.2018	268	20:16:45	144°17'48.4"E 144°17'8.067"E 144°29'68"E	80°40'41.8"N 80°40'6.967"N 80°6'783"N	26.09.2018	269	07:07:45	138°52'06.2"E 138°52'1.033"E 138°86'84"E	80°40'30.4"N 80°40'5.067"N 80°67'51"N	4	3931	3927	-	
20180375	26.09.2018	269	08:08:11	138°57'01.5"E 138°57'0.250"E 138°95'04"E	80°40'24.3"N 80°40'4.050"N 80°6'734"N	26.09.2018	269	19:22:43	138°57'05.2"E 138°57'0.867"E 138°95'14"E	79°44'12.4"N 79°44'2.067"N 79°73'68"N	8	4191	4183	-	
20180380	26.09.2018	269	20:19:08	138°57'00.1"E 138°57'0.017"E 138°95'00"E	79°44'57.8"N 79°44'9.633"N 79°74'94"N	26.09.2018	269	22:47:40	140°04'27.1"E 140°04'4.517"E 140°07'42"E	79°44'59.5"N 79°44'9.917"N 79°74'99"N	1	849	849	-	
20180385	27.09.2018	270	00:03:45	140°00'02.4"E 140°00'0.400"E 140°00'07"E	79°45'00.0"N 79°45'0.000"N 79°75'00"N	27.09.2018	270	09:00:47	140°00'10.7"E 140°00'1.783"E 140°00'3"E	80°29'20.8"N 80°29'3.467"N 80°489'1"N	1	3301	3301	-	

6.1 Seismic Reflection

Tab. 6.1.2: Setup of streamer and airguns

Profile	Streamer	Lead in	Airgun	Pressure	Chan	dx Chan	Dist. Source -first receiver	Sample rate	Record length	Shot Interval	Shot Interval	Streamer depth
	[m]	[m]	G-Gun à 4.1 ltr	[bar]		[m]	[m]	[ms]	[s]	[m]	[s]	[m]
20180300	600	50	4 x G =16.4	4 x 145	96	6.25	73	2	14	37.5	15	12
20180310	600	50	4 x G =16.4	4 x 145	96	6.25	73	2	14	37.5	15	12
20180320	600	50	4 x G =16.4	4 x 145	96	6.25	73	2	14	37.5	15	12
20180330	600	50	4 x G =16.4	4 x 145	96	6.25	73	2	14	37.5	15	12
20180340	600	50	4 x G =16.4	4 x 145	96	6.25	73	2	14	37.5	15	12
20180350	600	50	4 x G =16.4	4 x 145	96	6.25	73	2	14	37.5	15	12
20180355	3000 (2400+600)	50	4 x G =16.4	4 x 145	1-192	12.5	73	2	9.5	25	10	12
					193-288	6.25	73	2	9.5	25	10	12
20180360	3000 (2400+600)	50	4 x G =16.4	4 x 145	1-192	12.5	73	2	9.5	25	10	12
					193-288	6.25	73	2	9.5	25	10	12
20180365	3000 (2400+600)	50	4 x G =16.4	4 x 145	1-192	12.5	73	2	9.5	25	10	12
					193-288	6.25	73	2	9.5	25	10	12
20180370	3000 (2400+600)	50	4 x G =16.4	4 x 145	1-192	12.5	73	2	9.5	25	10	12
					193-288	6.25	73	2	9.5	25	10	12
20180375	3000 (2400+600)	50	4 x G =16.4	4 x 145	1-192	12.5	73	2	9.5	25	10	18
					193-288	6.25	73	2	9.5	25	10	18
20180380	3000 (2400+600)	50	4 x G =16.4	4 x 145	1-192	12.5	73	2	9.5	25	10	18
					193-288	6.25	73	2	9.5	25	10	18
20180385	3000 (2400+600)	50	4 x G =16.4	4 x 145	1-192	12.5	73	2	9.5	25	10	18
					193-288	6.25	73	2	9.5	25	10	18

A permanent quality control (QC) was performed during registration with the *SEAL428* acquisition system of *SERCEL*.

In summary, we gathered seismic data with the following setups (Tables 6.1.1 and 6.1.2):

Streamer	Airguns	Shots	Dist.	Length
600 m BGR-Sentinel streamer (96 chan.)	4 BGR G-guns	21,035	37.5m	788 km
3000 m combined Sentinel streamers	4 BGR G-guns	23,643	25 m	590 km
AWI: 2400m (192chan.) + BGR: 600m (96 chan.)				
Total quantity of seismic data is: (162 h)		44,678		1,378 km
Pure lines length:				1,160 km

Three sonobuoys were deployed, one (SB-1801) at proposed drilling site LR-06A, and two (SB-1802, 1803) at the eastern slope of the Lomonosov Ridge transitioning into the Makarov (Podvodnikov) Basin (MB). During the deployment the streamer depth was temporally set to 30 m to avoid entangling. The sonobuoys recorded signals up to a distance of about 35 km (Table 6.1.3).

Tab. 6.1.3: Sonobuoys statistics

Sonobuoy	Profile	Date	Jul. Day	Time UTC	Shot	Lon° E	Lat° N	Comment	Comment
1801	20180310	17.09.2018	260	19:45	8875	140.737°E 140° 44.22'E	81.4557°N 81° 27.34'N	Streamer 35m	Lomonosov Ridge close to LR_06A
1802	20180330	18.09.2018	261	5:31 5:39	11220 11272	144.2147° 144° 13.510'	80.9156° 80° 54.741'	Streamer 35m	Makarov Basin
1803	20180330	18.09.2018	261	09:11	12131	146° 09.35'E 146,1545°	80° 50.747'N 80.8511°N	Streamer 35m	Makarov Basin

All seismic measurements were accompanied by gravity and magnetic recording by an on-board KSS 31 Gravimeter (Chapter 6.3) and Fluxgate magnetometers (Chapter 6.4), respectively to gain information on crustal structure and age. Swath bathymetric and sediment echosounder (PARASOUND) data, which are described in chapters 5 and 7.2, respectively, supplement the seismic survey.

Preliminary results

Processing of the multichannel seismic data on board was performed by colleagues of the BGR with the software “SeisSpace/Promax”. The procedure comprised single-channel quality control, CDP-sorting, velocity analyses, brute-stack, as well as filtering to reduce the bubble-pulse, improve the signal-to-noise ratio, suppress multiples, and finally apply a migration (Kai Berglar). First interpretation of seismic data is done on pre-stack time migrated sections with the software “GeoFrame/IESX” (Christoph Gaedicke).

The recorded new seismic lines across and along the Lomonosov Ridge show similar reflection characteristic for the upper seismic units as on seismic lines gathered in 1998, 2008 and 2014 indicating four major depositional stages in the southeastern Arctic Ocean (Weigelt et al., 2014). A prominent high-amplitude-reflector sequence (HARS), indicating widespread changes in tectonic and deposition conditions can be traced on all lines. On top of the Lomonosov Ridge it is expressed as a sequence of strong-amplitude reflectors, in the Amundsen and Makarov Basin as an unconformity, distinguished by high-amplitude reflections. The unconformity is associated with the subsidence of the Lomonosov Ridge and gradual opening of the Fram Strait, and will be taken as tie point for dating the strata above over a large region.

Lomonosov Ridge (LR) (lines 20180310, 350):

Lines 20180310 and 20180350 serve a major aim of the expedition: the acquisition of cross lines to former surveys covering the location of the proposed IODP-sites LR-06A, LR-05A, LR-04A, LR-03A. The new profiles confirm the presence of about 1,600m thick undisturbed and parallel running sedimentary layers. The strata can be directly correlated to the seismic stratigraphy made for former lines (e.g. the High-Amplitude-Reflector Sequence (HARS)). However, some minor shifts of site locations would improve the target to drill a complete section. As example for LR-06A, the new cross line 20180310 indicates erosion of the uppermost layers (80 m depth) (Fig. 6.1.2, around CDP 7500). Undisturbed and complete layering is revealed only 2 km eastwards of the proposed location. Consequently, a slight shift of the proposed site presents a much better location for coring an entire Pliocene section. Such detailed analyses have to be performed onshore to detect if a shift of other proposed site locations would also be favourable.

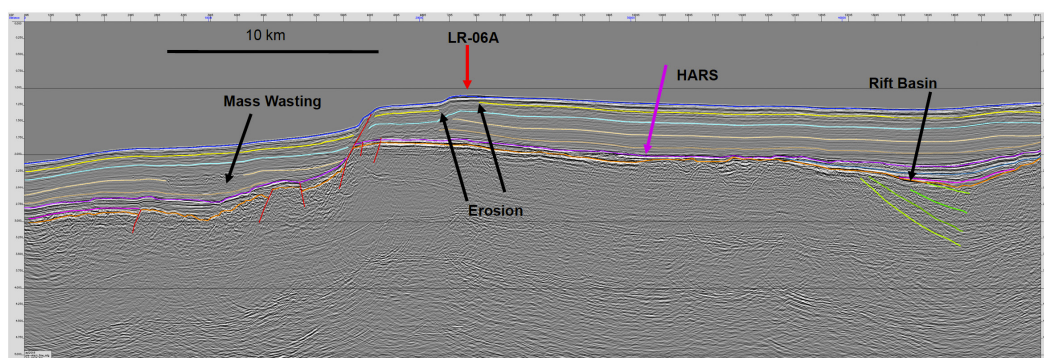


Fig. 6.1.2: Part of line 20180310 along the Lomonosov Ridge around the location of Site LR-06A (about CDP7500, red arrow). Erosion of the uppermost sedimentary sequence is indicated around CDP7500. A mass wasting structure is evident between CDP 3000 and 4200, and extending from CDP 13500 to 15100 a rift basin is clearly imaged.

Further findings on the slopes of the LR are several traces of mass wasting (e.g. Fig. 6.1.2, CDP 3000-4200) indicating slumping events during the subsidence of the ridge. Some small rift basins (e.g. Fig. 6.1.2, CDP 13500-15100) can be related to tectonic processes during the breakup and subsidence of the LR.

Amundsen Basin (AB) (line 20180300):

An about 300 km long transect across the Amundsen Basin (Fig. 6.1.3) image at least a 2.5 s TWT (~ 3 km) thick sedimentary sequence over a rough surface of the acoustic basement (Fig. 6.1.3a). The lowermost sedimentary sequences are faulted, tilted, eroded, and occasionally uplifted. A prominent unconformity (highlighted in turquoise) marks a large deformation event. The strata above are at some parts faulted and tilted (Fig. 6.1.3a, CDP 40800-45600).

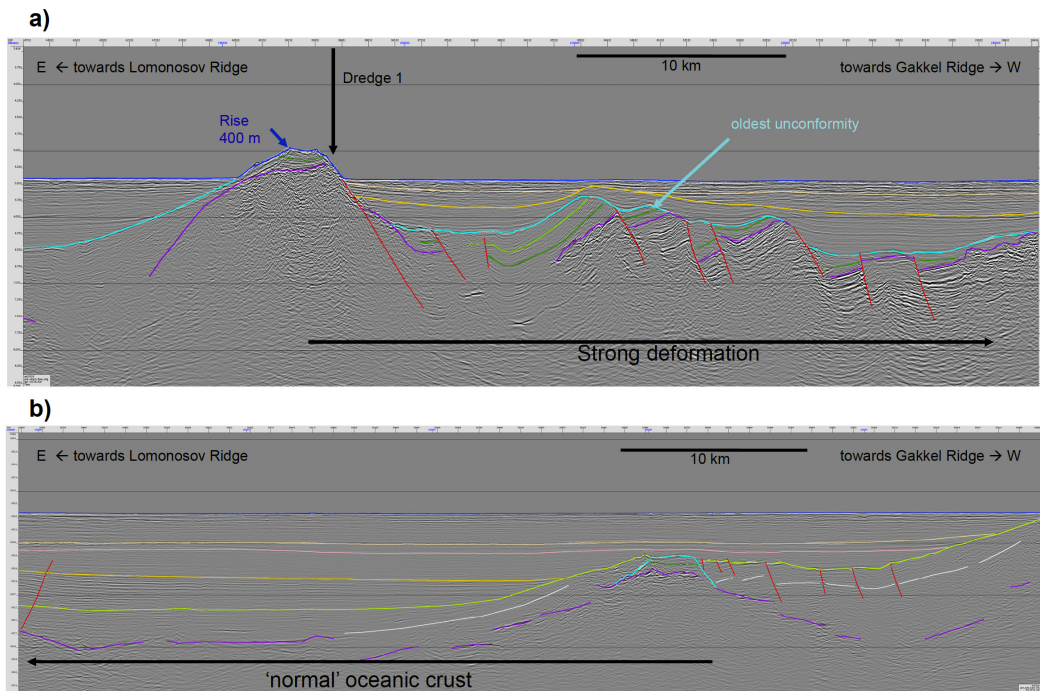


Fig. 6.1.3: Two parts of line 20180300 across the Amundsen Basin. Part a) shows a section across a topographic high located about 65 km east of the Gakkel Deep. Part b) is located ca. 90 km west of the Lomonosov Ridge and images a topographically smooth acoustic basement.

Between CDPs 3800-4500 (Fig. 6.1.3a) an about 600 m high elevation is imaged. A part of this rise was already recorded in 2014 by sub-bottom profiling and bathymetry surveys. But up to now it was not clear if this rise results from a mud volcano close to the seafloor, or if it presents a deeper structure. As imaged in the new seismic lines this seamount rises from the crust and penetrates all sedimentary layers, thus indicating a magmatic origin. Dredge-sampling on an outcrop at the western slope of the rise (Fig. 6.1.3a) reveal consolidated sand-, silt- and claystones (for details see Chapter 7.5, Figs 7.5.13 and 7.5.14).

Towards the LR the crustal surface shows minor deformations and the shape of 'normal' oceanic crust with a calm deep-sea sedimentation (Fig. 6.1.3b). Whereas the strong deformations in the western AB, can be associated with a re-organisation of tectonic plates accompanied by a significant decrease in spreading rates, the origin of the smooth crustal topography in the eastern basin remains enigmatic.

Transition of LR to Siberian Shelf (20180355-385):

Lines over the transition from the LR to the Laptev Sea Shelf (LSS) image a more than 2 km thick sedimentary sequence overlying a rugged and faulted acoustic basement (Fig. 6.1.4). At a first glance no indications of a larger transform fault can be detected, which could elucidate

the tectonic relation of the LR to the LSS. Exemplarily for all lines across the transition, line 20180355 (Fig. 6.1.4) shows sedimentary bodies with transparent to chaotic reflection pattern (CDP 1600 to end) indicating large mass wasting events or debris flows. An erosional channel (CDPs 12600-13700) with a sediment drift on its southern edge (CDPs 13700-14100) may provide clues to ocean current development.

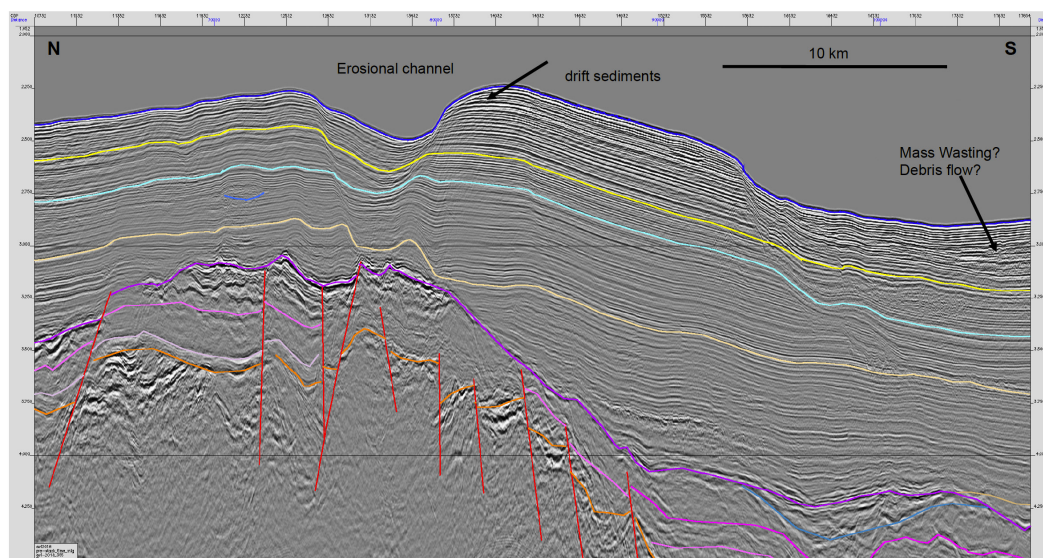


Fig. 6.1.4: Part of line 20180355 from the Lomonosov Ridge southwards to the Laptev Sea Shelf

Data management

Seismic reflection data will be made available upon request after a phase of restricted access of 4 years after data acquisition.

References

- Björk G, Jakobsson M, Assmann K, Andersson LG, Nilsson J, Stranne C, and Mayer L (2018) Bathymetry and oceanic flow structure at two deep passages crossing the Lomonosov Ridge. *Ocean Sci.*, 14, 1–13, 2018, doi: 10.5194/os-14-1-2018.
- Chernykh AA and Krylov AA (2011) Sedimentogenesis in the Amundsen Basin from Geophysical and Drilling Evidence on Lomonosov Ridge, *Doklady Earth Sciences*, 440, 1372-1376.
- Heezen B and Ewing M (1961) The mid-oceanic ridge and its extension through the arctic basin. In Raasch, G., editor, *Geology of the Arctic*, volume 1, pages 622-642. University of Toronto Press, Toronto.
- Jakobsson M, Backman J, Rudels B, Nycander J, Mayer L, Sangiorgi F, Brinkhuis H, O'Regan M, Jokat W, Frank M, King J, Moran K (2007) The early Miocene onset of a ventilated circulation regime in the Arctic Ocean. *Nature*, 447, 987-990, doi:10.1038/nature05924.
- Jokat W, Weigelt E, Kristoffersen Y, Rasmussen T, Schöne T (1995) New insights into evolution of the Lomonosov Ridge and the Eurasian Basin. *Geophys. J. Internat.*, 122, 378-392.
- Jokat W (2005) The sedimentary structure of the Lomonosov Ridge between 88°N and 80°N: Consequences for tectonic and glacial processes, *Geophysical Journal International*, 163, 698-726. doi:10.1111/j.1365-246X.2005.02786.x.

6.1 Seismic Reflection

- Kristoffersen Y (1990) Eurasian Basin, in: Grantz A, Johnson L, Sweeny J.F. (Eds.), The Arctic Ocean Region, Geology of North America Vol. L., Geol. Soc. Am., Boulder, Colorado, pp. 365-378.
- Stein R (ed) (2015) The Expedition PS87 of the Research Vessel *Polarstern* to the Arctic Ocean in 2014, Reports on Polar and Marine Research 688, Bremerhaven, Alfred Wegener Institute for Polar and Marine Research 688, 273 pp (http://epic.awi.de/37728/1/BzPM_0688_2015).
- Stein R (2017) From Greenhouse to Icehouse: The late Mesozoic-Cenozoic Arctic Ocean sea-ice and climate history. *Polarforschung* 87, 61-78.
- Stein R, Jokat W, Niessen F, Weigelt E (2015) Exploring the long-term Cenozoic Arctic Ocean Climate History – A challenge within the International Ocean Discovery Program (IODP). *Arktos* 1, doi: 10.1007/s41063-015-012-x.
- Weigelt E, Franke D, Jokat W (2014) Seismostratigraphy of the Siberian Arctic Ocean and adjacent Laptev Sea Shelf, *J. Geophys. Res.* 119 (7), pp. 5275-5289.

6.2 Passive seismology

John-R. Scholz¹, Adalbert Pfeiffer¹, Estella Weigelt¹, ¹AWI
 Winfried Markert², not on board: Vera Schlindwein¹, ²Polarstern Crew
 Henning Kirk¹, Marc Hiller¹

Grant-No. AWI_PS115/2_01

Objectives

Gakkel Ridge as one of the slowest spreading mid-ocean ridges on Earth is a key research target to better understand how new ocean lithosphere is being created with very little mantle melting. Despite the very low spreading rate at eastern Gakkel Ridge of less than 9 mm/y, a number of prominent volcanoes emerge from the sediment cover of the rift valley. There is an eye-catching depression in the rift valley floor at eastern Gakkel Ridge, called Gakkel Deep, that has recently caught scientific attention. It has been thought to result from a gigantic caldera collapse (Piskarev & Elkina, 2017), or been considered as mainly volcanic structure (Nikishin et al., 2017). We investigate with our passive seismic experiment, whether Gakkel Deep is a volcanic structure or potentially its rims represent ejection material from a past eruption in which case we would not expect present day magmatic seismicity. In addition, this installation of a small-scale ocean bottom seismometer network on a presumably volcanic feature near the western termination of Gakkel Deep serves as a first test of our newly developed ocean bottom seismometers that can operate underneath dense sea ice. We further expect a valuable record of ocean noise during an entire year from an ice-marginal zone. We will record ocean micro-seismics and wave development in the increasingly open Arctic Ocean providing valuable information on the impact of wave action on sea ice.

Work at sea

For the passive seismology programme, four newly developed ice ocean-bottom seismometers (ice-OBSs, Fig. 6.2.1) were deployed. These prototypes – developed at AWI by Marc Hiller and Henning Kirk – can operate underneath dense sea ice. The instruments were assembled in Tromsø, Norway, before *Polarstern* Expedition 115/1 so that during this cruise they only had to be turned on before deployment. Likewise before this cruise, the four ice-OBS releaser units had been tested by M. Hiller (AWI) on *Polarstern* Expedition PS115/1. Two releaser units failed that test and were subsequently exchanged (stations ‘GKD01’ and ‘GKD03’).

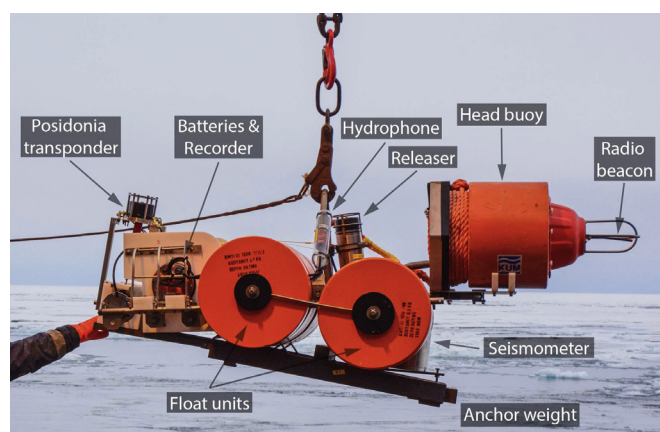


Fig. 6.2.1: AWI-developed prototype of the ice ocean-bottom seismometer (ice-OBS), moments before deployment (station ‘GKD03’). The most significant changes in contrast to AWI’s standard ocean-bottom seismometers from the DEPAS pool are the additional head buoys carrying the beacon system (emitting only upon re-surfacing), and the Posidonia transponders attached to the device via a long rope (rope releasing only upon recovery from the sea floor). (Photo: Ryan Love)

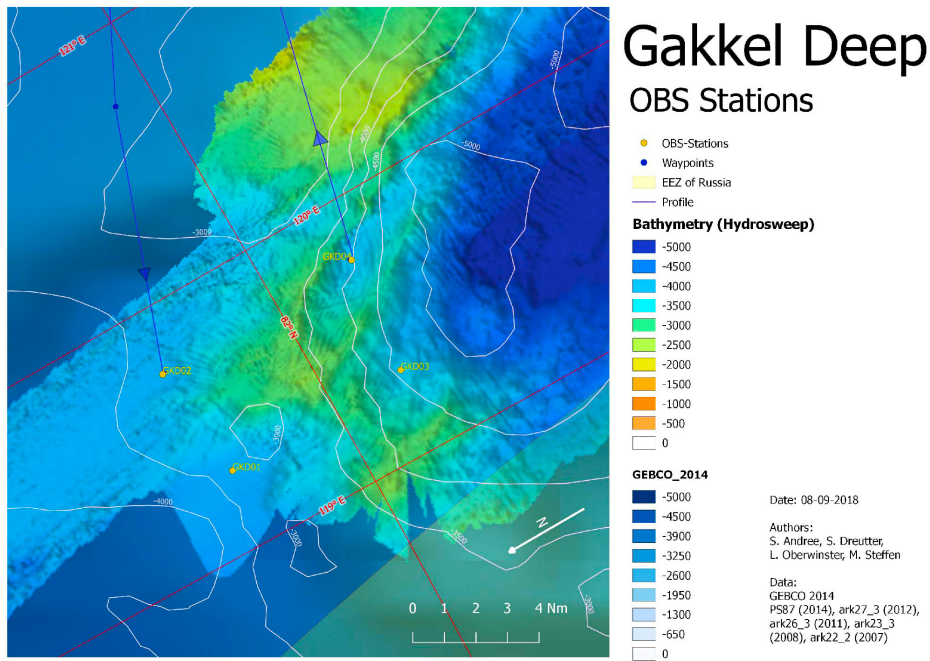


Fig. 6.2.2: Rectangular deployment scheme of the four ice-OBSs (yellow circles), centred around the bathymetric elevation just North of the pronounced Gakkel Deep. Note that the Russian EEZ (exclusive economic zone) is not far. (Plot: bathymetry group)

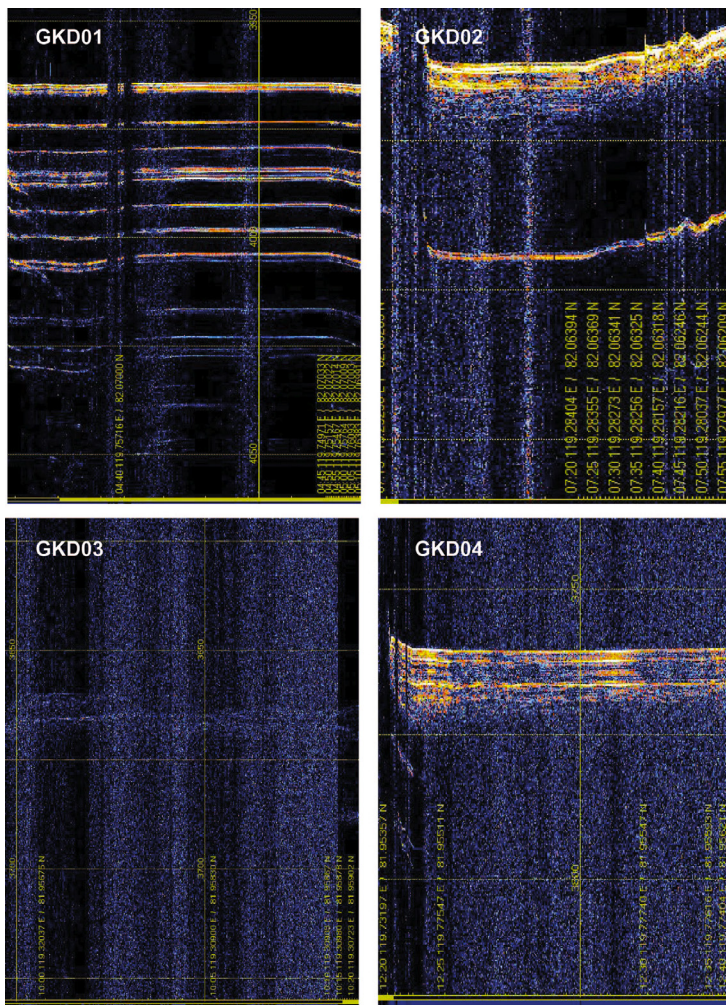


Fig. 6.2.3: Screenshots of the PARASOUND data recorded during the approach of the ice-OBS deployment sites. Note the laminar and horizontal layers for stations ‘GKD01’, ‘GKD02’, and ‘GKD04’, indicating flat bathymetry and thick sediment layers optimal for OBS deployments. For station ‘GKD03’, however, the synopsis of bathymetry and PARASOUND data suggests similar sea floor conditions with a slightly inclined surface. (Screenshots: Jolien van der Krogt, Frank Niessen)

Using *Polarstern's* crane 3 (15 tons), the four ice-OBSs were deployed on 15 September 2018, just North of the Gakkel Deep around a bathymetric elevation that may represent a volcanic structure (see Objectives). The deployment scheme was rectangular, with inter-station distances of about 5-10 km (Fig. 6.2.2). The precise deployment locations were chosen with respect to the bathymetry; a flat sea floor of the extent of 1x1 km was preferred so in the case of the instruments drifting during their free-fall to the sea floor chances are high they still land on a flat spot. Furthermore during the approach of these targeted sites, *Polarstern's* PARASOUND data had been evaluated to ensure, as far as possible, deployment onto a horizontal cover of sediments that would improve the seismometers' coupling to the sea floor. With the exception of 'GKD03', the PARASOUND profiles show acoustic sediment penetration and more or less horizontal reflection geometry indicative of undisturbed flat deep-sea sedimentary environments (Fig. 6.2.3). For station 'GKD03' this indication is only subtle. The explanation is a slightly inclined sediment surface at this location as seen in the bathymetric map, whereas the sea floor of the three other locations is flat (Fig. 6.2.2). Inclined strata of more than 4° relative to horizontal can only be poorly resolved in PARASOUND data. However, the relative smooth topography at 'GKD03' together with some backscatter from sediment layers let to assume similar bottom conditions as to the other three deployment sites. The weather conditions during all deployments were favourable, with no precipitation, true wind velocities of less than 4 m/s, moderate ice covers, and no waves or swell of the sea (Fig. 6.2.4).



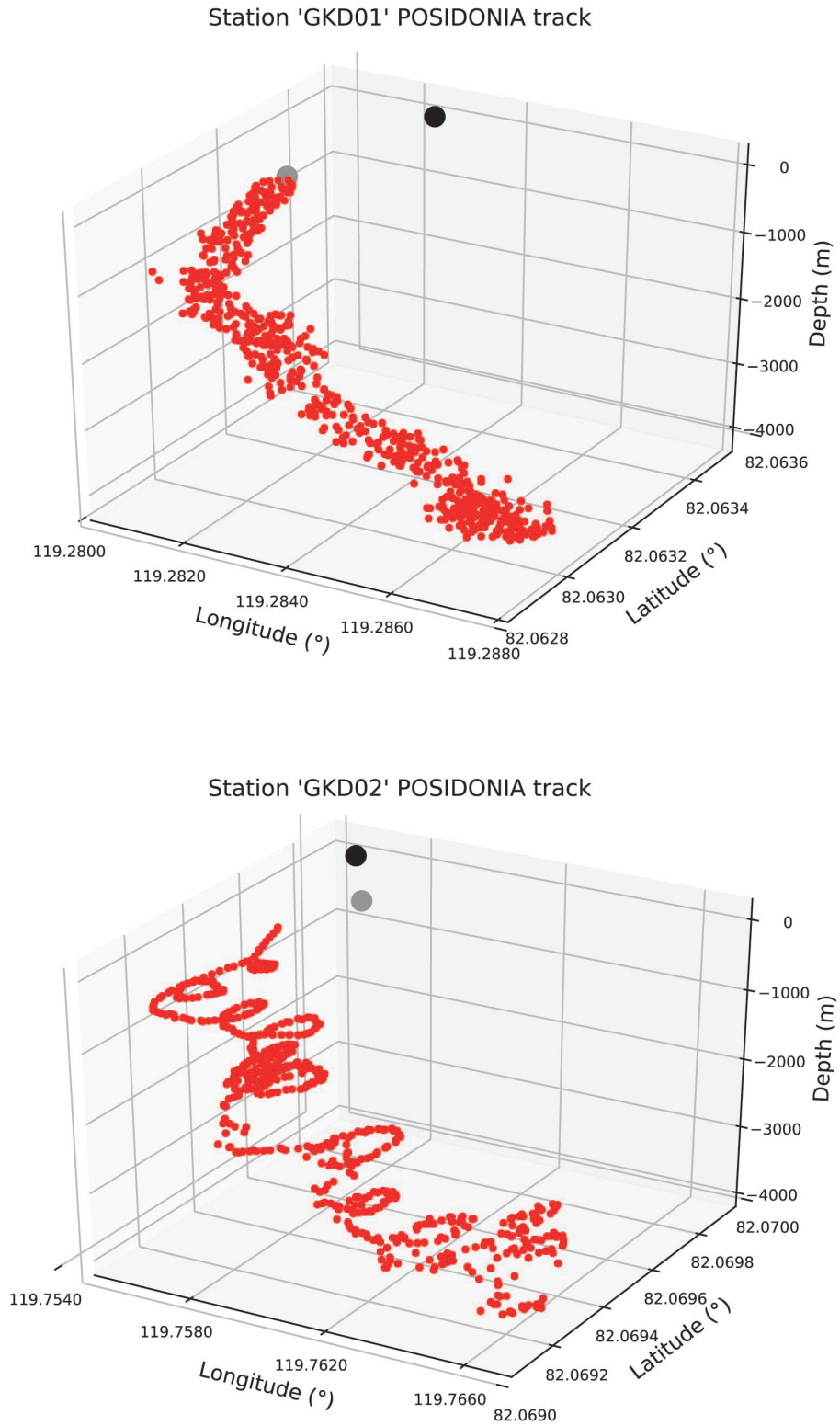
Fig. 6.2.4: Deployment of ice-OBS 'GKD03'. Note the calm weather conditions with no precipitation, almost no wind, and the lack of sea waves or swell

All four ice-OBSs were equipped with a Posidonia positioning transponder that had been successfully tested by M. Hiller (AWI) on the previous *Polarstern* expedition PS115.1. The Posidonia system allowed the quasi-continuous tracking of the ice-OBSs – that are subject to movements by the ocean currents – during their free fall to the sea floor. Due to a malfunction of the sonde that measures the sound velocities in the different water layers (sound velocity profile – SVP), the Posidonia system could not be calibrated / improved prior to the ice-OBS deployments. However, the system still possesses an accuracy of about 10 meters per 1,000 meters of water depth (pers. comm. Winfried Markert, lab electrician). Using the Posidonia transponders, we could determine the landing spots of the ice-OBSs within the stated margin of errors. This is important knowledge, as it will increase the chances of a successful instrument recovery next year in an area potentially covered with dense sea

ice throughout the year. After arrival to the seafloor, the Posidonia unit of station ‘GKD04’ could not be inhibited (put ‘asleep’) even after multiple attempts of the following scheme: 1x inhibition command (still responding), 1x inhibition command (still responding), 1x inhibition command (still responding), 3x inhibition commands (still responding), 3x inhibition commands (leave of site without further attempts of communication). One speculation is that the used frequencies of the awake and pinging commands are too close to each other so the pinging command itself wakes up the transponder unintentionally. Nevertheless, the manual states the Posidonia unit will inhibit itself after 30 or 60 minutes in case of no further communications. No problems for the Posidonia unit of station ‘GKD04’ (SN 1018) may therefore be expected upon station recovery. All deployment data of the four ice-OBSs are summarised in Table 6.2.1. The Posidonia tracks of the instruments on the way down to the seafloor are shown in Fig. 6.2.5. The programmed reaser auto-relaese times are: 01.10.2019 at 07:00 UTC for ‘GKD01’; 30.09.2019 at 06:00 UTC for ‘GKD02’; 01.10.2019 at 02:30 UTC for ‘GKD03’; 30.09.2019 at 22:00 UTC for ‘GKD04’.

Tab. 6.2.1: Deployment data of all four prototype ice ocean-bottom seismometers (ice-OBSs), with stations named ‘GKD01’ to ‘GKD04’. All four ice-OBSs were deployed on September 15th, 2018, according to the Universal Time Coordinated (UTC). The Posidonia system could not be calibrated / improved prior to all deployments (see text). After arrival to the sea floor, the Posidonia unit of station ‘GKD04’ could not be inhibited (put ‘asleep’) even after several attempts (see text). Depths of “Deployment from ship” were taken from the ship’s navigation (centre beam of hydrosweep), depths of “Arrival at the sea floor” were calculated by the Posidonia system. The “Deployment from ship” positions are corrected, i.e. referenced to the actual deployment positions starbord astern as opposed to the ship’s GPS reference point at the time of deployment; applied correction values were 33 m towards stern, 19 m towards starbord.

		GKD01	GKD02	GKD03	GKD04
DEPLOYMENT from SHIP (gray points in Fig. 6.2.4)	Lat (° + decimal ‘)	82 03.809	82 04.194	81 57.517	81 57.357
	Lon (° + decimal ‘)	119 16.950	119 45.370	119 18.471	119 46.496
	Depth (m)	4165	3964	3662	3742
	Time (hh:mm in UTC)	07:24	04:55	10:10	12:33
	Ship heading (N to E, °)	45	340	85	120
ARRIVAL at SEAFLOOR	Lat (° + decimal ‘)	82 03.784	82 04.155	81 57.514	81 57.363
	Lon (° + decimal ‘)	119 17.230	119 45.966	119 18.147	119 46.246
	Depth (m)	4089	3927	3633	3728
	Time (hh:mm in UTC)	08:50	06:21	11:28	13:53
POSIDONIA system	Serialnumber	1019	1014	1017	1018
	No. track points	640	634	562	569
	positioning with SVP	x	x	x	x
	inhibited after landing	✓	✓	✓	(x)
STATISTICS	Sink time (min)	86	86	78	80
	Ø sink velocity (m/s)	0.75	0.73	0.76	0.76
	Lateral displacement (m)	82	132	56	48

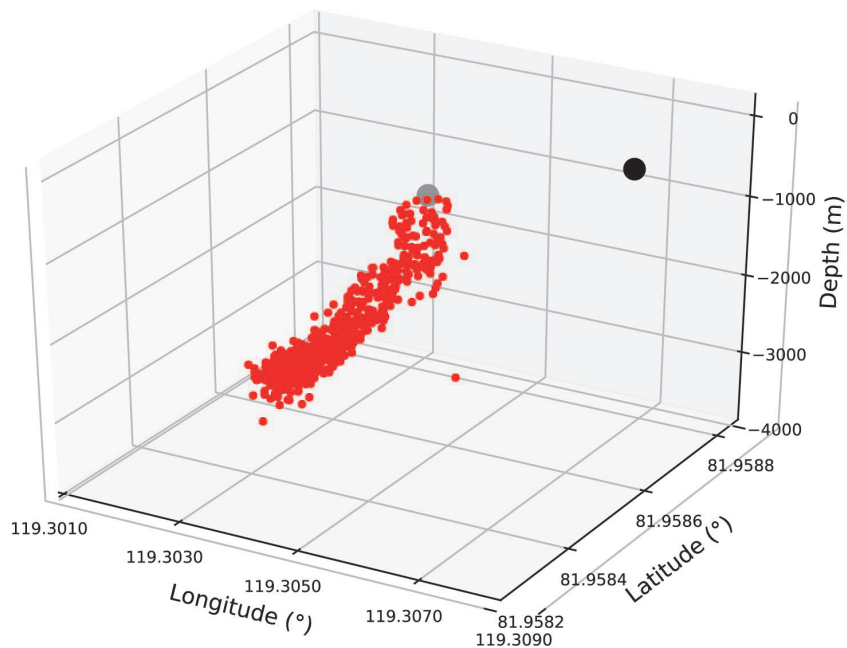


Part 1:

Fig. 6.2.5: see next page for figure caption

Station 'GKD03' POSIDONIA track

Part 2:



Station 'GKD04' POSIDONIA track

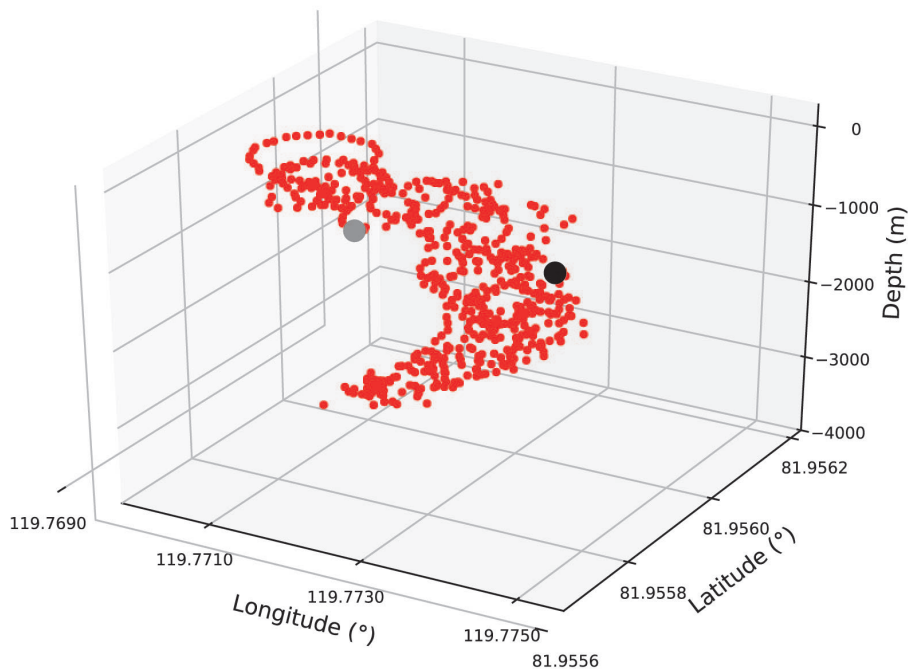


Fig. 6.2.5: Transmitted Posidonia positions during the ice-OBSs' free fall down to the seafloor after deployment (= red dots). Part (1): stations 'GKD01' and 'GKD02'; Part (2): stations 'GKD03' and 'GKD04'. Black dots = the ship's GPS positions at the time of instrument deployment; gray dots = corrected GPS positions with respect to the actual instrument deployment starboard astern (see caption Tab. 6.2.1). For stations 'GKD02' and 'GKD04' (eastern flank of the bathymetric elevation, Fig. 6.2.2), circular sinking trajectories are observed. This could, if not purely related to the Posidonia's margin of error, signify stronger / more turbulent water currents East of the seafloor elevation than West of it. For 'GKD02' the circular trajectory appears left-oriented, for 'GKD04' right-oriented.

Preliminary results

The ice-OBS prototypes will only be recovered after a recording period of one year, such that no measurements or results were obtained during this cruise.

Data management

Once recovered in autumn 2019, the passive seismic data will be made available through the GEOFON data-centre after a phase of restricted access of four years.

References

- Nikishin AM, Gaina C, Petrov EI, Malyshev NA, Freiman SI (2017) Eurasia Basin and Gakkel Ridge, Arctic Ocean: Crustal asymmetry, ultraslow spreading and continental rifting revealed by new seismic data, Tectonophysics, in press.
- Piskarev A, Elkina D (2017) Giant caldera in the Arctic Ocean: Evidence of the catastrophic eruptive event. Scientific Reports, 7, 46248, doi: 10.1038/srep46248.
- Vogt PR, Taylor PT, Kovacs LC, Johnson GL (1979) Detailed aeromagnetic investigations of the Arctic Basin, Jour. Geophys. Res. 84: 1071-1089.

6.3 Magnetic measurements

Sergei Freiman¹, John-R. Scholz², Winfried Markert³,
Estella Weigelt², not on board: Graeme Eagles²,
Wolfram Geissler²

¹UoM

²AWI

³Polarstern Crew

Grant-No. AWI_PS115/2_01

Objectives

Magnetic data were collected throughout expedition PS115/2 using *Polarstern's* vector magnetometer system as part of ongoing reconnaissance. The system is permanently installed midships in the crew's nest. Above decks, it consists of two orthogonal three-component digital fluxgate sensors from MAGSON GmbH (Fig. 6.3.1). Data from the magnetometers reach an industrial PC in the ship's computer room via a fibre optic connection. From here they are forwarded to the DSHIP system. Data are displayed in real time on the computer's monitor (Fig. 6.3.2).



Fig. 6.3.1: Fluxgate magnetometer system (two sensors marked by arrows) on *Polarstern*

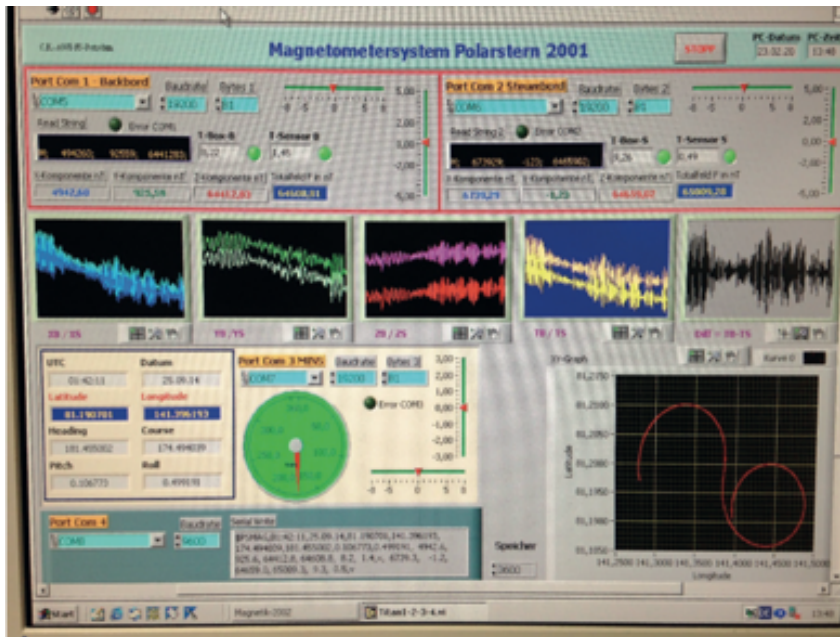


Fig. 6.3.2:
Magnetometer data
capture and display
in the computer
room

Key technical specifications of the 3 component ringcore sensors are as follows:

noise level	<10 pT/sqrt(Hz)
long term stability	<10 nT/year
dynamic range	+/-100000 nT in all components
resolution	+/-10 pT
temperature measurement	separately for electronics and sensor
housing for electronics and sensor	waterproof aluminium box
power supply	12-20V DC
input current	200mA
signal processor	TMS320F206
tilt meter	dual axis inclinometer SSY0090C

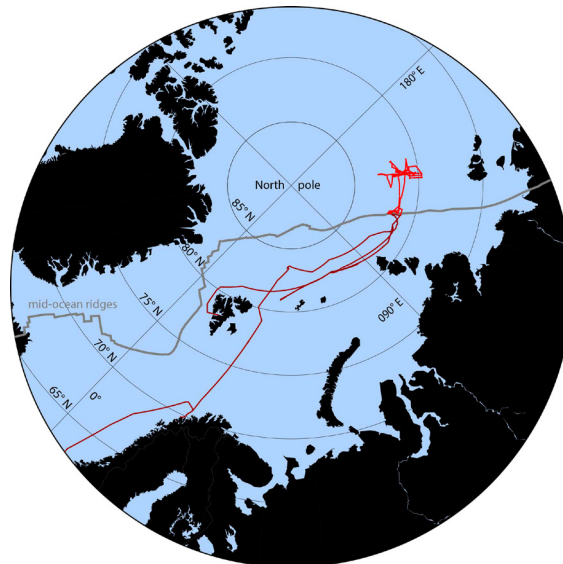
Work at sea

Magnetic data from the two magnetometers were recorded and logged continuously at 1 Hz. No planned magnetic survey track pattern was followed, as the main aims of the leg were seismic surveying and geological sampling. Data were logged everywhere except where permission to do so is normally required, but had not been sought or granted. Fig. 6.3.3 shows the locations of the logged magnetic data.

Preliminary results

Working with the system involves the important step of compensating for transient effects on the data that come from induced and remanent magnetic fields related to the ship's ferromagnetic bulk and its movement within Earth's magnetic field. Two calibration loops in form of an „8“ and with a loops-diameter of 1 nm were completed at different locations in order to calculate the coefficients that are necessary for this compensation (see Table 6.3.1 for locations and Fig. 6.3.4 for an example). It is advisable to complete loops like these at regular intervals in order to be able to compensate for slow changes in the ship's permanent magnetisation or in the eddy fields brought about by changes in the ship's cargo placement.

Fig. 6.3.3: Polarstern track during Expedition PS115/2 from Longyearbyen, Norway, to Bremerhaven, Germany; dark-red colour = track along which no magnetic & gravimetric data have been recorded (e.g., Russian EEZ), red colour = track along which magnetic & gravimetric data have been recorded.



Tab. 6.3.1: Summary of the two calibration circles for compensating the ship's magnetic field. Locations are given with respect to the centres of the calibration circles.

Date	Latitude	Longitude
6 Sep. 2018	80.34623° N	10.85707° E
8 Oct. 2018	77.19557° N	29.52627° E

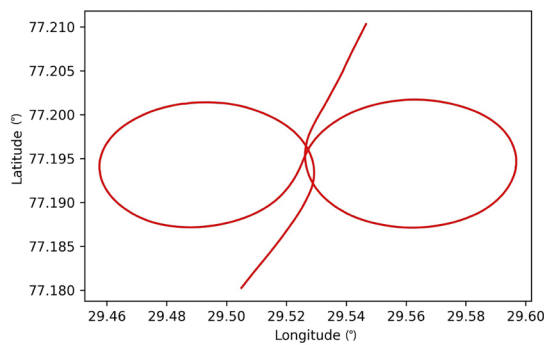


Fig. 6.3.4: Example of a compensation loop ship track from 8 October 2018.

Data management

All of the fluxgate data were downloaded from the DSHIP system at the end of the leg. Calculation of compensated magnetic profile values will be completed in Bremerhaven later. Data acquisition was stopped before entering the Russian EEZ.

6.4 Gravity measurements

Sergei Freiman¹, John-R. Scholz²,
Winfried Markert³, Estella Weigelt²
not on board: Graeme Eagles², Wolfram
Geissler²

¹UoM
²AWI
³Polarstern Crew

Grant-No. AWI_PS115/2_01

Objectives

Polarstern's permanently-installed “Bodenseewerk KSS-32” gravimeter measured relative gravity throughout expedition PS115/2 as part of its ongoing reconnaissance gravity surveying effort. Data were logged at all locations except in Russian waters where permission to do so was not sought or granted. Two sets of onshore tie measurements were made at the end of the leg, in Tromsø and in Bremerhaven. Together with measurements made earlier in Tromsø and Bremerhaven, these measurements allow us to convert the shipboard data to absolute gravity values and correct them for instrument drift. Fig. 6.3.3 (Chapter 6.3) shows the locations of logged gravimetric data.

Work at sea

Tie and drift measurements in Bremerhaven, Germany, and Tromsø, Norway

Measurements were made before the *Polarstern* Expedition 115/2 with the portable “LaCoste & Romberg gravity meter G-1031” next to the ship at the ports of Bremerhaven and Tromsø, and at the IGSN absolute gravity points at the Nordnorsk Kunstmuseum (formerly the Police Station) and Tromsø Museum (Tables 6.4.1 — 6.4.10). The KSS-32 instrument logged continuously during the periods of tie measurements in order to use the G-1031 measurements for estimating dockside tie values. Details of the tie measurements made at stations with known absolute g values are given below:

Tie and drift measurements in Bremerhaven before Expedition PS114

Measurements 1, **before** visiting the tie station in “Hafenlager” Bremerhaven (Table 6.4.1):

Instrument	LaCoste & Romberg gravimeter, G-1031 with feedback
Location	Quai in Lloyd yard, next to <i>Polarstern</i>
Date	11 July 2018
Conditions	Little wind, much traffic
Present	Graeme Eagles

Five measurements were completed manually. The KSS-32 gravimeter inside the ship was determined to be situated 1.5 m below the LaCoste & Romberg instrument on the quayside. The free-air correction is 0.3086 mGal per metre of elevation. The absolute value is determined from the average of available measurements, via the absolute point at AWI Building D in Bremerhaven, where the absolute value is 981356.72 mGal.

Tab. 6.4.1: Gravity measurements at quay in Lloyd yard, next to *Polarstern*. The scaling factor for transfer from scale units (scu) to mGal is 1.02250

UTC	Counter [scu]	Type	mGal (quayside)	mGal (KSS-32)
08:14	4912.54	Manual	5020.74	5021.20
08:15	4912.57	Manual	5020.77	5021.23
08:17	4912.62	Manual	5020.82	5021.28
08:18	4912.62	Manual	5020.82	5021.28
08:19	4912.57	Manual	5020.77	5021.23

The difference in mGal measurement between the KSS-32 instrument and the absolute gravity measurement point at the Hafenlager is -0.39 mGal. Absolute gravity at the KSS-32 at the time of this measurement was therefore **981357.19 mGal**. The instrument's relative reading has to be extracted onshore.

Measurements 2 (Table 6.4.2):

Instrument	LaCoste & Romberg gravimeter, G-1031 with feedback
Location	AWI-Hafenlager, absolute point
Date	11 July 2018
Conditions	Breezy, traffic
Abs. gravity	981357.58 mGal
Present	Graeme Eagles

Tab. 6.4.2: Gravity measurements at AWI-Hafenlager, Bremerhaven. The scaling factor for transfer from scale units (scu) to mGal is 1.02250

UTC	Counter [scu]	Type	mGal (Abs. point)
08:30	4913.40	Manual	5021.62
08:31	4913.41	Manual	5021.63
08:32	4913.44	Manual	5021.66
08:34	4913.37	Manual	5021.59
08:35	4913.45	Manual	5021.67

Tie and drift measurements in Tromsø after Expedition PS114 and before Expedition PS115/1

Measurements 3, **before** visiting the tie stations in Tromsø (Table 6.4.3):

Instrument	LaCoste & Romberg gravimeter, G-1031 with feedback
Location	Kai 25 Breivika, next to <i>Polarstern</i>
Date	4 August 2018
Conditions	-
Present	Ingo Heyde

6.4 Gravity measurements

Three measurements were completed manually. The KSS-32 gravimeter inside the ship was determined to be situated 3.2 m below the LaCoste & Romberg instrument on the quayside.

Tab. 6.4.3: Gravity measurements at Kai 25, Breivika, next to *Polarstern*. The scaling factor for transfer from scale units (scu) to mGal is 1.02123

UTC	Counter [scu]	Type	mGal (quayside)	mGal (KSS-32)
12:00	6085.62	Manual	6219.58	6220.57
12:03	6085.62	Manual	6219.58	6220.57
13:05	6085.63	Manual	6219.59	6220.58

Measurements 4 (Table 6.4.4):

Instrument	LaCoste & Romberg gravimeter, G-1031 with feedback
Location	Tromsø, Tromsø Museum Bolt R (Tromsø R)
Date	4 August 2018
Conditions	-
Abs. gravity	982552.140 mGal
Present	Ingo Heyde

Tab. 6.4.4: Gravity measurements at Tromsø Museum Bolt R. The scaling factor for transfer from scale units (scu) to mGal is 1.02123

UTC	Counter [scu]	Type	mGal (Abs. point)
12:35	6081.48	Manual	6215.35
12:40	6081.51	Manual	6215.38
12:42	6081.51	Manual	6215.38

Measurements 5 (Table 6.4.5):

Instrument	LaCoste & Romberg gravimeter, G-1031 with feedback
Location	Tromsø, Tromsø Museum Bolt Q (Tromsø Q)
Date	4 August 2018
Conditions	-
Abs. gravity	982551.448 mGal
Present	Ingo Heyde

Tab. 6.4.5: Gravity measurements at Tromsø Museum Bolt Q. The scaling factor for transfer from scale units (scu) to mGal is 1.02123

UTC	Counter [scu]	Type	mGal (Abs. point)
12:55	6082.22	Manual	6216.11
12:58	6082.23	Manual	6216.12
13:00	6082.23	Manual	6216.12

Measurements 6, **after** visiting the tie stations in Tromsø (Table 6.4.6)

Instrument	LaCoste & Romberg gravimeter, G-1031 with feedback
Location	Kai 25 Breivika, next to <i>Polarstern</i>
Date	4 August 2018
Conditions	-
Present	Ingo Heyde

Three measurements were done with the feedback unit and on the plate. Three measurements were completed manually. The KSS-32 gravimeter inside the ship was determined to be situated 3.25 m below the LaCoste instrument on the quayside.

Tab. 6.4.6: Gravity measurements at Kai 25, Breivika, next to *Polarstern*. The scaling factor for transfer from scale units (scu) to mGal is 1.02123

UTC	Counter [scu]	Type	feedback [mGal]	mGal (quayside)	mGal (KSS-32)
13:30	6085.63	Manual		6219.59	6220.59
13:33	6085.63	Manual		6219.59	6220.59
13:36	6085.64	Manual		6219.60	6220.60
13:40	6085	Feedback	+0.702	6219.65	6220.65
13:45	6085	Feedback	+0.681	6219.63	6220.63
13:48	6085	Feedback	+0.680	6219.62	6220.63

Tie and drift measurements in Tromsø after Expedition PS115/1 and before Expedition PS115/2

Disregarding the feedback measurements, which were not repeated at the quayside, the difference in mGal measurement between the KSS-32 instrument and the absolute gravity measurement point at Bolt R in the museum is +5.21 mGal (using the grand average of the quayside measurements from both parts of the day). The difference with respect to Bolt Q is +4.46 mGal. Absolute gravity at the KSS-32 at the time of the measurement, tied to Bolt R was therefore **982557.35 mGal**, or **982555.91 mGal** tied to Bolt Q. The instrument's relative reading has to be extracted onshore.

Between the end of expedition PS115/1 (3 September) and the beginning of expedition PS115/2 (4 September), *Polarstern* was anchored at a roadstead and therefore no tie and drift measurements were made.

Tie and drift measurements in Tromsø on the way back during Expedition PS115/2

Measurements 7, **before** visiting the tie stations in Tromsø (Table 6.4.7)

Instrument	LaCoste & Romberg gravimeter, G-1031 with feedback
Location	Measurements at quay next to <i>Polarstern</i> , 69°44,832'N, 19°08,548'E
Date	10 October 2018
Conditions	Calm weather, no harbor activities
Present	Estella Weigelt, Winfried Markert

6.4 Gravity measurements

Three measurements were completed manually. The KSS-32 gravimeter inside the ship was determined to be situated 1.4 m above the LaCoste & Romberg instrument on the quayside.

Tab. 6.4.7: Gravity measurements at Kai 25, Breivika, next to *Polarstern*. The scaling factor for transfer from scale units (scu) to mGal is 1.02123

UTC	Counter [scu]	Type	feedback [mGal]	mGal (quayside)	mGal (KSS-32)
10:04	6092.3	Manual		6226.40	6225.97
10:06	6092.3	Manual		6226.40	6225.97
10:07	6092.3	Manual		6226.40	6225.97
10:08	6092.36	Manual		6226.46	6226.03
10:11	6092.42	Manual		6226.52	6226.09
10:16	6092.0	Feedback	-1.440	6224.65	6224.22
10:18	6093.0	Feedback	-2.372	6224.74	6224.31
10:20	6094.0	Feedback	-3.477	6224.66	6224.23
10:21	6095.0	Feedback	-4.483	6224.67	6224.24
10:23	6096.0	Feedback	-5.490	6224.69	6224.26

Measurements 8 (Table 6.4.8):

Instrument	LaCoste & Romberg gravimeter, G-1031 with feedback
Location	Tromsø, Kunstmuseum, Sjøgata 1 (ASSUMING BOLT Q)
Date	10 October 2018
Conditions	Construction works outside the museum building, dry and no wind
Abs. gravity	982551.448 mGal
Present	Estella Weigelt, Winfried Markert

Tab. 6.4.8: Gravity measurements at Tromsø Kunstmuseum. The scaling factor for transfer from scale units (scu) to mGal is 1.02123

UTC	Counter [scu]	Type	feedback [mGal]	mGal (Abs. point)
11:11	6092.0	Feedback	-10.802	6215.29
11:12	6093.0	Feedback	-11.815	6215.30
11:14	6094.0	Feedback	-12.843	6215.29
11:15	6095.0	Feedback	-13.869	6215.29
11:17	6096.0	Feedback	-14.892	6215.29
11:21	6083.24	Manual		6217.15
11:23	6083.22	Manual		6217.13
11:25	6083.23	Manual		6217.14
11:26	6083.01	Manual		6216.91
11:28	6086.24	Manual		6220.21

No further measurements were taken in the harbour next to *Polarstern* after visiting the tie stations in Tromsø.

The difference in mGal measurement between the KSS-32 instrument and the absolute gravity measurement point at the Kunstmuseum is (assuming from the raw measurement that it was Bolt Q that was visited) is +4.46 mGal. Absolute gravity at the KSS-32 at the time of the measurement, tied to Bolt Q, was thus 982559.75 mGal. The instrument's relative reading at the same time has to be extracted onshore).

Tie and drift measurements in Bremerhaven after PS115/2

Measurements 9, **before** visiting the tie station in AWI-Hafenlager, Bremerhaven (Table 6.4.9)

Instrument	LaCoste & Romberg gravimeter, G-1031 with feedback
Location	Measurements at quay next to <i>Polarstern</i> , 53°34,011'N, 008°33,323'E
Date	16 October 2018
Conditions	Dry and wind still, much harbour activities (unloading), T=53.5°C
Present	Estella Weigelt, Winfried Markert, Sergei Freiman

Five measurements were done with the feedback unit and on the plate. Five measurements were completed manually. The KSS-32 gravimeter inside the ship was determined to be situated 3.0 m above the LaCoste & Romberg instrument on the quayside.

Tab. 6.4.9: Gravity measurements at quay in Lloyd yard, next to *Polarstern*. The scaling factor for transfer from scale units (scu) to mGal is 1.02250

UTC	Counter [scu]	Type	feedback [mGal]	mGal (quayside)	mGal (KSS-32)
07:50	4913.51	Manual		5021.73	5020.81
07:51	4913.52	Manual		5021.74	5020.82
07:52	4913.48	Manual		5021.70	5020.78
07:54	4913.44	Manual		5021.66	5020.74
07:55	4913.58	Manual		5021.81	5020.88
07:57	4913.0	Feedback	-1.326	5019.89	5018.96
07:58	4914.0	Feedback	-2.310	5019.93	5019.00
08:00	4915.0	Feedback	-3.304	5019.95	5019.02
08:01	4916.0	Feedback	-4.315	5019.97	5019.04
08:02	4917.0	Feedback	-5.335	5019.97	5019.04

Measurements 10 (Table 6.4.10):

Instrument	LaCoste & Romberg gravimeter, G-1031 with feedback
Location	AWI-Hafenlager, absolute point
Date	16 October 2018
Conditions	unstable conditions, T=53.5°C
Abs. gravity	981357.58 mGal (via tie at Building D, see above)
Present	Estella Weigelt, Winfried Markert, Sergei Freiman

6.4 Gravity measurements

Tab. 6.4.10: Gravity measurements at AWI-Hafenlager (Fig. 6.4.1), Bremerhaven. The first five manual measurements were conducted whilst a container was next to the measurement site, the second five manual measurements were done once this container was removed. The scaling factor for transfer from scale units (scu) to mGal is 1.02250.

UTC	Counter [scu]	Type	feedback [mGal]	mGal (Abs. point)
08:17	4913	Feedback	-0.506	5020.71
08:20	4914	Feedback	-1.509	5020.73
08:22	4915	Feedback	-2.550	5020.71
08:26	4916	Feedback	-3.531	5020.75
08:27	4917	Feedback	-4.576	5020.73
08:29	4914.34	Manual		5022.58
08:30	4914.32	Manual		5022.56
08:31	4914.30	Manual		5022.54
08:31	4914.29	Manual		5022.53
08:32	4914.32	Manual		5022.56
08:38	4914.36	Manual		5022.60
08:38	4914.25	Manual		5022.49
08:39	4914.28	Manual		5022.52
08:40	4914.27	Manual		5022.51
08:40	4914.22	Manual		5022.46

Using the manual measurements only, the difference in mGal measurement between the KSS-32 instrument and the absolute gravity measurement point at the Hafenlager is -1.73 mGal. Absolute gravity at the KSS-32 at the time was therefore **981355.85 mGal**. The instrument's relative reading at the same time has to be extracted onshore). Fig. 6.4.1 shows the front side of the AWI-Hafenlager (a) and the location of the absolute point on a small foot below a power socket (b).

KSS-32 Drift

Quayside absolute gravity at the KSS-3 was 1.34 mGal lower at the end than at the start of *Polarstern's* field season. Assuming measurements were made at the same quay in Bremerhaven, the difference in vertical separations between the portable and ship's gravimeters before and after the season was 4.5 m, with the instrument lying higher above the ellipsoid at the end of the season measurement. This vertical separation is equivalent to 1.39 mGal in free air. Based on this, instrument drift in the KSS-32 can be assumed to have been negligible over the course of the season.

Preliminary results

No significant problems with the data were recognized during the cruise. Fig. 6.4.1 shows an example of raw gravity values collected during seismic profiling in Amundsen basin, comparing reduced data from the KSS-32 to bathymetry, a key influence on measured gravitational accelerations at sea.

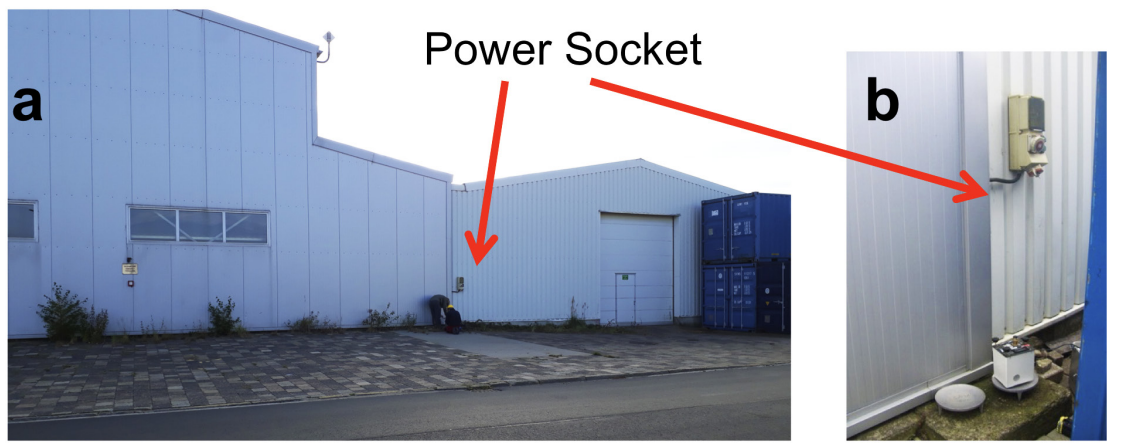


Fig. 6.4.1: Front side of the AWI-Hafenlager (a) and the location of the absolute point on a small foot below a power socket (b).

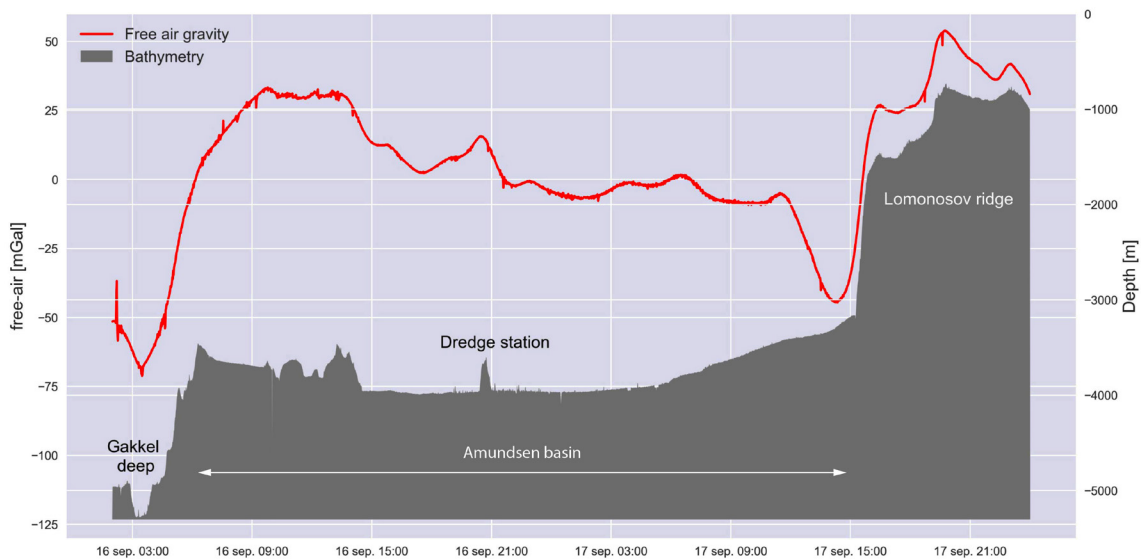


Fig. 6.4.2: Gravity data without reductions and bathymetry data during a transect above the Amundsen basin and Lomonosov Ridge in the Arctic Ocean, recorded on September 16 and 17, 2018.

Data management

With the end of PS115/2 scientific activities on October 4, *Polarstern* passed into the Russian EEZ and the gravimeter measurements were stopped. By this point, all of the leg's gravity data had been reduced, plotted and saved in a format ready for further processing.

6.5 Marine mammal observation (MMO)

Estella Weigelt¹, Ovie Benson¹, Pascal Bourgault², Camille Brice³, Charles Brunette², Myriam Caron⁴, Amelie Desmarais², Niels Fuchs¹, Cristoph Gaedicke⁵, Rémi Ienny⁶, Aliaksandra Kazlova⁷, Marcel König⁸, Ryan Love⁹, Dimitrii Murashkin⁷, Elena Popova¹⁰, Natasha Ridenour¹¹, Damien Ringeisen¹, Samira Samimi¹², Cynthia Sassenroth¹⁰, Anouk Vlug⁶, Junjie Wu¹, Heike Zimmermann¹³

¹AWI,
²McGill
³UQAM,
⁴UQAR
⁵BGR,
⁶UoB-MARUM
⁷UoB-IEP,
⁸CAU
⁹MUoN,
¹⁰UoStP
¹¹UoAE,
¹²UoC,
¹³AWI-P

Grant-No. AWI_PS115/2_01

Objectives

Marine mammal observations were conducted from Sept.16 ,2018 to Sept.27, 2018 during the seismic measurements across the Amundsen Basin, southeastern Lomonosov Ridge, and southwestern edge of the Makarov Basin. The aim of the observations was to inform the seismic watches to interrupt the running seismic profiling in case these animals would appear in a range of 500 m around the ship.

Work at sea

Observations were undertaken from the bridge of *Polarstern*. For the first succession of seismic lines between 16 and 18 September 2018, we performed our observations continuously for 24 h per day. For the second succession of seismic profiles from 22 September to 27 September, observations were carried out during daylight only. This succession was performed with a streamer including a PAM system.

On the 16 m high bridge of *Polarstern*, a good and clear view of the sea surface around the ship is ensured. The observers in charge used naked eye and binoculars (Fujinon 7-50 FTM/MT Field of view 7-300) to scan the sea surface. The officers on duty supported the MMO for the distance estimation of detected marine mammals.

All observers were scientists instructed onboard to follow the guidelines of the “Marine Mammal Mitigation guidelines during Operations” and to fill the “Marine Mammal Recording Form Effort” (see: www.jncc.gov.uk/page-1534).

Observation during airgun operation

Several actions were undertaken in order to minimize the risk of disturbing marine mammals by seismic data acquisition.

- A pre-shooting search was carried out by the observers on the bridge prior to any seismic action (Table 6.5.1). Ramp-up of the airguns could only start after 60 min. without sightings of marine mammals.
- For the ramp-up, we started with one single gun, and added one additional gun every 3 min. until all guns were shooting and full acoustic power for the planned seismic profile was reached.

- All seismic actions were to stop immediately in case of sighting of a marine mammal within a zone of 500 m distance to the seismic source (mitigation zone) during ramp-up or airgun operation. After a 30 min delay from the sighting, shooting could be restarted with a ramp-up.

During the pre-shooting search, ramp up and acquisition of the seismic reflection profiles, no marine mammals were sighted within the mitigation zone or further away by the observers.

Tab. 6.5.1: Marine mammal observation before and during airgun operation

Date	Time [UTC]	Operation	Sightings during operation
16.09.2018	03:03	Start of pre-shooting search	no
16.09.2018	04:59	Start of ramp-up	no
16.09.2018	05:08	Reduced power	no
16.09.2018	05:40	Full power; begin of profile succession	no
18.09.2018	23:51	End of profile succession	
23.09.2018	15:00	Start of pre-shooting search	no
23.09.2018	16:57	Start of ramp-up	no
23.09.2018	17:15	Full power; begin of profile succession	no
27.09.2018	08:57	End of profile succession	

7. PS115/2 MARINE GEOLOGY: RECONSTRUCTION OF PAST CLIMATIC CONDITIONS

7.1 Overview of the PS115/2 marine geology programme

Ruediger Stein ¹ , Michael Schreck ² , Frank Niessen ¹ , Jens Matthiessen ¹ (not on board), Ovie Miracle Benson ¹ , Camille Brice ³ , Myriam Caron ⁴ , Maximilian Dröllner ⁵ , Frithjof Lemmel ⁶ , Norbert Lensch ¹ , Ryan Love ⁷ , Adalbert Pfeiffer ¹ , Elena Popova ⁸ , Cynthia Sassenroth ⁸ , Nikolai Wöhljtjen ¹ , Junjie Wu ¹ , Heike Zimmermann ⁹ and the ArcTrain Team	¹ AWI ² UoT ³ UQAM ⁴ UQAR ⁵ UoM ⁶ GEOMAR ⁷ MUoN ⁸ UoStP ⁹ AWI-P
---	--

Grant-No. AWI_PS115/2_01

Objectives

Key goals of the marine-geological research programme of expedition PS115/2 were detailed reconstructions of the long- and short-term climate history of the Arctic Ocean during Quaternary and pre-Quaternary times. In this context, especially studies of changes in circum-Arctic ice sheets, sea-ice cover, and surface- and deep-water characteristics were/are of major interest. These studies are directly related to the key objectives of IODP Expedition 377, a drilling campaign (Stein et al., 2015; Stein, 2017) that originally was scheduled for 2018, unfortunately cancelled and postponed in 2017, but most recently re-scheduled for summer/autumn 2021 (see ECORD's Headline #13; 11 November 2018, <http://www.ecord.org/outreach/headlines/> and <http://www.ecord.org/expedition377/>). In this context, one of the first-order objectives was the coring of undisturbed near-surface sediment sections (i.e., the uppermost about 10 m) at selected IODP first-priority sites from the southern Lomonosov Ridge close to the Laptev Sea continental margin (such as LR-02A, LR-04A, LR-06A, LR-09A, and LORI-16A; Figs. 1.1 and 7.1.1).

The main objectives of PS115/2 marine geological studies include:

- Development of a stratigraphic framework (chronology) of the sediment sequences, using a multi-proxy-approach (AMS¹⁴C, oxygen and carbon stable isotopes, biostratigraphy, natural radionuclides, physical properties, XRF scanning, cyclostratigraphy, and correlation to other existing Arctic Ocean records).
- Quantification and characterization of terrigenous sediment fraction in order to reconstruct transport processes, oceanic currents, and circum-Arctic ice-sheet history (Proxies/approach: grain size, clay minerals, heavy minerals, major, minor, trace and rare earth elements, organic carbon fractions, and physical properties; analytical techniques: X-ray diffraction (XRD), X-ray fluorescence (XRF), inductivity-coupled plasma mass spectrometry (ICP-MS), and microscopy of coarse fraction as well as MSCL-logging and XRF-scanning).

- Reconstruction of surface-water sub-surface and deep-water characteristics: paleo-sea-ice distribution, surface-water productivity, sea-surface and deep-water temperature, deep-water ventilation, etc., using specific biomarkers (e.g., *n*-alkanes, sterols, alkenones; U^{k}_{37} Index, TEX_{86} Index, IP_{25} Index), micropaleontological proxies (dinoflagellates, foraminifers, ostracodes, etc.), and inorganic-geochemical proxies (stable isotopes, radiogenic isotopes, etc.). Analytical techniques to be used include LECO ($CaCO_3$, TOC, C/N), Rock-Eval pyrolysis, gas chromatography (GC), gas chromatography/ mass spectrometry (GC/MS), and high-performance liquid chromatography/mass spectrometry (HPLC/MS), XRF, ICP-MS, and microscopy.
- Studies of sea ice and sea-ice sediments (biomarkers, mineralogy, geochemistry, etc.).
- DNA approach for identifying (sea ice) algae in sea ice and sediment samples.

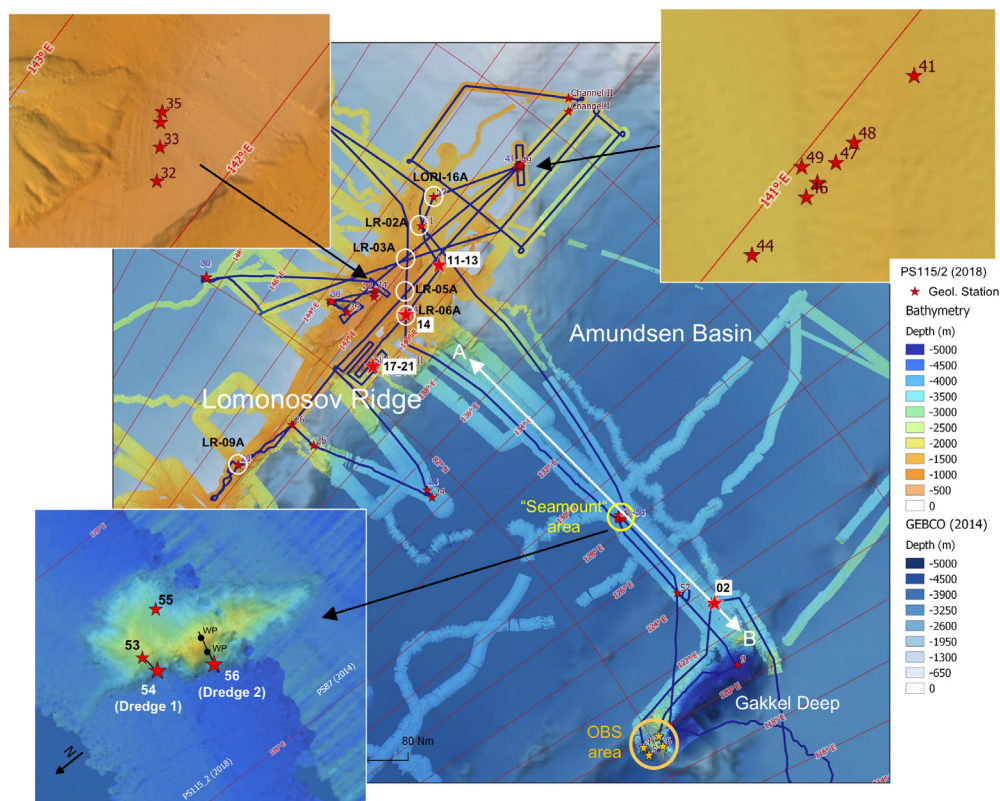


Fig. 7.1.1: Hydrosweep bathymetry maps with geological stations of expedition PS115/2 (red stars: 2, 9, 11, ... = PS115/2_02, PS115/2_09, PS115/2_11,; maps by courtesy of M. Steffen and S. Andree, AWI Bathymetry). Locations of PS115/2_2, 11-13, 14 and 17-21 are highlighted and further discussed in Chapter 7.5. Locations of selected potential future IODP sites are marked by white circles. PS115/2_17 to _21 are from the slide scar area (see Fig. 5.4). A-B PARASOUND profile shown in Fig. 7.5.7. For further explanation see Fig. 1.3.

Work at sea

In order to reach the main goals of the marine-geological programme, the recovery of undisturbed sediment sequences by means of Giant Box Corer (GKG), Multicorer (MUC), Gravity Corer (SL) and Kastenlot Corer (KAL) was one of the main foci of the shipboard geological work. Sampling was performed along and across the Lomonosov Ridge and the Amundsen Basin (Fig. 7.1.1). Of interest are areas of high sedimentation rates for high-resolution studies of late Quaternary (postglacial-Holocene) paleoenvironment and areas where older strata are cropping-out for studying Cenozoic sequences of paleoenvironmental change. Coring positions were collected carefully using detailed bathymetric mapping and sub-bottom profiling systems

7.1 Overview of the PS115/2 marine geology programme

(i.e., Hydrosweep and PARASOUND, respectively) to avoid areas of sediment redeposition (turbidites and slumps) and erosion, and to identify areas where preglacial sediments are cropping out.

In total, geological coring was carried out at 36 stations (Table 7.1.1). In addition, the dredge was used twice for sampling of stones across the newly discovered seamount (Fig. 7.1.1; Table 7.1.1).

Tab. 7.1.1: Locations and gears of the geological stations. SL – Gravity Corer (“Schwerelot”; SL-5 = 5-meter core barrel), MUC- Multicorer, GKG – Giant Box Corer, KAL – Kastenlot Corer; DRDGE – Dredge. Recovery of GKG, SL, and KAL cores (in cm) is listed as well. Four cores were recovered from the same locations as proposed IODP drill sites (red numbers) (Fig. 7.1.1). Depth = water depth in metres. Latitude and longitude are given in decimal degrees; for numbers in degrees & minutes see Appendix A4.

Station No	Gear No	Gear	Recovery	Latitude N	Longitude E	Depth (m)
PS115/2_2	PS115/2_2-1	GKG	46	81,2441	123,4799	3665
	PS115/2_2-2	KAL	764	81,2441	123,4839	3669
PS115/2_8	PS115/2_8-1	GKG	51	81,4476	120,8915	4959
	PS115/2_8-2	SL	538	81,4482	120,9001	4961
PS115/2_11	PS115/2_11-1	GKG	48	81,0878	140,9138	1698
	PS115/2_11-2	MUC		81,0878	140,9137	1696
	PS115/2_11-3	SL	624	81,0879	140,9133	1696
PS115/2_12	PS115/2_12-1	SL	643	81,0852	140,8905	1701
	PS115/2_12-2	GKG	36	81,0854	140,8925	1700
PS115/2_13	PS115/2_13-1	GKG	39	81,0819	140,8657	1705
	PS115/2_13-2	SL-5	401	81,0822	140,8639	1706
PS115/2_14	PS115/2_14-1	GKG	36	81,4566	140,7279	765
(IODP LR-06A)	PS115/2_14-2	MUC		81,4571	140,7295	777
	PS115/2_14-3	KAL	704	81,4572	140,7289	777
PS115/2_17	PS115/2_17-1	SL-5	342,5	81,8327	140,4945	1504
PS115/2_18	PS115/2_18-1	SL-5	17	81,8332	140,4774	1603
PS115/2_19	PS115/2_19-1	SL-5	0	81,8332	140,4809	1569
PS115/2_20	PS115/2_20-1	SL-5	319	81,8331	140,4866	1534
PS115/2_21	PS115/2_21-1	SL-5	36	81,8338	140,4593	1731
PS115/2_23	PS115/2_23-1	GKG	41	82,1821	134,7706	3844
	PS115/2_23-2	MUC		82,1826	134,8402	3871
	PS115/2_23-3	SL	513	82,1778	134,8853	3875
PS115/2_24	PS115/2_24-1	SL	650,5	82,1821	134,5323	3904
	PS115/2_24-2	GKG	42	82,1805	134,5321	3900
PS115/2_25	PS115/2_25-1	GKG	41	82,4430	140,1893	2365
	PS115/2_25-2	MUC		82,4435	140,1913	2351
	PS115/2_25-3	SL	710,5	82,4420	140,1504	2339
PS115/2_26	PS115/2_26-1	SL	662	82,4320	141,5876	1636
	PS115/2_26-2	GKG	48	82,4347	141,6171	1632

7. PS115/2 Marine Geology: Reconstruction of Past Climatic Conditions

Station No	Gear No	Gear	Recovery	Latitude N	Longitude E	Depth (m)
PS115/2_28	PS115/2_28-1	GKG	32	82,8315	142,4672	1247
(IODP LR-09A)	PS115/2_28-2	MUC		82,8357	142,4489	1247
	PS115/2_28-3	KAL	579,5	82,8401	142,4325	1237
PS115/2_30	PS115/2_30-1	GKG	?	81,9891	148,4277	2620
	PS115/2_30-2	GKG	18	81,9886	148,5716	2634
	PS115/2_30-3	MUC		81,9830	148,7349	2648
	PS115/2_30-4	KAL	879	81,9829	148,7427	2649
PS115/2_32	PS115/2_32-1	GKG	38	81,4908	142,2343	819
	PS115/2_32-2	MUC		81,4907	142,2343	818
	PS115/2_32-3	SL	672	81,4906	142,2340	809
PS115/2_33	PS115/2_33-1	SL	747	81,4716	142,3175	797
PS115/2_34	PS115/2_34-1	SL	429	81,4580	142,3847	818
PS115/2_35	PS115/2_35-1	SL-5	360	81,4516	142,4083	826
PS115/2_36	PS115/2_36-1	SL	582	81,6898	143,6481	1815
	PS115/2_36-2	GKG	51	81,6897	143,6482	1822
PS115/2_39	PS115/2_39-1	GKG	36	81,6682	142,7410	767
	PS115/2_39-2	MUC		81,6681	142,7407	767
	PS115/2_39-3	SL	596	81,6680	142,7401	769
PS115/2_40	PS115/2_40-1	SL-5	443	81,6665	142,9326	940
PS115/2_41	PS115/2_41-1	SL	638	80,2717	140,9588	1602
	PS115/2_41-2	GKG	51	80,2710	140,9634	1600
	PS115/2_41-3	MUC		80,2707	140,9663	1583
PS115/2_44	PS115/2_44-1	GKG	34,5	80,3196	140,9746	1777
	PS115/2_44-2	SL	617	80,3197	140,9735	1776
PS115/2_45	PS115/2_45-1	SL	592	80,3003	140,9680	1660
PS115/2_46	PS115/2_46-1	SL	488	80,3039	140,9682	1708
PS115/2_47	PS115/2_47-1	SL	630	80,2950	140,9631	1630
PS115/2_48	PS115/2_48-1	SL	663	80,2897	140,9636	1607
PS115/2_49	PS115/2_49-1	SL	539	80,3099	140,9942	1765
PS115/2_50	PS115/2_50-1	SL	655	80,7768	142,7851	1746
(IODP LORI-16A)	PS115/2_50-2	GKG	50	80,7764	142,7845	1746
PS115/2_51	PS115/2_51-1	GKG	45,5	80,9652	142,4731	1440
(IODP LR-02A)	PS115/2_51-2	MUC		80,9650	142,4732	1441
	PS115/2_51-3	KAL	838	80,9650	142,4730	1438
PS115/2_53	PS115/2_53-1	SL-5	486	81,4072	128,5219	3652
PS115/2_54	PS115/2_54-1	DRDGE		81,4059	128,5634	3586
PS115/2_55	PS115/2_55-1	SL	655	81,3885	128,6139	3668
PS115/2_56	PS115/2_56-1	DRDGE		81,3827	128,3593	3834
PS115/2_57	PS115/2_57-1	SL	572	81,3903	124,5551	3491

(1) Surface sediment sampling

Surface and near-surface sediment sampling was carried out by using a Giant Box Corer (GKG) and a Multicorer (MUC).

Giant box corer (GKG)

The GKG (weight of ca. 500 kg; volume of sample 50*50*60 cm; manufactured by Fa. Wuttke, Henstedt-Ulzburg, Germany) was used at 20 stations and failed only once due to a malfunction of the trigger mechanism (Table 7.1.1). All cores were documented (e.g. photographed) with respect to their surface and vertical profile.

After removing the excess water, the sediment surface was photographed and the macrofauna (organisms >5 mm) was sampled. Macrofaunal remains were found at most of the sites and primarily consist of fragments of bivalve shells and worms tubes. Molluscs shells and sea cucumbers were also found. Ice-rafted debris (i.e., dropstones), on the other hand, was not observed at the surface. Subsequently, two AWI archive tubes (diameter 12 cm) were pushed into the sediment. The detailed surface sediment sampling was performed as followed:

- 1 x whirl-pack bag (dinoflagellate cysts: A. de Vernal/GEOTOP Montreal)
- 2 x 50 ml glass vials (organic geochemistry; deep-frozen: R. Stein/AWI)
- 3 x 100 ml plastic beakers (sedimentology, mineralogy: R. Stein/AWI)
- 1 x 8 ml glass vials (genetics, biology; deep-frozen: H. Zimmermann/AWI-Potsdam)
- 1 x 500 ml Kautex bottle for all remaining surface sediment (R. Stein/AWI)

After opening the box corer from the side, down-core sampling has been performed as followed:

- 1 x Plastic box (R. Stein/AWI)
- 1 x Plastic box (R. Spielhagen/Geomar)
- 2 x X-ray slabs (R. Stein/AWI)

Contrary to the archive tube sampling, the archive boxes and X-ray slabs were pushed into the sediment perpendicular to the stratification. In addition to the standard procedure, discrete subsampling has been carried out at five selected coring locations (PS115/2_32-1, 36-2, 41-1, 50-2 and 51-1).

Multicorer (MUC)

The standard 8-tubes-version MUC (manufactured by Fa. Wuttke, Henstedt-Ulzburg, Germany) with an inner tube diameter of 10 cm was used. The penetration weight was always 250 kg. The Multicorer was successfully used 10 times at 10 stations, and usually recovered undisturbed surface sediments and overlying bottom water.

From the recovered 8 tubes, the general sampling plan was as follows:

- One tube was sampled at 1 cm interval for bulk parameters/sedimentology (R. Stein/AWI).
- One tube was sampled at 1 cm interval for biomarkers (deep-frozen; R. Stein/AWI).

-One tube was sampled at 1 cm interval for DNA analyses (deep-frozen; H. Zimmermann/AWI).

- One tube was sampled at 1 cm steps as archive back-up (R. Stein/AWI).

- One tube was sampled at 1 cm interval for palynology (A. de Vernal/UQAM).

From the remaining tubes, only the surface sediments were stored as archive back-up (R. Stein/AWI).

(2) Sampling of long sediment cores

Long sediment cores were taken by a Gravity Corer (GC = "Schwerelot", SL) and a Kastenlot Corer (KAL).

The SL has a penetration weight of 1.5 t. It was successfully used with barrel length of 10 m at 22 stations and with 5 m core barrel at 9 stations (Table 7.1.1). The recovery of the SL varied between 0.38 and 7.47 m (Fig. 7.1.2; Table 7.1.1).

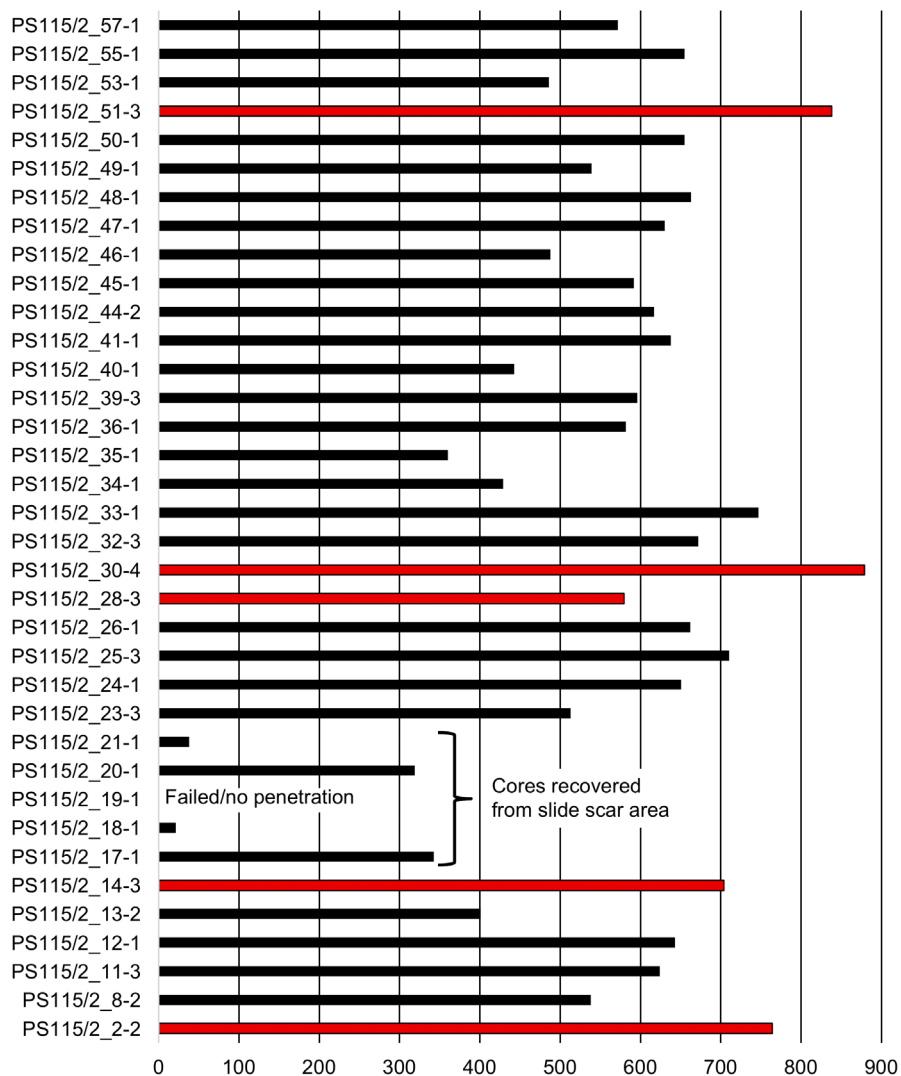


Fig. 7.1.2: Recovery of PS115/2 gravity cores (black bars) and kastenlot cores (red bars). For location and characteristics of the slide scar area see Figs. 7.1.1 and 5.4, respectively.

7.1 Overview of the PS115/2 marine geology programme

The KAL, a gravity corer with a rectangular cross section of 30 x 30 cm, has a penetration weight of 3.5 t and a core box segment sized 30 x 30 x 575 cm (manufactured by Hydrowerkstätten Kiel). The length of the KAL boxes used was 11.75 m plus about 30 cm for the core catcher. The great advantage of the KAL is a wall-thickness of the barrel of only 2 mm. Because of the great cross-sectional area (900 cm²) and the small thickness of the barrels, the quality of the cores was generally excellent. The KAL was successfully used at 5 stations. The recovery of the KAL cores varied between 5.80 and 8.79 m (Fig. 7.1.2; Table 7.1.1).

The lab work on the long sediment cores follows a general work flow scheme as summarized in Fig. 7.1.3. Some of this work (e.g., XRF scanning, X-Ray photographs, etc.) will be done later in the home laboratories.

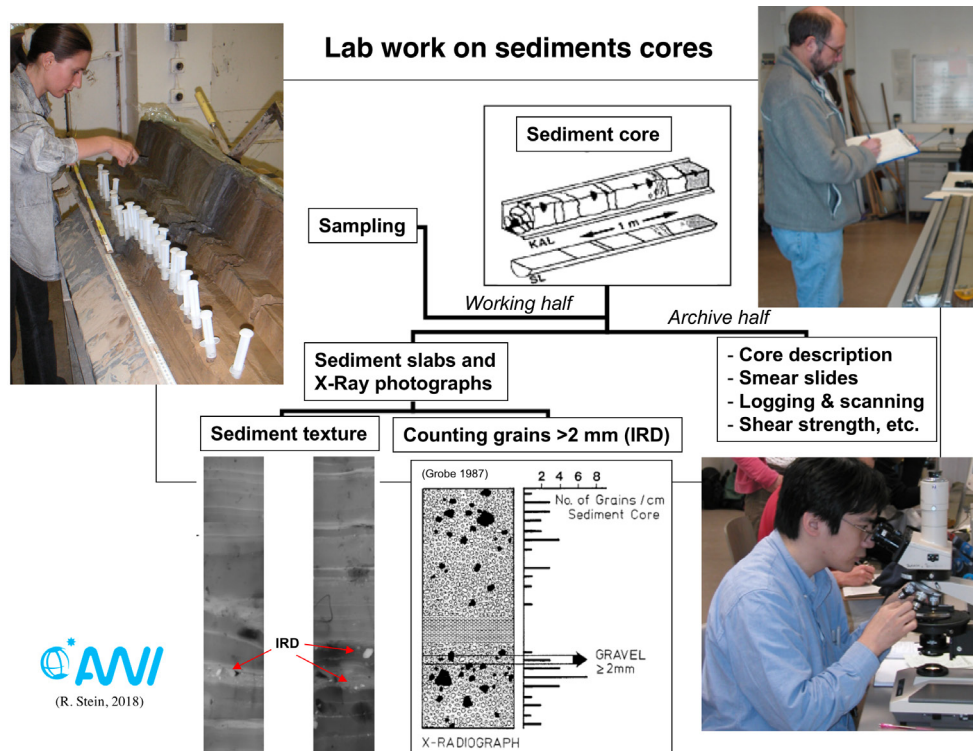


Fig. 7.1.3: Flow chart of working steps carried out on the gravity cores and kastenlot cores recovered during expedition PS115/2 (R. Stein/AWI)

All Kastenlot sediments were sampled and stored in plastic boxes, in general in five series per interval (Fig. 7.1.4):

- Series 1 (S1): Archive (Large box 100 x 12)
- Series 2 (S2): Physical Properties (Small box 100 x 8)
- Series 3 (S3): Sedimentology (Large box 100 x 12)
- Series 4 (S4): Organic Geochemistry (Small box 100 x 8)
- Series 5 (S5): Mineralogy/Geochemistry (Large box 100 x 12)

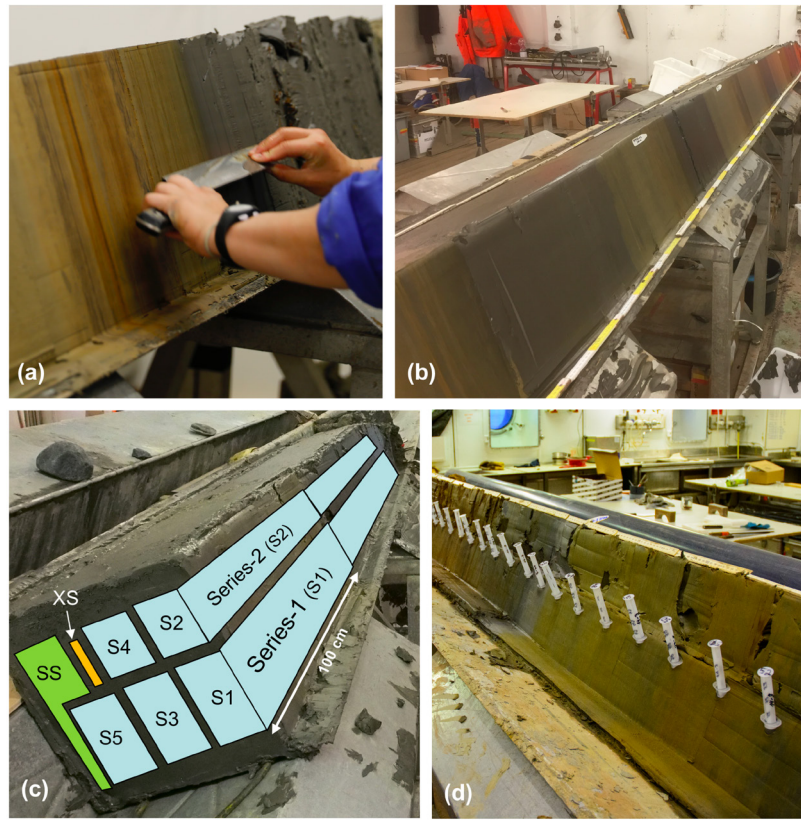


Fig. 7.1.4: Sampling procedure of kastenlot cores. (a), (b) Preparing/cleaning the surface before pushing the plastic boxes into the sediment; (c) scheme showing where/how the five series of plastic boxes (S1 – S5), X-Ray slabs (XS) and further single samples (SS) were taken (further explanation see text), and (d) example for taking single syringe samples after the boxes S1 – S5 and the X-Ray slabs were removed. Photos (a) G. Birnbaum/AWI, (b) and (c) R. Stein/AWI, and (d) R. Love/MUoN.

In addition, sediment slabs were taken for X-ray photography to be carried out later at the AWI. Sediment slabs (250 x 100 x 8 mm) were taken continuously with a plastic container from every opened sediment core (GKG, SL, KAL) for X-Ray images. The plastic containers (slabs) were slowly pushed into the smoothed sediment surface and carefully removed. To avoid any damages, the slabs were sealed in a plastic cover and the air was removed. At the AWI, X-Ray images will be produced from these slabs, and the X-Ray negatives will be studied by using a light table to determine sedimentary and biogenic structures and to count the number of coarse-grained terrigenous particles >2 mm as indicator for the content of ice-rafted debris (Fig. 7.1.3).

From the remaining sediments, samples of about 10 to 50 cm³ (ca. every 5 to 10 cm) were taken for coarse-fraction analysis to be done on board as well as for later geochemical, mineralogical and sedimentological studies to be done at the AWI and the UoM.

All SL cores were logged before they were opened whereas plastic boxes of two series of the KAL cores (Series III and IV) were logged (MSCL; Chapter 7.3). After opening, from all core sections (archive half) photographs were taken (see below). From a selected number of core sections, a detailed visual core description was carried out. Colour of sediments was described using the Munsell Soil Colour Chart. From a few cores, smear-slide analysis was performed

7.1 Overview of the PS115/2 marine geology programme

for rough evaluation of grain-size composition, preliminary determination of mineralogical composition (quartz, feldspars, carbonates, opaques), and content of biogenic components (foraminifers, coccoliths, diatoms, sponge spicules). For coarse-fraction analysis, the fraction >63 µm was isolated by means of wet sieving, and the abundance of the major sediment components (siliciclastics, detrital carbonates, planktic and benthic foraminifers, ostracods, etc.) were estimated by using a binocular microscope (see Chapter 7.4).

Photographs of sediment cores (R. Love, MUoN)

Onboard PS115/2 several different photographic procedures were followed for both typical photography of SL and KAL core sections as well as additional documentation of KAL and GKG cores prior to sampling. Expedition PS115/2 had no onboard line scanning equipment, thus no onboard comparison of digital photographs and line scans were made. For SL and KAL samples the photography station shipped for expedition PS115/2 was constructed and utilized. Included in this setup is a lighting system (4 lamps and power supply), frame elements, clamps, a core holder, a Nikon D700 with a AF-S Nikkor 24-70mm lens and Speedlight flash, and an Apple Macbook Pro which was used to remotely control the camera (see Fig. 7.1.5). For the *in-situ* GKG and KAL cores a Nikon D7100 with a AF-S Nikkor 18-70 mm 1:3.5-4.5G lens was used along with the aforementioned Speedlight flash when poor lighting conditions for GKG photography prevailed (primarily during night stations).

The *in-situ* photography of the GKG cores was straightforward in procedure and comprised of two end product photographs: a top view for documentation of surface sediments and macrofauna present and a side view for down core sediment structure. Before any sampling of surface sediments was conducted, an image of the surface sediments was taken from an overhead perspective, generally about the center of the GKG and at a focal length such that the frame was mostly comprised of the sediments. Due to variable lighting and sea conditions present there were no uniform settings used for these images. However, the following trends were present: generally, a wide aperture around f5.0 was used, the ISO was usually between 1600 and 3200, and shutter speeds used were between 1/60s and 1/200s depending on sea conditions. When needed, due to poor lighting conditions, the Speedlight flash unit was also used at a lower power setting. A low power setting was used as GKG surface sediment tended to be very reflective and higher flash power levels often led to large overexposed areas of the surface sediments even when used with the on-flash diffuser unit. A label arrow for each image was always present to allow for ready identification. After the sampling of the surface and push core placement, images of the open side of the GKG were taken using similar settings once the sediments were cleaned. For these photos, a ruler and labelling arrow were also present (however, due to construction of the GKG and the rulers, the measurements are from the base to the top in the images. For those GKGs which were to comprise the top layers of a KAL core two Kodak colour cards (one colour, one greyscale) were also present to allow for colour correction and matching later on in processing if needed. Future core photographers should note that in all lighting conditions, safety orange outerware should be kept at least 1m away from any element of the photo where colour is of importance. Close proximity of such clothing will distort the colours of any element of the image as they are highly reflective by necessity and design.

The procedure for *in-situ* photography of the KAL cores is slightly more involved than that of the GKG. The photographs are taken after the determination of the depth of the KAL and the surface of the sediment has been cleaned. Here the camera settings were more uniform as the light conditions in Nasslabor II are more consistent than on the working deck. ISO values were between 1600 and 2000, shutter speeds were between 1/40s and 1/80s, aperture was between f5.0 and f5.6, and the focal length was set to between 35 mm and 50 mm on the lens (equivalent to ~50 mm-75 mm) when accounting for the DX sensor crop factor). To ensure that

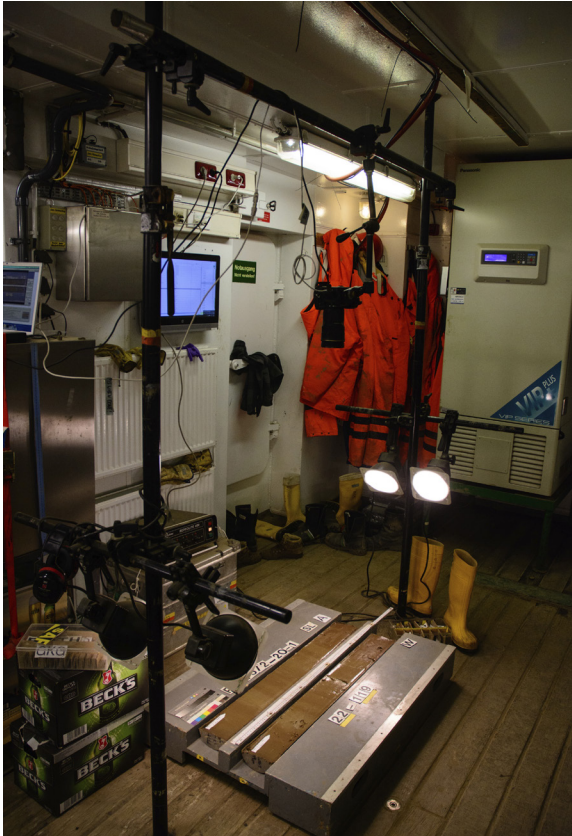


Fig. 7.1.5: The SL & KAL photography station as used during expedition PS115/2. All elements, with the exception of the MacBook Pro are present in this image (Photo: R. Love/MUoN)

the exposure between frames was consistent the camera was operated in full manual mode. The operator stood approximately 1 m away from the core (when possible) and the core was centered in the frame. Two rulers were present and readable in the images and served as guides to help the operator keep the images aligned. Photographs were taken approximately 10 cm apart and the field of view allowed for approximately 25 cm to either side of the center line. When possible the operator moved parallel to the core surface rather than rotated to achieve the 10 cm difference. Here again Kodak colour cards were used for later colour correction. Note however that ambient florescent lighting in the lab was the only source of illumination so colour accuracy could be markedly improved by the use of light sources with higher Colour Rendering Index (CRI, a measure of the ability for a given light source to allow for the accurate representation of colour). After the photography of the KAL core the individual images were blended together through the use of the open source Hugin Panorama Stitcher software. Presently the use of this software still involves the manual stitching for KAL cores longer than approx. 4 m but we note that a different workflow could eliminate the need for this step and may improve the horizontal accuracy of the composite.

Photography of the SL and KAL core sections using the photography station was also a simple process. The photography station (Fig. 7.1.5) was setup such that the lamps are set at a low angle relative to the cores, this serves to reduce reflections but provide even illumination. The camera was aligned and the lens focal length set such that the core holder was the entirety of the frame. Then core sections were placed into the core holder (or, in the case of the KAL cores, they were placed on top with spacers underneath as they were too wide to fit the core holder), and other elements such as the ruler and the number, letter, and colour cards were placed. The exposure settings used were f6.3, ISO value of 800, and the exposure time was generally 1/30s-1/40s. These settings were chosen as f6.3 was sufficient to keep all relevant elements of the photos in focus, the exposure time was short enough to mitigate motion blur from ship induced camera movement, and ISO800 had an acceptable noise level. A wider aperture could be used in future if all relevant elements can be kept on the same plane, this would require only the widening of the core holder section to allow for the KAL core sections to be inset the same as SL core sections.

For future expeditions, several improvements could help improve the existing workflow, we note these here. A dark and matte screen to suspend around the SL/KAL photography station would be useful to reduce the contamination from ambient lighting and allow for more accurate white point and colours in the images. For *in-situ* photography of the KAL and GKG cores a tripod (or potentially a monopod) would increase image quality by reducing the impact of motion blur.

Some means of providing higher quality illumination for the *in-situ* KAL photography would also be a marked improvement, again by reducing the reliance on poor quality ambient illumination. For easier identification of core depths, several washable measuring tapes at least the length of a KAL would be exceptionally useful for both the photography and the general marine geology KAL workflow. Such devices would benefit both the documentation procedure and reduce the likelihood of measurement errors from user error and/or damaged rulers. A selection of additional flash diffusers could be useful for dealing with poor exterior lighting conditions. A new means of attaching the D700 camera to the photography framing would make for shorter and more reliable setup and teardown, the current device has issues with holding position and reliability. Additionally, a second camera (for PS115/2 this was the personal camera of R. Love, MUoN) is of great benefit to the overall workflow and serve as a backup should some failure of a camera occur. We recommend another Nikon to make use of the existing photographic equipment such as the Speedlight flash unit and lens and to be a compatible backup unit for the photography station.

Preliminary results

Preliminary results of the shipboard studies of surface sediments as well as selected sediment cores are presented and discussed in the following subchapters 7.2 to 7.5 and the annex.

Data management

Raw data and processed data (shipboard and shorebased) will be made available in PANGAEA.

References

- Stein R (2017) From Greenhouse to Icehouse: The late Mesozoic-Cenozoic Arctic Ocean sea-ice and climate history. *Polarforschung* 87, 61-78.
- Stein R, Jokat W, Niessen F and Weigelt E (2015) Exploring the long-term Cenozoic Arctic Ocean Climate History – A challenge within the International Ocean Discovery Program (IODP). *Arktos* 1, doi: 10.1007/ s41063-015-012-x.

7.2 PARASOUND sub-bottom profiling

Frank Niessen¹, Jolien van der Krogt¹,
Almut Schmengler¹ and 19 PARASOUND Watchkeepers ¹AWI

Scientific objectives

In the Arctic Ocean, bottom and sub-bottom reflection patterns obtained by PARASOUND characterize the uppermost sediments in terms of their acoustic behavior down to about 100 m below the sea floor. This can be used to study depositional environments on larger scales in terms of space and time, of which the uppermost sediments may also be sampled.

In June 2017, the Deep-Sea Sediment Echo Sounder PARASOUND (Teledyne Reson, Bremen, Germany), system PS3-P70, was successfully upgraded to PS3MK2-P70, which includes significant modifications in both hardware and software components. The system was then tested using different settings during expedition PS110 (Niessen in prep.). expedition PS115/2 is one of the first scientific expeditions using the upgraded system intensively.

The general objectives of sediment echosounding during expedition PS115/2 were:

- to provide the data base for an acoustic facies interpretation indicative for different sedimentary environments
- to obtain different pattern of high-resolution acoustic stratigraphy useful for lateral correlation over shorter and longer distances thereby aiding correlation of sediment cores retrieved during the cruise
- to select coring stations based on acoustic pattern and reflection amplitude
- to provide a high-resolution counterpart for the uppermost sections of seismic profiles recorded during the cruise
- to gain further experience using the recently upgraded PARASOUND system during a scientific expedition

Cruise and area-specific objectives of the sediment echosounding of expedition PS115/2 include:

- to identify older sediments (Early Pleistocene to Mesozoic), which crop out at or near the sediment surface in the context of planned deep ocean drilling projects (IODP, MEBO)
- to further identify and interpret truncation and sedimentation related to local or large-scale erosion and reworking by grounded ice (icebergs or ice shelves) on top of the Lomonosov Ridge
- to identify current-induced sedimentation (channel-levee, drift deposits) in the acoustic record to interpret palaeoceanographic changes in the Arctic Ocean in space and time.
- to identify and interpret acoustic sedimentary facies and landforms related to Pleistocene glaciations close to the East-Siberian continental margin

Work at sea

During expedition PS115/2 digital data acquisition and storage were switched on after *Polarstern* left the EEZ of Russia north-east of the Severnaya Zemlya Archipelago and close to the Gakkel Deep on September 14 at 07:56 UTC and was switched off after the last station (PS115/2_57) over the Gakkel Deep on October 04 at 03:52 UTC near the EEZ of Russia. PARASOUND was in 24-hour operation along all track lines within the working area (Fig. 7.2.1). The total time of operation and data storage was 470 hours. The work at sea included the following specific topics:

- Monitoring and documentation of depositional environments at deployment locations of four OBS at the northern end of Gakkel Deep
- Improve profile coverage across the Amundsen Basin as well as along and across the Lomonosov Ridge
- Further analyze depositional environments at locations of the Lomonosov Ridge where old strata were identified during expedition PS87
- Further analyze glacial landforms in shallow areas of the Lomonosov Ridge
- Explore unknown areas at the southern end of the Lomonosov Ridge near the EEZ of Russia along seismic lines
- Select coring locations in areas not previously explored

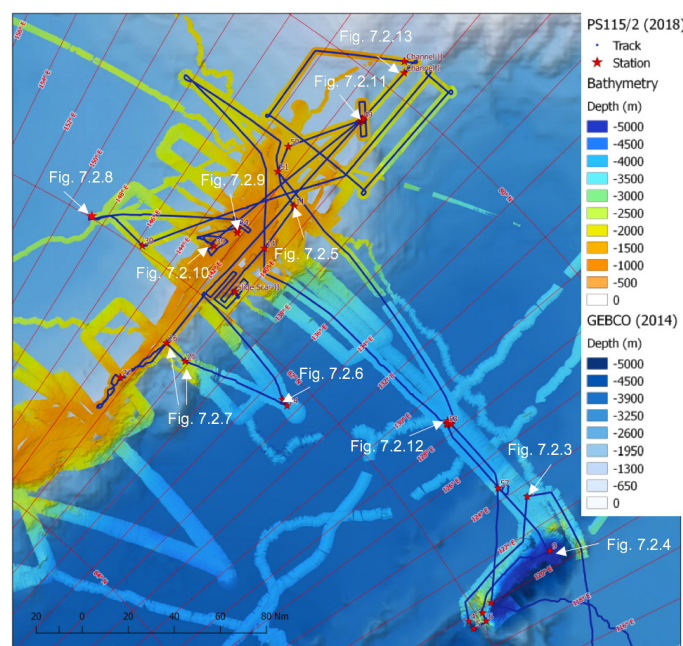


Fig. 7.2.1: Bathymetric map of the working area with track lines along which PARASOUND data were recorded. Specific locations are indicated for which PARASOUND examples are presented in figures in this report (map by courtesy of M. Steffen and S. Andree, AWI Bathymetry).

In addition to the general data recording along ship tracks, specific PARASOUND surveys were carried out in five different locations in the working area (Fig. 7.2.2), which have specific station numbers (Tab. 7.2.1). In the order of temporal operation these include:

1. Steep slope ($>10^\circ$ inclination) of an escarpment at the western edge of the Lomonosov Ridge, where older (Early Quaternary and/or Neogene) sediments are exposed at, and/or, present close to the sediment surface
2. Glacial landforms on top of the Lomonosov Ridge

3. Steep slope (about 10° inclination) of an escarpment at the eastern edge of the Lomonosov Ridge
4. Channel-levee complex at the southern end of the Lomonosov Ridge (bypass area for water exchange between the Amundsen and Makarov basins)
5. Top of the submarine seamount exposed in the middle of the Amundsen Basin

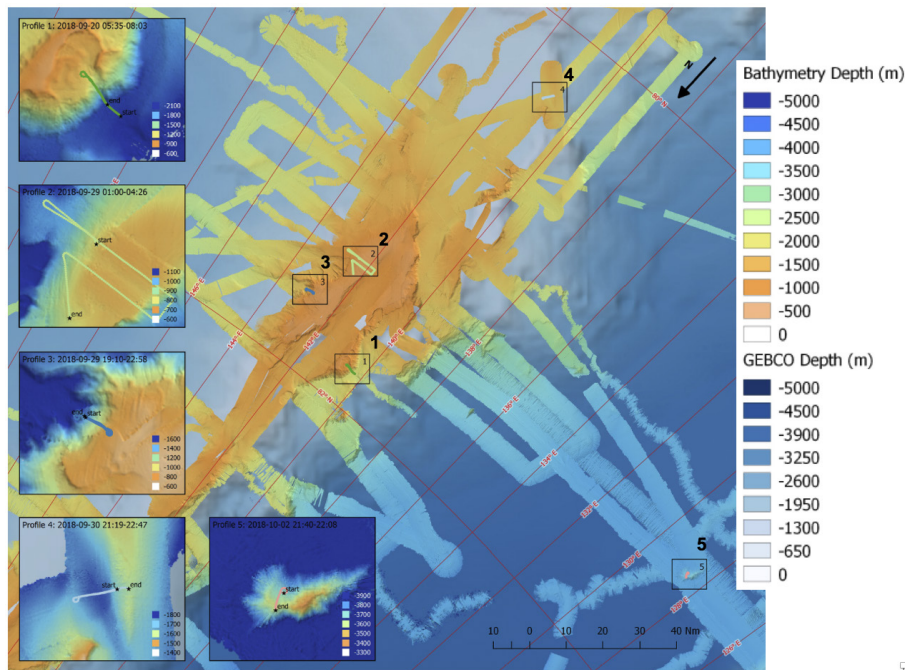


Fig. 7.2.2: Bathymetric map, locations and track lines of specific PARASOUND surveys carried out during expedition PS115/2 (map by courtesy of M. Steffen and S. Andree, AWI Bathymetry)

The hull-mounted PARASOUND system generates two primary frequencies, of which the lower frequency is selectable between 18 and 23.5 kHz transmitting in a narrow beam of 4° at high power (PHF). As a result of the non-linear acoustic behavior of water, the so-called “Parametric Effect”, two secondary harmonic frequencies are generated, one of which is the difference (e.g. 4 kHz, SLF) and the other the sum (e.g. 40 kHz, SHF) of the two primary frequencies, respectively. As a result of the longer wavelength, the difference parametric frequency allows sub-bottom penetration up to 100 m in the Arctic Ocean (depending on sediment conditions) with a vertical resolution of about 0.3 m. The primary advantage of parametric echosounders is based on the fact that the sediment-penetrating pulse is generated within the narrow beam of the primary frequencies, thereby providing a very high lateral resolution compared to conventional 4 kHz-systems. For vertical beam transmission (conventional) this capability, however, limits good survey results on sea-floor slopes, which are inclined to more than 4° relative to horizontal. The reason is that the energy reflected from the small inclined footprint on the seafloor is out of the lateral range of the receiving transducers in the hull of the vessel. As a consequence, the survey results are poor over longer lateral distances along the slopes of ridges in the Arctic Ocean such as the Gakkel Ridge and the Lomonosov Ridge, which were major targets of expedition PS115/2. In particular at relatively steep slopes of the Lomonosov Ridge, where slide scars are often observed, different inclination angles of old strata covered by a thin veneer of younger sediments can cause problems in terms of correct interpretation of the deposits to be sampled. During expedition PS115/2 we have addressed this problem using different angles of PARASOUND beam steering as described below.

Tab. 7.2.1: PARASOUND Surveys (Start-End-Subject)

Station - Device Operation	Date 2018 Time (Start)	Latitude (Start) [deg]	Longitude (Start) [deg]	Depth (Start) [m]	Date 2018 Time (End)	Latitude (End) [deg]	Longitude (End) [deg]	Depth (End) [m]	Aim of Survey
PS115/2_16-1	20.09.05:35	81.8378	140.2618	2077.9	20.09.08:03	81.8374	140.3796	2052.9	exploration of drape on escarpment
PS115/2_31-1	29.09.01:00	81.4182	142.4010	777.6	29.09.04:26	81.4891	142.2483	819.4	cross sections of glacial landforms
PS115/2_37-1	29.09.19:10	81.6702	143.0596	1438.2	29.09.22:58	81.6698	143.0710	1413.7	exploration of drape on escarpment
PS115/2_42-1	30.09.21:19	80.2996	140.9461	1637.7	30.09.22:47	80.2926	140.8972	1579.1	station survey using beam steering
PS115/2_52-1	02.10.21:40	81.3890	128.5871	3657.6	02.10.22:08	81.4053	128.5338	3592.9	station survey on sea mount (AB)

PARASOUND DS III-P70 is controlled by two different operator software packages plus server software running in the background. These processes are running simultaneously on a PC under Windows-7. (i) Atlas HYDROMAP CONTROL (AHC) is used to run the system by an operator. The selected modes of operation, sounding options and ranges used during the cruise are summarized in Table 7.2.2. A list of abbreviations is given at the end of this chapter. (ii) Atlas PARASTORE-3 is used by the operator for on-line visualization (processing) of received data on PC screen, for data storage and printing. It can also be used for replaying of recorded data, post-processing and further data storage in different output formats (PS3 and/or SEG-Y). For any further details the reader is referred to the operator manuals of Atlas HYDROMAP CONTROL and Atlas PARASTORE.

One major modification of the PS3MK2-P70 upgrade is the implementation of the frequency-modulated (chirped) wave for water depth of more than 500 m in addition to the previously used continuous waves. This results in both slight improvement of sediment penetration and vertical resolution. Another major modification is such that for PHF, SHF and SLF settings of Band Width, Frequency and Pulse Resolution as well as Pulse Length and Number of Periods per Pulse are displayed on screen and can be changed by sliders (Pulse Control, Pulse Extension, PHF Frequency, SLF Frequency). During expedition PS115/2 we have used this option along a specific survey as outlined below. In QED mode, the pulses are now adjusted for each sounding according to the actual water depth and not in one-minute intervals like in the previous version of P70. This means that the depth control of the system is critical at any time. For QED pulses a time interval between pulses of 1,200 to 2,000 ms was a good standard. In order to avoid complications caused by depth control via HYDROSWEET, during expedition PS115/2 PARASOUND PHF was used as depth control for most of the time (for further details see Niessen in prep.). In particular during times of operation in sea ice, it was necessary to maintain a particular depth window for bottom detection using the Fixed Min./Max. Depth Limit window.

Tab. 7.2.2: Technical Settings of PARASOUND during expedition PS115/2

Used Settings	Selected Options	Selected Ranges
Mode of Operation	P-SBP/SBES	PHF, SLF
Frequency	PHF	18 kHz (19.935 kHz)
	SLF	4 kHz (3.987 kHz)
Pulselength	No. of Periods	4
	Length	1 ms
Transmission Source Level	Transmission Power	100%
	Transmission Voltage	160 V
Beam Steering	See station report PS115/2_16-1, 31-1, 42-1 and 52-1.	
Mode of Transmisson	Single Pulse Quasi-Equidistant (QED)	Auto according to water depth Interval 500-1200 ms
Pulse Type	Frequency Modulated (Chirped)	
Pulse Shape	Default	
Receiver Band Width	Output Sample Rate (OSR) Band Width (% of OSR)	6.1 kHz 66%
Reception Shading	none	
System Depth Source	PARASOUND PHF Manual HYDROSWEEP DS PHF	Fixed Min./Max. Depth Limit
Water Velocity	C-Mean C-Keel	Manual 1500 m/s System C-keel
Data Recording	PHF-PS3 SLF-PS3	200 m 200 m

Preliminary Results

Stations and Sampling Areas

Based on preexisting bathymetric information, four sites for PS115/2 OBS deployments were selected. In the vicinity of these sites, PARASOUND records along the PS115/2 ship track were checked for depositional conditions in these areas. Examples are presented and described in the geophysics chapter of this report (Fig. 6.2.3, Weigelt et al. this volume).

7.2 PARASOUND sub-bottom profiling

Tab. 7.2.3: Coring-Station PARASOUND Summary

Core No PS115/2	Device	Water Depth (m)	Area	Parasound Survey	Acoustic Pattern	Variability in lateral accum.	Comments	Figure 7.2.
2-2	KAL	3669	E' of Gakkel Deep	PS87	well strat.	low	condensed section	3
8-1	SL	4961	Gakkel Deep	PS87	strat./ transp.	low to high	condensed with event redeposition	4
11-3	SL	1696	SW' LR	PS87	strat.	medium	channel cross section (flank), sedimentation	5
12-1	SL	1701	"	PS87	strat.	high	channel cross section (lower flank), sedimentation	
13-1	SL	1706	"	PS87	strat.	high	channel cross section (bottom), erosion possible	
14-3	KAL	777	SW' LR.	PS87	well strat.	low	medium accum. rates; IODP site LR-06	6
17-1	SL	1504	W' LR	PS115/2	diffuse backsc.	unknown	"old" sediments with drape? (escarpment)	
18-1	SL	1603	W' LR	PS115/2	diffuse backsc.	unknown	"old" sediments with drape? (escarpment)	
19-1	SL	1569	W' LR	PS115/2	diffuse backsc.	unknown	"old" sediments with drape? (escarpment)	
20-1	SL	1534	W' LR	PS115/2	diffuse backsc.	unknown	"old" sediments with drape? (escarpment)	
21-1	SL	1731	W' LR	PS115/2	diffuse backsc.	unknown	"old" sediments with drape? (escarpment)	
23-3	SL	3875	E' AB	PS87	strat.	medium	silty turbidites, high accumulation	
24-1	SL	3904	E' AB	PS88	strat.	medium	silty turbidites, more condensed	7
25-3	SL	2390	W' upper flank of LR	PS87	well strat.	low	higher accumulation	
26-1	SL	1636	W' upper flank of LR	PS87	well strat.	low	more condensed	8
28-3	KAL	1237	top of LR	PS87	well strat.	low	medium accum. rates; IODP site LR-09	
30-4	KAL	2649	W' LR slope of MB	PS115/2	well strat.	very low	medium accumulation rates	9
32-3	SL	809	top of LR	PS87	strat./ transp.	medium	pelagic over redeposition	
33-1	SL	797	top of LR	PS87	strat./ transp.	low	pelagic intercalated with debris flows	
34-1	SL	818	top of LR	PS87	strat./ transp.	medium	pelagic over subglacial diamicton	10
35-1	SL	826	top of LR	PS87	strat./ transp.	low	pelagic over morainic MSGSL diamicton	
36-1	SL	1815	lower slope of LR at MB	PS87	strat./ transp.	low/medium	pelagic drape after slide deposition	10
39-3	SL	769	top of LR	PS87	strat./ transp.	low/high	pelagic over subglacial diamicton	
40-1	SL	940	upper slope of LR at MB	PS87	flat strat.	medium	"old" sediments with drape? (escarpment)	10

7. PS115/2 Marine Geology: Reconstruction of Past Climatic Conditions

Core No PS115/2	Device	Water Depth (m)	Area	Parasound Survey	Acoustic Pattern	Variability in lateral accum.	Comments	Figure 7.2.																
41-1	SL	1602	between S' LR and ESCM	PS115/2	well strat.	high	channel-Levee cross section (top); high accum.	11																
44-2	SL	1776	between S' LR and ESCM	PS115/2	strat.	high	channel-Levee cross section (bottom); low accum./erosion																	
45-1	SL	1660	between S' LR and ESCM	PS115/2		high	channel-Levee cross section (middle); medium accum.																	
46-1	SL	1708	between S' LR and ESCM	PS115/2	strat.	high	channel-Levee cross section (lower); selective accum.																	
47-1	SL	1630	between S' LR and ESCM	PS115/2		high	channel-Levee cross section (upper); selective accum.																	
48-1	SL	1607	between S' LR and ESCM	PS115/2		high	channel-Levee cross section (near top); medium accum.																	
49-1	SL	1765	between S' LR and ESCM	PS115/2	strat.	high	channel-Levee cross section (near bottom); selective accum.																	
50-1	SL	1746	S' LR	PS87	well strat.	medium	medium accum. rates; IODP site LORI-16A																	
51-3	KAL	1438	S' LR	PS87	well strat.	low	medium accum. rates; IODP site LR-02																	
53-1	SL	3652	top of "Polarstern Seamount"	PS115/2	diffuse backsc.		"old" sediments with condensed drape? Top end of W' steep slope	12																
55-1	SL	3668	top of "Polarstern Seamount"	PS115/2	strat.	low	condensed section; pelagic on plateau E' of peak																	
57-1	SL	3491	top of tect. rotated block	PS115/2	diffuse backsc.		"old" sediments with condensed drape? Top end of W' steep slope, escarpment																	
<table border="1"> <thead> <tr> <th>Color Code</th> <th>Description</th> </tr> </thead> <tbody> <tr> <td></td> <td>Undisturbed pelagic sedimentation</td> </tr> <tr> <td></td> <td>Alteration of pelagic sedimentation with debris-flow deposits</td> </tr> <tr> <td></td> <td>Current-induced sedimentation/erosion in channel-levee or contourite-drift depositional systems</td> </tr> <tr> <td></td> <td>Proposed IODP (Exp 377 - ArcOP) drilling locations (mostly pelagic)</td> </tr> <tr> <td></td> <td>Submarine escarpments with the exhumation of older strata or rock to the surface, partially draped by a thin veneer of young Pleistocene sediments</td> </tr> <tr> <td></td> <td>Deep-sea fan environment with strong lateral sediment transport and deposition in levee systems and/or sediment-wave complexes</td> </tr> <tr> <td></td> <td>Streamlined glacial landforms, subglacial diamicton and glacial debris-flow deposits commonly covered by a thin veneer of young Pleistocene sediments</td> </tr> </tbody> </table>									Color Code	Description		Undisturbed pelagic sedimentation		Alteration of pelagic sedimentation with debris-flow deposits		Current-induced sedimentation/erosion in channel-levee or contourite-drift depositional systems		Proposed IODP (Exp 377 - ArcOP) drilling locations (mostly pelagic)		Submarine escarpments with the exhumation of older strata or rock to the surface, partially draped by a thin veneer of young Pleistocene sediments		Deep-sea fan environment with strong lateral sediment transport and deposition in levee systems and/or sediment-wave complexes		Streamlined glacial landforms, subglacial diamicton and glacial debris-flow deposits commonly covered by a thin veneer of young Pleistocene sediments
Color Code	Description																							
	Undisturbed pelagic sedimentation																							
	Alteration of pelagic sedimentation with debris-flow deposits																							
	Current-induced sedimentation/erosion in channel-levee or contourite-drift depositional systems																							
	Proposed IODP (Exp 377 - ArcOP) drilling locations (mostly pelagic)																							
	Submarine escarpments with the exhumation of older strata or rock to the surface, partially draped by a thin veneer of young Pleistocene sediments																							
	Deep-sea fan environment with strong lateral sediment transport and deposition in levee systems and/or sediment-wave complexes																							
	Streamlined glacial landforms, subglacial diamicton and glacial debris-flow deposits commonly covered by a thin veneer of young Pleistocene sediments																							

Abbreviations				
AB	Amundson Basin	accum.	accumulation	E' Eastern
ESCM	East Siberian Continental Margin	backsc.	backscatter	S' Southern
IODP	Internat. Ocean Discovery Program	strat.	stratified	SW' South-Western
LR	Limonosov Ridge	tec.	tectonic	W' Western
MB	Macarov Basin	trans.	transparent	

Due to the limited time available for expedition PS115/2 for operation in the working area and the fact given, that large parts of the area have been surveyed during expedition PS87 in 2014 with high data quality, we have preselected in total 14 sites or sampling profiles for PS115/2 coring stations based on PS87 PARASOUND data. In addition, 6 sites or sampling profiles were discovered and/or surveyed during expedition PS115/2 (Fig. 7.2.3 to 7.2.12). For this report, a sampling profile is defined as a PARASOUND profile of a few kilometers in length, which exhibits relatively large lateral changes in the depositional environment worth the recovery of more than one core over short distances (Fig. 7.2.5, 7.2.6, 7.2.9, 7.2.11). In order to distinguish PARASOUND records from expedition PS87 (2014) and expedition PS115/2 (2018), all profiles presented are labeled to indicate the time window (year, month, date, time in UTC) during which they were recorded (yyyymmddThhmm-hhmm, Fig. 7.2.3. to 7.2.13). With reference to recording time, track data (GPS positions) can be downloaded from the data base DShip (<https://dms.awi.de/>).

Based on the acoustic sub-bottom conditions as seen in PARASOUND profiles, coring sites were selected in 6 different types of acoustic facies. For most of the cores, these are summarized in Table 7.2.3 and include the following facies:

- Well-stratified acoustic records associated with undisturbed pelagic sedimentation, which can represent areas with lower (condensed) or higher accumulation rates (Fig. 7.2.4, 7.2.7, 7.2.8, in parts 7.2.12).
- Well-stratified sediments intercalated with transparent layers or lenses associated with pelagic sedimentation and stratigraphic events such as debris flows, respectively (Fig. 7.2.4).
- Well-stratified sediments with large differences in sedimentation rates over short lateral distances typical for channel-levee complexes of contourite drifts (indicative of environments affected by bottom currents) (Fig. 7.2.5, 7.2.11); see also Chapter 7.5, Fig. 7.5.6.
- Well-stratified sediments with notable differences in sedimentation rates over short lateral distances associated with, in places, small-scale syn-sedimentary stair-case rotational faults towards the basin typical for environments at the slopes of deep-sea fans with high sedimentation rates.
- Relatively steep-slope areas (inclination 10° or higher) described as escarpments or slide scars, where older (Early Quaternary and/or Neogene) sediments are exposed at, and/or, are present close to the sediment surface (Fig. 7.2.10).
- Assemblage of truncated older strata covered by lenses or layers of acoustically transparent sediments overlain by a thin veneer of well-stratified sediments, typically associated with subglacial erosion and deposition of diamicton, re-sedimentation out of glacially induced debris flows covered by postglacial pelagic muds (Fig. 7.2.9).

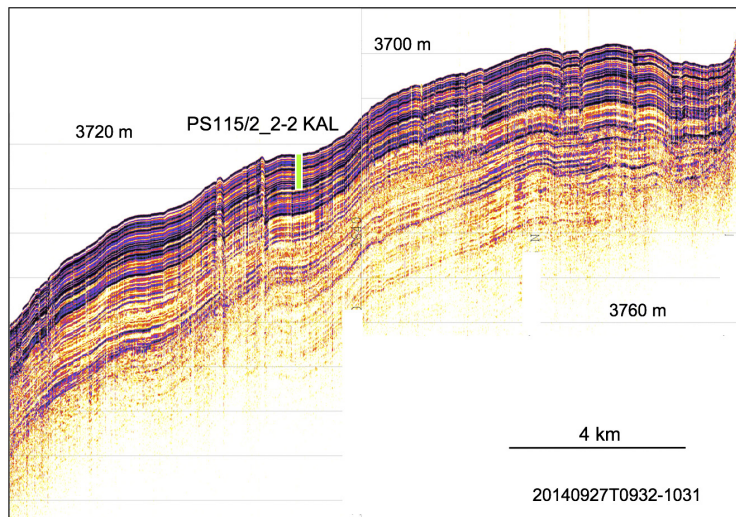


Fig. 7.2.3: PARASOUND profile east of Gakkel Deep with coring station 2-2 of pelagic sediments

In addition, cores were retrieved at four proposed IODP sites (Tab. 7.2.3; see Chapter 7.5 for the lithologies of selected cores) for the planned mission expedition 377 'Arctic Paleoceanography' (ArcOP), now scheduled for 2021. The PARASOUND profiles along these sites are presented in Stein et al. (2015) and Stein (2016). Also, along two seismic profiles at the southernmost end of the working area close to the Siberian shelf edge, in HYDROSWEEP and PARASOUND data we discovered two parallel palaeochannels, each 300 to 400 m wide and 15 m deep, with orientations perpendicular to the continental slope (Fig. 7.2.13). Tentatively, they are interpreted as glacially induced by meltwater released at the grounding line of ice sheets, which covered the East Siberian Shelf during major Quaternary glaciations (e.g. MIS 6; Niessen et al. 2013; Jakobsson et al. 2015; Stein et al. 2016).

Specific PARASOUND Surveys

Surveys (Fig. 7.2.2) at steep slopes included a comparison of two different modes of acoustic beam steering, vertical (conventional) and inclined up to 10° (the maximum possible at present PARASOUND settings). Beam steering was carried out in locations (1), (3) and (4) listed above, while surveying along the same track at least two times in each location in upslope direction. With this experiment we were successful to resolve two different types of geometries of the strata: reflections from old strata with almost horizontal bedding below a major unconformity (slide scar), and the drape of a few meters of sediments above the unconformity. The latter has the same steep inclination as the slope so that reflections can only return to the ship originated from an inclined beam. Thus, the old strata are only visible in case vertical beaming (conventional) is applied, whereas the drape is only resolved using a beam inclined by 10°. The result is best illustrated for location (3) as outlined in Fig. 7.3.10. Beam steering was also successful to indicate a drape on top of an unconformity at location (1) and to better resolve the steeper slopes of the channel-levee-complex (4) as outlined in Fig. 7.2.11. The aim of the beam steering was to find locations along steep slopes where no or almost no drape is present in order to directly sample old strata using the gravity coring device. Unfortunately, during expedition PS115/2 only short time windows were available for surveying and locations with clearly no drape overlying older sediments could not be identified.

Conventional surveys at locations (2) and (3) were carried out to study the cross sections of what appears to be glacial ridges and to survey for an undisturbed pelagic cover on top of the sea mount, respectively.

7.2 PARASOUND sub-bottom profiling

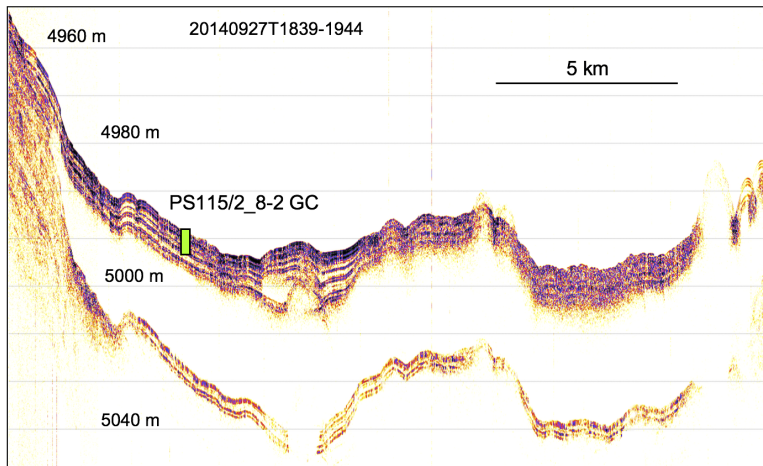


Fig. 7.2.4: PARASOUND profile from inside the Gakkel Deep with coring station 8-2. Note that acoustically transparent layers and lenses of partly significant thickness are interpreted as redeposition from debris flows and may be associated with event stratification triggered by tectonic activity of the Gakkel Ridge.

Data management

Acquisition included PHF and SLF data within the working area from 14.09.2018 at 07:56 UTC until 04.10.2018 at 03:52 UTC. Both PHF and SLF traces were visualized as online profiles on screen. SLF and PHF profiles (200-m-depth window) and online status reports (60-s-intervals or shorter) were saved as PNG files.

For the entire period above, and simultaneously with sounding, six different types of data files were stored on hard disc:

- PHF data in ASD format
- PHF data in PS3 format (carrier frequency, lat.long)
- SLF data in ASD format
- SLF data in PS3 format (carrier frequency, lat.long)
- Navigation and Auxiliary data (60s intervals) in ASCII format
- PHF and SLF Online "Prints" as A-4 pages in PNG format
- ATLAS PARASTORE 3 settings in XML files

Tab. 7.2.4: Malfunctions of Atlas PARASTORE and HYDROMAP CONTROL

Date, Time (UTC)	Application	Error
2018-09-14 16:54	HYDROMAP CONTROL	CM synchronization failed
2018-09-16 05:11	PARASTORE	Stopped without message
2018-09-17 06:10	PARASTORE	Stopped without message
2018-09-18 18:50	PARASTORE	Stopped without message
2018-09-22 04:23	PARASTORE	Stopped without message
2018-09-24 05:51	PARASTORE	Stopped without message
2018-09-25 16:10	PARASTORE	Stopped without message
2018-09-26 19:10	PARASTORE	Stopped without message
2018-09-27 15:20	PARASTORE	Stopped without message
2018-09-29 23:38	HYDROMAP CONTROL	CM synchronization failed
2018-10-02 21:57	PARASTORE	Stopped without message

In total, 11 system crashes were observed during the cruise those of Atlas PARASTORE for no obvious reasons (Tab. 7.2.4). In total 5.45 hours of potential data storage were lost.

All ASD data are automatically packed into “cabinet files” by Atlas software. The files are named according to date and time of recording (containing 10 minutes of acquired data per file). The data have been sorted by the operator into folders according to data type and recording dates (0 to 24 hours UTC), copied to the storage PC via LAN and checked for completeness and readability (Atlas PARASTORE-3 in replay mode, selectively only). Once checked, the data folders were copied to the *Polarstern* mass storage for daily back-ups and final transfer into the AWI database after the end of cruise. In total data with a total volume of 96.2 GB (18,638 files in 119 folders) were produced. These data will be transferred to AWI after the cruise and stored in a data base. Once georeferenced, the data will be linked for external accessibility to the data base PANGAEA.

During the cruise, the SLF PS3 files that were stored with latitude/longitude projection and Carrier Frequency mode to enable the Import of the data in IHS Kingdom. The PS3 data was converted into SEG-Y files using the PS32SGY converter (Hanno Keil, Bremen). The new SG-Y files covered a time period of 4 hours, instead of the 10 Minute files produced by PARASTORE. A MATLAB script was used to divide the navigational data and the SGY data and then these coupled files were imported into IHS Kingdom to further investigate the sub bottom data.

During the entire period of acquisition, the system was operator controlled (watch keeping). Book keeping was carried out including basic PARASOUND system settings, some navigation information, various kinds of remarks.

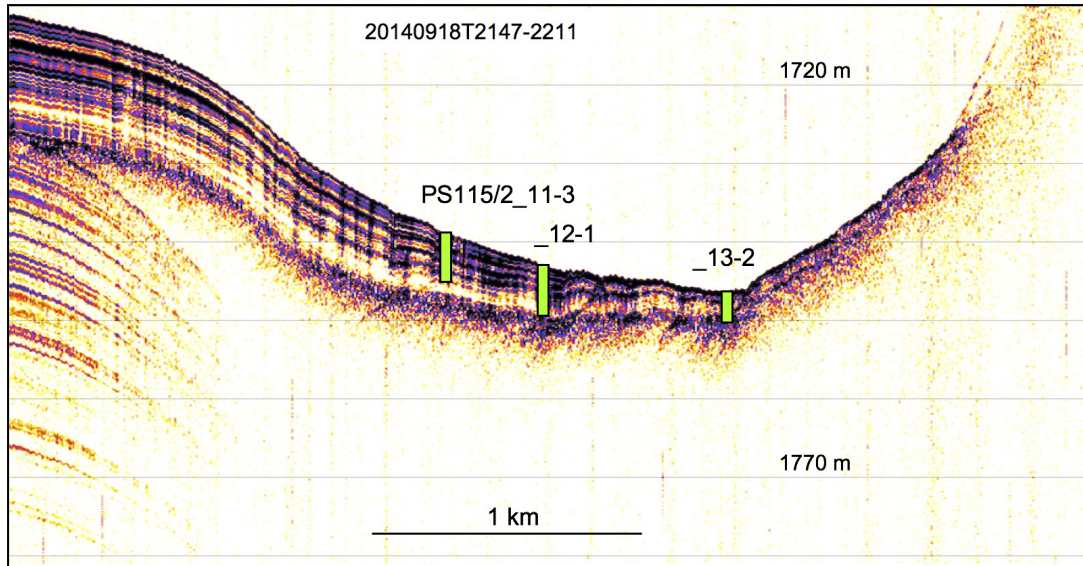


Fig. 7.2.5: PARASOUND profile from a channel-levee system at the western edge of Lomonosov Ridge with coring sites 11-3 to 13-2. Note that coring depth ended at or near the top of a lenticular debris-flow deposit. For lithologies of cores see Chapter 7.5, Fig. 7.5.6.

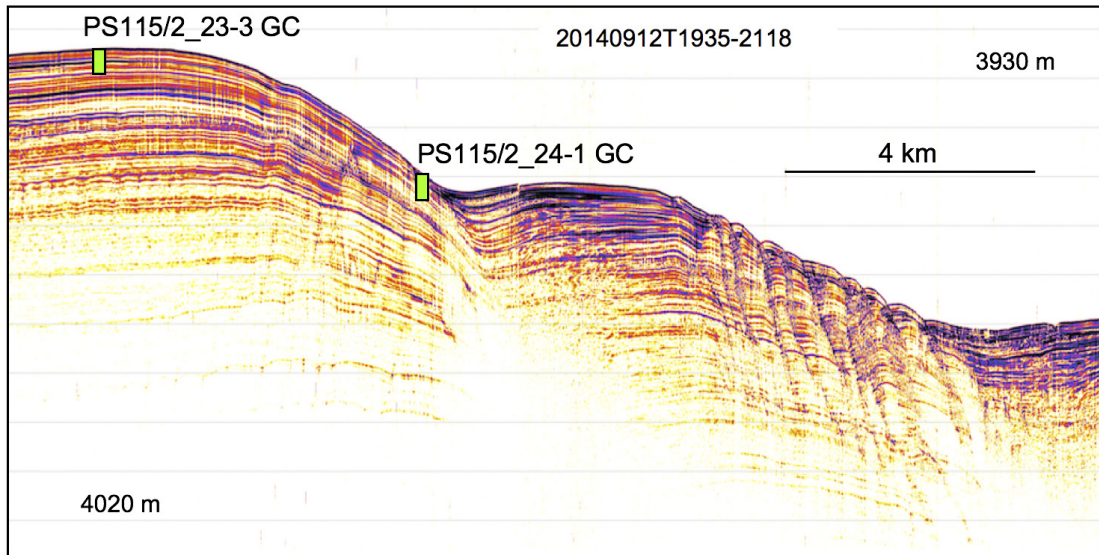


Fig. 7.2.6: PARASOUND profile across the lower end of the western slope of Lomonosov Ridge (transition into Amundsen Basin abyssal plain). The facies is interpreted as levee deposits of a deep-sea fan fed by debris from Siberian rivers and/or ice sheets

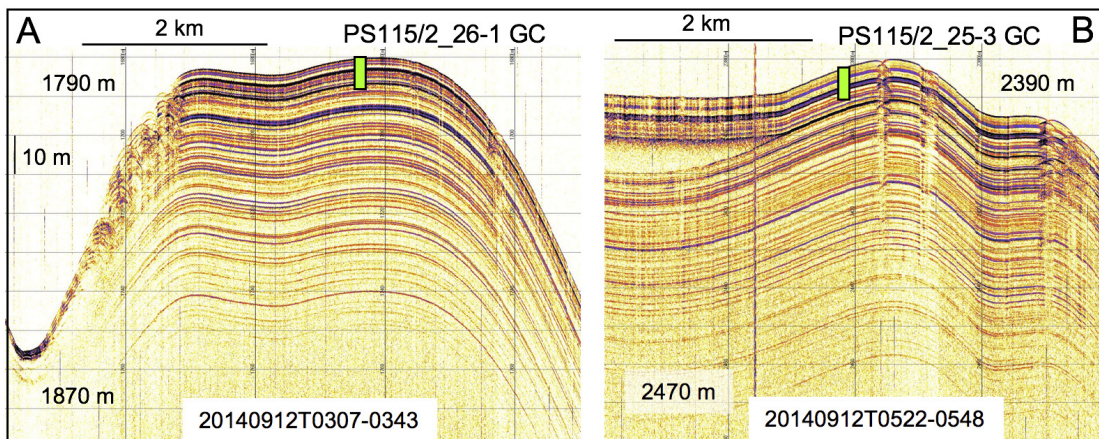


Fig. 7.2.7: PARASOUND profile across the upper (A) and middle (B) part of the western slope of Lomonosov Ridge with coring stations 26-1 and 25-3, respectively. Acoustic facies are pelagic with some indication of slope failure (A, left end) and re-deposition from debris flows (B, right left end).

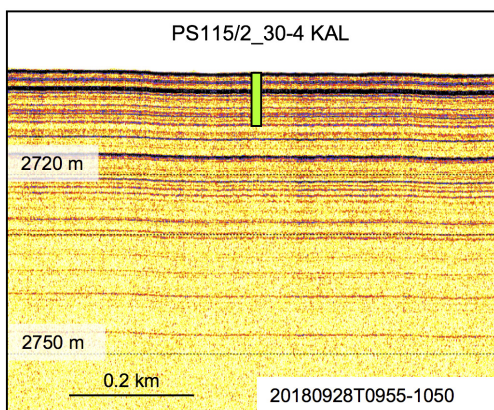


Fig. 7.2.8: PARASOUND profile across the lower end of the eastern slope of Lomonosov Ridge into the Makarov abyssal plain with coring station 30-4. Well-stratified sediments visible are widespread in the entire area with little variation in sedimentation rates.

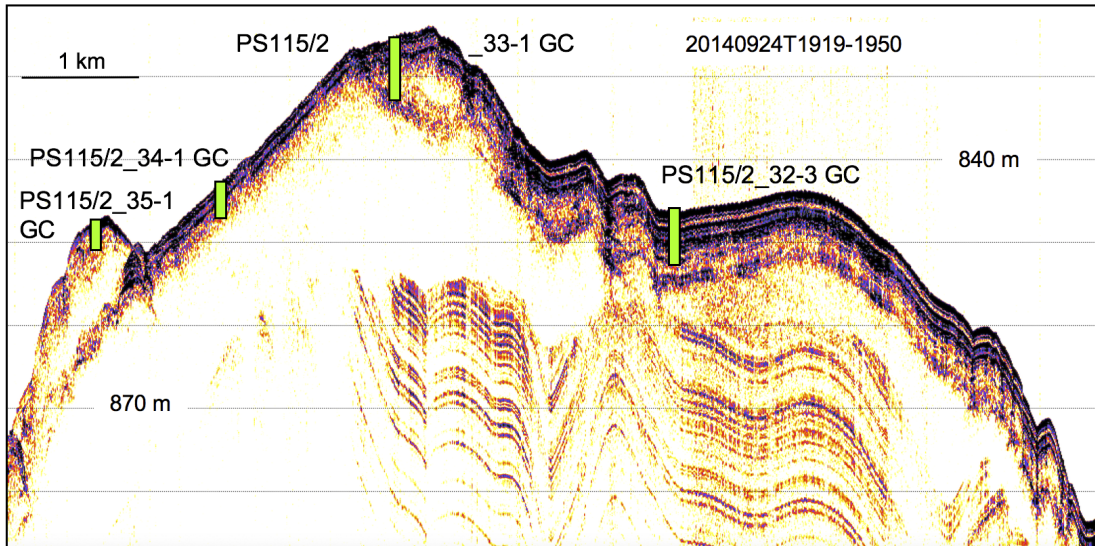


Fig. 7.2.9: PARASOUND profile across the top of Lomonosov Ridge. An older pelagic drape of the ridge is truncated by grounded ice overlain by four units of acoustic transparent sediments (diamiction) and draped by a few meters of stratified mud. Cores 34-1 and 35-1 penetrated into the top of the oldest and youngest glacial unit, respectively. Cores 32-3 and 33-1 penetrated the second and third oldest glacial units, respectively.

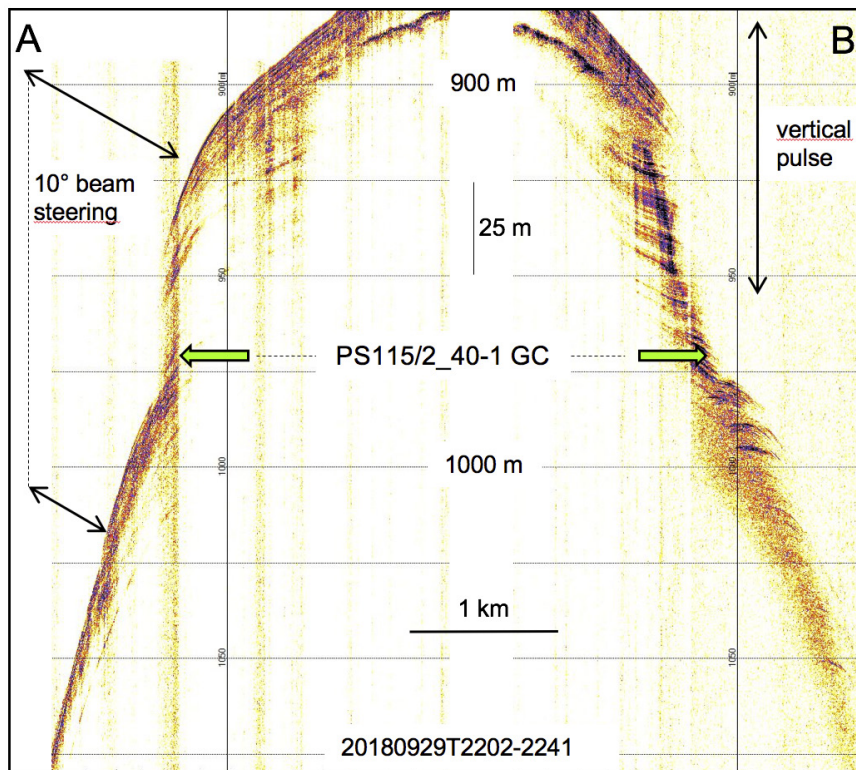


Fig. 7.2.10 :PARASOUND profiles across the upper end of the eastern slope of Lomonosov Ridge with coring station 40-1 (survey location 3, Table 7.2.1). Data of sections A and B were recorded along the same line. Note the difference in resolution for beam steering (A, about 5 m pelagic drape) overlying an escarpment under which older sediments are resolved, when a vertical pulse is applied (B, 915 to 1,000 m).

7.2 PARASOUND sub-bottom profiling

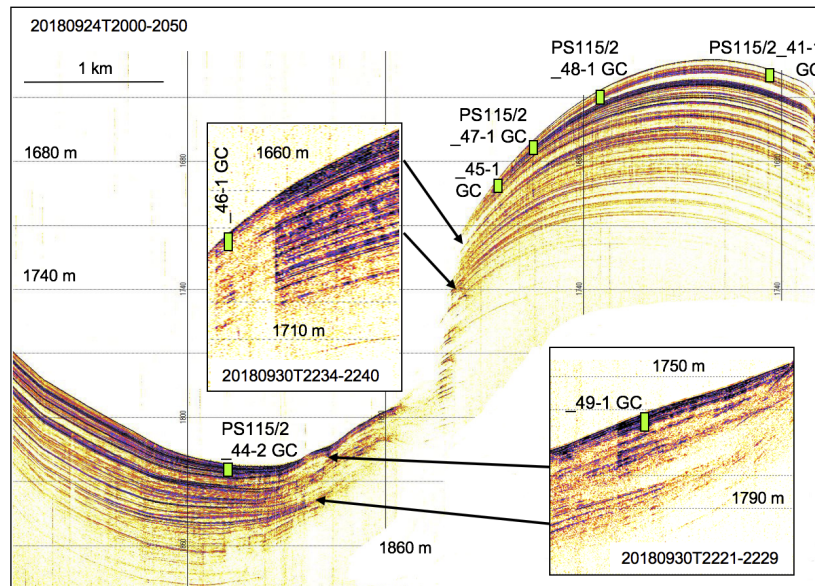


Fig. 7.2.11: PARASOUND profile across a channel levee complex south-west of Lomonosov Ridge with coring station transect from high accumulation (41-1) to condensed (49-1). Sub-profiles A and B were recorded along separate lines using the PARASOUND beam steering function in order to better resolve the transition between the channel and levee area.

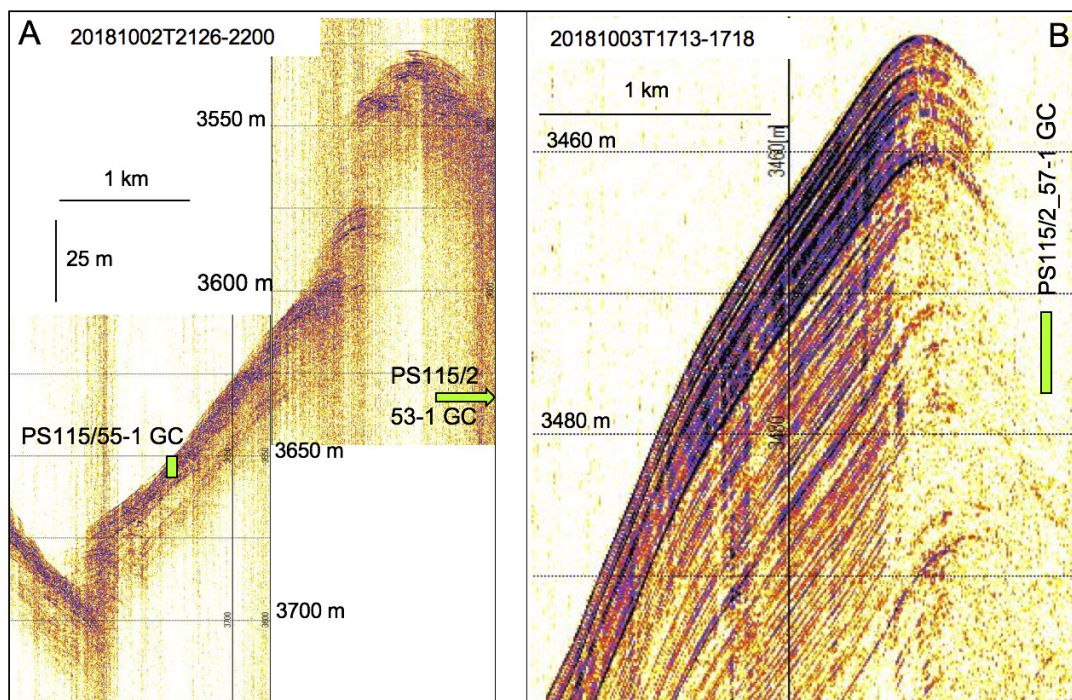


Fig. 7.2.12: PARASOUND profiles across tectonically uplifted areas of basement covered with old sediments (according to tentative seismic interpretation) and partly draped by pelagic mud at the top of (A), the discovered sea mount in the Amundsen abyssal plain, and (B), an escarpment towards the western end of the Amundsen Basin. Cores 53-1 and 57-1 were retrieved to sample older sediments from the escarpment surface (not resolved in PARASOUND data), while site 55-1 was selected to core the undisturbed pelagic drape. Note that acoustic stratigraphy of pelagic strata of section B is similar to that seen in Fig. 7.2.3. of this report.

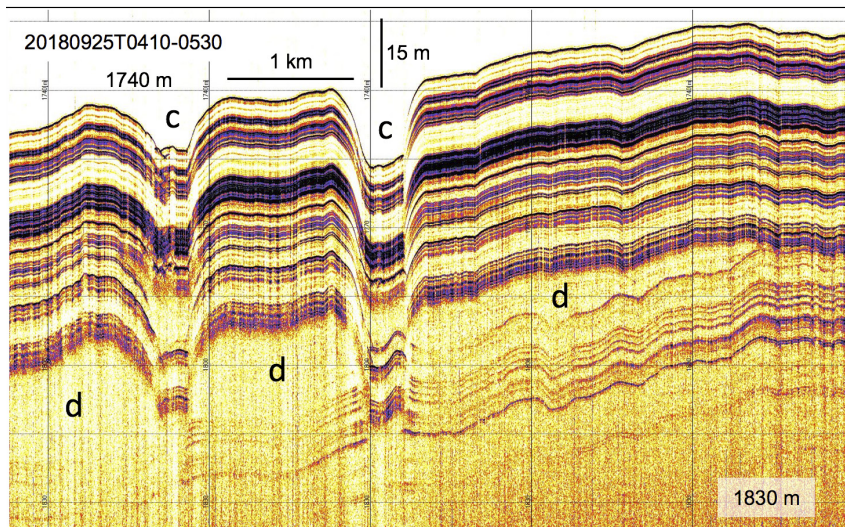


Fig. 7.2.13: At the southern end of the working area, PARASOUND profile across two palaeochannels (c), draped by about 50 m thick well-stratified mud and associated with the deposition from debris flows (d).

List of Abbreviations

ASD	Atlas Sounding Data
PHF	Primary High Frequency
P-SBP	Parametric Sub-bottom Profiling
PS3	Export format of PARASOUND data
SBES	Single-Beam Echo-Sounder
SHF	Secondary High Frequency
SLF	Secondary Low Frequency
QED	Quasi-Equidistant Operation
PNG	Portable Network Graphic
XML	Extensible Markup Language (text format)
GC	Gravity Core
SL	Schwere Lot (= GC)
KAL	Kastenlot Core
IODP	International Ocean Discovery Program

References

- Jakobsson M et al. (2016) Evidence for an ice shelf covering the central Arctic Ocean during the penultimate glaciation. *Nature Communications*, 7, 10365, DOI: 10.1038/ncomms10365, 1-10.
- Niessen F et al. (2013) Repeated Pleistocene glaciation of the East Siberian continental margin. *Nature Geoscience*, 6 (10), 842-846.
- Niessen F (in prep.) The Expedition PS110 of the Research Vessel POLARSTERN, Atlantic transit cruise in 2017/2018. *Berichte zur Polar- und Meeresforschung*.
- Stein R, Jokat W, Niessen F, Weigelt E (2015) Exploring the long-term Cenozoic Arctic Ocean Climate History – A challenge within the International Ocean Discovery Program (IODP)., *Arktos*, pp. 1-25. doi: 10.1007/s41063-015-012-x.
- Stein R (2016) Arctic Ocean Paleooceanography: Towards a Continuous Cenozoic Record from a Greenhouse to an Icehouse World (ACEX-2), IODP 708 full proposal – Add, <http://www.ecord.org/expedition377/>.
- Stein R, Fahl K, Gierz P, Niessen F, Lohmann G (2017). Arctic Ocean sea ice cover during the penultimate glacial and the last interglacial. *Nature Communications*, 373, 1-13.

7.3. Physical-properties core logging

Frank Niessen¹, Almut Schmengler¹

¹AWI

Objectives

Physical properties of sediments provide data for initial core characterization with a very high vertical resolution. Such as measured using Multi Sensor Core Loggers (MSCL) manufactured by GEOTEK Ltd. (UK), physical properties can be used to define and interpret stratigraphic patterns, including a comparison with lithology. In combination with other data, down-core patterns of physical properties provide a powerful tool for lateral core correlation. MSCL data are also useful to link the cores to high-resolution echosounding profiles obtained by systems such as the PARASOUND DSIII-P70 on *Polarstern* thereby aiding the projection of core data from a single spot of a coring station into larger spatial and temporal scales. During expedition PS115/2 a major goal of MSCL core logging is to provide high-resolution records of density, sonic velocity, and loop as well as some point-sensor magnetic susceptibility. In combination with existing age models, core physical-property results from previous expeditions provide an excellent stratigraphic-chronological framework for regional correlation of cores within the working area of expedition PS115/2 (Rachor 1997; Stein 2015; Stein et al. 2001, 2016, 2017).

In the following paragraphs, we briefly describe the acquisition of the data and provide an example for one sampling location including a transect of seven cores based on preliminary results. In addition, combined plots of wet bulk density (WBD) and volume-specific magnetic susceptibility (VMS) of cores PS115/2_2-2, PS115/2_11-3, PS115/2_12-1, PS115/2_13-2 and PS115/2_14-3 are presented in Chapter 7.5 of this report. For a more detailed description of the physical properties data acquisition the reader is referred to the cruise reports of the *Polarstern* expedition PS87 (Stein 2014) and expedition PS93/1 (Stein 2015). Descriptions of detailed analysis and core-to-core correlation are beyond the scope of this report and will be carried out after the cruise.

Work at sea

The physical properties were measured on whole cores (gravity cores GC = “Schwerelot” cores SL), subsampling cores trumped from box cores (GKG) using GC liner, and subsampling boxes used to cut off sediments from Kastenlot cores (KAL). The logged cores including the state of data acquisition and processing are summarized in Table 7.3.1.

Whole-core measurements in the ship laboratory included non-destructive, continuous determinations of core geometry (diameter), WBD, P-wave velocity (V_p), and loop sensor MS at 10 mm intervals on all cores obtained during the cruise. A standard MSCL-S track (GEOTEK) Ltd., UK, Ser. No. 25) was used to measure temperature, core diameter, P-wave travel time, gamma-ray attenuation, and MS. In the year 2017, the right-hand “pushing” side of the AWI MSCL-25 track has been replaced by up-to-date GEOTEK hardware including the processor unit and PC now using GEOTEK software Version 6. The active pushing element is connected to a ball screw, driven by a stepper motor which can position a core to an accuracy of better than 0.5 mm. The detection of the reference point is automated using a laser unit, except for MS logging using the point sensor (manual reference-point setting). The technical specifications of the MSCL system are summarized in Table 7.3.2. The principle of logging cores is described in more detail in the GEOTEK manual “Multi-Sensor Core Logging”, which can be downloaded from the web (<http://www.geotek.co.uk>). The orientation of the P-wave and gamma sensors was horizontal. GC were measured in coring liners including end caps, whereas KAL cores were measured in sub-cores retrieved from the original core using length-wise open transparent plastic boxes of 990 mm nominal length pushed into the KAL core. In

7. PS115/2 Marine Geology: Reconstruction of Past Climatic Conditions

the following we summarize the data acquisition of the different sensors, data conversion to standard parameters and the calculation of secondary physical properties.

Tab. 7.3.1: Summary of cores logged for physical properties during expedition PS115/2 and state of processing (Proc) at the end of the cruise. x = processing is finished for core. MS = Magnetic Susceptibility, L = Loop Sensor, P = Point Sensor, (OG) = Boxes subsampled for organic matter, (PP) = Boxes subsampled for physical properties, PTO = P-wave Travel time Offset.

Core No.	Device	Logged (Date)	Proc 1	Proc 2	Recovery [cm]	MS Sensor	PTO [μ s]
PS115/2_2-1	GKG	27.09.18	x		46.0	MSL	18.6
PS115/2_2-2	KAL (OG)	18.09.18	x	x	764.0	MSL	22.4
PS115/2_2-2	KAL (PP)	19.09.18	x		768.0	MSP	28.7
PS115/2_2-2	KAL (PP)	20.09.18	x		768.0	MSL	18.7
PS115/2_8-1	GKG	27.09.18	x		51.0	MSL	18.6
PS115/2_8-2	SL	17.09.18	x	x	538.0	MSL	15.3
PS115/2_11-1	GKG	27.09.18	x		48.0	MSL	18.6
PS115/2_11-3	SL	21.09.18	x	x	624.0	MSL	20.5
PS115/2_12-1	SL	21.09.18	x	x	643.0	MSL	22.4
PS115/2_12-2	GKG	27.09.18	x		36.0	MSL	18.6
PS115/2_13-1	GKG	27.09.18	x		39.0	MSL	18.6
PS115/2_13-1S	GKG	27.09.18	x		43.0	MSL	18.6
PS115/2_13-1S	GKG-Split	27.09.18	x		43.0	MSP	
PS115/2_13-2	SL	21.09.18	x	x	401.0	MSL	18.4
PS115/2_14-1	GKG	27.09.18	x		36.0	MSL	18.6
PS115/2_14-3	KAL (OG)	25.09.18	x	x	704.0	MSL	25.4
PS115/2_14-3	KAL (PP)	27.09.18	x		704.0	MSL	26.65
PS115/2_17-1	SL	22.09.18	x	x	342.5	MSL	18.5
PS115/2_18-1	SL	22.09.18	x		17.0	MSL	17.8
PS115/2_20-1	SL	22.09.18	x	x	319.0	MSL	18.5
PS115/2_21-1	SL	22.09.18	x		36.0	MSL	17.7
PS115/2_23-1	GKG	27.09.18	x		41.0	MSL	18.6
PS115/2_23-3	SL	23.09.18	x	x	513.0	MSL	18.8
PS115/2_24-1	SL	23.09.18	x		650.5	MSL	18.6
PS115/2_24-2	GKG	27.09.018	x		42.0	MSL	18.6
PS115/2_25-1	GKG	27.09.019	x		41.0	MSL	18.6
PS115/2_25-3	SL	24.09.18	x		710.5	MSL	18.3
PS115/2_26-1	SL	24.09.18	x		662.0	MSL	18.4
PS115/2_26-2	GKG	27.09.018	x		48.0	MSL	18.6
PS115/2_28-1	GKG	27.09.019	x		32.0	MSL	18.6
PS115/2_28-3	KAL	25.09.18	x		579.5	MSL	23.5
PS115/2_28-3	KAL	26.09.18	x		579.5	MSL	26
PS115/2_30-4	KAL (OG)	30.09.18	x		299.0	MSL	22
PS115/2_30-4	KAL (PP)	30.09.18	x		299.0	MSL	18.5

7.3. Physical-properties core logging

Core No.	Device	Logged (Date)	Proc 1	Proc 2	Recovery [cm]	MS Sensor	PTO [μ s]
PS115/2_30-4	KAL (OG)	06.10.18	x		299-879	MSL	20.2
PS115/2_30-4	KAL (PP)	06.10.18	x		299-877	MSL	22.4
PS115/2_32-3	SL	01.10.18	x	x	672.0	MSL	17.6
PS115/2_33-1	SL	01.10.18	x	x	474.0	MSL	18.8
PS115/2_34-1	SL	01.10.18	x	x	429.0	MSL	18.8
PS115/2_35-1	SL	01.10.18	x	x	360.0	MSL	18.9
PS115/2_36-1	SL	02.10.18	x		582.0	MSL	19.1
PS115/2_39-3	SL	02.10.18	x		596.0	MSL	19
PS115/2_40-1	SL	02.10.18	x	x	443.0	MSL	18.9
PS115/2_41-1	SL	03.10.18	x	x	638.0	MSL	19
PS115/2_44-2	SL	03.10.18	x	x	617.0	MSL	18.9
PS115/2_44-2	SL-split	09.10.18	x		617.0	MSP	
PS115/2_45-1	SL	03.10.18	x	x	592.0	MSL	18.8
PS115/2_46-1	SL	03.10.18	x	x	488.0	MSL	19
PS115/2_46-1	SL-split	09.10.18	x		488.0	MSP	
PS115/2_47-1	SL	04.10.18	x	x	630.0	MSL	19
PS115/2_47-1	SL-split	09.10.18	x		630.0	MSP	
PS115/2_48-1	SL	04.10.18	x	x	663.0	MSL	18.9
PS115/2_49-1	SL	04.10.18	x	x	539.0	MSL	18.9
PS115/2_50-1	SL	04.10.18	x	x	655.0	MSL	18.9
PS115/2_51-3	KAL (OG)	07.10.18	x		838.0	MSL	14.6
PS115/2_51-3	KAL (PP)	08.10.18	x		838.0	MSL	21
PS115/2_53-1	SL	05.10.18	x		486.0	MSL	18.8
PS115/2_55-1	SL	04.10.18	x		655.0	MSL	19.1
PS115/2_57-1	SL	05.10.18	x		572.0	MSL	19

- **Geometry:** The core diameter (GC including liner) and core width (KAL including sub-sample box) is measured as the distance between the faces of the Vp-transducers by using pre-calibrated lasers linked to transducer displacement mechanics. For GC (SL) and KAL, a standard plastic cylinder and an empty sampling box are used as the Reference Core Thickness (RCT), respectively, both of known geometries (Tab. 7.3.5). It is mandatory by the MSCL system that the RCT is captured prior to each core-logging run in order to “zero” the measurements of core-thickness deviations from the RCT. The sediment thickness is calculated using the following equation of the GEOTEK processing software module:

$$X = RCT - W + CTD/10;$$

with RCT = Reference Core Thickness;

W = total wall thickness of liner (GC) or box (KAL);

CTD = core thickness deviation (raw data in mm, see above).

In case the cores are measured including the section caps, the thickness deviation caused by caps is added to the sediment thickness, because W is assumed to be constant. The software does not allow an extra input for wall thickness of the caps (plus tape). This induces an error to

WBD calculations using GEOTEK processing software (see below). The GEOTEK processing software adds the thickness of the caps to the sediment thickness although the actual sediment core diameter will hardly vary at the caps compared to the rest of the core. A correction for this error is described in detail in the MSCL Chapter of the PS87 cruise report (Stein 2015).

Tab. 7.3.2: Technical specifications of the GEOTEK MSCL-25 used during expedition PS115/2

Displacement transducer orientation: horizontal Transducer Type: Standard Geotek Rolling Transmitter pulse frequency: 230 kHz Received pulse resolution: 50 ns Seismogram sampling frequency: 12.5 MHz
Density Radiation beam orientation: horizontal Gamma ray source: Cs-137, Ser. No. 0875/13 Activity: 356 Mbq (year 2013) Energy: 0.662 MeV Collimator diameter: 5.0 mm (GC, GKG), 2.5 mm (KAL) Gamma detector: Gammasearch2, Model SD302D, Ser. Nr. 3114, John Count Scientific Ltd., 10 s counting time
Temperature Sensor: PT-100
Magnetic susceptibility Loop sensor: BARTINGTON MS-2C Loop sensor diameter: 14 cm Alternating field frequency: 565 Hz, counting time 10 s, precision $0.1 \cdot 10^{-5}$ (SI) Magnetic field intensity: ca. 80 A/m RMS Point sensor: BARTINGTON MS-2F Counting time: 10 s

C- Density: Wet Bulk Density (WBD) was determined from attenuation of a gamma-ray beam transmitted from a radioactive source (^{137}Cs). A collimator was used to focus the radiation through the core-centre into a gamma detector (Table 7.3.2). To calculate density from gamma counts, GEOTEK-MSCL processing software module was used (www.geotek.co.uk), which applies the following function:

$$\ln(GA) = A(GD \cdot X)^2 + B(GD \cdot X) + C;$$

with GA = Gamma Attenuation (raw data, cps);
 X = Sediment thickness (see above);
 A, B, C = constants.

For calibration, A, B and C are determined empirically several times during the cruise by logging a standard core consisting of different proportions of aluminum and water as described in Best

7.3. Physical-properties core logging

and Gunn (1999). The data of the standard stair-shaped blocks of aluminum logged in a liner (GC, GKG) or in transparent boxes (KAL) filled with water are given in Table 7.3.3 and 7.3.4.

Tab. 7.3.3: Thickness and density of gamma-attenuation calibration box (KAL, transparent) filled with stair-shaped block of aluminum in water. Density of aluminum: 2.71 g cm⁻³, density of water: 0.998 g cm⁻³, internal box width along gamma ray: 7.3 mm

Aluminium Thickness (cm)	Average Density (g cm ⁻³)	Av. Den. * Thickness (g cm ⁻²)
7.02	2.644	19.3
6.58	2.54	18.54
5.76	2.348	17.14
4.93	2.153	15.72
4.12	1.963	14.33
3.29	1.768	12.91
2.48	1.58	11.53
1.65	1.385	10.11
0.93	1.216	8.88
0.00	0.998	7.29

Tab. 7.3.4: Thickness and density of gamma-attenuation calibration liner (GC/GKG) filled with stair-shaped block of aluminium in water. Density of aluminium: 2.71 g cm⁻³, density of water: 0.998 g cm⁻³, internal liner diameter along gamma ray: 12.25 mm.

Aluminium Thickness (cm)	Average Density (g cm ⁻³)	Av. Den. * Thickness (g cm ⁻²)
10.00	2.40	29.35
9.01	2.26	27.65
8.01	2.12	25.94
7.01	1.98	24.22
6.00	1.84	22.49
5.01	1.70	20.80
4.00	1.56	19.08
3.01	1.42	17.37
2.00	1.28	15.64
1.01	1.14	13.96
0.00	0.998	12.23

Also, postprocessing included WBD corrections for liner sections affected by end caps (see -Density above):

$$WBD_{\text{corr}} = WBD + ((ct-x)/(x/100)*WBD/100-0.015)$$

Ct is the measured core thickness at end caps, x is the mean core thickness between the end caps and 0.015 is the empirical effect on core density caused by additional gamma ray absorption of plastic caps. These corrections were only applied to depth intervals of GC cores, which exhibit significant larger core thickness values in the logged data caused by caps (see -Geometry above). This correction has been fully applied for all post-processed GC (Tab. 7.3.1).

Tab. 7.3.5: Density calibration parameter used during expedition PS115/2 (The core numbers as part of the Calibration File refer to cores, which were logged before or after the calibration run (see Table 7.1.1 for dates, RCT = reference core thickness, R² = correlation coefficient for determination of calibration constants A, B and C).

Name of Calibration (File)	Logging Interval (cm)	RCT (cm)	Wall Thickness of Liners (cm)	Ref. Vp in Water (m/s)	A	B	C	R ²
PS115_2_2-2_DENSCAL_KAL	0.5	7.55	0.6	1486	-0.00008113	-0.0678	8.7659	0.9994
PS115_2_11-3_DENSCAL_SL	0.5	12.5	0.5	1485	-0.0002	-0.0551	10.078	0.9998
PS115_2_12-3_DENSCAL_SL	0.5	12.5	0.5	1484	-0.0002	-0.0569	10.082	0.9998
PS115_2_32-3_DENSCAL_SL	0.5	12.5	0.5	1486	-0.0002	-0.0561	10.064	0.9998
PS115_2_30-4_DENSCAL_KAL	0.5	7.96	0.6	1487	-0.0002	-0.0638	8.7735	0.9998
PS115_2_51-3_DENSCAL_KAL	0.5	7.5	0.6	1485	-0.0004	-0.0572	8.7407	0.9995

- Porosity: Fractional Porosity (FP) is the ratio of the total volume over the volume of the pores filled with water. FP determined by MSCL-logging is not an independent data-acquisition parameter, but can be calculated from the WBD using the GEOTEK processing software module as follows:

$$FP = (dg - WBD) / (dg - dw);$$

with dg = grain density (2.7 g cm⁻³);

dw = pore-water density (1.03 g cm⁻³).

This approach makes the assumption that grain density and pore-water density are constant.

- Temperature: Temperature (T) was measured as room temperature in air on top of the logging bench in the laboratory. The cores were stored for 24 hours in the laboratory before logging in order to allow equilibration with room temperature.

- Velocity: For determination of sonic velocity across the core the travel time (TT) of ultrasonic pulses (Tab. 7.3.2) are measured which are transmitted and received via rolling transducers (see geometry above). Vp was then calculated using the following equation from the GEOTEK processing software module:

$$Vp = X / (TT-PTO);$$

with: X = Sediment Thickness (see above);

TT = total travel time measured between the transducers (raw data in μs);

PTO = P-Wave Travel-time Offset.

The PTO is the travel time through the core liner walls (see geometry above), transducer, electronic delay, and detection offset between the first arrival and second zero-crossing of the received waveform (see GEOTEK Manual for details), where the travel time can be best detected. This travel-time offset was determined using a GC/KAL-liner filled with freshwater (Vp = 1481 m/s) logged together with the density standard (see above) and together with all logged cores (Initial Calibration Piece, see GEOTEK Manual for details). In order to find the correct PTO we used the GEOTEK processing software approaching the correct Vp in water (table-output function) by inputs of different PTO values into the processing panel and repetitive processing. The PTO values determined during PS115/2 are presented in Table 7.3.1. The Vp amplitudes remained unprocessed in the final data sets.

- Magnetic Susceptibility (MS): The specifications of the Bartington MS-2 loop sensor used on board are summarized in Table 7.3.2. The MS-2 meter was set to zero 200 mm before the

7.3. Physical-properties core logging

core reached the MS sensor. Sensor was checked for possible drift above the top and below the bottom of the core by logging a 200 mm long liner (GC) and a 500 mm long box (KAL), respectively, filled with water as initial and final calibration piece. Any drift observed, which was larger than 1 or -1, was corrected assuming a linear drift over the entire core length.

$$MS_{dc} = MS - CD \cdot (\text{Drift/Core Length});$$

with MS_{dc} = the drift corrected MS;

MS = the MS raw data;

CD = depth in core (raw data, mbsf).

The first processing of data using GEOTEK Software does not change MS data from raw data. In order to calculate volume-specific magnetic susceptibility (VMS) data are corrected for loop-sensor and core diameter as follows:

$$MS (10^{-6} \text{ SI}) = \text{measured value} (10^{-5} \text{ SI}) / K\text{-rel} \cdot 10$$

with K-rel empirically determined by GEOTEK (www.geotec.co.uk):

$$K\text{-rel} = 4.8566(d/D)^2 - 3.0163(d/D) + 0.6448$$

D is the diameter of the MS-2-meter loop sensor (140 mm) and d is the reference diameter of the core (Tab. 7.3.5). For KAL-cores, the rectangular cross section of the core was equalized to a size-equivalent circular section, of which a fictive core diameter was calculated as input parameter for loop-sensor correction coefficient:

$$d_{KAL} = 2 \sqrt{a \cdot b / \pi}$$

The sediment height of KAL-cores (a) was measured for each section of KAL cores. The average height per core was used to calculate d_{KAL} . The width of KAL-cores (b) is measured at each logging interval by the MSCL (core thickness, see geometry above). In addition, MS of some of the KAL sections were measured using the Bartington MS point sensor (MS-2F) on the flat surfaces of foil-covered cores (Tab. 7.3.1). The point MS data remained in raw-data format (10^{-5} SI).

Preliminary results

Minor gaps of data are at or near the end of individual liner sections. No meaningful Vp data are recorded along the end caps of GC core sections, because the arrival times of the acoustic pulse were not detectable through end caps. The same effect was observed for several core sections between the caps. It is assumed that the sediments inside the liners were not in contact with the liner wall and, thus, did not allow sound propagation between transducers. In addition, for unknown reasons, we were facing problems to maintain stable zero-crossing detection conditions in seismograms using the digital P-wave oscilloscope provided by the GEOTEK software. As a result, sections of cores or some entire cores have no Vp-data. On the other hand, MS and WBD logs provide nearly complete records in all cores. Thus, these parameters offer a good database for core correlation. In particular, combined plots of MS and WBD versus depth (Fig. 7.3.1) are very useful to document numerical response to changes in the sedimentary environments, which also correlate with lithological changes and with cores having an age model (see Chapter 7.5 of this report). During expedition PS115/2 there was not enough time to systematically check the quality of Vp data and provide a comparison/correlation with WBD or FP.

In this chapter, we present preliminary results of combined VMS/WBD logs of seven cores (PS115/_41-1 to _49-1, Fig. 7.3.1) for one sampling profile of expedition PS115/2 (see PARASOUND profile in Chapter 7.2, Fig. 7.2.11). As in previous core logs from the working area, we notice that VMS down-core pattern differs from that of WBD. Thus, the VMS signal is not simply a function of porosity (or water content) of the cores but is controlled by variable

supply of magnetic grains. In particular, in case increased or peak values of WBD correspond to lower or minimal values in VMS these patterns offer a very good tool for lateral core correlation. Although the correlation lines of physical property pattern (Fig. 7.3.1) is tentative, there is a good agreement of the correlation with reflector geometries along the PARASOUND profile (Fig. 7.2.11). Sedimentation rates of younger sediments are much higher on the levees compared to the channel (centre of the profile). Also, it is interesting to note that most of the younger sediments of the levees are very condensed (or more likely not present) within the channel. On the other hand, older units are correlated across the channel with nearly constant thicknesses (Fig. 7.3.1). More work is needed to verify or confirm the correlation, to provide chronology and interpret the noted variation in space and time.

Data management

Data acquisition and processing of whole cores are summarized in Table 7.3.1 and went through several steps:

MSCL Raw-data acquisition of whole cores using GEOTEK software.

First processing of whole-core data using GEOTEK software. This includes the calculation of core thickness, V_p , and WBD. WBD data have errors along liner caps. MS sensor response remained in raw-data state (10^{-5} SI). For GC cores the “Butt-Error” function was used to correct total core length for errors induced by end caps.

Second processing of whole-core data using software Kaleidagraph™. This includes a data quality control on calibration sections logged on top and below the bottom of the core (200 mm liner filled with water) and a removal of these data from the core. For KAL cores, it also includes a correction of core-section length according to the obtained recovery and cleaning for odd data points. In addition, MS is corrected for sensor drift. MS data are converted to volume-specific susceptibility. WBD of GC cores are corrected for end-cap errors.

All data will be available to the shipboard science party for joint publication. In addition, once fully processed and corrected on land, the data are stored as a function of core depth in form of text-files in the databank PANGAEA (www.pangaea.de).

References

- Best AI, Gunn DE (1999) Calibration of marine sediment core loggers for quantitative acoustic impedance studies. *Marine Geology*, 160, 137-146.
- Rachor E (1997) Scientific cruise report of the Arctic Expedition ARK-XI/1 of RV “Polarstern” in 1995: (German-Russian Project LADI: Laptev Sea - Arctic Deep Basin Interrelations). *Berichte zur Polarforschung (Reports on Polar Research)*, Bremerhaven, Alfred Wegener Institute for Polar and Marine Research, 226, 173p.
- Stein R, Boucsein B, Fahl K, Garcia de Oteyza T, Knies J, Niessen F (2001). Accumulation of particulate organic carbon at the Eurasian continental margin during late Quaternary times: Controlling mechanisms and paleoenvironmental significance. *Global and Planetary Change*, 31, 87-104.
- Stein R (2015) The Expedition PS87 of the Research Vessel POLARSTERN to the Arctic Ocean in 2014 with contributions of the participants. *Reports on Polar and Marine Research*, 688, 273pp. doi:10.2312/BzPM_0688_2015 or http://doi.org/10.2312/BzPM_0688_2015.
- Stein R (2016) The Expedition PS93.1 of the Research Vessel POLARSTERN to the Greenland Sea and the Fram Strait in 2015. *Reports on polar and marine research*, Bremerhaven, Alfred Wegener Institute for Polar and Marine Research, 695, 151p.
- Stein R, Fahl K, Schreck M, Knorr G, Niessen F, Forwick M, Gebhardt C, Jensen L, Kaminski M, Kopf A, Matthiessen J, Jokat W, Lohmann G.(2016) Evidence for ice-free summers in the late Miocene central Arctic Ocean. *Nature Communications*, 7 , pp. 1-13. doi:10.1038/ncomms11148.
- Stein R, Fahl K, Gierz P, Niessen F, Lohmann G (2017) Arctic Ocean sea ice cover during the penultimate glacial and the last interglacial. *Nature Communications*, (373). doi:10.1038/s41467-017-00552-1.

7.3. Physical-properties core logging

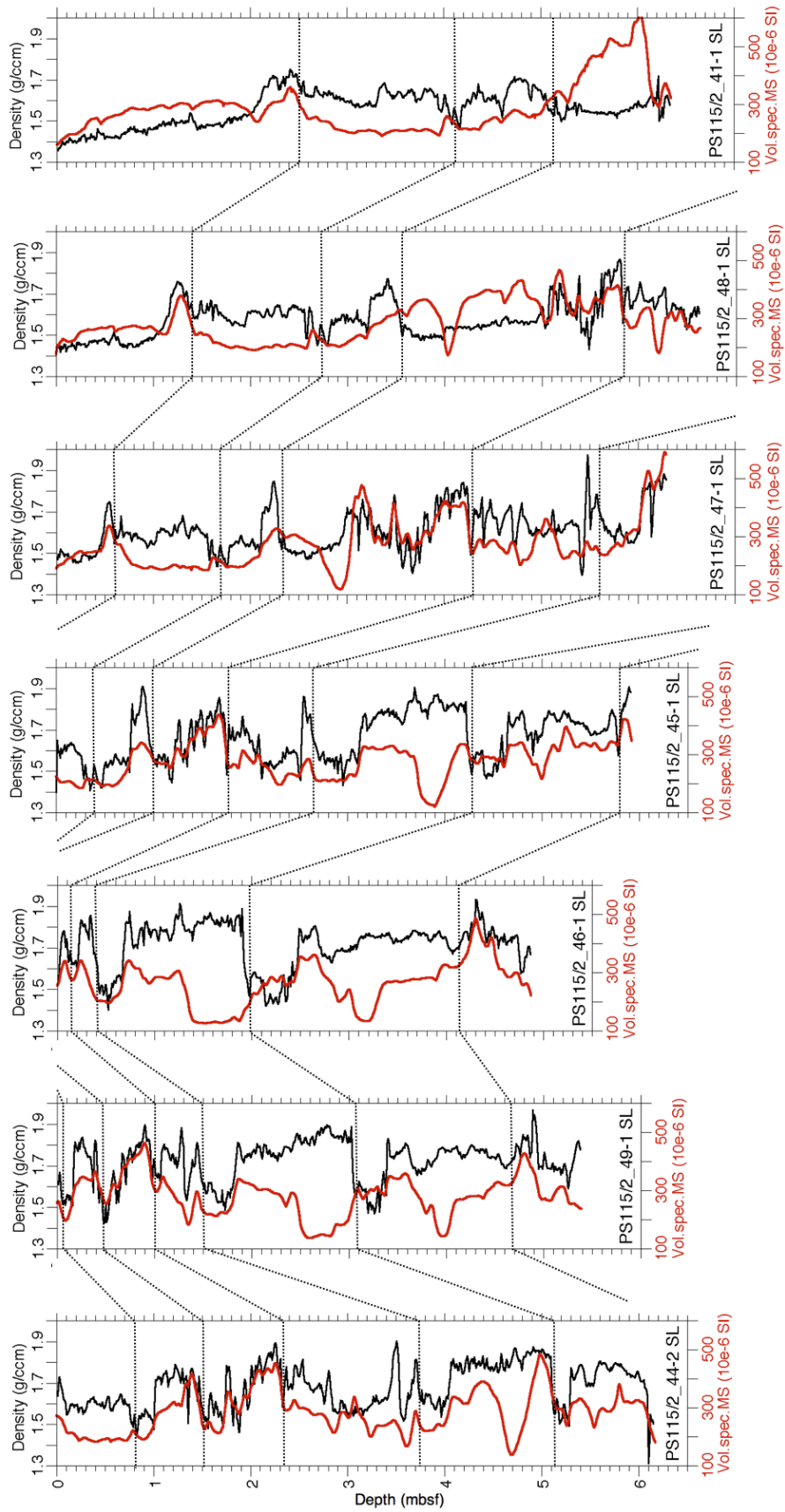


Fig. 7.3.1: Examples of VMS and WBD logs of seven GC cores obtained during PS115/2

7.4 Sediment composition of selected sediment cores based on smear slide and coarse-fraction analyses

Maximilian Dröllner¹,
Frithjof Lemmel²

¹UoM
²GEOMAR

Grant-No. AWI_PS115/2_01

Objectives

On a restricted number of sediment cores and samples, smear slide and coarse-fraction analyses were carried out to get some first information about the composition and grain size distribution of the recovered sediments. The results were used as complementary information to the lithological descriptions of the cores.

Work at sea

During the PS115/2 (ARK-XXXII/3) expedition, smear slides from KAL cores PS115/2_2-2 (28 samples) and PS115/2_51-3 (19 samples) were prepared following instructions described in details in the IODP Technical Note (2013) and Stein (2015). An optical adhesive (epoxy jelly) was used for mounting slides. Smear-slides were studied using the petrographic microscope Leitz Laborlux 11 POL at various magnifications. Grain-size distribution was analysed by estimating the sand (> 63 µm) and silt (2-63 µm) contents. The quantification of the sand fraction was carried out using 10x magnification while the 63x magnification was used for analysing the silt fraction. Due to the degree of certainty, however, no quantitative values were given for mineral abundances. Since biogenic components (e.g. diatoms, radiolarians) are only rare to absent, they were not examined in detail.

For coarse-fraction analysis, samples from KAL cores PS115/2_2-2, PS115/2_14-3 and PS115/2_51-3 were sieved using a 63 µm mesh and analysed on board *Polarstern*. In total, 126 samples were sieved and analysed. The abundance of foraminifera was roughly estimated by analysing the coarse fraction (>63 µm) using a binocular microscope. The semi-quantitative estimates of abundance are presented from 0 to 5, where 0 = barren, 1 = very rare, 2 = rare, 3 = common, 4 = abundant, 5 = dominant.

Preliminary results

Smear slide data

Based on the grain-size distribution (Fig. 7.4.1 and Table 7.4.1), sediments from KAL core PS115/2_2-2 (only lower part) can be classified as silty clay. Main mineral phases in the silt and sand fraction are quartz, feldspar, and biotite. The heavy mineral suite is characterized by the dominance of amphibole, pyroxene, and epidote/zoisite minerals. Less common are rutile, apatite, and zircon minerals. Both the reddish/pinkish layer at 560 cmbsf and the layers 535 and 545 cmbsf probably contain carbonate minerals. However, unambiguous identification of carbonate minerals was not possible. In general, mineral identification in this core was challenging due to the overall small grain size of the sediment. Nonetheless, changes in mineralogy were recognized at 315 cmbsf where the biotite abundance decreases, and at 657 cmbsf where the biotite abundance increases again. Additionally, the smear slide at 680 cmbsf is different in terms of heavy mineral composition as epidote/zoisite minerals appear to be the major components.

7.4 Sediment composition of selected sediment cores

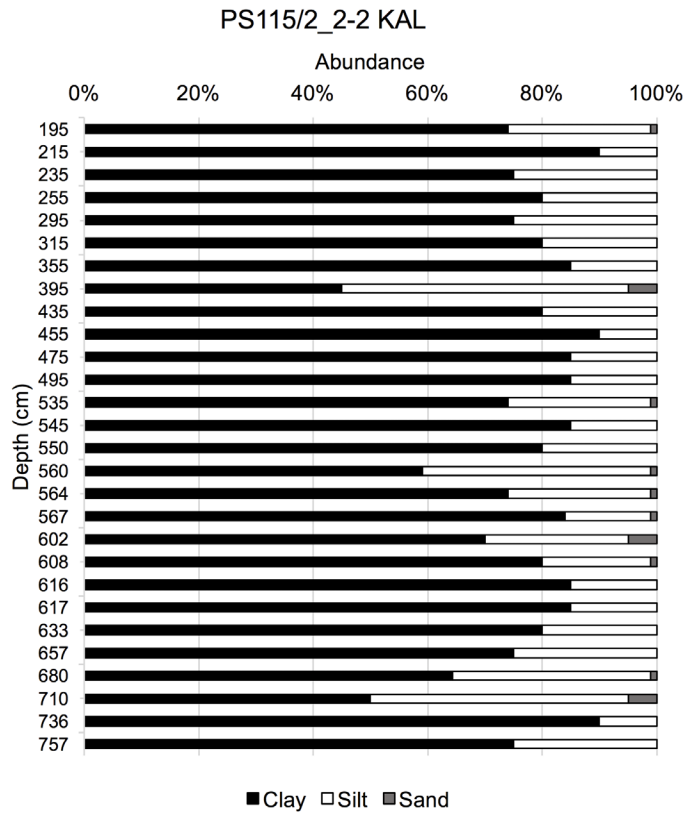


Fig. 7.4.1: Grain-size distribution based on smear-slide analysis (PS115/2_2-2)

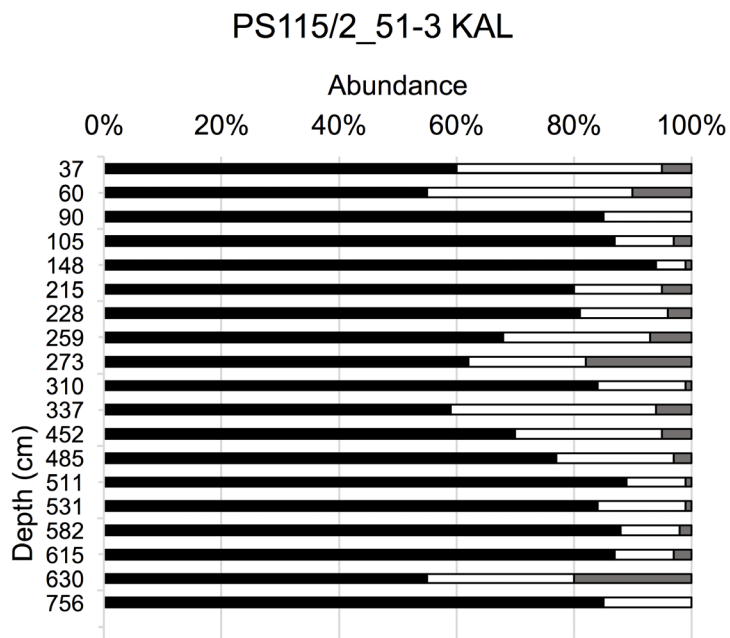


Fig. 7.4.2: Grain-size distribution based on smear-slide analysis (PS115/2_51-3)

7. PS115/2 Marine Geology: Reconstruction of Past Climatic Conditions

Based on smear-slide data, the sediments from KAL core PS115/2_51-3 can be classified as silty clay and sandy silty clay (Table 7.4.1 and Fig. 7.4.2). Main mineral phases in the silt and sand fraction are quartz and feldspar (predominantly plagioclase). The heavy mineral suite is characterized by the dominance of pleochroitic hornblende minerals, which were distinguished by their green to blue colour. Biotite, epidote/zoisite, and garnets were identified as minor components. In the fine silt fraction apatite, rutile, and zircon minerals are present. There are also minor occurrences of carbonate minerals (e.g. 259 cmbsf). In addition, there are a few rock fragments with different origin present (i.e. volcanic, metamorphic, sedimentary). In general, the mineralogy is homogenous. Exception is the smear slide at 273 cmbsf, which is characterized by abundant opaque phases, despite being very coarse compared to other smear slides. Most likely these are pyrite minerals, which may be the result of syn-sedimentary redox processes.

Tab. 7.4.1: Grain-size distribution based on smear-slide data. (a) PS115/2_2-2; (b) PS115/2_51-3

(a) PS115/2_2-2 KAL				(b) PS115/2_51-3 KAL			
Depth [cm]	Clay	Silt	Sand	Depth [cm]	Clay	Silt	Sand
195	74	25	1	37	60	35	5
215	90	10	0	60	55	35	10
235	75	25	0	90	85	15	0
255	80	20	0	105	87	10	3
295	75	25	0	148	94	5	1
315	80	20	0	215	80	15	5
355	85	15	0	228	81	15	4
395	45	50	5	259	68	25	7
435	80	20	0	273	62	20	18
455	90	10	0	310	84	15	1
475	85	15	0	337	59	35	6
495	85	15	0	452	70	25	5
535	74	25	1	485	77	20	3
545	85	15	0	511	89	10	1
550	80	20	0	531	84	15	1
560	59	40	1	582	88	10	2
564	74	25	1	615	87	10	3
567	84	15	1	630	55	25	20
602	70	25	5	756	85	15	0
608	80	19	1				
616	85	15	0				
617	85	15	0				
633	80	20	0				
657	75	25	0				
680	65	35	1				
710	50	45	5				
736	90	10	0				
757	75	25	0				

7.4 Sediment composition of selected sediment cores

The data presented here should be regarded as preliminary, i.e., further investigations (e.g. point counting) of mineralogy are needed to obtain more detailed information about changes in mineral abundance.

Coarse-fraction data

Surface and near-surface sediments at GKG site PS115/2_51-1 only contain abundant foraminifera down to 15 cm below seafloor (cmbsf; Fig. 7.4.3), while no foraminifera were observed below this stratigraphic level. The most abundant species include planktic foraminifera (*Neogloboquadrina pachyderma sinistral*) and benthic foraminifera (*Cibicidoides wuellerstorfi*). However, planktic species are usually more abundant than benthic (Fig. 7.4.3). In contrast to the uppermost 10 cmbsf, where both planktic and benthic species were observed, the sample 10-15 cmbsf only contains the planktic species *N. pachyderma sin.* Below 15 cmbsf, all samples are barren.

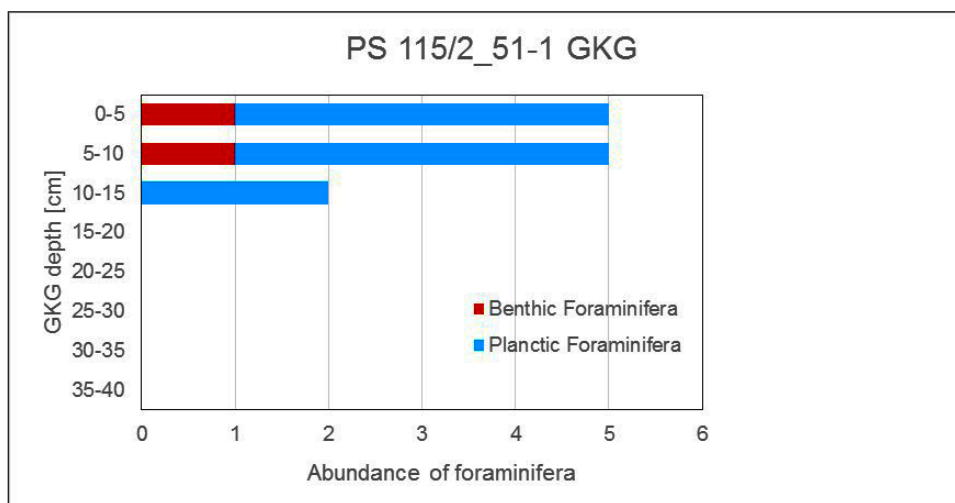


Fig. 7.4.3: Semi-quantitative abundance estimates of foraminifera in the box corer at site PS115/2_51-1

At KAL cores PS115/2_2-2, PS115/2_14-3 and PS115/2_51-3, abundant foraminifera, mainly the planktic species *N. pachyderma sin.*, were found within the first meter of sediment with absolute maxima in the uppermost centimetres, whereas only isolated occurrences of *N. pachyderma sin.* could be observed in greater core depth (Figs. 7.4.4, 7.4.5 and 7.4.6). At KAL Core PS115/2_2-2, sporadic occurrences were observed between 155 to 175 cmbsf, at 331 cmbsf, and in the core catcher (Fig. 7.4.4). In KAL Core PS115/2_14-3, foraminifera are only present at 30 and 210 cmbsf, while all other samples are barren (Fig. 7.4.5). In KAL Core PS115/2_51-3, foraminifera occur continuously from the top to 15 cmbsf and between 43 to 92 cmbsf, however, no foraminifera were encountered below 92 cmbsf (Fig. 7.4.6). The maximum abundances in the uppermost 15 cm of this core is in accordance with the record from the giant box corer PS115/2_51-1 recovered from the same location (Fig. 7.4.3), however, benthic foraminifers were not found in the KAL Core.

It has to be noticed, that foraminifera are generally very rare to rare in all analysed cores, except for the surface samples.

7. PS115/2 Marine Geology: Reconstruction of Past Climatic Conditions

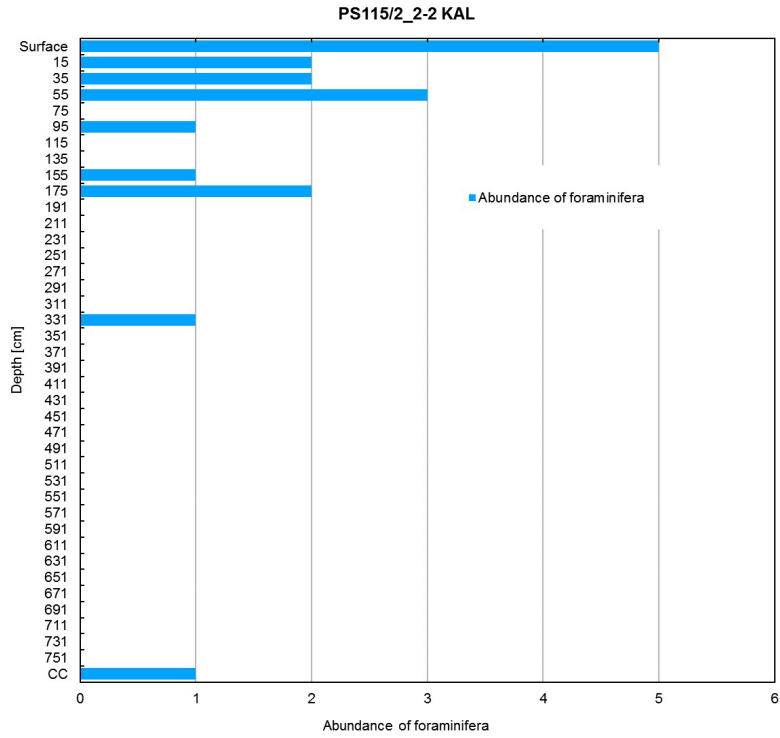


Fig. 7.4.4: Semi-quantitative abundance estimates of foraminifera in KAL core PS115/2_2-2

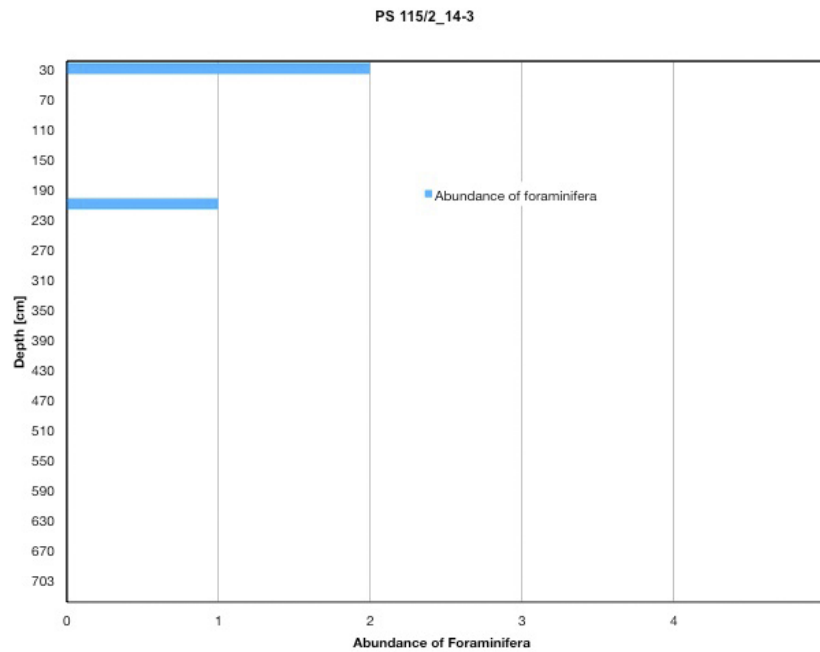


Fig. 7.4.5: Semi-quantitative abundance estimates of foraminifera in core PS115/2_14-3

7.4 Sediment composition of selected sediment cores

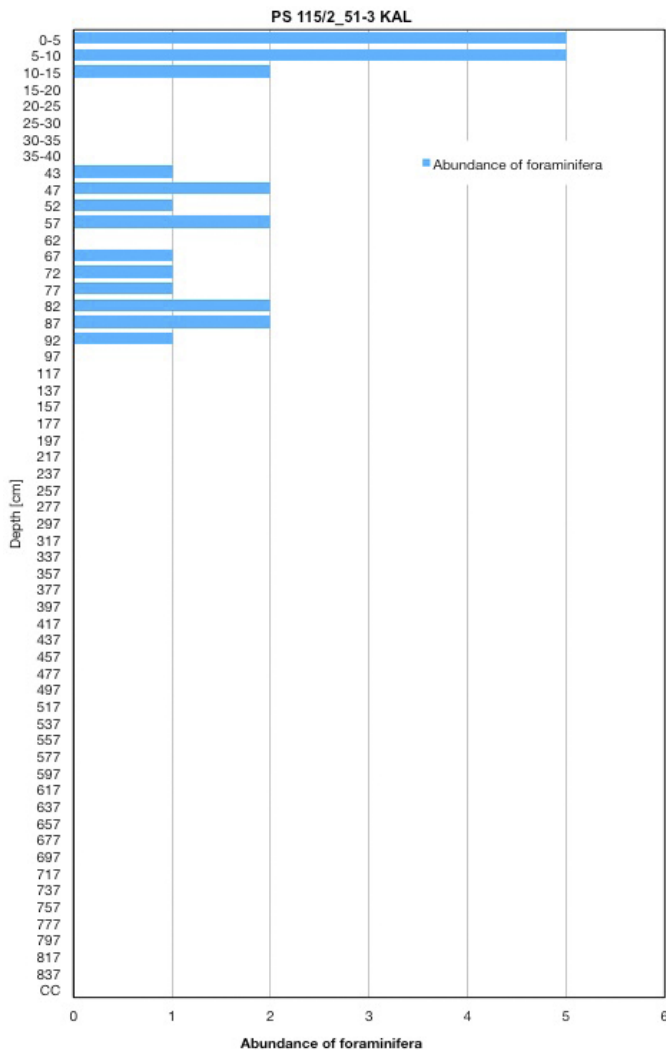


Fig. 7.4.6: Semi-quantitative abundance estimates of foraminifera in core PS115/2_51-3. No foraminifera were found below 92 cm.

The fact that foraminifera are rare to absent may have different reasons. These include dissolution of carbonate shells before, during or after deposition, a sampling bias where barren intervals are overrepresented, or they have just been overseen during microscope analyses. For the latter it has to be mentioned that separation into different grain size classes (e.g. 125 μm , 250 μm etc.) using a shifter was not carried out. Thus, the samples were composed of all grain sizes > 63 μm with the highest amount of material in the fine fraction, which have hampered the observation of smaller sized foraminifera.

Data management

All results of the smear-slide analysis will be stored in the PANGAEA Data Publisher for Earth & Environmental Science. The smear slides will be stored at Department of Marine Geology at the AWI, Bremerhaven.

References

- Stein R (Ed) (2015) The Expedition PS87 of the Research Vessel POLARSTERN to the Arctic Ocean in 2014, doi:10.2312/BzPM_0688_2015.
- Marsaglia K, Milliken K, and Doran L (2013) IODP digital reference for smear slide analysis of marine mud. Part 1: Methodology and atlas of siliciclastic and volcanogenic components. IODP Technical Note 1, doi:10.2204/iodp.tn.1.2013.

7.5 Sediment characteristics and lithostratigraphy of some PS115/2 cores

Ruediger Stein¹, Frank Niessen¹, Ryan Love²

¹AWI

²MUoN

Grant-No. AWI_PS115/2_01

Objectives

The key goals of the marine-geological research programme of expedition PS115/2 and the relationship to the proposed IODP drilling campaign (IODP expedition 377; see Stein et al., 2015; Stein, 2017; <http://www.ecord.org/expedition377/>) were already outlined in Chapter 7.1. In this context, one of the important objectives of the shipboard studies of the PS115/2 sediment cores was a first identification of the major lithologies and the establishment of a preliminary lithostratigraphy and age model of these cores, based on correlation with (dated) sediment cores from the southern Lomonosov Ridge area (80°N - 83°N) and adjacent Eurasian continental margin (*Polarstern* expedition ARK-XI/1 in 1995: Rachor, 1997; *Polarstern* expedition ARK-XIV/1a in 1998: Jokat 1999; *Polarstern* expedition PS87 in 2014: Stein, 2015) (Figs. 7.1.1, 7.5.1 and 7.5.2).

For sediment cores recovered in 1995 from the Siberian side of the Lomonosov Ridge (for core locations see Fig. 7.5.1), Stein et al. (1997) established a first lithostratigraphic framework based on a detailed visual core description (and supported by physical property data; Niessen et al., 1997), and proposed an age model representing MIS 6 to 1 (Fig. 7.5.3). This tentative age model has later been further supported by a few AMS ¹⁴C datings, magnetic stratigraphy, correlation with other dated sediment cores, etc. (see Stein, 2008 details and references).

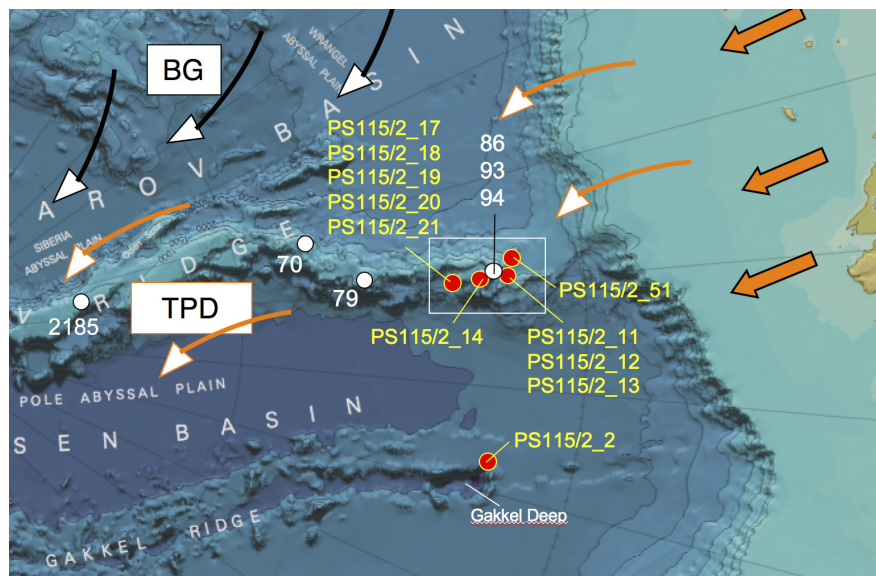


Fig. 7.5.1: Map of southern Lomonosov Ridge, Amundsen Basin and Gakkel Ridge with locations of selected PS115/2 cores (red circles with yellow numbers, and PS87 cores and Core PS2185 (white circles with white numbers) discussed in this chapter. The Transpolar Drift (TPD) and Beaufort Gyre (BG) current systems are shown by orange and black arrows, respectively. Thicker orange arrows mark sediment input from Siberia. White box indicates area of Fig. 7.5.2 (for overview map with all stations see also Fig. 7.1.1).

7.5 Sediment characteristics and lithostratigraphy of some PS115/2 cores

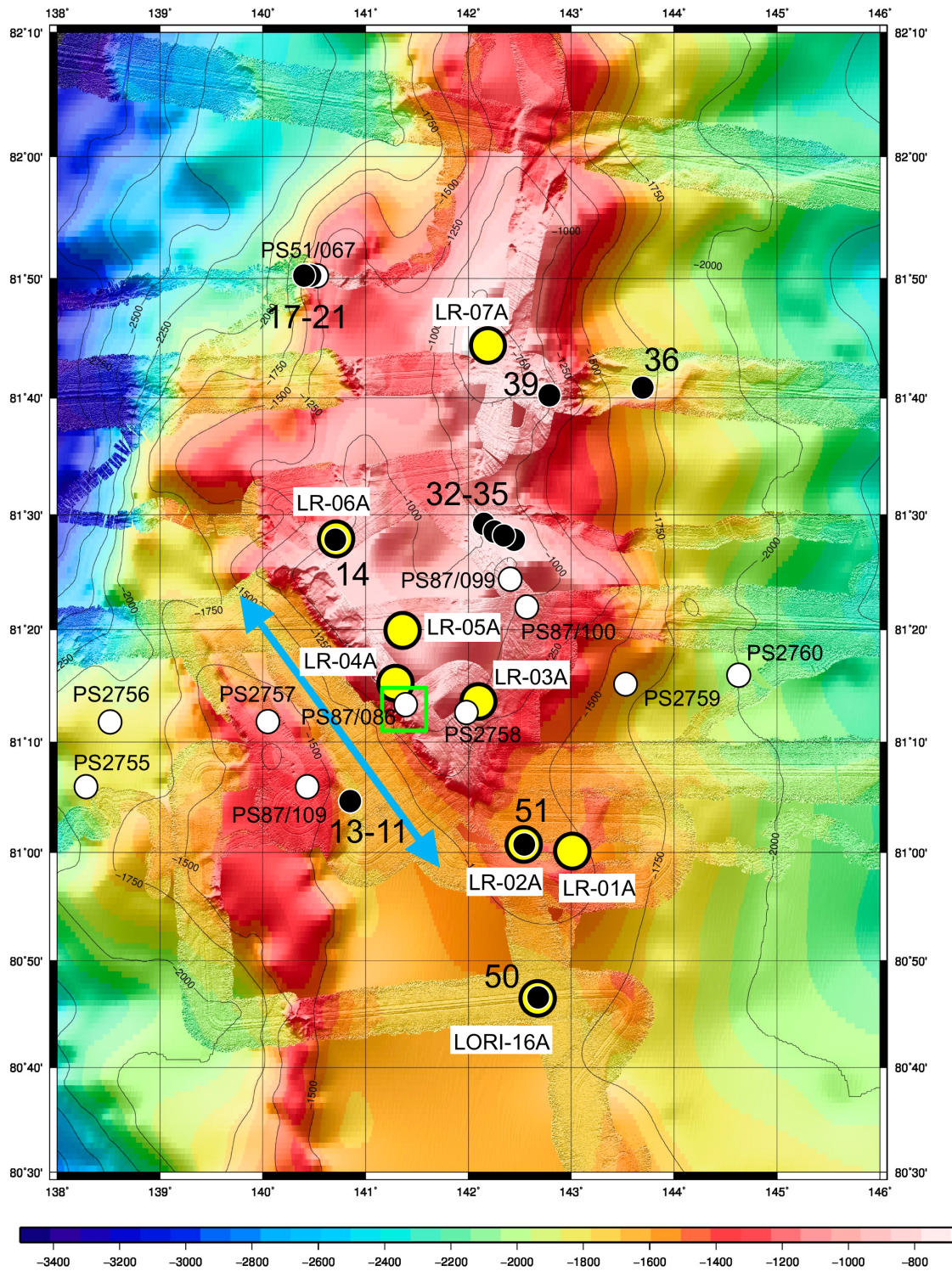


Fig. 7.5.2: Map of southern Lomonosov Ridge showing locations of Polarstern expeditions 1995, 1998, and 2014 (white circles) and expedition PS115/2 (black circles) as well as the proposed locations for potential future IODP drill sites (yellow circles). Blue arrow highlights NW-SE striking channel in the southernmost part of Lomonosov Ridge as bypass area for water mass exchange between the Amundsen Basin and the Makarov Basin. Numbers 11, 12, etc. represent PS115/2_11, PS115/2_12, etc.. Within the green box, 16 gravity cores were taken during Polarstern expedition PS87 in 2014, including cores PS87/070-1, PS87/079-1, PS87/86-3, PS87/093-1 and PS87/094-1 (Stein, 2015). For lithologies of these cores see Fig. 7.5.3.

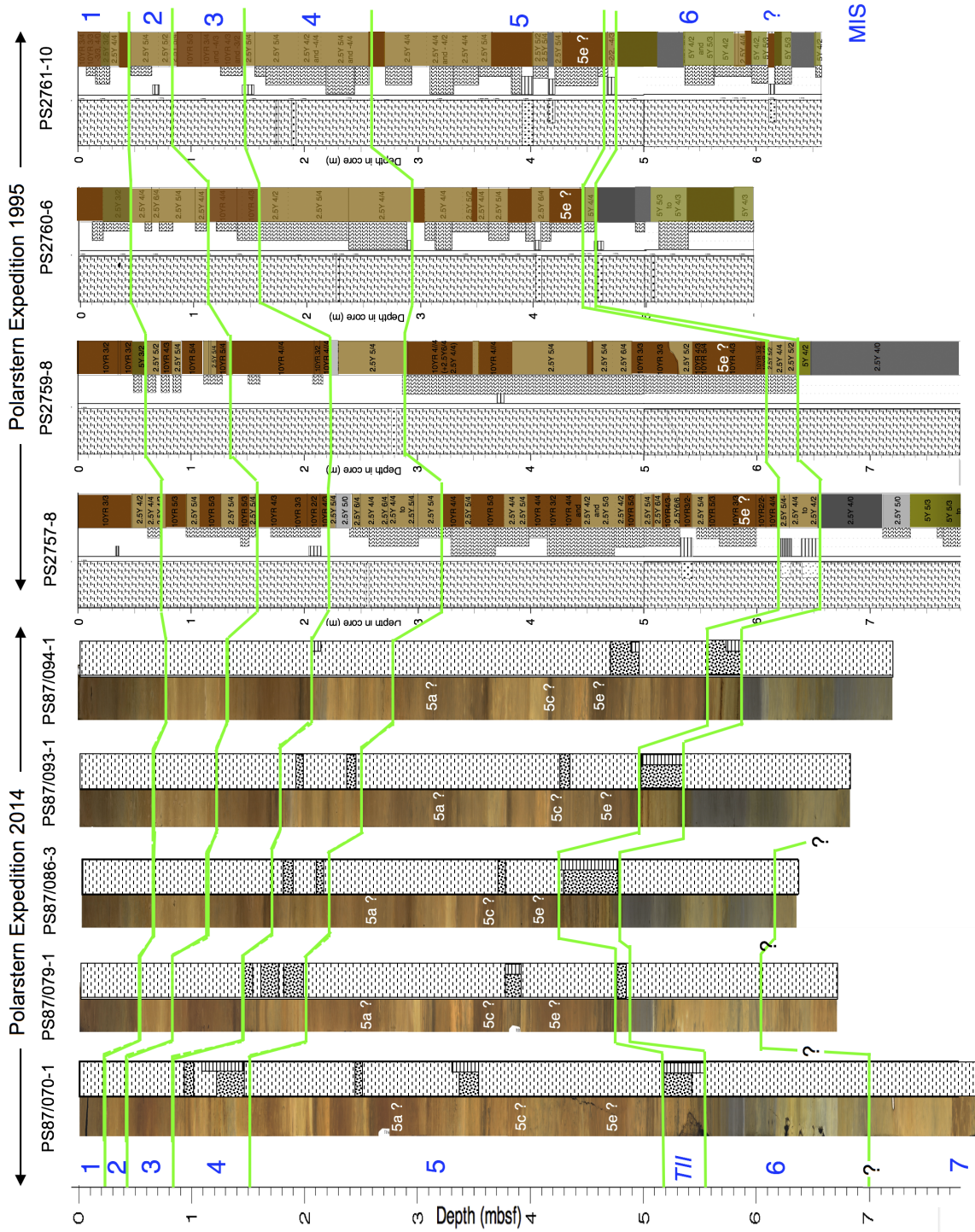


Fig. 7.5.3: Main lithologies (brown to dark brown, beige and gray silty clay horizons; sandy intervals) of sediment cores recovered during Polarstern expeditions 1995 (Rachor, 1991) and 2014 (Stein, 2015) on the „Siberian side“ of Lomonosov Ridge. Proposed preliminary chronology (Marine Isotope Stages - MIS - in blue numbers; 5a, 5c, 5d in white numbers) are shown (according to Stein et al., 1997, 2015a, 2016). For locations of the cores see Figs. 7.5.1 and 7.5.2.

During expedition PS87 in 2014, further sediment cores were recovered from southern Lomonosov Ridge that can be correlated very well with the 1995 sediment cores based on the main lithologies (Fig. 7.5.3; Stein et al., 2015a, 2016). Main characteristics in grain size, structure and sediment colour were identified and allowed to transfer the age model of the 1995 cores to those recovered during expedition PS87. The stratigraphic framework shown in Fig. 7.5.3 is still valid.

Work at sea

During the *Polarstern* expedition PS115/2, a total of 35 long sediment cores were taken, most of them on Lomonosov Ridge (Fig. 7.1.1 and Table 7.1.1). The whole-round sections of all the cores were already logged by means of the MSCCL, and 20 of the gravity cores were opened and the archive halves were logged with the point sensor (see Chapter 7.3). The different working steps carried out on the opened sediment cores recovered during expedition PS115/2 are outlined in detail in Chapter 7.1. For a selected set of cores, the sediment composition was determined based on smear-slide and coarse-fraction analyses (see Chapter 7.4). Furthermore, main lithologies of recovered sediments and sedimentary rocks were described, and some preliminary interpretations are presented. We concentrate on two main aspects:

- (1) to establish a lithostratigraphic concept and preliminary age model of selected key cores (especially from locations of potential future IODP sites) and
- (2) to identify and characterize old (“pre-Quaternary”) sediments that might crop out in the PS115/2 working area.

Preliminary results

Lithostratigraphy and sedimentation rates on southern Lomonosov Ridge

Kastenlot cores PS115/2_14-3 and PS115/2_51-3 were recovered from southern Lomonosov Ridge at the locations of proposed IODP sites LR-06A and LR-02A, respectively (Fig. 7.5.2). The main lithologies of both cores are in general quite similar to those of neighbourhood cores recovered during *Polarstern* expeditions in 1995 and 2014, representing marine isotope stages (MIS) 6 to 1 (Figs. 7.5.4 and 7.5.5; Stein, 2015; Stein et al., 2015a, 2016). The sediments of MIS 6 consists of very dark gray (sandy) and olive gray silty clay, separated by more coarse-grained, partly laminated sediments (correlating with Termination II; TII) from the overlying MIS 5 sediments. The latter are characterized by dominantly dark brown and beige silty clay. The warm interstadials MIS5e, 5c and 5e are represented by prominent dark brown intervals. The sediments of MIS 4 consist of mainly beige silty clay and more coarse-grained sandy intervals. The upper part of the sediment sequences representing MIS 3 to 1, are composed of dark brown, brown and beige silty clay. In both cores, foraminifers were only found in the uppermost part (MIS 1) of the records (Figs. 7.5.4 and 7.5.5; more details in Chapter 7.4, Figs. 7.4.5 and 7.4.6). The core correlation based on main lithologies is clearly supported by the MSCCL data as shown for the wet bulk density and magnetic susceptibility records of Core PS115/2_14-3 (Figs. 7.5.5).

7. PS115/2 Marine Geology: Reconstruction of Past Climatic Conditions

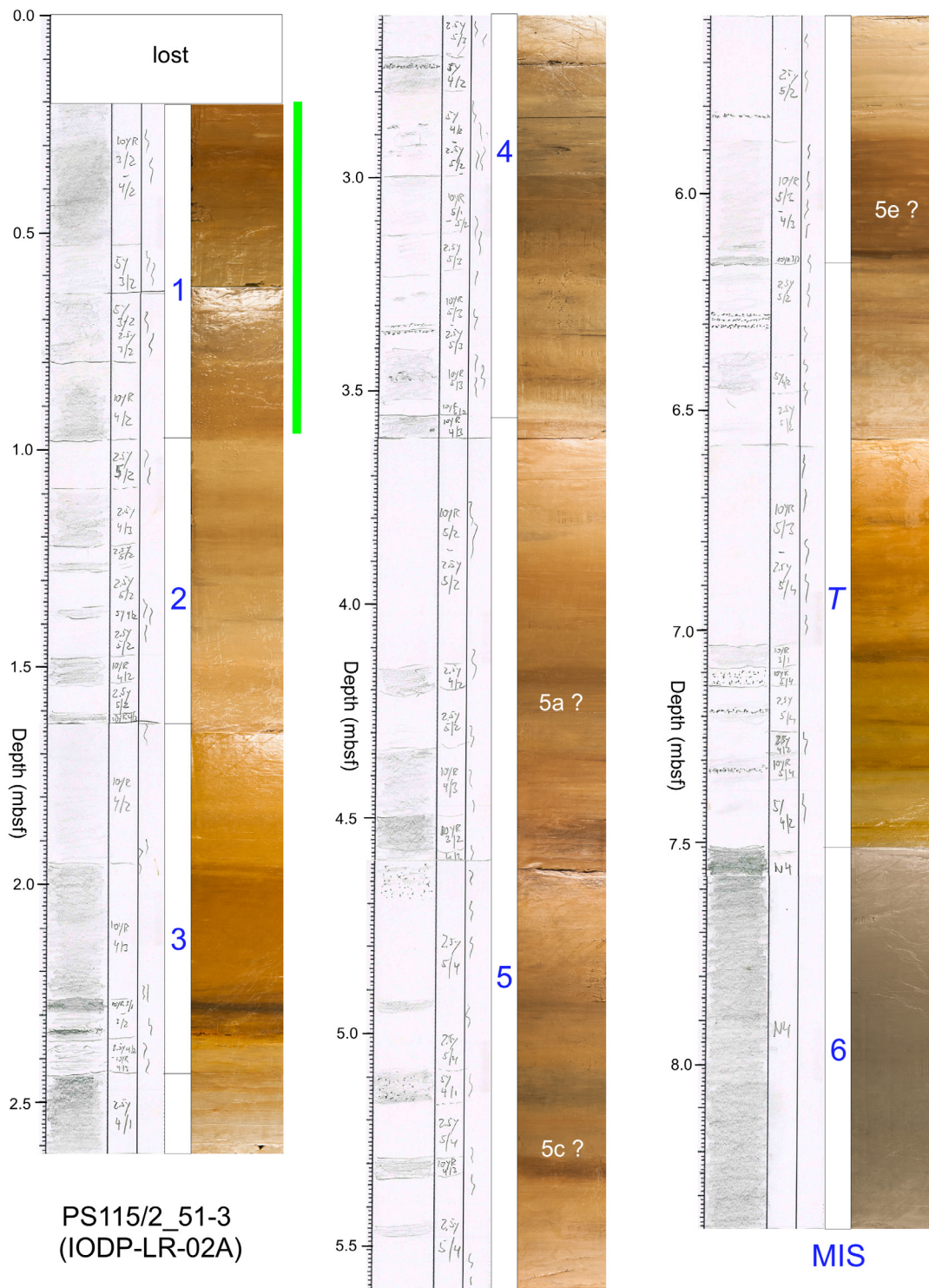


Fig. 7.5.4: Composite photograph and main lithologies of kastenlot Core PS115/2_51-3 (recovered at the location of the proposed IODP Site LR-02A; for location see Fig. 7.5.2). Green bar indicates occurrence of foraminifers (see Chapter 7.4). The tentative age model is based on correlation with Core PS115/2_14-3 (see Fig. 7.5.5). Note: the very light (white) intervals at about 0.65, 1.65, 2.65, 3.65, 4.65, 6.6 and 7.5 m are an artifact and related to light reflection at the core section boundaries.

7.5 Sediment characteristics and lithostratigraphy of some PS115/2 cores

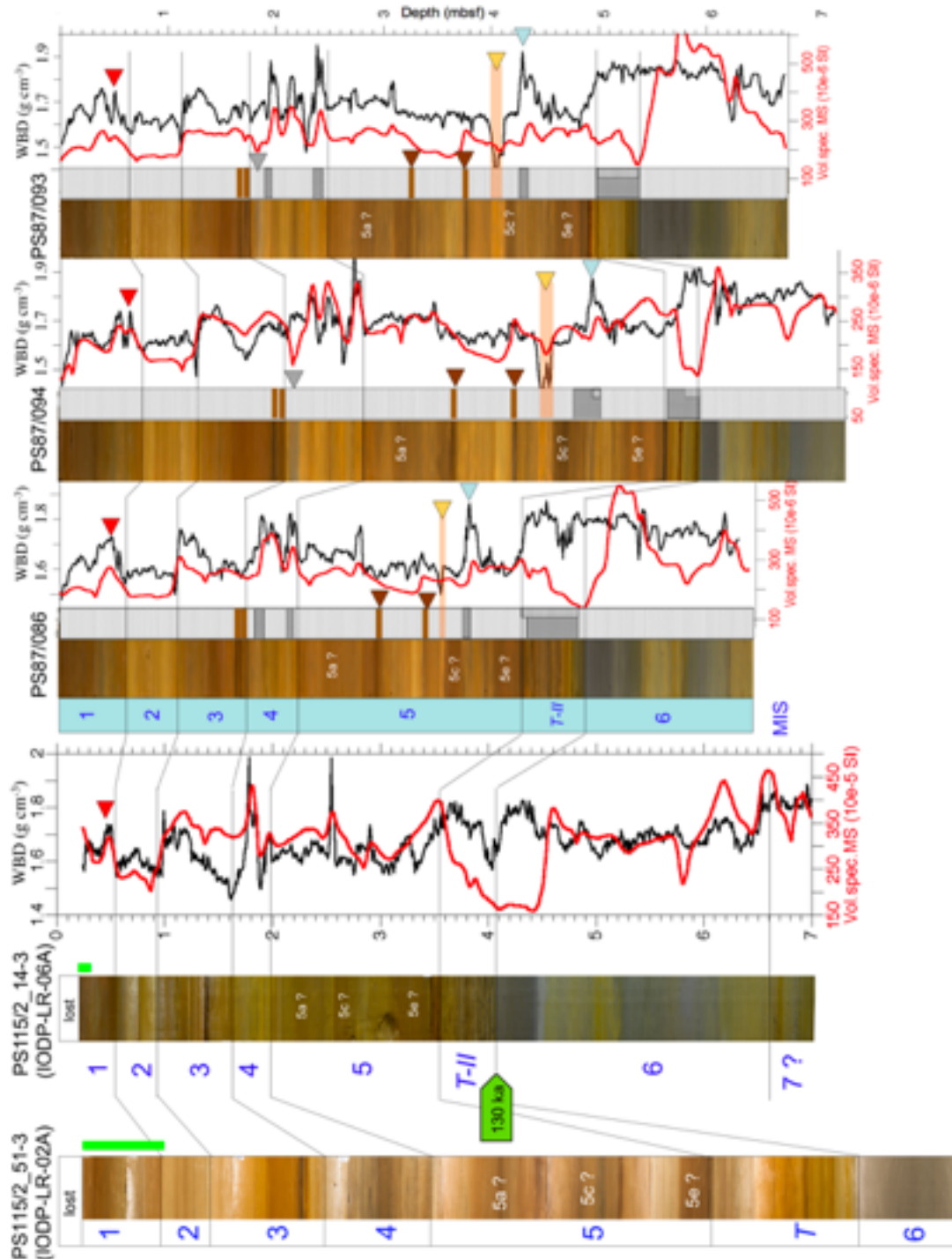


Fig. 7.5.5: Composite photograph of the sections of kastenlot Core PS115/2_14-3 (recovered at the location of the proposed IODP Site LR-06A; for location see Fig. 7.5.2) and wet bulk density (WBD) and magnetic susceptibility (MS) records obtained by means of the Multi-Sensor Core Logger (MSCL). These records are compared with corresponding records from dated sediment cores PS87/086-3, PS87/093-1 and PS87/094-1 (Stein et al., 2016). This allows the development of a preliminary age model of Core PS115/2_14-3 probably representing top MIS 7 to MIS 1. In addition, this age model is transferred to Core PS115/2_51-3 (for lithology see Fig. 7.5.4), recovered from the same location as the proposed IODP Site LR-02A. Green bar indicates occurrence of foraminifers (see Chapter 7.4).

Based on our age model, mean linear sedimentation rates (LSR) of the MIS 5 to MIS 1 time interval (i.e., the last 130 ka) on southern Lomonosov Ridge (81°05'N - 83°50'N) are quite high and vary between 3 and 5 cm ky⁻¹ (Table 7.5.1). Towards the north, the LSR decreases (Core PS2185-6: 1.9 cm ky⁻¹) whereas towards the south, i.e., the Laptev Sea continental margin, the LSR increases (Core PS115/2_51-3: 5.8 cm ky⁻¹) (Table 7.5.1; see Fig. 7.5.1 for core locations). The general decrease in sedimentation rates from the Eurasian continental margin along Lomonosov Ridge towards the North is most probably caused by the decrease in terrigenous sediment input from the Eurasian continent and the increase in sea-ice cover (cf., Stein et al., 2010). In general, however, the high LSRs on Lomonosov Ridge, i.e., an area underneath the influence of the Transpolar Drift system (Fig. 7.5.1), can be related to the higher sediment input from Eurasia, shorter transportation pathway, and less sea-ice concentration in comparison to the Amerasian Basin. There, lowest LSRs of about 0.5 cm ky⁻¹ or less occur on the ridges in the interior of the Amerasian Basin, caused by the combination of highest sea-ice concentration and long transportation pathway in the Beaufort Gyre circulation system (Polyak et al., 2009; Stein et al., 2010).

Tab. 7.5.1: Location, water depth, and thickness and mean linear sedimentation rates (LSR) of the MIS5-MIS1 interval of kastenlot (KAL) and gravity corer (SL) cores from the Lomonosov Ridge area

Core	Gear	Latitude	Longitude	WD	MIS6/5	LSR (MIS1-5)	Comments	Comments
				(m)	(cmbsf)	(cm/ky)		
PS2185-6	KAL	87° 32.2' N	144° 55.6' E	1052	250	1.9	Lomonosov Ridge (LR)	(northern part)
PS87/070-1	SL	83° 48.17' N	146° 7.01' E	1340	557	4.3	Lomonosov Ridge (LR)	
PS87/079-1	SL	83° 12.06' N	141° 22.77' E	1361	470	3.6	Lomonosov Ridge (LR)	
PS115/2_28-3	KAL	82° 50.406' N	142° 25.950' E	1236.8	372	2.9	Lomonosov Ridge (LR)	IODP LR-09A
PS115/2_14-3	KAL	81° 27.434' N	140° 43.737' E	777	428	3.3	Lomonosov Ridge (LR)	IODP LR-06A
PS115/2_02-2	KAL	81° 14.646' N	123° 29.036' E	3669	177	1.4	Amundsen Basin	
PS87/086-3	SL	81° 13.04' N	141° 23.02' E	901	485	3.7	Lomonosov Ridge (LR)	close to IODP LR-04A
PS87/094-1	SL	81° 12.57' N	141° 18.49' E	1168	592	4.6	Lomonosov Ridge (LR)	close to IODP LR-04A
PS87/093-1	SL	81° 12.48' N	141° 17.62' E	1216	538	4.1	Lomonosov Ridge (LR)	close to IODP LR-04A
PS87/088-1	SL	81° 12.31' N	141° 16.40' E	1378	446	3.4	Lomonosov Ridge (LR)	close to IODP LR-04A
PS87/087-1	SL	81° 12.29' N	141° 15.92' E	1408	478	3.8	Lomonosov Ridge (LR)	close to IODP LR-04A
PS2757-8	KAL	81° 09.8' N	140° 12.0' E	1230	655	5.0	Lomonosov Ridge (LR)	
PS2758-3	SL	81° 09.8' N	141° 51.3' E	937	375	2.9	Lomonosov Ridge (LR)	close to IODP LR-03A
PS2759-8	KAL	81° 13.6' N	143° 28.5' E	1667	640	4.9	Lomonosov Ridge (LR)	
PS2760-6	SL	81° 13.8' N	144° 48.8' E	2096	455	3.5	Lomonosov Ridge (LR)	
PS2761-10	SL	81° 11.5' N	150° 29.8' E	2640	478	3.7	Makarov Basin	
PS87/109-2	SL	81° 07.70' N	140° 34.99' E	1307	490	3.8	LR channel levée	(top of sediment drift)
PS115/2_11-3	SL	81° 05.273' N	140° 54.796' E	1696	448	3.4	LR channel levée	(lower flank)
PS115/2_12-1	SL	81° 05.114' N	140° 53.428' E	1701	313	2.4	LR channel levée	(lowermost flank)
PS115/2_13-2	SL	81° 04.931' N	140° 51.835' E	1706	89	0.7	LR channel, central part	Temporal erosion?
PS115/2_51-3	KAL	80° 57.898' N	142° 28.378' E	1438	750	5.8	Lomonosov Ridge (LR)	IODP LR-02A
PS115/2_50-1	SL	80° 46.610' N	142° 47.104' E	1745.9			Lomonosov Ridge (LR)	IODP LORI-16A

Current-induced sedimentation on southernmost Lomonosov Ridge

Whereas the LSRs are relatively high and do not vary significantly along the ridge crest between 81°05'N - 83°50'N, locally a distinct variability of the LSRs seems to be obvious in areas of strong bottom current influence. Such current-induced sedimentation typical for channel-levee complexes of contourite drifts was recorded in two of our PS115/2 PARASOUND profiles at the southern edge of Lomonosov Ridge (see Chapter 7.2, Figs. 7.2.5 and 7.2.11). Based on these PARASOUND profiles, a series of gravity cores were taken for detailed sedimentological studies in order to reconstruct paleoclimatic and paleoceanographic changes in the Arctic Ocean.

In the following, some first results from shipboard studies of three sediment cores (i.e., PS115/2_11-3, PS115/2_12-1 and PS115/2_13-2) recovered in the NW-SW striking channel that was cut into the southernmost part of Lomonosov Ridge (Fig. 7.5.2), will be presented. Here, the influence of bottom current activity is clearly obvious in the PARASOUND profile across the channel with reduced sedimentation in the central (main stream) part of the channel, but increasing towards the flank of the levee, i.e., towards the lower energy environment (Fig. 7.5.6). How this is reflected in the sedimentary sequences of the three cores?

Based on the MSCL records and the main lithologies, the three cores as well as Core PS87/109 which is located on top of a sediment drift structure on the western side of the same channel and representing the more pelagic, less current-influenced conditions (see Fig. 7.5.2 for location), can be correlated between each other but also correlated to other dated cores from southern Lomonosov Ridge (see above and Fig. 7.5.5). Thus, we propose that the sedimentary sequences represent the time interval from MIS 7 to MIS 1 (Fig. 7.5.6). When looking at the mean LSRs for the MIS 5 to MIS 1 time interval (Tables 7.5.1 and 7.5.2), the LSRs reflect the same general pattern as shown in the PARASOUND profile, i.e. reduced sedimentation in the center (Core PS115/2_13: 0.7 cm ky⁻¹) and increased sedimentation towards the flank of the channel (Core PS115/2_12: 2.3 cm ky⁻¹; Core PS115/2_11: 3.4 cm ky⁻¹). At Core PS87/109, the LSR is even 3.8 cm ky⁻¹ (Table 7.5.1).

When looking at the lithologies and the stratigraphic framework of the three cores in more detail, however, the picture becomes more complicated. At all three cores distinct differences in the grain size distribution throughout the sedimentary sequences are obvious. During the interglacials MIS 7 and MIS 5 (including Termination II), numerous prominent coarse-grained layers were found whereas the Glacial MIS 6 in between is characterized by the dominance of silty clay and the absence of coarser-grained layers. Furthermore, the general decrease in sedimentation towards the central part of the channel seems to be restricted to MIS 5 to MIS 1, but is not obvious for MIS 6 (Table 7.5.2). That means, the thickness of the MIS 6 interval and the related LSRs are higher at cores PS115/2_12-1 (thickness of 240 cm, LSR = 4.0 cm ky⁻¹) and PS115/2_13-2 (thickness of 195 cm, LSR = 3.3 cm ky⁻¹), but significantly lower at cores PS115/2_11-3 and PS87/109-2 towards the upper flank and top of the sediment drifts, respectively (i.e., thickness of 120 cm, LSR = 2.0 cm ky⁻¹ and thickness of 100 cm, LSR = 1.7 cm ky⁻¹, respectively) (Table 7.5.2; Fig. 7.5.6).

These data suggest increased accumulation of fine-grained material in the central deeper part of the channel due to the significantly reduced bottom current velocities during Glacial Stage MIS 6. During MIS 5 to MIS 1, on the other hand, bottom current velocities in this channel-levee system were distinctly increased. The current velocities may have reached a high level that even erosion might have been possible in the central part of the channel. This is assumed from the sedimentary sequence of Core PS115/2_13-2 where probably the entire late MIS 5 to MIS 2 interval is missing (Table 7.5.2; Fig. 7.5.6).

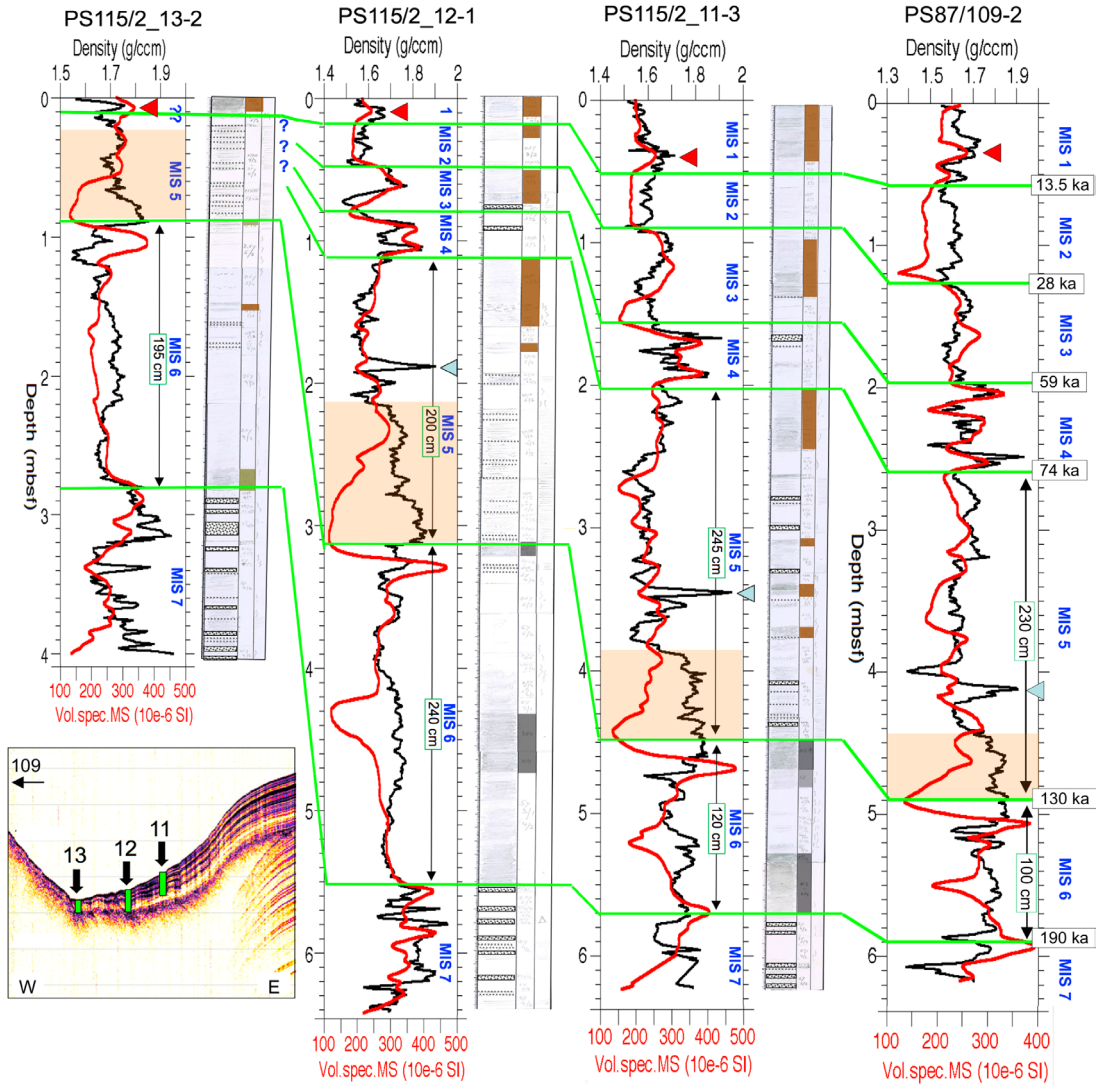


Fig. 7.5.6: MSCL records (i.e., wet bulk density and magnetic susceptibility) and lithological columns of cores PS115/2_11-3, PS115/2_12-1, and PS115/2_13-2 recovered from the SW edge of Lomonosov Ridge (for locations of cores see Fig. 7.5.2). Coarser-grained horizons/layers are indicated as dotted intervals/lines. In addition, MSCL records from Core PS87/109-2 are shown. In the left lower corner a PARASOUND profile with the locations of the three cores within the channel-levee system is shown (cf., Chapter 7.2, Fig. 7.2.5). A preliminary age model with isotope stages MIS 7 to MIS 1, based on correlation of lithologies and MSCL data (see Fig. 7.5.5), is presented. Intervals marked by light orange background colour highlight lower MIS 5 including Termination II (cf., Fig. 7.5.5). Black numbers at the right are ages of MIS boundaries in ka = thousands years BP (cf., Lisiecki and Raymo 2005). The numbers surrounded by green rectangles are thicknesses (in centimetres) of the MIS 5 and MIS 6 intervals.

7.5 Sediment characteristics and lithostratigraphy of some PS115/2 cores

Tab. 7.5.2: Sedimentation rates for the MIS 6 to MIS 1 intervals from cores PS115/2_11-3, PS115/2_12-1, PS115/2_13-2, and PS87/109-2 recovered at the SW edge of Lomonosov Ridge (for locations of cores see Fig. 7.5.2; for basic data see Fig. 7.5.6).

Core	PS115/2_13-2	PS115/2_12-1	PS115/2_11-3	PS87/109-2
Latitude	81° 04.931' N	81° 05.114' N	81° 05.273' N	81° 07.70' N
Longitude	140° 51.835' E	140° 53.428' E	140° 54.796' E	140° 34.99' E
Water depth	1706	1701	1696	1307
Channel-levee complex	center (bottom)	lowermost flank	lower flank	top sed. drift
MIS 6				
Thickness (cm)	195	240	120	100
Duration (ky)	60	60	60	60
LSR (cm ky ⁻¹)	3.3	4.0	2.0	1.7
MIS 5				
Thickness (cm)	??	200	245	230
Duration (ky)	56	56	56	56
LSR (cm ky ⁻¹)	??	3.6	4.4	4.1
MIS 4				
Thickness (cm)	??	32	46	63
Duration (ky)	15	15	15	15
LSR (cm ky ⁻¹)	erosion ?	2.1	3.1	4.2
MIS 3				
Thickness (cm)	??	31	67	71
Duration (ky)	31	31	31	31
LSR (cm ky ⁻¹)	erosion ?	1.0	2.2	2.3
MIS 2				
Thickness (cm)	??	31	39	68
Duration (ky)	14.5	14.5	14.5	14.5
LSR (cm ky ⁻¹)	erosion ?	2.1	2.7	4.7
MIS 1				
Thickness (cm)	11 ?	19	51	58
Duration (ky)	13.5	13.5	13.5	13.5
LSR (cm ky ⁻¹)	0.8 ?	1.4	3.8	4.3
MIS 5 - MIS 1				
Thickness (cm)	89	313	448	490
Duration (ky)	130	130	130	130
Mean LSR (cm ky ⁻¹)	0.7	2.4	3.4	3.8

Based on these preliminary shipboard data we may speculate that these changes in bottom current velocities in water depths between about 1,300 and 1,700 m might be a measure for the water mass exchange between the Eurasian and Amerasian basins, triggered by the inflow of Atlantic Intermediate Water into the Arctic Ocean. This hypothesis, however, has to be approved by further detailed “multi-proxy research”. That means, some of the recovered sediment cores will be used for the development of a reliable chronological framework, for micropaleontological and geochemical studies, for detailed sedimentological studies, i.e., determinations of sediment facies, grain-size distribution (especially the sortable silt fraction), etc., in order to reconstruct the late Quaternary history of bottom current activity, water mass exchange between the Eurasian and Amerasian basins and the relationship to (global) climate change.

Lithostratigraphy of Core PS115/2_2-2: A 500 ka record of Arctic paleoclimate from the central Eurasian Basin?

During *Polarstern* expedition PS87, a Hydrosweep and PARASOUND survey was carried out crossing the Amundsen Basin from the eastern Gakkel Ridge flank to the western Lomonosov Ridge flank (for location of profile see Fig. 7.1.1). In the PARASOUND profile, distinct topographic and sedimentary features are obvious such as prominent topographic highs (including the

seamount fully mapped and developed during this cruise), channel-levee complex, and debris flow (Fig. 7.5.7). In the area of the channel-levee complex at the eastern flank of the Gakkel ridge representing well-stratified pelagic sediments, a 7.6 m long kastenlot core (PS115/2_2-2) was recovered (Figs. 7.5.7 and 7.5.8; see also Chapter 7.2, Fig. 7.2.3).

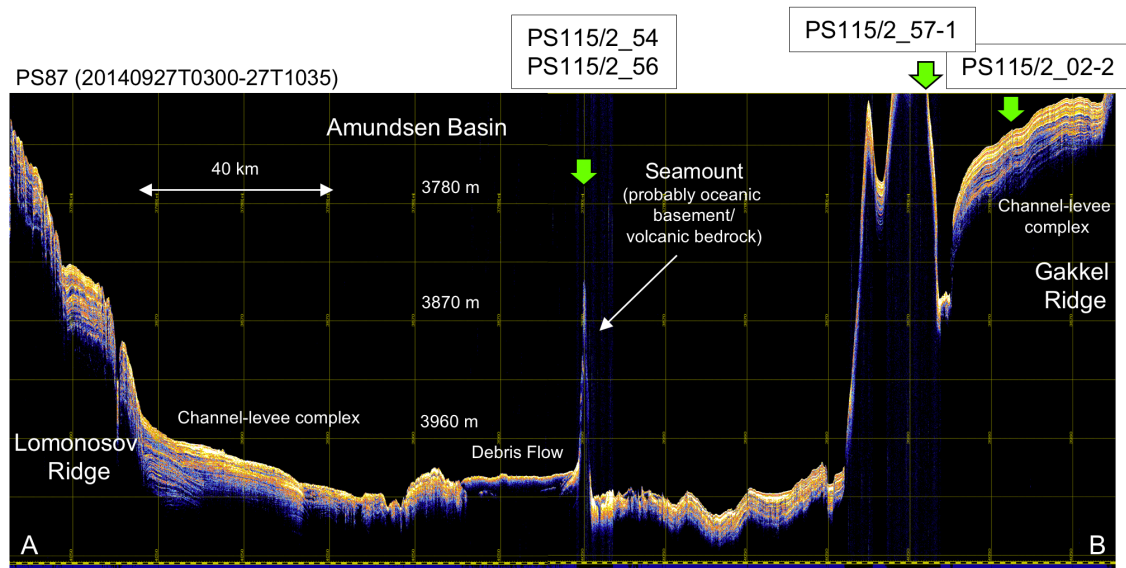


Fig. 7.5.7: PARASOUND profile across the Amundsen Basin from Lomonosov Ridge (A) to Gakkel Ridge (B), obtained during Polarstern expedition PS87 in 2014; for location of profile see Fig. 7.1.1.

The locations of coring stations PS115/2_02-2 and PS115/2_57-1 and the dredge runs on the discovered seamount (PS115/2_54 and PS115/2_56) as well as specific features of near-surface sediments are shown.

Core PS115/2_2-2 (see Figs. 7.1.1 and 7.5.1 for location) is characterized by three main lithologies (Fig. 7.5.8): (1) brown to dark brown (10YR 4/3 and 3/3) and light olive brown (2.5Y 5/4) and grayish brown (2.5Y 5/2), partly bioturbated silty clays, (2) alternations of thin silty clay/silt/sandy layers of grayish brown (2.5Y 5/2), dark grayish brown (2.5Y 3/2), olive gray (5Y 5/2) and gray (5Y 5/1) ("laminated sediments"), and (3) very dark gray (10YR 3/1) and dark gray (N3) silty clays. The brown sediments are restricted to depth intervals between 6.2-6.0 m and the upper 1.3 m of the core. The dark gray sediments that may reach thicknesses of about 20 to 70 cm, are mostly overlain by 20 to 50 cm thick sequences of laminated clayey to sandy sediments. A prominent pinkish horizons of silty clay with sand occurs at 5.56 to 5.62 m core depth (Figs. 7.5.8 and 7.5.9).

7.5 Sediment characteristics and lithostratigraphy of some PS115/2 cores

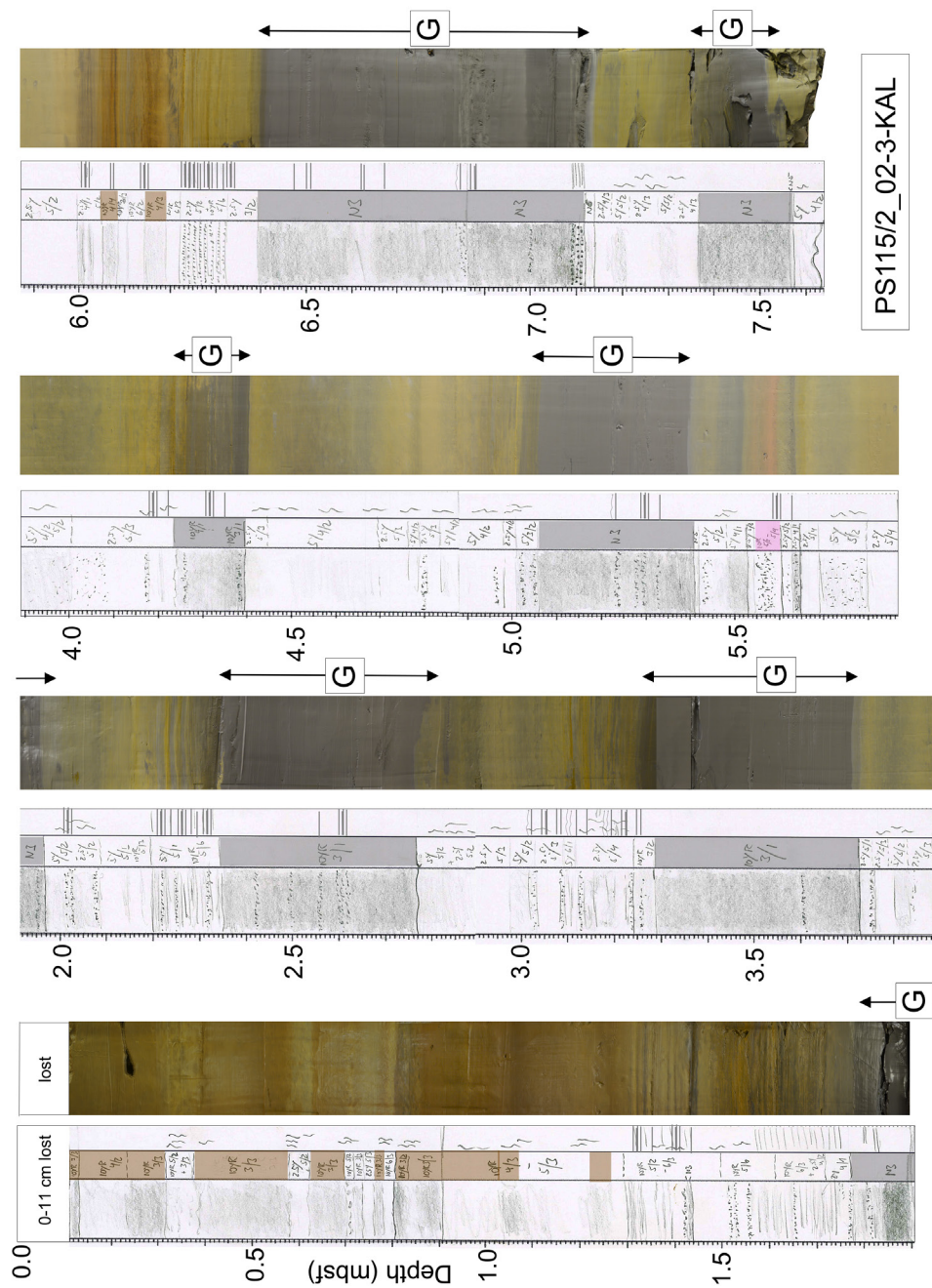


Fig. 7.5.8: Composite photograph and lithologies of kastenlot Core PS115/2_02-2 (recovered in the Amundsen Basin; for location see Fig. 7.1.1). The sediments are characterized by prominent differences in colors with predominantly (dark) brown, light olive brown, dark gray colors (Color codes from Munsell Soil Color Charts 1975), laminated intervals and coarser grained layers. The dark gray intervals ("G") probably represent cold (glacial) stages.

Based on the lithostratigraphic framework as well as the MSCL data from numerous cores from our study area (cf., Figs. 7.5.3 to 7.5.6) we suggest that the uppermost dark gray interval between about 1.8 and 2.0 m represents the top of MIS 6, the following laminated interval between about 1.3 and 1.8 m represents Termination II, and the brownish sediments of the upper 1.3 m represent MIS 5 to MIS 1. Below 2 m core depth, several very prominent dark gray intervals occur, alternating with more grayish brown to olive brown, partly laminated sequences (Fig. 7.5.8). Assuming that these dark gray intervals (“G”) also document cold (glacial) stages, the sediment cycles as well as the MSCL cycles of Core PS115/2_2-2 were correlated with the global benthic isotope stack (Lisiecki and Raymo 2005) (Fig. 7.5.10). Based on this correlation and the obtained preliminary age model, the entire sequence of Core PS115/2_02-2 may represent MIS 12 to MIS 1. Then, the deeper brownish sediments restricted to a short interval near 6 m core depth (i.e., sediments similar to those between 1.3 and 0.8 m core depth and correlated with Interglacial MIS 5) may coincide with the prominent Interglacial MIS 11 (Figs. 7.5.9 and 7.5.10). The mean LSR for the entire interval of MIS 12 to MIS 1 (i.e., the last about 500 ka) would be about 1.4 cm ky⁻¹ (Table 7.5.1). Of course, this age model is quite tentative and has to be approved by future studies.

Selected lithologies of Core PS115/2_02-2

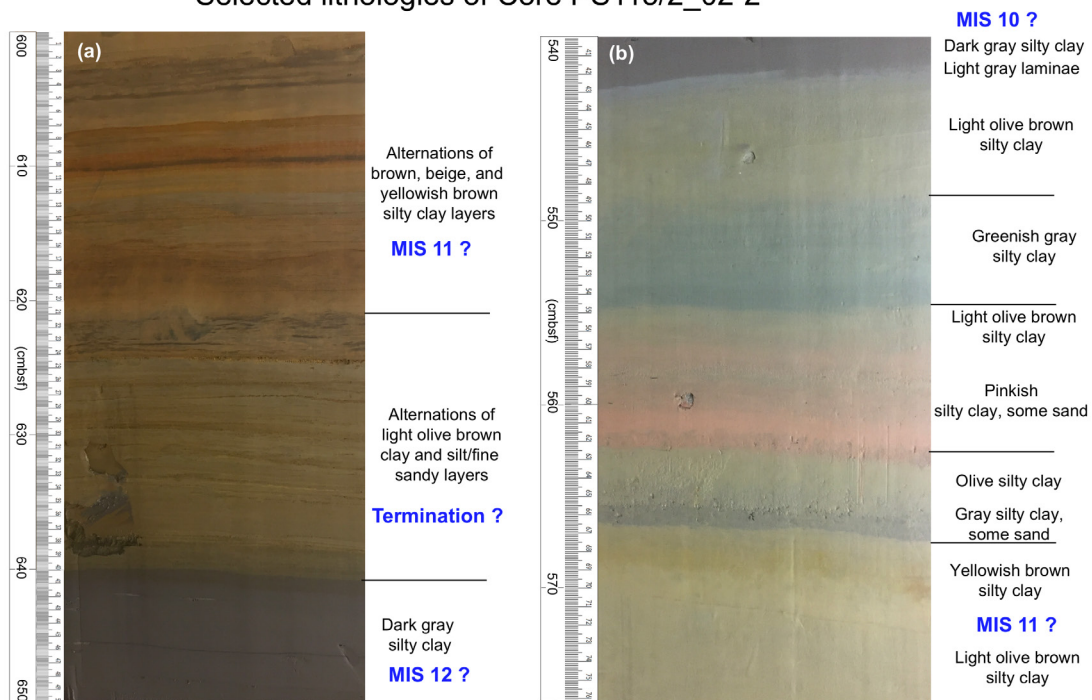


Fig. 7.5.9: Photographs and description of two selected intervals of kastenlot Core PS115/2_02-3 characterized by distinct changes in lithologies; for whole core record see Fig. 7.5.8. (a) Interval MIS 12- to MIS 11; (b) Interval MIS 11 to MIS 10.

If this still very preliminary chronostratigraphy is correct, however, the undisturbed well-preserved sedimentary sequence of Core PS115/2_2-2 can be used for detailed multi-proxy work on reconstruction of the paleoclimatic and paleoenvironmental history of the Arctic Ocean throughout the last about 500 ka, i.e., over five complete glacial-interglacial cycles. As Core PS115/2_2-2 was recovered by kastenlot coring, several complete subcores are available for these studies. This allows large-volume sampling for micropaleontological studies, U-channel

7.5 Sediment characteristics and lithostratigraphy of some PS115/2 cores

sampling for paleomag studies, etc.. Furthermore, a complete large-volume subcore was deep-frozen and is available for detailed biogeochemical studies (including specific biomarkers, DNA, etc.).

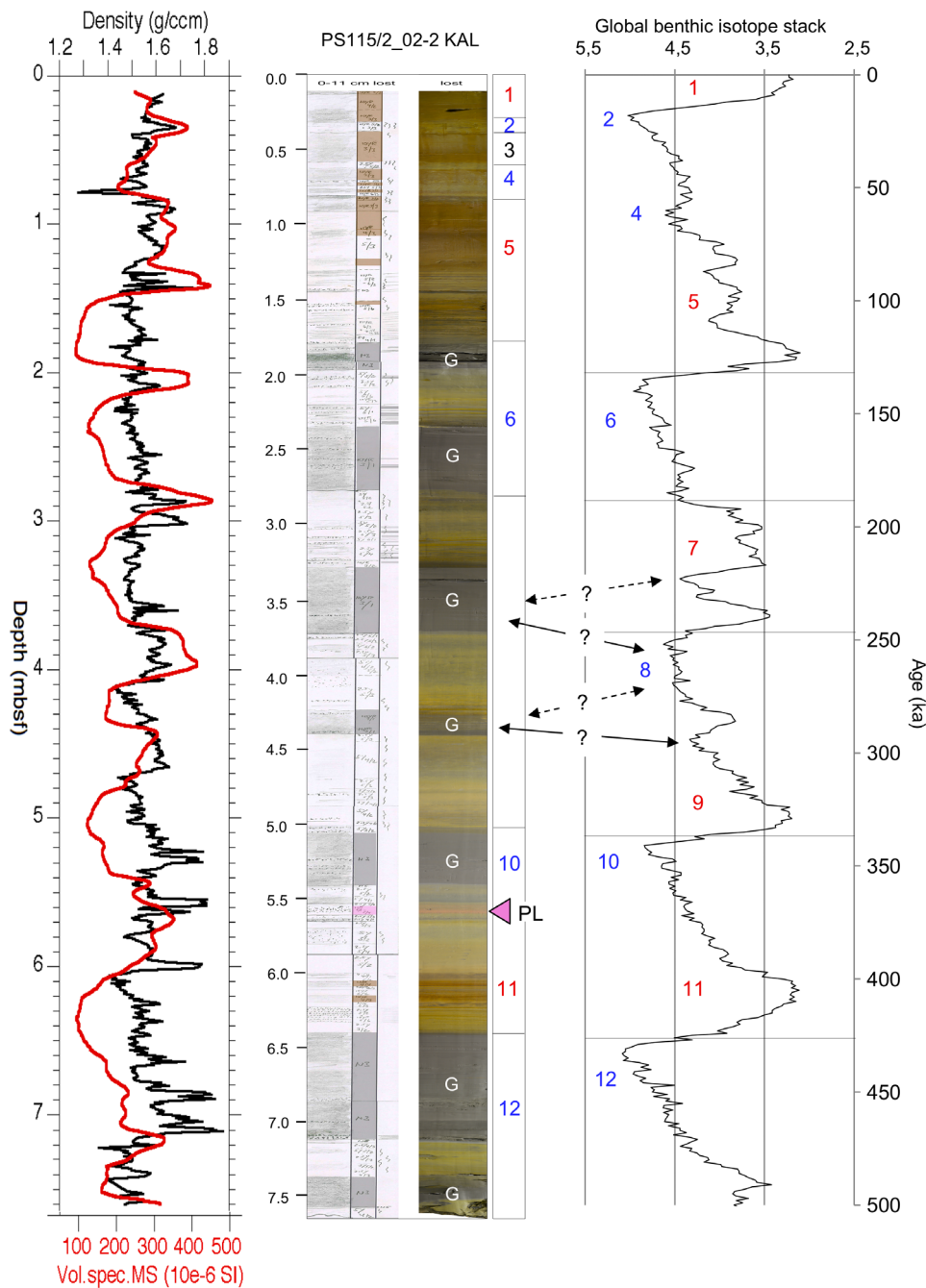


Fig. 7.5.10: Composite photograph, lithologies and MSCL (wet bulk density and magnetic susceptibility) records of kastenlot Core PS115/2_02-3. Assuming that the dark gray intervals ("G") represent cold (glacial) stages, the kastenlot sequence was correlated with the global benthic isotope stack (Lisiecki and Raymo 2005). Based on this correlation and obtained preliminary age model, Core PS115/2_02-3 probably represents MIS 12 to MIS 1. PL = prominent pink layer (see Fig. 7.5.9b).

Old sediments (1) – Coring across a slide-scar area at western Lomonosov Ridge

One of the first-order programs of expedition PS115/2 was to identify areas where pre-Quaternary sediments are cropping out. Several of such areas have already been identified by a PARASOUND profiling survey during earlier expeditions in 1998 and 2014. Some of these areas such as the slide scar area visited during expedition PS51 (Jokat 1999), were revisited during expedition PS115/2 for a detailed coring program (Fig. 7.5.11; cf., Chapter 7.2, Table 7.2.3).

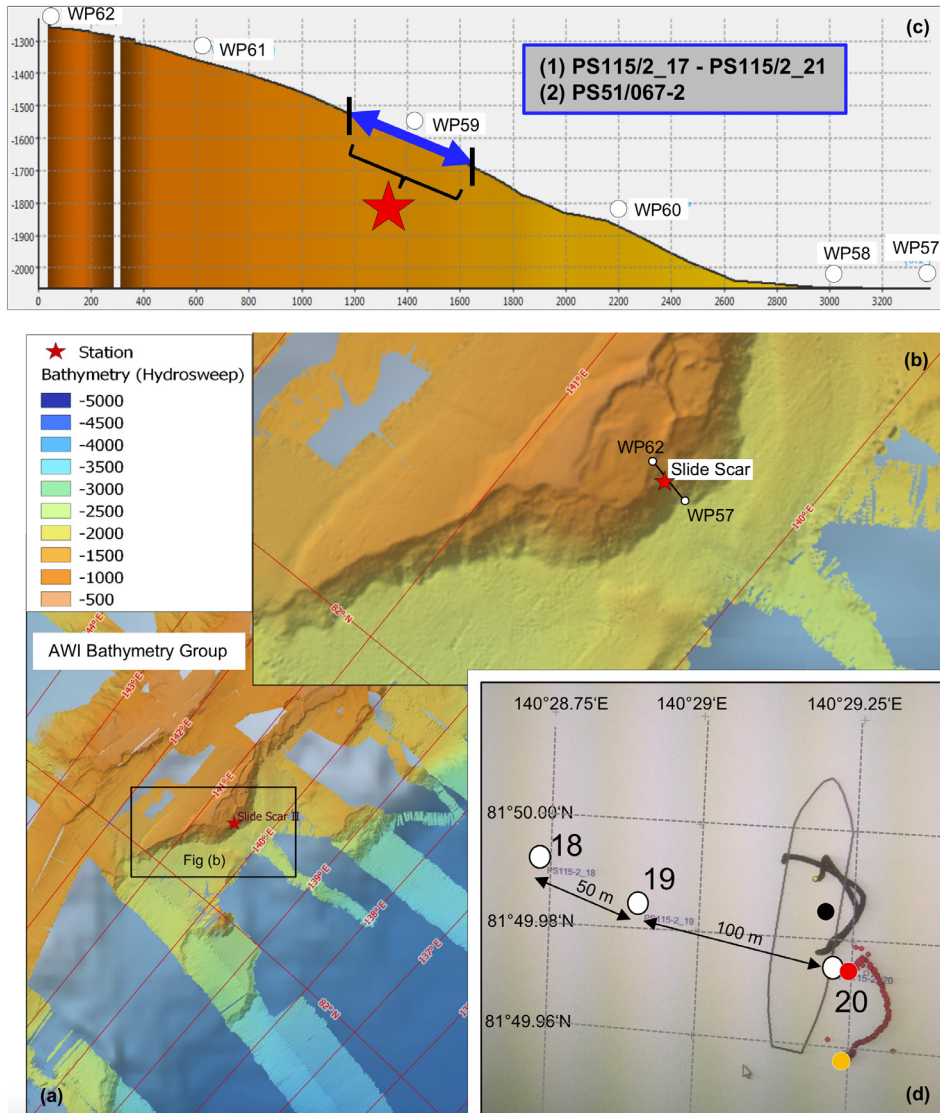


Fig. 7.5.11: Hydrosweep bathymetry map of the slide scar area on Lomonosov Ridge near 81°50'N/140°30'E (cf., Chapter 5, Fig. 5.3; map by courtesy of M. Steffen and S. Andree, AWI Bathymetry). Bathymetry profile between Waypoint (WP) 57 and 62. Blue arrow indicate depth range of cores PS115/2_17 to PS115/2_21 recovered from the steepest slope of the slide scar. The red star in (a) to (c) represents the location of the four cores (for location of the single cores see Table 7.1.1) as well as Core PS51/067-2 recovered from the same location during Polarstern expedition PS51 in 1998. (d) Screen shot of "Posidonia" navigation monitor with selected (= given) locations of cores PS115/2_18, PS115/2_19 and PS115/2_20 (white circles); for further explanation see text.

Before starting the coring activity, an additional Hydrosweep and PARASOUND survey was carried out, and the slide scar area on Lomonosov Ridge near 81°50'N/140°30'E was mapped in more detail to identify the steepest slope (cf., Chapter 5, Fig. 5.3). Based on this survey the slope between about 1,500 and 1,700 m of water depth was selected for coring (Fig. 7.5.11a to 11c). As the coring stations at this steep slope of Lomonosov Ridge are located very close to each other (i.e., about one ship's length or even less!), a precise navigation and the use of a special acoustic pinger system ("Posidonia") was needed to locate the ship and the gravity corer exactly on the spot (Fig. 7.5.11d).

For cores PS115/2_18, PS115/2_19 and PS115/2_20, the distance between the coring stations is only about 50 m and 100 m, respectively (Fig. 7.5.11d). In this figure, the monitoring of the lowering of the gravity corer at station PS115/2_20 is shown, i.e., red and black small circles monitor the exact position of the gravity corer and the ship, respectively. The large red and black circles mark the position of the gravity corer and the ship, respectively, at time when the gravity corer is on ground, i.e., penetrated into the seafloor. Note that the ship's position at time when the gravity corer is on ground, is always listed in the station lists (see Tables 7.1.1 and A4) which is, in our example, about 35 m off the real position of the gravity core PS115/2_20 (Fig. 7.5.11d, i.e., the distance between the large black and red circles). The distance between the large white circle (= given coring position) and the red large circle (= Posidonia pinger position when the gravity corer is on ground = real position) (Fig. 7.5.11d), on the other hand, is only a very few meters, indicating the exact positioning with the Posidonia system.

At all five coring stations (Fig. 7.5.11), a five-meter core barrel was used, and the corer was veered at high speed of 1.3 m/s into the ground. Nevertheless, the penetration depths for all runs was limited (Fig. 7.1.2). Furthermore, there are a few other "unusual" observations that may also point to older (pre-Quaternary), partly more lithified sediments almost cropping out at the seafloor:

- At location PS115/2_17, the core catcher became totally damaged when hitting a hard horizon at about 4 m core depth.
- At location PS115/2_18, there was almost no penetration (only 17 cm!), and the gravity corer toppled over. Below about 10 cm of dark brown, soft sediments with some large-sized dropstones, a light olive brown to dark brown more sandy and partly lithified horizon was hit. The coarse fraction of the core catcher sediment was composed of carbonate rocks (limestones) and common fragments of echinoderms, bryozoans, gastropods, corals, and brachiopods. Furthermore and most important, some of the fragments might be fragments of ammonites, suggesting a Cretaceous age.
- At location PS115/2_19, the gravity corer did not penetrate at all and toppled over, stiff mud and stones were found outside the core catcher.

Finally, at Core PS115/2_20, a distinct break in the sedimentary sequence is obvious at about 2.3 m core depth, represented by a more or less abrupt change in the wet bulk density (Fig. 7.5.12). This break may represent an unconformity, suggesting significantly (?) older, more consolidated sediments may have been recovered in the lowermost part of the sedimentary section. This break in sedimentation is also reflected in the lithology as well as physical property data at Core PS51/067-2 recovered from the same location during *Polarstern* expedition PS51 in 1998 and interpreted as major hiatus (Fig. 7.5.12; Stein et al., 1999). In his master thesis, Soltmann (2009) compared this record of Core PS51/067-2 with the ACEX drill core (Backman et al., 2006; Moran et al., 2006; for location of ACEX Site see Fig. 1.1) and proposed that the lowermost part of Core PS51/067-2 may be of late/middle Miocene age.

Certainly more work has to be done on the PS115/2 sediment cores to get a better chronology of the sedimentary records. If new data will approve that some of the PS115/2 sediment cores recovered on Lomonosov Ridge really represent older pre-Quaternary time intervals, however, this would give the unique chance to get information about the older (preglacial) climate history of the Arctic Ocean.

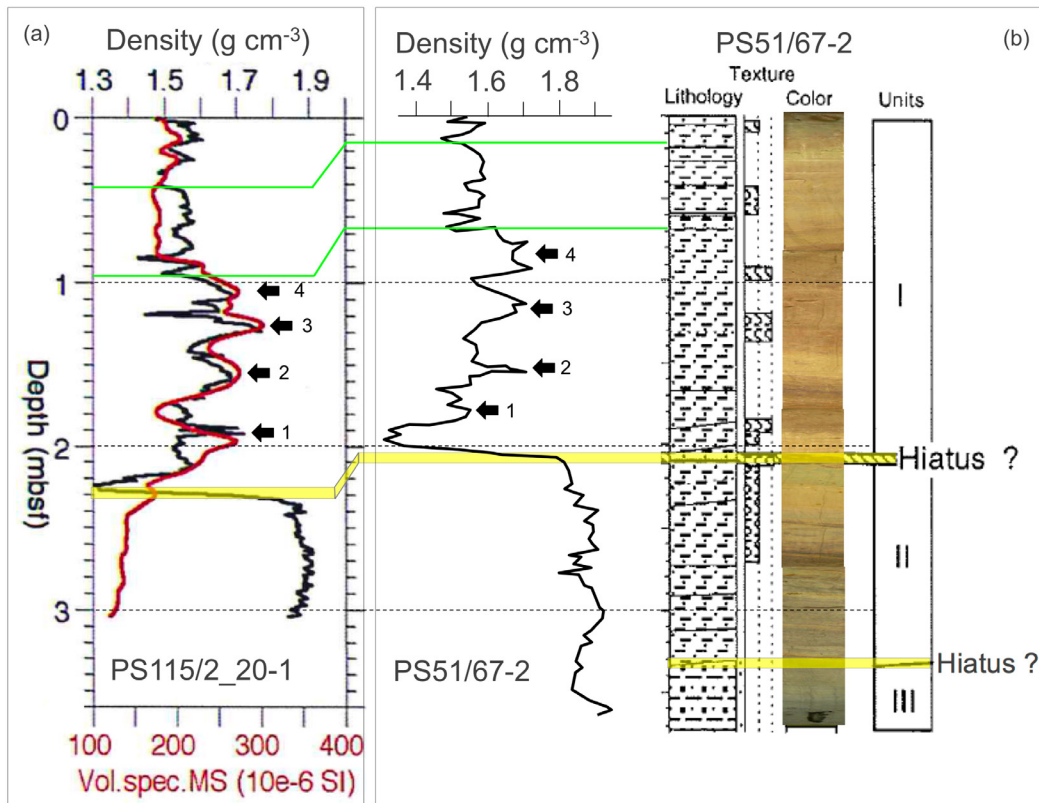


Fig. 7.5.12: Plot of wet bulk density and magnetic susceptibility of (a) Core PS115/2_20-1 (this expedition) and (b) wet bulk density, main lithology, and sediment colour of Core PS51/067 (from Stein et al., 1999). Position of proposed hiatuses are marked by yellow bars. Black arrows (1 – 4) highlight maxima in density. Both density records can be correlated perfectly.

Old sediments (2) – Dredging across a seamount in the southern Amundsen Basin

During expedition PS115/2, a 600 m high seamount was newly discovered in the central southern Amundsen Basin (Figs. 5.5, 7.1.1, and 7.5.13). Based on the new PS115/2 seismic data, this seamount has most probably a magmatic origin and magmatic rocks might crop out near the seafloor (see Chapter 6, Fig. 6.1.3a). In order to test this hypothesis and to sample such magmatic rocks, two dredge runs were carried out across the seamount (Fig. 7.5.13a).

The rocks dredged from the seamount unfortunately did not contain any magmatic/basaltic material, instead, they are more or less exclusively composed of sand-, silt- and clay-stones. Some of the stones show fresh cracks, suggesting that they were cut from the in-situ rock formation by the dredging process. A large number of stones are covered by manganese crusts and/or contain manganese concretions (Fig. 7.5.14a and 14c). Furthermore, a series of stones are composed of beige-colored partly laminated sandstones and laminated dark gray silt-/clay-stones (Fig. 7.5.15). In these stones, prominent features such as fining upwards, convolute bedding and load casts are obvious.

7.5 Sediment characteristics and lithostratigraphy of some PS115/2 cores

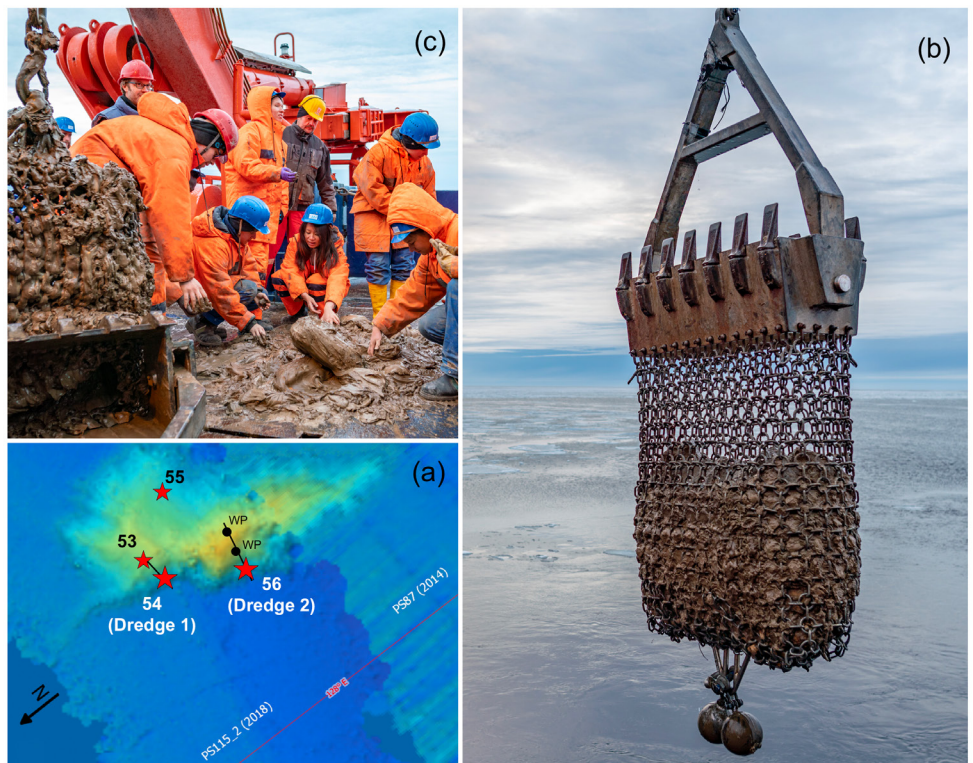


Fig. 7.5.13: (a) Location of dredge runs across the seamount (see also overview map, Fig. 7.1.1), (b) dredge hanging at the A-frame and filled with stones and mud (Dredge 1: PS115/2_54), and (c) Dredge 1 on deck, scientists are selecting the recovered stones.
Photos (b) and (c): C. Rohleder/DWD.

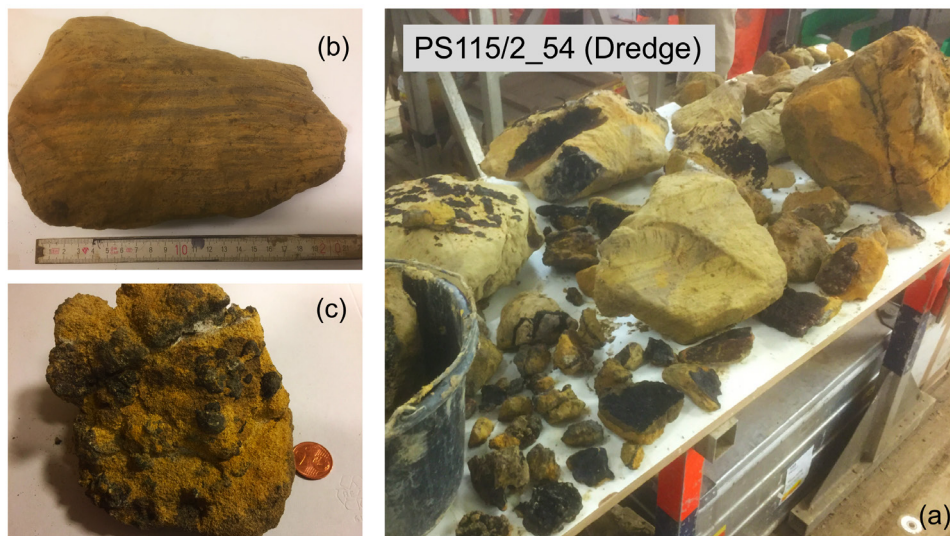


Fig. 7.5.14: (a) Collection of stones (sedimentary rocks) recovered during dredge run 1 (PS115/2_54). Numerous of these stones display black (manganese) coatings and crusts. (b) Some of the sand-/siltstones are laminated (see also Fig. 7.5.15). (c) Sandstone with manganese crusts and concretions.
Photos (a) - (c): R. Stein/AWI.

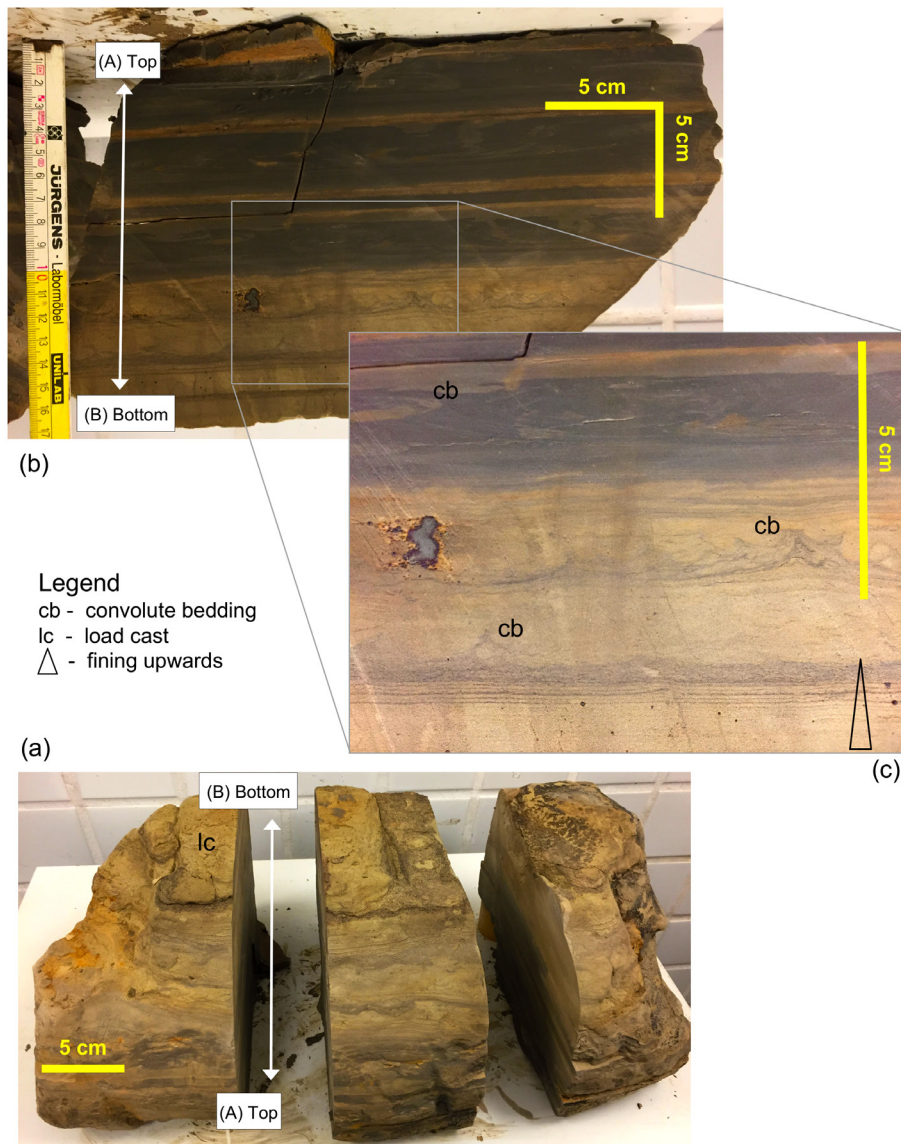


Fig. 7.5.15: Large-sized sedimentary rock (diameter of about 45 cm) recovered during dredge run 1 (PS115/2_54). (a) Rock has been cut into three parts using a stone saw. (b) and (c) The stone is composed of beige-colored partly laminated sandstones (lower part) and laminated dark gray silt/clay stones (upper part). Prominent features such as fining upwards, convolute bedding and load casts are obvious. Photos (a) - (c): R. Stein/AWI.

Looking at the seismic profile, these in-situ rocks are probably more or less directly overlying the oceanic (magmatic) basement (Fig. 6.1.3a). Thus, they may allow to get some information about the age of the basement and the tectonic evolution of the Eurasian Basin, for example, by dating based on the occurrence of specific microfossils (e.g., dinoflagellates). A first-order age information is already coming from the chronology based on magnetic anomalies e.g., (Berggren et al., 1995; Glebovsky et al., 2006; Doré et al., 2008). Taking the ages of the magnetic anomalies in the Eurasian Basin and the location of the dredge site PS115/2_54, the sedimentary rocks recovered from the seamount might have a mid-Eocene age (i.e., between Chron 24 and 20; Fig. 7.5.16). Furthermore, if old, these rocks may allow to carry out sedimentological and geochemical studies that will give some important insight into the early

7.5 Sediment characteristics and lithostratigraphy of some PS115/2 cores

Cenozoic climate and environmental history of the preglacial warm and ice-free Arctic Ocean (cf., work done on IODP ACEX sediments by Sluijs et al., 2006; Weller and Stein, 2009; Stein et al., 2014; for location of ACEX site see Fig. 7.5.16).

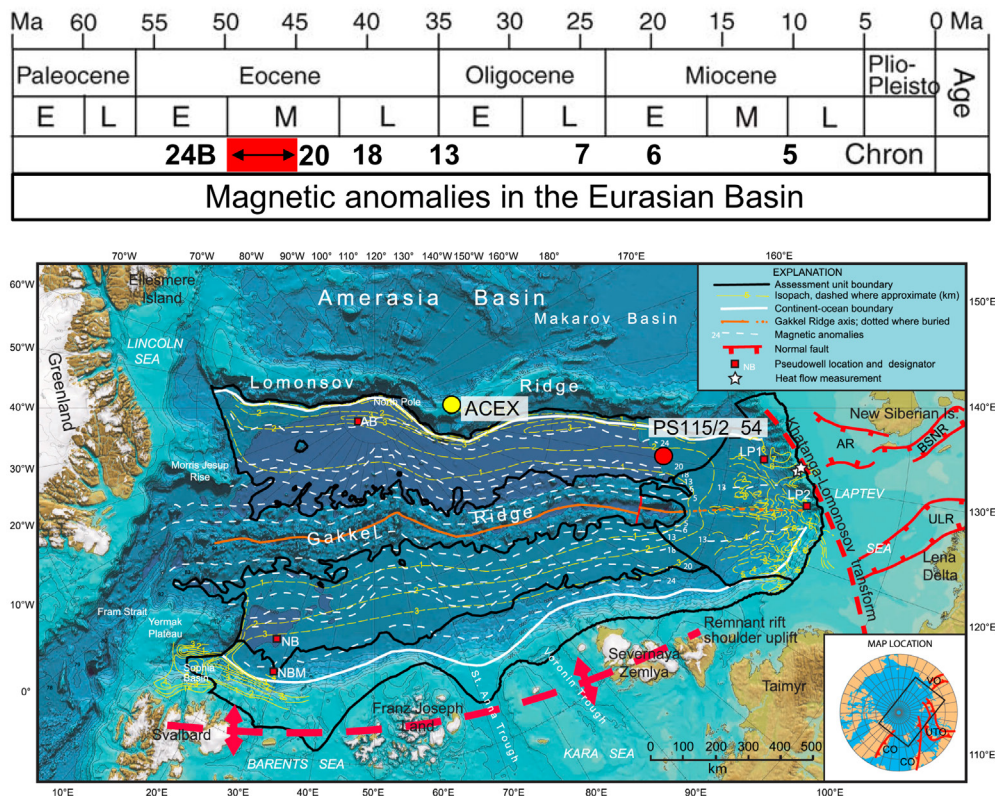


Fig. 7.5.16: Map showing major structural features of the Eurasia Basin (from Moore and Pitman, 2011; supplemented) and related ages of the magnetic chrons (Berggren et al., 1995; Glebovsky et al., 2006; Doré et al., 2008). Isopachs and continent–ocean boundaries from Grantz et al. (2011); magnetic isochrons from Glebovsky et al. (2006); selected faults and grabens from Drachev et al. (2003). Abbreviations: ULR, Ust Lena Rift; BSNR, Bel’kov-Svyatoi Nos Rift; AR, Anisin rift. Locations of the IODP-ACEX drill site on Lomonosov Ridge (yellow circle) and the location of the dredge site PS115/2_54 (red circle) are shown. In addition, locations of heat flow measurements on the Laptev Sea margin and pseudo-wells for burial history models are marked as white stars and red squares, respectively (not discussed here but in Moore and Pitman, 2011). For location of the seamount with Site PS115/2_54 where oceanic basement almost reaches the seafloor, see Figs. 7.1.1 and 7.5.7.

Data management

Raw data and processed data (shipboard and shorebased) will be made available in PANGAEA.

References

- Backman J, Moran K, McInroy DB, et al. (2006) Proceedings IODP, 302, College Station, Texas (Integrated Ocean Drilling Program Management International, Inc.). doi:10.2204/iodp.proc.302.104.2006.
- Berggren WA, Kent DV, Swisher CC, Aubry MP (1995) A revised Cenozoic geochronology and chronostratigraphy. *Geochronology Time Scales and Global Stratigraphic Correlation*. SEPM Special Publication No. 5-1, 129-212.

- Doré AG, Lundin ER, Kuszniir NJ, Pascal C (2008) Potential mechanisms for the genesis of Cenozoic domal structures on the NE Atlantic margin: pros, cons and some new ideas. In: Johnson H et al (Eds), *The Nature and Origin of Compression in Passive Margins*. Geological Society, London, Special Publications 306, 1–26; doi: 10.1144/SP306.1.
- Drachev SS, Kaul N, Beliaev VN (2003) Eurasia spreading basin to Laptev Shelf transition: structural pattern and heat flow. *Geophysical Journal International* 152, 688–698.
- Glebovsky VY, Kaminsky VD, Minakov AN, Merkur'ev SA, Childers VA, Brozena JM (2006) Formation of the Eurasia Basin in the Arctic Ocean as Inferred from Geohistorical Analysis of the Anomalous Magnetic Field. *Geotectonics*, 40/4, 263–281.
- Grantz A, Scott RA, Drachev SS, Moore TE, Valin ZC (2011) Sedimentary successions of the Arctic Region (58–64° to 90°N) that may be prospective for hydrocarbons. In: Spencer AM, Embry AF, Gautier DL, Stoupakova AV, Sørensen K (eds) *Arctic Petroleum Geology*, Geological Society London, Memoirs 35, pp 17–37.
- Jokat W (Ed.) (1999) Arctic '98: The Expedition ARK-XIV/1a of RV Polarstern in 1998, Rep. Pol. Mar. Res. 308, 159 pp.
- Jokat W (Ed.) (2009) Arctic '98: The Expedition of the Research Vessel Polarstern to the Arctic in 2008 (ARK-XXIII/3), Rep. Pol. Res. 597, 221 pp.
- Lisiecki LE, Raymo ME (2005) A Pliocene-Pleistocene stack of 57 globally distributed benthic $\delta^{18}O$ records. *Paleoceanography* 20, PA1003, doi:10.1029/2004PA001071.
- Moore TE, Pitman JK (2011) Geology and petroleum potential of the Eurasian Basin. In: Spencer AM, Embry AF, Gautier DL, Stoupakova AV, Sørensen K (eds) *Arctic Petroleum Geology*, Geological Society London, Memoirs 35, pp 731–750.
- Moran K, Backman J, Brinkhuis H, Clemens SC, Cronin T, Dickens GR, Eynaud F, Gattacceca J, Jakobsson M, Jordan RW, Kaminski M, King J, Koc N, Krylov A, Martinez N, Matthiessen J, McInroy D, Moore TC, Onodera J, O'Regan AM, Pälike H, Rea B, Rio D, Sakamoto T, Smith DC, Stein R, St. John K, Suto I, Suzuki N, Takahashi K, Watanabe M, Yamamoto M, Frank M, Jokat W, Kristoffersen Y (2006) The Cenozoic palaeoenvironment of the Arctic Ocean. *Nature* 441, 601-605.
- Niessen F, Nørgaard-Pedersen N, Musatov E (1997) Physical properties in marine sediments. In: Rachor E (Ed.), *Scientific cruise report of the Arctic Expedition ARK-XI/1 of RV „Polarstern“ in 1995*, Rep. Pol. Res. 226, pp. 133-143.
- Polyak L, Bischof J, Ortiz JD, Darby DA, Channell JET, Xuan C, Kaufman DS, Løvlie R, Schneider DA, Eberl DD, Adler R, Council EA (2009) Late Quaternary stratigraphy and sediment pattern in the western Arctic Ocean. *Global Planet. Change XREF*, doi:10.1016/j.gloplacha.2009.03.014.
- Rachor E (Ed.) (1997) *Scientific cruise report of the Arctic Expedition ARK-XI/1 of RV „Polarstern“ in 1995*. Rep. Pol. Res. 226, 157 pp.
- Sluijs A, Schouten S, Pagani M, Woltering M, Brinkhuis H, Damsté JSS, Dickens GR, Huber M, Reichert G-J, Stein R, Matthiessen J, Lourens LJ, Pedentchouk N, Backman J, Moran K and the Expedition 302 Scientists (2006) Subtropical Arctic Ocean temperatures during the Palaeocene/Eocene thermal maximum. *Nature* 441(7093), 610-613.
- Soltmann Y (2009) Lithostratigraphie von Sedimentabfolgen vom Lomonosov-Rücken: Signifikanz für Paläoumweltrekonstruktionen des spätquartären Arktischen Ozeans. Unpubl. Diplomarbeit, Universität Bremen, 103 pp.
- Stein R (Ed) (2015) The Expedition PS87 of the Research Vessel Polarstern to the Arctic Ocean in 2014, Reports on Polar and Marine Research 688, Bremerhaven, Alfred Wegener Institute for Polar and Marine Research 688, 273 pp (http://epic.awi.de/37728/1/BzPM_0688_2015.pdf).

7.5 Sediment characteristics and lithostratigraphy of some PS115/2 cores

- Stein R (2017) From Greenhouse to Icehouse: The late Mesozoic-Cenozoic Arctic Ocean sea-ice and climate history. *Polarforschung* 87, 61-78 ([hdl:10013/epic.52040](https://hdl.handle.net/10013/epic.52040))
- Stein R, Behrends M, Spielhagen RF (1997) Lithostratigraphy and sediment characteristics. In: Rachor E (Ed), Scientific cruise report of the Arctic Expedition ARK-XI/1 of RV „Polarstern“ in 1995, Rep. Pol. Res. 226, pp. 143-153.
- Stein R, Fahl K, Schreck M, Knorr G, Niessen F, Forwick M, Gebhardt C, Jensen L, Kaminski M, Kopf A, Matthiessen J, Jokat W, Lohmann G (2016) Evidence for ice-free summers in the late Miocene central Arctic Ocean. *Nature Communications* 7:11148, doi:10.1038/ncomms11148.
- Stein R, Forwick M, Niessen F (2015a) Lithostratigraphy and chronology of PS87 sediment cores, in: Stein R (Ed), The Expedition PS87 of the Research Vessel *Polarstern* to the Arctic Ocean in 2014, Rep. Pol. Mar. Res. 688, pp. 128-147.
- Stein R, Jokat W, Niessen F and Weigelt E (2015b) Exploring the long-term Cenozoic Arctic Ocean Climate History – A challenge within the International Ocean Discovery Program (IODP). *Arktos* 1, doi: 10.1007/s41063-015-012-x
- Stein R, Kukina N, Matthiessen J, Müller C, Nørgaard-Pedersen N, Usbeck R (1999) Lithostratigraphy of Alpha Ridge sediments cores., in: Jokat W (Ed.), Arctic'98: The Expedition ARKXIV/ 1a of RV Polarstern in 1998, Rep. Pol. Res. 308, pp. 60-75
- Stein R, Matthiessen J, Niessen F, Krylov R, Nam S, and Bazhenova E (2010) Towards a Better (Litho-) Stratigraphy and Reconstruction of Quaternary Paleoenvironment in the Amerasian Basin (Arctic Ocean). *Polarforschung* 79 (2), 97-121.
- Stein R, Weller P, Backman J, Brinkhuis H, Moran K, Pälike H (2014) Cenozoic Arctic Ocean Climate History: Some highlights from the IODP Arctic Coring Expedition (ACEX). In: Stein R, Blackman D, Inagaki F, Larsen HC (Eds.), *Earth and Life Processes Discovered from Subseafloor Environment - A Decade of Science Achieved by the Integrated Ocean Drilling Program (IODP), Series Developments in Marine Geology, Vol. 7*, Elsevier Amsterdam/New York, pp. 259-293.
- Weller P, Stein R (2008) Paleogene biomarker records from the central Arctic Ocean (IODP Expedition 302): Organic-carbon sources, anoxia, and sea-surface temperature *Paleoceanography* 23, PA1S17, doi:10.1029/2007PA001472.

8. THE “ARCTRAIN FLOATING UNIVERSITY”

Pascal Bourgault ¹ , Camille Brice ² ,	¹ McGill
Charles Brunette ¹ , Myriam Caron ³ ,	² UQAM
Amelie Desmarais ¹ , Rémi Lenny ⁴ ,	³ UQAR
Aliaksandra Kazlova ⁵ , Ryan Love ⁶ ,	⁴ UoB-MARUM
Dimitri Murashkin ⁵ , Natasha Ridenour ⁷ ,	⁵ UoB-IEP
Damien Ringeisen ⁸ , Samira Samimi ⁹ ,	⁶ MUoN
Anouk Vlug ⁴ , Gunnar Spreen ⁵ , Ruediger	⁷ UoAE
Stein ⁸	⁸ AWI
	⁹ UoC

Grant-No. AWI_PS115/2_01 and AWI_PS115/2_02

Objectives

Due to a complex set of feedback processes collectively known as “polar amplification”, the Arctic realm is expected to experience a greater-than-average response to global climate forcing. The cascades of feedback processes that connect the Arctic cryosphere, ocean and atmosphere remain incompletely constrained by observations and theory and are difficult to simulate in climate models. Our capacity to predict the future of the region and assess the impacts of Arctic change processes on global and regional environments hinges on the availability of interdisciplinary experts with strong international experience and understanding of the science/society interface. This is the basis of the International Research Training Group “Processes and impacts of climate change in the North Atlantic Ocean and the Canadian Arctic – ArcTrain”, which was initiated in 2013 and will be funded until 2022. ArcTrain aims to educate PhD students in an interdisciplinary environment that combines paleoclimatology, physical oceanography, remote sensing and glaciology with comprehensive Earth system modelling, including sea-ice and ice-sheet components. The qualification programme for the PhD students includes joint supervision, mandatory research residences at partner institutions, field courses on land and on sea (Floating University), annual meetings and training workshops and a challenging structured training in expert skills and transferrable skills. Its aim is to enhance the career prospects and employability of the graduates in a challenging international job market across academic and applied sectors.

ArcTrain is a German - Canadian collaboration, in Germany located at the University of Bremen and the Alfred Wegener Institute Helmholtz Centre for Polar and Marine Research in Bremerhaven. The German part of the project is designed to continue for nine years and educate three cohorts of twelve PhD students each. The Canadian partners comprise a consortium of eight universities led by the GEOTOP cluster at the Université du Québec à Montréal and including Dalhousie University, McGill University, Memorial University of Newfoundland, University of Alberta, University of British Columbia, University of Calgary and Université du Québec à Rimouski.

Further details about ArcTrain are available at: <https://www.marum.de/ArcTrain.html>



Fig. 8.1: The ArcTrain Team!

Work at sea

As part of the ArcTrain qualification programme, a “Floating University” was held onboard *Polarstern* during the PS115/2 Expedition. The main goal of the programme was to provide a practical introduction to the different science fields worked on during PS115/2. The *ArcTrain Team* consists of 13 Canadian and German PhD and master students with very different scientific backgrounds (i.e., geosciences, sea ice, glaciers, oceanography, remote sensing, and modelling; Fig. 8.1). Their work was coordinated by two ArcTrain PIs. The participants were introduced into the different technical aspects of field work in marine sciences. All participants were given the opportunity to gain a broad experience of the work on the aft deck, in the laboratories, and on sea ice (parts of the group) by rotating between the different working groups. Each participant then picked one or two topics they were particularly interested in and got more involved in the practical work, and helped with the evaluation and interpretation of the collected scientific data.

Reports by the ArcTrain participants on these activities can be found in Appendix A.7. The *ArcTrain Team* helped with several monitoring programs and joint the following watches (Appendix A.7.1.1):

- Ice Watch – routine observations of sea ice from the bridge
- PARASOUND – monitoring of the PARASOUND echo-sounder for correct operation
- Marine Mammals – watch for mammals from the bridge during seismic surveys
- Polar Bear Watch – watch for polar bears during sea ice stations

This help was greatly appreciated by the different working groups and helped them to achieve their research goals. From the science topics during PS115/2, ArcTrain members in particular worked and reported on the following subjects:

- Marine Geology (Appendix A.7.2)
 - Box corer (GKG)
 - Multi-Corer (MUC)

- Gravity corer (SL)
- Kastenlot (KAL)
- Dredge

- Meteorology (Appendix A.7.3)
 - Weather balloon
 - Cloud camera

- Sea Ice (Appendix A.7.4)
 - Sea ice watch
 - Infrared camera and thin ice thickness
 - Hyperspectral camera: Melt pond and snow spectra
 - Ship radar for sea ice dynamics
 - Sea ice buoys
 - Ice thickness and temperature/salinity profiles

Besides the practical work, ArcTrain members presented their work in two seminars. The first seminar was held at the beginning of the cruise and ArcTrain participants and students from other working groups reported on their own research:

1st ArcTrain Seminar

Friday, 7.9.2018, 19:30–21:30

- Charles Brunette – Dynamic Preconditioning as a Seasonal Sea Ice Predictor: Example from the Laptev Sea
- Anouk Vlug – The Influence of Natural Variability on Canadian Arctic Glaciers during the last Millennium
- Natasha Ridenour – Fresh Water Dynamics in the Hudson Bay Complex
- Aliaksandra Kazlova – Sea Ice Dynamics from Satellite Observations
- Ryan Love – Echoes of Past Climate into the Future: An examination from the Perspective of GIA and Climate Modelling
- Damien Ringeisen – Breaking the Ice

Saturday, 8.9.2018, 19:30–21:30

- Amélie Desmarais – Sea Ice Variability in the Arctic
- Samira Samimi – Melt Water Retention
- Camille Brice – Holocene Paleoceanography in Isfjorden, Svalbard
- Pascal Bourgault – Heat Fluxes under Sea Ice Leads (in Climate Models)
- Myriam Caron – Paleoceanography in the Baffin Bay during the Holocene
- Rémi Ienny – Fate and impact of deglacial meltwater runoff in the north western Atlantic Ocean

Thursday, 13.9.2018, 16:00–17:30

- Dmitrii Murashkin – Satellite Altimetry and SAR for Sea Ice Research Applications
- Max Dröllner – Detrital U-Pb Zircon Geochronology
- Cynthia Sassenroth – A Geology Trip to Mars and Back

- Frithjof Lemmel – Glacial History of the Arctic Ocean
- Sergei Freiman – Tectonic and Sedimentary History of Chukchi Sea and Adjacent Areas

The second seminar was held at the end of the cruise and ArcTrain participants reported on their experience and first results:

2nd ArcTrain Seminar, Saturday, 13.10.2018, 16:00–19:00

- To the sky and beyond – Aliaksandra Kazlova and Amélie Desmarais
- Watching Ice – Anouk Vlug and Charles Brunette
- Drifting with the ice: the untold story of SVPs and pokéballs – Natasha Ridenour
- Breaking the Ice, Vol.2 – Damien Ringeisen
- Spectrum of the Arctic – Dmitrii Murashkin and Charles Brunette
- The Predator’s vision – Dmitrii Murashkin and Pascal Bourgault
- Marine Geology – Myriam Caron, Remi Ienny, Anouk Vlug, Ryan Love, Camille Brice
- Sea ice thickness measurements – Aliaksandra Kazlova, Samira Samimi

During the cruise additional seminars covering the four topics meteorology, sea ice, geophysics, and geology were presented by the individual PIs introducing their work and preliminary results.

Preliminary (expected) results

Experiences, a summary of their work, and preliminary and expected results of the *ArcTrain Team* are reported on in nine different sub-sections in Appendix A.7: The “ArcTrain Floating University” Onboard of *Polarstern* Expedition PS115/2.

An overview of the day to day life and work including the different watches done is given in Appendix A.7.1. In A.7.2 a description of the different coring tools and analysis in the lab for the marine geology work is presented. How to launch weather balloons, operate a cloud camera, and analyze the data is described in the meteorology section A.7.3. The sea ice related work is summarized in A.7.4 and covers the sea ice watch from the bridge, experiments with an infrared and hyperspectral camera, ice movement derived from the ship ice radar, a first analysis of the ice drift buoys, and a summary of the sea ice thickness measurements.

All participants in the ArcTrain Floating University proved to be extremely enthusiastic about the different activities on board and willing to connect to other disciplines. For example, the marine geology work was not only carried out by the two ArcTrain geologist onboard but three other ArcTrain participants with very different scientific backgrounds became fully part of the geology team. And the complete *ArcTrain Team* helped on the working deck and in the wet-lab when new sediments came onboard. Also, the meteorology and sea ice work were carried out by groups of diverse science backgrounds. This truly interdisciplinary experience will certainly enable the ArcTrain participants to value the different observations taken during the cruise and make proper use of them in their future careers.

All scientists highly appreciated the assistance of the ArcTrain participants and praised their interest and dedication. With their support, more work got done and more samples were taken.

Data management

All data collected with the help of the *ArcTrain Team* will be delivered to the PANGAEA or similar databases as described in the individual chapters of this report.

APPENDIX

- A.1 Teilnehmende Institute / Participating Institutions**
- A.2 Fahrtteilnehmer / Cruise Participants**
- A.3 Schiffsbesatzung / Ship's Crew**
- A.4 Stationsliste / Station List**
- A.5 Sampling and Publication Policy**
- A.6 Buoy Deployment Sheets**
- A.7 The “Arctrain Floating University” onboard of *Polarstern* Expedition PS115/2**

A.1 TEILNEHMENDE INSTITUTE / PARTICIPATING INSTITUTIONS

	Address
AWI	Alfred-Wegener-Institut Helmholtz-Zentrum für Polar- und Meeresforschung Postfach 120161 27515 Bremerhaven Germany
AWI-P	Alfred-Wegener-Institut Helmholtz-Zentrum für Polar- und Meeresforschung Telegrafenberg A43 14473 Potsdam Germany
BGR	Bundesanstalt für Geowissenschaften und Rohstoffe (BGR) Department B1.4 Stilleweg 2 30644 Hannover Germany
CAU	Institute for Geography Christian-Albrechts-Universität zu Kiel Ludewig-Meyn-Str. 14 24118 Kiel Germany
DWD	Deutscher Wetterdienst Geschäftsbereich Wettervorhersage Seeschiffahrtsberatung Bernhard-Nocht-Str. 76 20359 Hamburg Germany
GEOMAR	Helmholtz-Zentrum für Ozeanforschung (GEOMAR) Wischhofstr. 1-3 24148 Kiel Germany
HeliService	HeliService International GmbH Gorch Fock Str. 105 26721 Emden Germany

	Address
McGill	Department of Atmospheric and Oceanic Sciences McGill University 805 Sherbrooke Street West Montreal Quebec, H3A 0B9 Canada
MPI	Max Planck Institute for Meteorology Bundesstr. 53 20146 Hamburg Germany
MSU	Geology Department Moscow State University Leninskie Gory 1 119234 Moscow Russian Federation
MUoN	Department of Physics and Physical Oceanography Memorial University of Newfoundland 283 Prince Philip Drive A1B 3X7 St. John's Canada
NOAA	National Oceanic & Atmospheric Administration 4301 Rickenbacker Cswy Miami, Florida 33149 USA
UoAE	Department of Earth & Atmospheric Sciences 1-26 Earth Sciences Building University of Alberta Edmonton Edmonton, Alberta, T6G 2E3 Canada
UoB-MARUM	Center for Marine Environmental Sciences (MARUM) University of Bremen Klagenfurterstr. 2-4 28359 Bremen Germany
UoB-IEP	Institute of Environmental Physics (IEP) University of Bremen Otto-Hahn-Allee 1 28359 Bremen Germany

	Address
UoC	Department of Geography University of Calgary 2500 University Dr NW, AB T2N 1N4 Calgary Canada
UoM	Institute for Geology and Paleontology University of Münster Corrensstr. 24 48149 Münster Germany
UoStP	University of St. Petersburg Universitetskaya 7-9 199034 St. Petersburg Russian Federation
UoT	Department of Geosciences The Arctic University of Norway Dramsveien 201 9037 Tromsø Norway
UoW	Applied Physics Laboratory University of Washington (APL-UW) 1013 NE 40th St, Seattle, WA 98105 USA
UQAM	GEOTOP & Département des Sciences de la Terre Université du Québec à Montreal CP 8888 Montréal Québec, H3C 3P8 Canada
QQAR	Marine Geology (UQAR-ISMER) Université du Québec à Rimouski 310 allée des Ursulines Rimouski Québec, G5L 3A1 Canada

A.2 FAHRTTEILNEHMER / CRUISE PARTICIPANTS

	Name/Last name	Vorname/ First name	Institut/ Institute	Beruf/ Profession	Fachrichtung/ Discipline
1	Andree	Sophie	AWI	Student	Bathymetry
2	Benson	Ovie Miracle	AWI	Master student	Geology
3	Berglar	Kai	BGR	Scientist	Geophysics
4	Birnbaum	Gerit	AWI	Scientist	Remote sensing/sea ice
5	Bourgault	Pascal	McGill	Master student ArcTrain	
6	Brice	Camille	UQAM	PhD student ArcTrain	
7	Brunette	Charles	McGill	PhD student ArcTrain	
8	Caron	Myriam	UQAR	Master student ArcTrain	
9	de Jager	Harold	HeliService	HeliService	
10	Desmarais	Amelie	McGill	Master student ArcTrain	
11	Dröllner	Maximilian	UoM	Master student	Geology
12	Ebert	Timo	BGR	Technician	Geophysics
13	Eggers	Thorsten	AWI	Technician	Geophysics
14	Freiman	Sergei	MSU	Scientist	Geophysics
15	Fuchs	Niels	AWI	PhD student	Remote sensing/sea ice
16	Gaedicke	Christoph	BGR	Scientist	Geophysics
17	Heim	Thomas	HeliService	HeliService	
18	Ienny	Rémi	UoB- MARUM	PhD student ArcTrain	
19	Kazlova	Aliaksandra	UoB-IEP	PhD student ArcTrain	
20	König	Marcel	CAU	M.Sc.	Remote sensing/sea ice
21	Lemmel	Frithjof	Geomar	Master student	Geology
22	Lensch	Norbert	AWI	Technician	Geology & Geophysics
23	Love	Ryan	MUoN	PhD student ArcTrain	
24	Miller	Max	DWD	DWD	Meteorology
25	Murashkin	Dimitrii	UoB-IEP	PhD student ArcTrain	
26	Niessen	Frank	AWI	Scientist	Geophysics
27	Oberwinster	Lamis	AWI	Student	Bathymetry
28	Olonscheck	Dirk	MPI	Scientist	Meteorology

	Name/Last name	Vorname/ First name	Institut/ Institute	Beruf/ Profession	Fachrichtung/ Discipline
29	Pfeiffer	Adalbert	AWI	Engineer	Geology & Geophysics
30	Piotrowski	Lukas	HeliService		HeliService
31	Popova	Elena	UoStP	POMOR MS student	Geology
32	Ridenour	Natasha	UoAE	PhD student ArcTrain	
33	Ringeisen	Damien	AWI	PhD student ArcTrain	
34	Rohleder	Christian	DWD	DWD	Meteorology
35	Samimi	Samira	UoC	PhD student ArcTrain	
36	Santos	Victor	HeliService	HeliService	
37	Sassenroth	Cynthia	UoStP	(POMOR MS student)	Geology
38	Schmengler	Almut	AWI	Scientist	Geophysics
39	Scholz	John-Robert	AWI	Scientist	Geophysics
40	Schreck	Michael	UoT	PhD	Geology
41	Spreen	Gunnar	UoB-IEP	PI ArcTrain	Remote sensing
42	Steffen	Melanie	AWI	Student	Bathymetry
43	Stein	Ruediger	AWI	Chief scientist	Geology
44	van der Krogt	Jolien	AWI	Student	Geophysics
45	Vlug	Anouk	UoB-MARUM	PhD student ArcTrain	
46	Weigelt	Estella	AWI	Scientist	Geophysics
47	Wöhlten	Nikolai	AWI	Technician	Geology & Geophysics
48	Wu	Junjie	AWI	Student	Geology
49	Zimmermann	Heike	AWI-P	Scientist	Geology & sea ice

A.3 SCHIFFSBESATZUNG / SHIP'S CREW

No.	Name	Rank
01.	Wunderlich, Thomas	Master
02.	Grundmann, Uwe	1.Offc.
03.	Westphal, Henning	Ch.Eng.
04.	Fischer, Tibor	2.Offc.Lad.
05.	Hering, Igor	2.Offc.
06.	Peine, Lutz	2.Offc.
07.	Jaeger, Norbert	Doctor
08.	Hofmann, Jörg	Comm.Offc.
09.	Schnürch, Helmut	2.Eng.
10.	Brose, Thomas	2.Eng.
11.	Rusch, Torben	2.Eng.
12.	Brehme, Andreas	Elec.Tech.
13.	Frank, Gerhard	Electron.
14.	Markert, Winfried	Electron.
15.	Winter, Andreas	Electron.
16.	Feiertag, Thomas	Electron.
17.	Sedlak, Andreas	Boatsw.
18.	Neisner, Winfried	Carpenter
19.	Clasen, Nils	A.B.
20.	Schröder, Norbert	A.B.
21.	Burzan, Gerd-Ekkehard	A.B.
22.	Hartwig-Labahn, Andreas	A.B.
23.	Fölster, Michael	A.B.
24.	Müller, Steffen	A.B.
25.	Brickmann, Peter	A.B.
26.	Schröder, Horst	A.B.
27.	Beth, Detlef	Storekeep.
28.	Neumann, Niels	Mot-man
29.	Waterstradt, Felix	Mot-man
30.	Krösche, Eckard	Mot-man
31.	Dinse, Horst	Mot-man
32.	Watzel, Bernhard	Mot-man
33.	Meißner, Jörg	Cook
34.	Tupy, Mario	Cooksmate
35.	Martens, Michael	Cooksmate
36.	Wartenberg, Irina	1.Stwdess

No.	Name	Rank
37.	Tscheuschner, Andre	Stwd/KS
38.	Hischke ,Peggy	2.Stwdess
39.	Mack, Ulrich	2.Stwdess
40.	Krause, Tomasz	2.Steward
41.	Hu, Guo Yong	2.Steward
42.	Chen, Quan Lun	2.Steward
43.	Ruan, Hui Guang	Laundrym.

A4. STATIONSLISTE / STATION LIST

Station	Date	Time	Latitude	Longitude	Depth [m]	Gear	Action	Comment
PS115/2_0_Underway-6	2018-09-05	04:00	78.23520	15.62401	57	WST	profile start	
PS115/2_0_Underway-6	2018-10-16	05:57	53.56697	8.55440	2.5	WST	profile end	
PS115/2_0_Underway-7	2018-09-14	07:35	81.13080	119.72925	354	ADCP_150	profile start	
PS115/2_0_Underway-7	2018-10-04	03:59	81.81879	119.54439	5107	ADCP_150	profile end	entering Russian EEZ
PS115/2_0_Underway-7	2018-10-07	04:16	81.52715	33.79054	NA	ADCP_150	profile start	leaving Russian EEZ
PS115/2_0_Underway-7	2018-10-15	14:07	55.33311	6.58461	26	ADCP_150	profile end	
PS115/2_0_Underway-8	2018-09-14	07:35	81.13080	119.72925	354	MAG	profile start	
PS115/2_0_Underway-8	2018-10-04	03:55	81.82375	119.58239	5162	MAG	profile end	entering Russian EEZ
PS115/2_0_Underway-8	2018-10-07	04:16	81.52555	33.78576	NA	MAG	profile start	leaving Russian EEZ
PS115/2_0_Underway-8	2018-10-16	08:16	53.56681	8.55504	NA	MAG	profile end	
PS115/2_0_Underway-9	2018-09-14	07:35	81.13080	119.72925	354	TSG_KEEL	profile start	
PS115/2_0_Underway-9	2018-10-04	03:58	81.81963	119.54808	5128	TSG_KEEL	profile end	entering Russian EEZ
PS115/2_0_Underway-9	2018-10-07	05:21	81.33302	33.20521	180	TSG_KEEL	profile start	leaving Russian EEZ
PS115/2_0_Underway-9	2018-10-15	12:45	55.51909	6.44749	32	TSG_KEEL	profile end	
PS115/2_0_Underway-10	2018-09-14	07:40	81.12660	119.78576	354	GRAV	profile start	
PS115/2_0_Underway-10	2018-10-04	03:55	81.82444	119.59101	5160	GRAV	profile end	entering Russian EEZ
PS115/2_0_Underway-10	2018-10-07	04:15	81.52939	33.79728	NA	GRAV	profile start	leaving Russian EEZ
PS115/2_0_Underway-10	2018-10-16	08:16	53.56681	8.55504	NA	GRAV	profile end	
PS115/2_0_Underway-11	2018-09-14	07:55	81.11507	119.97078	354	SVP	profile start	
PS115/2_0_Underway-11	2018-10-04	03:57	81.82185	119.56477	3727	SVP	profile end	entering Russian EEZ

Station	Date	Time	Latitude	Longitude	Depth [m]	Gear	Action	Comment
PS115/2_0_Underway-11	2018-10-07	05:03	81.38692	33.36633	171	SVP	profile start	leaving Russian EEZ
PS115/2_0_Underway-11	2018-10-14	14:20	58.51406	4.33652	275	SVP	profile end	
PS115/2_0_Underway-12	2018-09-14	08:21	81.10020	120.30303	2625	FBOX	profile start	
PS115/2_0_Underway-12	2018-10-04	03:56	81.82288	119.57309	5150	FBOX	profile end	entering Russian EEZ
PS115/2_0_Underway-12	2018-10-07	04:56	81.40668	33.42570	NA	FBOX	profile start	leaving Russian EEZ
PS115/2_0_Underway-12	2018-10-14	14:25	58.50151	4.34518	276	FBOX	profile end	
PS115/2_0_Underway-13	2018-09-14	08:21	81.10020	120.30303	2625	PCO2_GO	profile start	
PS115/2_0_Underway-13	2018-10-04	03:56	81.82332	119.57734	5151	PCO2_GO	profile end	entering Russian EEZ
PS115/2_0_Underway-13	2018-10-07	04:56	81.40559	33.42242	NA	PCO2_GO	profile start	leaving Russian EEZ
PS115/2_0_Underway-13	2018-10-14	14:25	58.50151	4.34518	276	PCO2_GO	profile end	
PS115/2_0_Underway-14	2018-09-14	11:00	81.08813	122.10772	3494	PCO2_SUB	profile start	
PS115/2_0_Underway-14	2018-10-04	03:56	81.82304	119.57457	5150	PCO2_SUB	profile end	entering Russian EEZ
PS115/2_0_Underway-14	2018-10-07	04:57	81.40254	33.41334	172	PCO2_SUB	profile start	leaving Russian EEZ
PS115/2_0_Underway-14	2018-10-14	14:25	58.50151	4.34518	276	PCO2_SUB	profile end	
PS115/2_1-1	2018-09-14	07:24	81.13667	119.60559	NA	HS	profile start	
PS115/2_1-1	2018-09-14	13:18	81.20505	123.36629	3644	HS	profile end	
PS115/2_2-1	2018-09-14	13:18	81.20540	123.36711	3654	GKG	station start	
PS115/2_2-1	2018-09-14	14:49	81.24413	123.47994	3665	GKG	at depth	
PS115/2_2-1	2018-09-14	15:58	81.24511	123.48904	3670	GKG	station end	
PS115/2_2-2	2018-09-14	16:40	81.24439	123.48193	3669	BC	station start	
PS115/2_2-2	2018-09-14	17:41	81.24410	123.48394	3669	BC	at depth	
PS115/2_2-2	2018-09-14	18:57	81.24394	123.53210	NA	BC	station end	

A4. Stationsliste / Station List

Station	Date	Time	Latitude	Longitude	Depth [m]	Gear	Action	Comment
PS115/2_3-1	2018-09-14	19:25	81.24454	123.48045	3671	HS	profile start	
PS115/2_3-1	2018-09-15	04:40	82.07022	119.75359	3989	HS	profile end	
PS115/2_4-1	2018-09-15	04:54	82.06998	119.75455	3966	OBS	station start	
PS115/2_4-1	2018-09-15	06:26	82.06613	119.79339	3963	OBS	station end	
PS115/2_5-1	2018-09-15	07:25	82.06354	119.28274	4162	OBS	station start	
PS115/2_5-1	2018-09-15	08:57	82.06020	119.25390	4127	OBS	station end	
PS115/2_6-1	2018-09-15	10:09	81.95860	119.30775	3663	OBS	station start	
PS115/2_6-1	2018-09-15	11:26	81.96262	119.27460	3597	OBS	station end	
PS115/2_7-1	2018-09-15	12:33	81.95587	119.77491	3739	OBS	station start	
PS115/2_7-1	2018-09-15	13:56	81.96208	119.76324	3691	OBS	station end	
PS115/2_8-1	2018-09-15	19:45	81.44646	120.92929	4952	GKG	station start	
PS115/2_8-1	2018-09-15	20:56	81.44755	120.89148	4959	GKG	at depth	
PS115/2_8-1	2018-09-15	22:21	81.45063	120.80939	4969	GKG	station end	
PS115/2_8-2	2018-09-15	23:20	81.44267	120.93682	4949	GC	station start	
PS115/2_8-2	2018-09-16	00:30	81.44821	120.90011	4961	GC	at depth	
PS115/2_8-2	2018-09-16	01:57	81.45673	120.87373	4962	GC	station end	
PS115/2_9-1	2018-09-16	03:31	81.31703	120.76877	5264	REFL	station start	deployment of seismic equipment
PS115/2_9-1	2018-09-16	04:44	81.31959	121.21641	4593	REFL	„at depth“	deployment completed
PS115/2_9-1	2018-09-16	04:53	81.31913	121.27071	4575	REFL	profile start	softstart
PS115/2_9-1	2018-09-16	04:59	81.31924	121.33476	4533	REFL	profile start	full power
	2018-09-17	19:45	81.45675	140.72950	767	REFL	station start	deployment of Sonobuoy
PS115/2_9-1	2018-09-18	05:28	80.91252	144.21763	1765	REFL	station start	deployment of Sonobuoy

Station	Date	Time	Latitude	Longitude	Depth [m]	Gear	Action	Comment
	2018-09-18	09:11	80.85110	146.15450	2125	REFL	station start	deployment of Sonobuoy
PS115/2_9-1	2018-09-18	14:55	80.78213	147.99221	2203	REFL	profile start	change of heading, new line name
PS115/2_9-1	2018-09-18	23:51	80.78164	143.38205	1543	REFL	profile end	
	2018-09-19	01:30	80.90481	142.83331	1552	REFL	station end	seismic equipment on board
PS115/2_10-1	2018-09-19	01:30	80.90481	142.83331	1552	HS	station start	
PS115/2_10-1	2018-09-19	03:40	81.08482	140.95981	1679	HS	station end	
PS115/2_11-1	2018-09-19	03:52	81.08763	140.91615	1694	GKG	station start	
PS115/2_11-1	2018-09-19	04:29	81.08782	140.91380	1698	GKG	at depth	
PS115/2_11-1	2018-09-19	05:06	81.08775	140.91395	1697	GKG	station end	
PS115/2_11-2	2018-09-19	05:35	81.08780	140.91387	1697	MUC	station start	
PS115/2_11-2	2018-09-19	06:03	81.08775	140.91372	1696	MUC	at depth	
PS115/2_11-2	2018-09-19	06:41	81.08697	140.91475	1695	MUC	station end	
PS115/2_11-3	2018-09-19	07:23	81.08786	140.91316	1697	GC	station start	
PS115/2_11-3	2018-09-19	07:51	81.08789	140.91327	1696	GC	at depth	
PS115/2_11-3	2018-09-19	08:30	81.08613	140.89479	1701	GC	station end	
PS115/2_12-1	2018-09-19	09:30	81.08525	140.89424	1701	GC	station start	
PS115/2_12-1	2018-09-19	10:00	81.08524	140.89047	1701	GC	at depth	
PS115/2_12-1	2018-09-19	10:39	81.08550	140.88792	1702	GC	station end	
PS115/2_12-2	2018-09-19	11:00	81.08556	140.88894	1701	GKG	station start	
PS115/2_12-2	2018-09-19	11:30	81.08537	140.89253	1700	GKG	at depth	
PS115/2_12-2	2018-09-19	12:05	81.08478	140.88042	1705	GKG	station end	
PS115/2_13-1	2018-09-19	12:26	81.08203	140.86237	1705	GKG	station start	

A4. Stationsliste / Station List

Station	Date	Time	Latitude	Longitude	Depth [m]	Gear	Action	Comment
PS115/2_13-1	2018-09-19	12:59	81.08186	140.86570	1705	GKG	at depth	
PS115/2_13-1	2018-09-19	13:36	81.08202	140.86570	1705	GKG	station end	
PS115/2_13-2	2018-09-19	14:15	81.08199	140.86545	1706	GC	station start	
PS115/2_13-2	2018-09-19	14:46	81.08218	140.86391	1706	GC	at depth	
PS115/2_13-2	2018-09-19	15:24	81.08203	140.86299	1700	GC	station end	
PS115/2_14-1	2018-09-19	19:53	81.45650	140.72744	764	GKG	station start	
PS115/2_14-1	2018-09-19	20:09	81.45661	140.72794	765	GKG	at depth	
PS115/2_14-1	2018-09-19	20:27	81.45663	140.72853	768	GKG	station end	
PS115/2_14-2	2018-09-19	20:50	81.45679	140.72857	776	MUC	station start	
PS115/2_14-2	2018-09-19	21:10	81.45706	140.72951	777	MUC	at depth	
PS115/2_14-2	2018-09-19	21:30	81.45724	140.73041	777	MUC	station end	
PS115/2_14-3	2018-09-19	22:01	81.45700	140.72896	777	BC	station start	
PS115/2_14-3	2018-09-19	22:18	81.45724	140.72894	777	BC	at depth	
PS115/2_14-3	2018-09-19	22:40	81.45834	140.72896	780	BC	station end	
PS115/2_15-1	2018-09-19	22:58	81.46346	140.74200	782	HS	profile start	
PS115/2_15-1	2018-09-20	05:03	81.83878	140.26408	2092	HS	profile end	
PS115/2_16-1	2018-09-20	05:35	81.83784	140.26179	2078	PS	profile start	
PS115/2_16-1	2018-09-20	08:03	81.83741	140.37958	2053	PS	profile end	
PS115/2_17-1	2018-09-20	08:40	81.83224	140.49682	1500	GC	station start	
PS115/2_17-1	2018-09-20	09:10	81.83271	140.49447	1504	GC	at depth	
PS115/2_17-1	2018-09-20	09:43	81.83266	140.49172	1520	GC	station end	
PS115/2_18-1	2018-09-20	10:21	81.83309	140.47989	1579	GC	station start	
PS115/2_18-1	2018-09-20	10:47	81.83321	140.47737	1603	GC	at depth	
PS115/2_18-1	2018-09-20	11:21	81.83339	140.48112	1566	GC	station end	

Station	Date	Time	Latitude	Longitude	Depth [m]	Gear	Action	Comment
PS115/2_19-1	2018-09-20	11:45	81.83334	140.48162	1557	GC	station start	
PS115/2_19-1	2018-09-20	12:10	81.83320	140.48094	1569	GC	at depth	
PS115/2_19-1	2018-09-20	12:41	81.83265	140.48260	1568	GC	station end	
PS115/2_20-1	2018-09-20	13:05	81.83303	140.48744	1534	GC	station start	
PS115/2_20-1	2018-09-20	13:30	81.83308	140.48655	1534	GC	at depth	
PS115/2_20-1	2018-09-20	14:05	81.83233	140.49410	1519	GC	station end	
PS115/2_21-1	2018-09-20	14:42	81.83396	140.46026	1714	GC	station start	
PS115/2_21-1	2018-09-20	15:15	81.83383	140.45933	1731	GC	at depth	
PS115/2_21-1	2018-09-20	15:53	81.83388	140.46012	1716	GC	station end	
PS115/2_22-1	2018-09-20	17:06	81.85241	140.25890	2079	HS	profile start	
PS115/2_22-1	2018-09-21	08:00	82.18135	134.79202	3846	HS	profile end	
PS115/2_23-1	2018-09-21	08:15	82.18188	134.78401	3845	GKG	station start	
PS115/2_23-1	2018-09-21	09:19	82.18208	134.77059	3844	GKG	at depth	
PS115/2_23-1	2018-09-21	10:32	82.18600	134.76025	3845	GKG	station end	
PS115/2_23-2	2018-09-21	11:04	82.18054	134.83584	3843	MUC	station start	
PS115/2_23-2	2018-09-21	12:04	82.18258	134.84024	3871	MUC	at depth	
PS115/2_23-2	2018-09-21	13:12	82.18684	134.86055	3873	MUC	station end	
PS115/2_23-3	2018-09-21	14:10	82.17702	134.83588	3871	GC	station start	
PS115/2_23-3	2018-09-21	15:09	82.17782	134.88532	3875	GC	at depth	
PS115/2_23-3	2018-09-21	16:16	82.17677	134.91857	3875	GC	station end	
PS115/2_24-1	2018-09-21	17:17	82.18432	134.49000	3904	GC	station start	
PS115/2_24-1	2018-09-21	18:16	82.18211	134.53225	3904	GC	at depth	
PS115/2_24-1	2018-09-21	19:28	82.18391	134.54120	3902	GC	station end	
PS115/2_24-2	2018-09-21	19:48	82.17650	134.51733	3905	GKG	station start	

A4. Stationsliste / Station List

Station	Date	Time	Latitude	Longitude	Depth [m]	Gear	Action	Comment
PS115/2_24-2	2018-09-21	20:50	82.18031	134.53086	3902	GKG	at depth	
PS115/2_24-2	2018-09-21	22:00	82.18255	134.53754	3903	GKG	station end	
PS115/2_25-1	2018-09-22	06:45	82.44214	140.18782	2349	GKG	station start	
PS115/2_25-1	2018-09-22	07:25	82.44303	140.18928	2365	GKG	at depth	
PS115/2_25-1	2018-09-22	08:12	82.44372	140.16467	2366	GKG	station end	
PS115/2_25-2	2018-09-22	08:37	82.44263	140.19750	2350	MUC	station start	
PS115/2_25-2	2018-09-22	09:11	82.44354	140.19130	2351	MUC	at depth	
PS115/2_25-2	2018-09-22	09:52	82.44536	140.16761	2350	MUC	station end	
PS115/2_25-3	2018-09-22	10:21	82.44059	140.15859	2350	GC	station start	
PS115/2_25-3	2018-09-22	11:41	82.44566	140.11797	2360	GC	station end	
PS115/2_26-1	2018-09-22	13:48	82.42793	141.60178	1641	GC	station start	
PS115/2_26-1	2018-09-22	14:14	82.43204	141.58755	1636	GC	at depth	
PS115/2_26-1	2018-09-22	14:48	82.43780	141.57784	1629	GC	station end	
PS115/2_26-2	2018-09-22	15:12	82.43023	141.61133	1636	GKG	station start	
PS115/2_26-2	2018-09-22	15:42	82.43469	141.61714	1632	GKG	at depth	
PS115/2_26-2	2018-09-22	16:12	82.43920	141.61035	1625	GKG	station end	
PS115/2_28-1	2018-09-23	08:47	82.83011	142.47240	1256	GKG	station start	
PS115/2_28-1	2018-09-23	09:11	82.83155	142.46725	1247	GKG	at depth	
PS115/2_28-1	2018-09-23	09:35	82.83303	142.46244	1241	GKG	station end	
PS115/2_28-2	2018-09-23	09:57	82.83442	142.46017	1254	MUC	station start	
PS115/2_28-2	2018-09-23	10:18	82.83567	142.44889	1247	MUC	at depth	
PS115/2_28-2	2018-09-23	10:40	82.83711	142.44348	1244	MUC	station end	
PS115/2_28-3	2018-09-23	11:09	82.83886	142.44018	1243	BC	station start	
PS115/2_28-3	2018-09-23	11:28	82.84009	142.43250	1237	BC	at depth	

Station	Date	Time	Latitude	Longitude	Depth [m]	Gear	Action	Comment
PS115/2_28-3	2018-09-23	11:52	82.84149	142.42731	1233	BC	station end	
PS115/2_29-1	2018-09-23	16:00	82.59886	141.61024	2015	REFL	station start	
PS115/2_29-1	2018-09-23	17:00	82.51874	141.61012	1803	REFL	profile start	
PS115/2_29-1	2018-09-27	09:01	80.49149	140.00168	1833	REFL	profile end	
PS115/2_29-1	2018-09-27	11:55	80.69175	140.00182	1913	REFL	station end	
PS115/2_29-2	2018-09-27	09:00	80.48887	140.00163	1834	AIMMMS	station end	
PS115/2_29-2	2018-09-28	01:00	81.93830	146.70292	2220	AIMMMS	information	
PS115/2_30-1	2018-09-28	04:04	81.98106	148.32001	2616	GKG	station start	
PS115/2_30-1	2018-09-28	05:27	81.98751	148.42193	2622	GKG	at depth	
PS115/2_30-1	2018-09-28	06:24	81.98910	148.48832	2625	GKG	station end	
PS115/2_30-2	2018-09-28	06:34	81.99135	148.51440	2627	GKG	station start	
PS115/2_30-2	2018-09-28	07:26	81.98905	148.56651	2633	GKG	at depth	
PS115/2_30-2	2018-09-28	08:16	81.98600	148.61996	2639	GKG	station end	
PS115/2_30-3	2018-09-28	08:47	81.98546	148.71716	2649	MUC	station start	
PS115/2_30-3	2018-09-28	09:35	81.98300	148.73491	2648	MUC	at depth	
PS115/2_30-3	2018-09-28	10:22	81.98298	148.74257	2649	MUC	station end	
PS115/2_30-4	2018-09-28	10:42	81.98214	148.74626	2648	BC	station start	
PS115/2_30-4	2018-09-28	11:22	81.98294	148.74265	2649	BC	at depth	
PS115/2_30-4	2018-09-28	12:07	81.98523	148.74557	2650	BC	station end	
PS115/2_31-1	2018-09-29	01:00	81.41824	142.40097	778	PS	profile start	
PS115/2_31-1	2018-09-29	04:26	81.48909	142.24827	819	PS	profile end	
PS115/2_32-1	2018-09-29	04:47	81.49186	142.23938	822	GKG	station start	
PS115/2_32-1	2018-09-29	05:05	81.49083	142.23427	819	GKG	at depth	
PS115/2_32-1	2018-09-29	05:28	81.49085	142.23398	819	GKG	station end	

A4. Stationsliste / Station List

Station	Date	Time	Latitude	Longitude	Depth [m]	Gear	Action	Comment
PS115/2_32-2	2018-09-29	05:48	81.49108	142.23651	821	MUC	station start	
PS115/2_32-2	2018-09-29	06:03	81.49067	142.23426	818	MUC	at depth	
PS115/2_32-2	2018-09-29	06:25	81.49053	142.23323	819	MUC	station end	
PS115/2_32-3	2018-09-29	07:18	81.49065	142.23077	817	GC	station start	
PS115/2_32-3	2018-09-29	07:38	81.49056	142.23396	809	GC	at depth	
PS115/2_32-3	2018-09-29	08:02	81.49017	142.22164	813	GC	station end	
PS115/2_33-1	2018-09-29	08:51	81.47147	142.31518	795	GC	station start	
PS115/2_33-1	2018-09-29	09:08	81.47159	142.31751	797	GC	at depth	
PS115/2_33-1	2018-09-29	09:30	81.47109	142.30651	791	GC	station end	
PS115/2_34-1	2018-09-29	10:21	81.45777	142.38143	816	GC	station start	
PS115/2_34-1	2018-09-29	10:37	81.45796	142.38469	818	GC	at depth	
PS115/2_34-1	2018-09-29	11:00	81.45736	142.37985	814	GC	station end	
PS115/2_35-1	2018-09-29	11:45	81.45155	142.40781	826	GC	station start	
PS115/2_35-1	2018-09-29	12:01	81.45165	142.40833	826	GC	at depth	
PS115/2_35-1	2018-09-29	12:18	81.45288	142.40818	824	GC	station end	
PS115/2_36-1	2018-09-29	15:12	81.69079	143.64748	1821	GC	station start	
PS115/2_36-1	2018-09-29	15:42	81.68975	143.64808	1815	GC	at depth	
PS115/2_36-1	2018-09-29	16:21	81.68990	143.64817	1821	GC	station end	
PS115/2_36-2	2018-09-29	16:42	81.68958	143.64797	1819	GKG	station start	
PS115/2_36-2	2018-09-29	17:13	81.68970	143.64820	1822	GKG	at depth	
PS115/2_36-2	2018-09-29	17:47	81.68967	143.65013	1824	GKG	station end	
PS115/2_37-1	2018-09-29	19:10	81.67016	143.05957	1438	PS	profile start	
PS115/2_37-1	2018-09-29	22:58	81.66980	143.07099	1414	PS	profile end	
PS115/2_38-1	2018-09-29	23:15	81.67410	143.25943	1683	HS	profile start	

Station	Date	Time	Latitude	Longitude	Depth [m]	Gear	Action	Comment
PS115/2_38-1	2018-09-30	03:10	81.66904	142.74143	768	HS	profile end	
PS115/2_39-1	2018-09-30	03:12	81.66881	142.74065	645	GKG	station start	
PS115/2_39-1	2018-09-30	03:36	81.66820	142.74098	767	GKG	at depth	
PS115/2_39-1	2018-09-30	03:54	81.66804	142.74042	766	GKG	station end	
PS115/2_39-2	2018-09-30	04:10	81.66805	142.74017	767	MUC	station start	
PS115/2_39-2	2018-09-30	04:27	81.66814	142.74066	767	MUC	at depth	
PS115/2_39-2	2018-09-30	04:45	81.66808	142.73971	766	MUC	station end	
PS115/2_39-3	2018-09-30	05:51	81.66784	142.73958	767	GC	station start	
PS115/2_39-3	2018-09-30	06:09	81.66803	142.74005	769	GC	at depth	
PS115/2_39-3	2018-09-30	06:31	81.66595	142.75876	761	GC	station end	
PS115/2_40-1	2018-09-30	07:30	81.66656	142.93246	955	GC	station start	
PS115/2_40-1	2018-09-30	07:53	81.66651	142.93257	940	GC	at depth	
PS115/2_40-1	2018-09-30	08:15	81.66377	142.93083	955	GC	station end	
PS115/2_41-1	2018-09-30	16:57	80.27256	140.95822	1598	GC	station start	
PS115/2_41-1	2018-09-30	17:30	80.27170	140.95878	1602	GC	at depth	
PS115/2_41-1	2018-09-30	18:10	80.27173	140.95726	1602	GC	station end	
PS115/2_41-2	2018-09-30	18:30	80.27177	140.95719	1604	GKG	station start	
PS115/2_41-2	2018-09-30	18:54	80.27100	140.96343	1600	GKG	at depth	
PS115/2_41-2	2018-09-30	19:42	80.27165	140.95703	1603	GKG	station end	
PS115/2_41-3	2018-09-30	19:52	80.27145	140.95568	1603	MUC	station start	
PS115/2_41-3	2018-09-30	20:21	80.27071	140.96635	1583	MUC	at depth	
PS115/2_41-3	2018-09-30	20:53	80.26833	140.97500	1599	MUC	station end	
PS115/2_42-1	2018-09-30	21:19	80.29959	140.94612	1638	PS	profile start	
PS115/2_42-1	2018-09-30	22:47	80.29257	140.89719	1579	PS	profile end	

A4. Stationsliste / Station List

Station	Date	Time	Latitude	Longitude	Depth [m]	Gear	Action	Comment
PS115/2_43-1	2018-09-30	23:18	80.31055	141.02040	1773	HS	profile start	
PS115/2_43-1	2018-10-01	03:57	80.31267	141.00333	1776	HS	profile end	
PS115/2_44-1	2018-10-01	04:13	80.32123	140.96662	1775	GKG	station start	
PS115/2_44-1	2018-10-01	04:41	80.31955	140.97456	1777	GKG	at depth	
PS115/2_44-1	2018-10-01	05:14	80.31959	140.97337	1776	GKG	station end	
PS115/2_44-2	2018-10-01	05:44	80.31943	140.97457	1775	GC	station start	
PS115/2_44-2	2018-10-01	06:17	80.31966	140.97355	1776	GC	at depth	
PS115/2_44-2	2018-10-01	06:55	80.31741	140.98373	1775	GC	station end	
PS115/2_45-1	2018-10-01	07:41	80.29991	140.97150	1662	GC	station start	
PS115/2_45-1	2018-10-01	08:00	80.30027	140.96797	1660	GC	at depth	
PS115/2_45-1	2018-10-01	08:45	80.30284	140.97578	1707	GC	station end	
PS115/2_46-1	2018-10-01	09:38	80.30390	140.96638	1704	GC	station start	
PS115/2_46-1	2018-10-01	10:08	80.30387	140.96816	1708	GC	at depth	
PS115/2_46-1	2018-10-01	10:44	80.30560	140.95756	1704	GC	station end	
PS115/2_47-1	2018-10-01	11:38	80.29504	140.96470	1616	GC	station start	
PS115/2_47-1	2018-10-01	12:03	80.29502	140.96311	1630	GC	at depth	
PS115/2_47-1	2018-10-01	12:37	80.29707	140.95124	1634	GC	station end	
PS115/2_48-1	2018-10-01	13:32	80.28953	140.96234	1606	GC	station start	
PS115/2_48-1	2018-10-01	13:57	80.28966	140.96360	1607	GC	at depth	
PS115/2_48-1	2018-10-01	14:33	80.28988	140.96292	1612	GC	station end	
PS115/2_49-1	2018-10-01	15:30	80.30973	140.99238	1765	GC	station start	
PS115/2_49-1	2018-10-01	16:01	80.30987	140.99422	1765	GC	at depth	
PS115/2_49-1	2018-10-01	16:40	80.30961	140.99699	1767	GC	station end	
PS115/2_50-1	2018-10-01	20:23	80.77672	142.78505	1746	GC	station start	

Station	Date	Time	Latitude	Longitude	Depth [m]	Gear	Action	Comment
PS115/2_50-1	2018-10-01	20:50	80.77684	142.78507	1746	GC	at depth	
PS115/2_50-1	2018-10-01	21:27	80.77648	142.78500	1747	GC	station end	
PS115/2_50-2	2018-10-01	21:49	80.77604	142.78259	1746	GKG	station start	
PS115/2_50-2	2018-10-01	22:18	80.77637	142.78446	1746	GKG	at depth	
PS115/2_50-2	2018-10-01	22:52	80.77359	142.77787	1748	GKG	station end	
PS115/2_51-1	2018-10-02	01:27	80.96530	142.47037	1440	GKG	station start	
PS115/2_51-1	2018-10-02	01:56	80.96522	142.47313	1440	GKG	at depth	
PS115/2_51-1	2018-10-02	02:26	80.96542	142.47509	1441	GKG	station end	
PS115/2_51-2	2018-10-02	02:43	80.96518	142.47282	1439	MUC	station start	
PS115/2_51-2	2018-10-02	03:09	80.96503	142.47317	1441	MUC	at depth	
PS115/2_51-2	2018-10-02	03:38	80.96486	142.47339	1439	MUC	station end	
PS115/2_51-3	2018-10-02	04:11	80.96496	142.47311	1439	BC	station start	
PS115/2_51-3	2018-10-02	04:36	80.96497	142.47296	1438	BC	at depth	
PS115/2_51-3	2018-10-02	05:14	80.96512	142.47280	1445	BC	station end	
PS115/2_52-1	2018-10-02	21:40	81.38904	128.58706	3658	PS	profile start	
PS115/2_52-1	2018-10-02	22:08	81.40533	128.53384	3593	PS	profile end	
PS115/2_53-1	2018-10-02	22:08	81.40533	128.53384	3599	GC	station start	
PS115/2_53-1	2018-10-02	23:03	81.40724	128.52187	3652	GC	at depth	
PS115/2_53-1	2018-10-03	00:06	81.41235	128.46938	3886	GC	station end	
PS115/2_54-1	2018-10-03	01:06	81.40480	128.40361	3940	DRDGE	station start	Dredge to water and lowering
PS115/2_54-1	2018-10-03	02:20	81.40528	128.47429	3820	DRDGE	at depth	Dredge at the seafloor
PS115/2_54-1	2018-10-03	02:22	81.40641	128.55611	3590	DRDGE	profile start	Start dredging
PS115/2_54-1	2018-10-03	03:23	81.40635	128.55530	3594	DRDGE	profile end	End dredging and heaving

A4. Stationsliste / Station List

Station	Date	Time	Latitude	Longitude	Depth [m]	Gear	Action	Comment
PS115/2_54-1	2018-10-03	04:30	81.40587	128.56338	3586	DRDGE	station end	Dredge on deck
PS115/2_55-1	2018-10-03	05:12	81.38840	128.62126	3675	GC	station start	
PS115/2_55-1	2018-10-03	06:21	81.38846	128.61392	3668	GC	at depth	
PS115/2_55-1	2018-10-03	07:24	81.38642	128.58238	3676	GC	station end	
PS115/2_56-1	2018-10-03	08:24	81.38204	128.35296	3924	DRDGE	station start	Dredge to water and lowering
PS115/2_56-1	2018-10-03	09:49	81.38265	128.35930	3834	DRDGE	at depth	Start dredging
PS115/2_56-1	2018-10-03	12:36	81.38516	128.47274	3453	DRDGE	station end	Dredge on deck
PS115/2_57-1	2018-10-03	17:21	81.38502	124.56581	3469	GC	station start	
PS115/2_57-1	2018-10-03	18:20	81.39032	124.55507	3491	GC	at depth	
PS115/2_57-1	2018-10-03	19:18	81.39620	124.54369	3490	GC	station end	

Gear abbreviations	Gear
ADCP_150	ADCP 150kHz
AIMMMS	AIMMMS
BC	Box Corer
DRDGE	Dredge
FBOX	FerryBox
GC	Gravity Corer
GKG	Box Grab
GRAV	Sea Gravimeter
HS	Hydrosweep
MAG	Magnetometer
MUC	Multi Corer
OBS	Ocean Bottom Seismograph
PCO2_GO	pCO2 GO
PCO2_SUB	pCO2 Subctech
PS	Parasound
REFL	Seismic reflection
SVP	Sound Velocity Profiler
TSG_KEEL	Thermosalinograph Keel
WST	Weatherstation

PS115/2 Sampling and Publication Policy

Some important remarks dealing with the use of *Polarstern* material and presentations & publications of shipboard as well as later shore-based results.

(1) Sample Request

If you work on any sediment material (surface sediments, sediment cores, rocks, sea-ice sediments), i.e., material you already took/got onboard during our expedition or material you will order/get post-cruise, you first have to fill out a “**Sample Request Form (SRF)**” and send it to the AWI Core Curator. In this form you have to outline what material you need, what type of study you will carry out, etc.. The SRF will be reviewed and discussed at the AWI (curator, chief scientist etc.). Further details are outlined in the SRF. Follow these instructions carefully.

The SRF can be down-loaded at: <https://epic.awi.de/37356/2/sample-request.pdf>

(2) Cruise-related AWI-Grant Number

In all publications, you must (!!) refer to our expedition in the acknowledgements, using a specific cruise-related AWI-Grant Number. The grant numbers of PS115/2 are the following:

Geoscientific research (i.e., geophysics and geology): **AWI_PS115/2_01**
All others (meteorology, sea ice, etc.): **AWI_PS115/2_02**

That means, in the acknowledgements you should include a statement:

- „This study used samples and/or data provided by AWI (Grant No. AWI_PS115/2_01)“ .
- or
- „This study used samples and/or data provided by AWI (Grant No. AWI_PS115/2_02)“ .

(3) Co-authorship of the Science Party

Within the first year - and here we follow rules similar to IODP – all presentations and publications of shipboard scientific data should include the PS115/2 Science Party as co-author.

A.6 BUOY DEPLOYMENT SHEETS

G. Spreen (UoB-IEP)

17 buoys were deployed during PS115/2. Details about the objectives, work at sea, and preliminary results can be found in Section 4.4. Here the deployment sheets for all buoys are collected. Deployment sheets are ordered by date and time of deployment.

Buoy deployment report

Buoy information

Buoy name: 2018P73

Modem-ID: 300234065802030

Buoy type: Surface Velocity Profiler

Deployment information

Date and Time (Time zone): 15.09.2018, 08:22 UTC

Position (Lat/Long): 82.061°N/119.272°E

Region: Arctic Ocean, north of Laptev Sea

Name and Institute: owner: NOAA; deployment: Gunnar Spreen, Univer. of Bremen

Contact e-mail: gunnar.spreen@uni-bremen.de

Expedition name: Polarstern PS115/2

Means of deployment: Mummy Chair from Polarstern

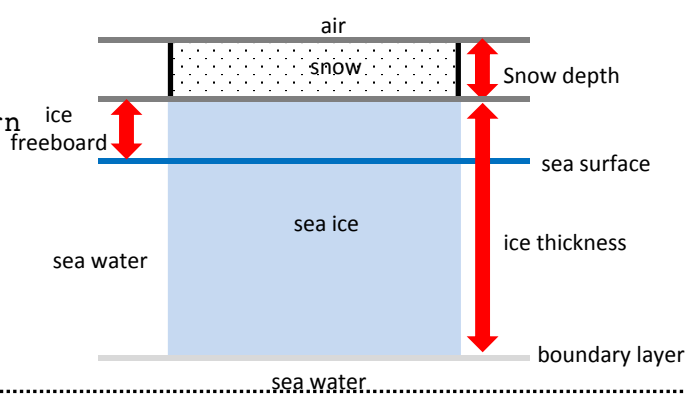
Snow and Ice conditions

Snow depth [m]: 0.08

Ice thickness [m]: 1.92

Ice Freeboard [m]: 0.13

Ice type: First-year ice



Required additional information for snow buoys

Snow thickness under sensors [m]: (3 measurements per sensor)

Sensor 1:

Sensor 2:

Sensor 3:

Sensor 4:

Required additional information for IMB (thermistor)

Thermistor chain length [m]:

Sensor interval [cm]:

Sensor numbers at interfaces

Sensor air - snow:

Sensor snow - ice:

Sensor sea surface:

Sensor ice - water:

Additional information (comments, weather, topography, ice floe size, etc.)

floe size approx 50m x 150m; floe was deformed; deployment about 50 m from ridge; nice weather;

air temperature: -3.8°C; water temperature: -1.9°C; pressure: 1026 hPa; humidity: 97%; wind speed 3 m/s; wind direction: 186°

Buoy deployment report



ALFRED-WEGENER-INSTITUT
HELMHOLTZ-ZENTRUM FÜR POLAR-
UND MEERESFORSCHUNG

Buoy information

Buoy name: 2018P66

Modem-ID: 300234065709990

Buoy type: Surface Velocity Profiler

Deployment information

Date and Time (Time zone): 18.09.2018, 12:26 UTC

Position (Lat/Long): 80.793°N/147.711°E

Region: Arctic Ocean

Name and Institute: owner: NOAA; deployment: Gunnar Spreen, Univer. of Bremen

Contact e-mail: gunnar.spreen@uni-bremen.de

Expedition name: Polarstern PS115/2

Means of deployment: open water deployment



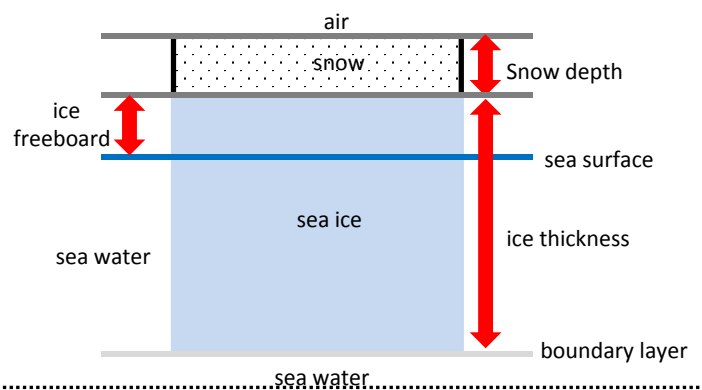
Snow and Ice conditions

Snow depth [m]:

Ice thickness [m]:

Ice Freeboard [m]:

Ice type: not deployed on ice



Required additional information for snow buoys

Snow thickness under sensors [m]: (3 measurements per sensor)

Sensor 1:

Sensor 2:

Sensor 3:

Sensor 4:

Required additional information for IMB (thermistor)

Thermistor chain length [m]:

Sensor interval [cm]:

Sensor numbers at interfaces

Sensor air - snow:

Sensor snow - ice:

Sensor sea surface:

Sensor ice - water:

Additional information (comments, weather, topography, ice floe size, etc.)

Deployment in open water on starboard side of Polarstern; foggy;
air temperature: -0.1°C ; water temperature: -1.5°C ; pressure: 1014 hPa;
humidity: 99%; wind speed 8.4 m/s; wind direction: 131° ; visibility 662 m

Buoy deployment report

Buoy information

Buoy name: 2018P72

Modem-ID: 300234065802000

Buoy type: Surface Velocity Profiler

Deployment information

Date and Time (Time zone): 21.09.2018, 03:49 UTC

Position (Lat/Long): 82.062° N/138.058° E

Region: Arctic Ocean, north of Laptev Sea

Name and Institute: owner: NOAA; deployment: Gunnar Spreen, University of Bremen

Contact e-mail: gunnar.spreen@uni-bremen.de

Expedition name: Polarstern PS115/2

Means of deployment: open water/grease ice

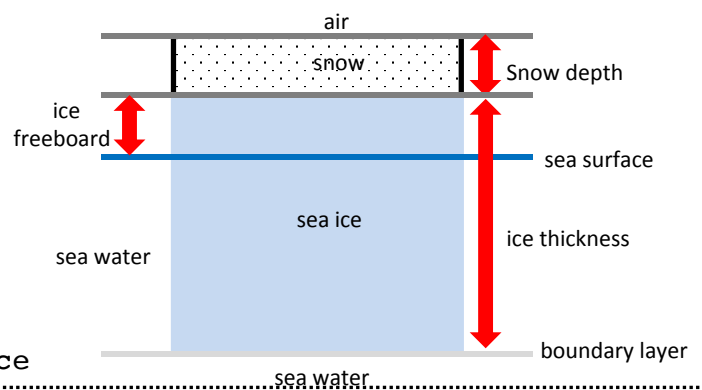
Snow and Ice conditions

Snow depth [m]:

Ice thickness [m]: 0.00 - 0.01

Ice Freeboard [m]:

Ice type: open water surrounded by grease ice



Required additional information for snow buoys

Snow thickness under sensors [m]: (3 measurements per sensor)

Sensor 1:

Sensor 2:

Sensor 3:

Sensor 4:

Required additional information for IMB (thermistor)

Thermistor chain length [m]:

Sensor interval [cm]:

Sensor numbers at interfaces

Sensor air - snow:

Sensor snow - ice:

Sensor sea surface:

Sensor ice - water:

Additional information (comments, weather, topography, ice floe size, etc.)

Deployment in open water in an area with new ice formation (mainly grease ice) on starboard side of Polarstern; good visibility but low clouds; air temperature: -3.9°C ; water temperature: -1.7°C ; pressure: 1014 hPa; humidity: 94%; wind speed 0.4 m/s; wind direction: 128° ; visibility 49 km; ceiling 600 ft

Buoy deployment report



ALFRED-WEGENER-INSTITUT
HELMHOLTZ-ZENTRUM FÜR POLAR-
UND MEERESFORSCHUNG

Buoy information

Buoy name: 2018P67

Modem-ID: 300234065800000

Buoy type: Surface Velocity Profiler

Deployment information

Date and Time (Time zone): 21.09.2018, 22:35 UTC

Position (Lat/Long): 82.180°N/134.495°E

Region: Arctic Ocean, north of Laptev Sea

Name and Institute: owner: NOAA; deployment: Gunnar Spreen, Univer. of Bremen

Contact e-mail: gunnar.spreen@uni-bremen.de

Expedition name: Polarstern PS115/2

Means of deployment: Mummy Chair from Polarstern



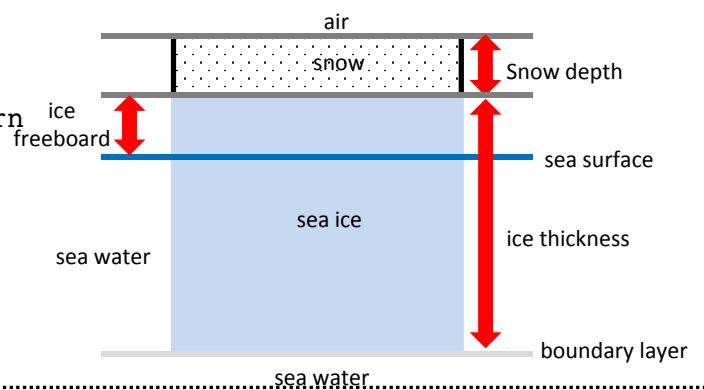
Snow and Ice conditions

Snow depth [m]: 0.09

Ice thickness [m]: 0.78

Ice Freeboard [m]: 0.06

Ice type: second-year ice



Required additional information for snow buoys

Snow thickness under sensors [m]: (3 measurements per sensor)

Sensor 1:

Sensor 2:

Sensor 3:

Sensor 4:

Required additional information for IMB (thermistor)

Thermistor chain length [m]:

Sensor interval [cm]:

Sensor numbers at interfaces

Sensor air - snow:

Sensor snow - ice:

Sensor sea surface:

Sensor ice - water:

Additional information (comments, weather, topography, ice floe size, etc.)

floe size approx. 150m x 70m; thinner ice at deployment site but some ridges on the floe; good visibility with some low clouds; air temperature: -4.3°C; water temperature: -1.7°C; pressure: 1012 hPa; humidity: 94%; wind speed 1.7 m/s; wind direction: 116°; visibility 73 km; ceiling 4200 ft

Buoy deployment report



ALFRED-WEGENER-INSTITUT
HELMHOLTZ-ZENTRUM FÜR POLAR-
UND MEERESFORSCHUNG

Buoy information

Buoy name: 2018P71

Modem-ID: 300234065801040

Buoy type: Surface Velocity Profiler

Deployment information

Date and Time (Time zone): 22.09.2018, 07:17 UTC

Position (Lat/Long): 82.418°N/140.084°E

Region: Arctic Ocean, north of Laptev Sea

Name and Institute: owner: NOAA; deployment: Gunnar Spreen, Univer. of Bremen

Contact e-mail: gunnar.spreen@uni-bremen.de

Expedition name: Polarstern PS115/2

Means of deployment: Helicopter Ice Station



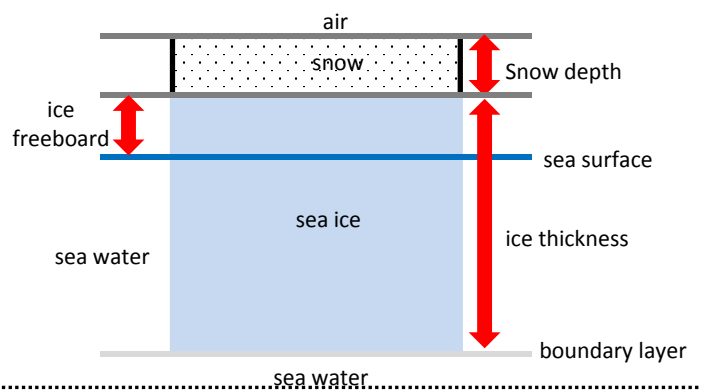
Snow and Ice conditions

Snow depth [m]: 0.07

Ice thickness [m]: 3.58

Ice Freeboard [m]: 0.63

Ice type: second-year ice



Required additional information for snow buoys

Snow thickness under sensors [m]: (3 measurements per sensor)

Sensor 1:

Sensor 2:

Sensor 3:

Sensor 4:

Required additional information for IMB (thermistor)

Thermistor chain length [m]:

Sensor interval [cm]:

Sensor numbers at interfaces

Sensor air - snow:

Sensor snow - ice:

Sensor sea surface:

Sensor ice - water:

Additional information (comments, weather, topography, ice floe size, etc.)

deformed ice, with an approx. 2 m high ridge; on one side some frozen over melt ponds; floe size approx. 100m x 200m; cloudy sky; meteorological data from Polarstern about 3 km away: air temperature: -3.6°C; water temperature: -1.7°C; pressure: 1012 hPa; humidity: 92%; wind speed 4.4 m/s; wind direction: 113°; visibility 71 km; ceiling 690 ft

Buoy deployment report



ALFRED-WEGENER-INSTITUT
HELMHOLTZ-ZENTRUM FÜR POLAR-
UND MEERESFORSCHUNG

Buoy information

Buoy name: 2018P68

Modem-ID: 300234065800030

Buoy type: Surface Velocity Profiler

Deployment information

Date and Time (Time zone): 23.09.2018, 05:00 UTC

Position (Lat/Long): 83.085°N/142.515°E

Region: Arctic Ocean, north of Laptev Sea

Name and Institute: owner: NOAA; deployment: Gunnar Spreen, University of Bremen

Contact e-mail: gunnar.spreen@uni-bremen.de

Expedition name: Polarstern PS115/2

Means of deployment: Mummy Chair from Polarstern

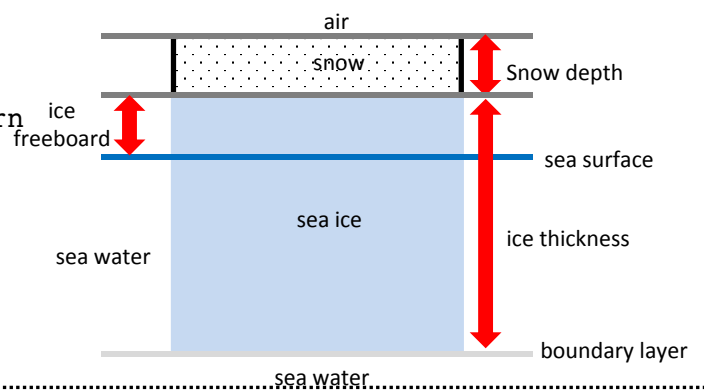
Snow and Ice conditions

Snow depth [m]: 0.12

Ice thickness [m]: 0.74

Ice Freeboard [m]: 0.02

Ice type: second-year ice



Required additional information for snow buoys

Snow thickness under sensors [m]: (3 measurements per sensor)

Sensor 1:

Sensor 2:

Sensor 3:

Sensor 4:

Required additional information for IMB (thermistor)

Thermistor chain length [m]:

Sensor interval [cm]:

Sensor numbers at interfaces

Sensor air - snow:

Sensor snow - ice:

Sensor sea surface:

Sensor ice - water:

Additional information (comments, weather, topography, ice floe size, etc.)

floe size approx. 150m x 300m; good visibility with some low clouds; ice station from 04:15 to 06:15 UTC; position and data from 05:00 UTC used here;

air temperature: -5.2°C; water temperature: -1.7°C; pressure: 1012 hPa; humidity: 95%; wind speed 6.4 m/s; wind direction: 124°; visibility 30 km; ceiling 7200 ft

Buoy deployment report

Buoy information

Buoy name: 2018P75

Modem-ID: 300234011880340

Buoy type: Microstar Drifter

Deployment information

Date and Time (Time zone): 24.09.2018, 04:00 UTC

Position (Lat/Long): 81.697°N/141.488°E

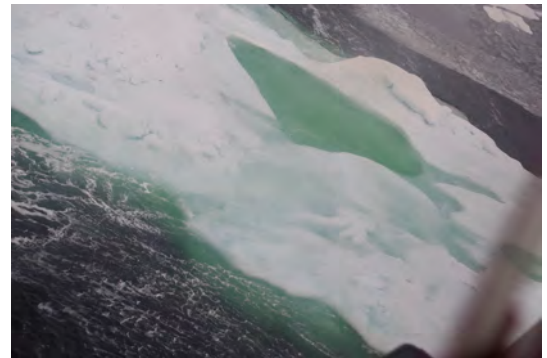
Region: Arctic Ocean, north of Laptev Sea

Name and Institute: owner: AWI; deployment: Gunnar Spreen, Univer. of Bremen

Contact e-mail: gunnar.spreen@uni-bremen.de

Expedition name: Polarstern PS115/2

Means of deployment: Helicopter



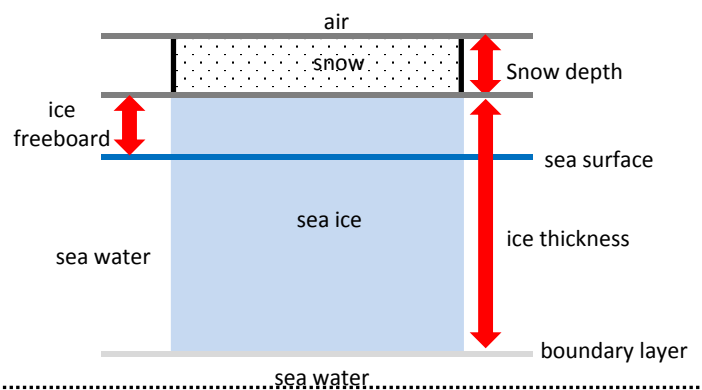
Snow and Ice conditions

Snow depth [m]:

Ice thickness [m]:

Ice Freeboard [m]:

Ice type: second-year ice



Required additional information for snow buoys

Snow thickness under sensors [m]: (3 measurements per sensor)

Sensor 1:

Sensor 2:

Sensor 3:

Sensor 4:

Required additional information for IMB (thermistor)

Thermistor chain length [m]:

Sensor interval [cm]:

Sensor numbers at interfaces

Sensor air - snow:

Sensor snow - ice:

Sensor sea surface:

Sensor ice - water:

Additional information (comments, weather, topography, ice floe size, etc.)

good weather with good visibility; deployment of array of eight buoys by helicopter from 3:30 to 5:30 UTC; small floes in ice margin did not allow a regular grid, however, target scales of 15km and 40km were covered; array dimension at deployment: 84km x 32km.

Meteorological conditions at 4 UTC at Polarstern:

air temperature: -1.4°C; water temperature: -1.7°C; pressure: 1013 hPa; humidity: 99%; wind speed 4.9 m/s; wind direction: 178°; visibility 42 km; ceiling 8900 ft

Buoy deployment report



ALFRED-WEGENER-INSTITUT
HELMHOLTZ-ZENTRUM FÜR POLAR-
UND MEERESFORSCHUNG

Buoy information

Buoy name: 2018P77

Modem-ID: 300234011882340

Buoy type: Microstar Drifter

Deployment information

Date and Time (Time zone): 24.09.2018, 04:30 UTC

Position (Lat/Long): 81.624°N/142.079°E

Region: Arctic Ocean, north of Laptev Sea

Name and Institute: owner: AWI; deployment: Gunnar Spreen, Univer. of Bremen

Contact e-mail: gunnar.spreen@uni-bremen.de

Expedition name: Polarstern PS115/2

Means of deployment: Helicopter

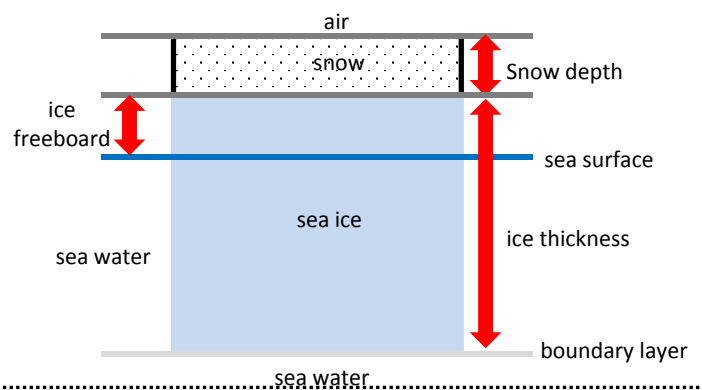
Snow and Ice conditions

Snow depth [m]:

Ice thickness [m]:

Ice Freeboard [m]:

Ice type: **second-year ice**



Required additional information for snow buoys

Snow thickness under sensors [m]: (3 measurements per sensor)

Sensor 1:

Sensor 2:

Sensor 3:

Sensor 4:

Required additional information for IMB (thermistor)

Thermistor chain length [m]:

Sensor interval [cm]:

Sensor numbers at interfaces

Sensor air - snow:

Sensor snow - ice:

Sensor sea surface:

Sensor ice - water:

Additional information (comments, weather, topography, ice floe size, etc.)

good weather with good visibility; deployment of array of eight buoys by helicopter from 3:30 to 5:30 UTC; small floes in ice margin did not allow a regular grid, however, target scales of 15km and 40km were covered; array dimension at deployment: 84km x 32km.

Meteorological conditions at 4 UTC at Polarstern:

air temperature: -1.4°C; water temperature: -1.7°C; pressure: 1013 hPa; humidity: 99%; wind speed 4.9 m/s; wind direction: 178°; visibility 42 km; ceiling 8900 ft

Buoy deployment report



ALFRED-WEGENER-INSTITUT
HELMHOLTZ-ZENTRUM FÜR POLAR-
UND MEERESFORSCHUNG

Buoy information

Buoy name: 2018P79

Modem-ID: 300234011885340

Buoy type: Microstar Drifter

Deployment information

Date and Time (Time zone): 24.09.2018, 04:30 UTC

Position (Lat/Long): 81.422°N/142.582°E

Region: Arctic Ocean, north of Laptev Sea

Name and Institute: owner: AWI; deployment: Gunnar Spreen, University of Bremen

Contact e-mail: gunnar.spreen@uni-bremen.de

Expedition name: Polarstern PS115/2

Means of deployment: Helicopter

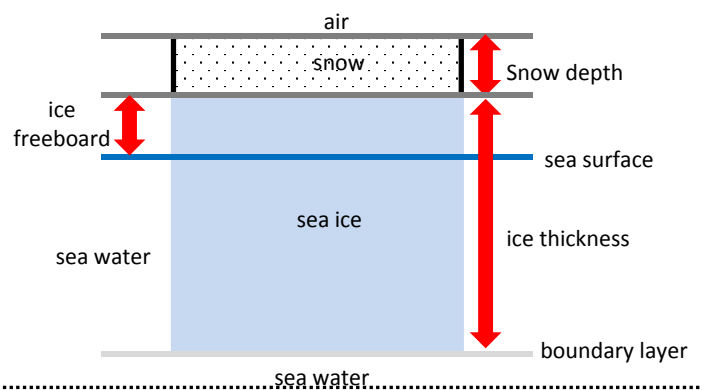
Snow and Ice conditions

Snow depth [m]:

Ice thickness [m]:

Ice Freeboard [m]:

Ice type: **second-year ice**



Required additional information for snow buoys

Snow thickness under sensors [m]: (3 measurements per sensor)

Sensor 1:

Sensor 2:

Sensor 3:

Sensor 4:

Required additional information for IMB (thermistor)

Thermistor chain length [m]:

Sensor interval [cm]:

Sensor numbers at interfaces

Sensor air - snow:

Sensor snow - ice:

Sensor sea surface:

Sensor ice - water:

Additional information (comments, weather, topography, ice floe size, etc.)

good weather with good visibility; deployment of array of eight buoys by helicopter from 3:30 to 5:30 UTC; small floes in ice margin did not allow a regular grid, however, target scales of 15km and 40km were covered; array dimension at deployment: 84km x 32km.

Meteorological conditions at 4 UTC at Polarstern:

air temperature: -1.4°C; water temperature: -1.7°C; pressure: 1013 hPa; humidity: 99%; wind speed 4.9 m/s; wind direction: 178°; visibility 42 km; ceiling 8900 ft

Buoy deployment report



ALFRED-WEGENER-INSTITUT
HELMHOLTZ-ZENTRUM FÜR POLAR-
UND MEERESFORSCHUNG

Buoy information

Buoy name: 2018P65

Modem-ID: 300234011889340

Buoy type: Microstar Drifter

Deployment information

Date and Time (Time zone): 24.09.2018, 05:00 UTC

Position (Lat/Long): 81.739°N/140.824°E

Region: Arctic Ocean, north of Laptev Sea

Name and Institute: owner: AWI; deployment: Gunnar Spreen, University of Bremen

Contact e-mail: gunnar.spreen@uni-bremen.de

Expedition name: Polarstern PS115/2

Means of deployment: Helicopter

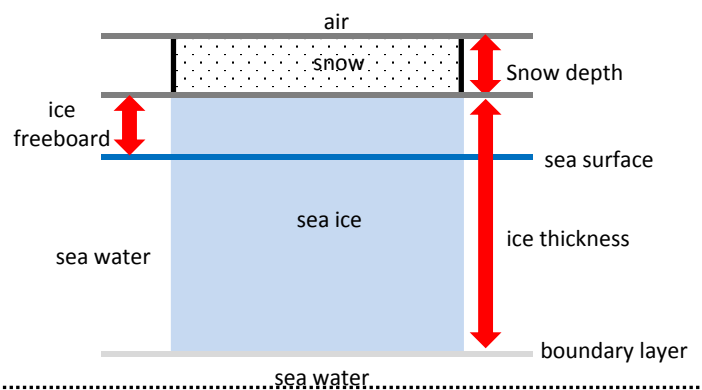
Snow and Ice conditions

Snow depth [m]:

Ice thickness [m]:

Ice Freeboard [m]:

Ice type: **second-year ice**



Required additional information for snow buoys

Snow thickness under sensors [m]: (3 measurements per sensor)

Sensor 1:

Sensor 2:

Sensor 3:

Sensor 4:

Required additional information for IMB (thermistor)

Thermistor chain length [m]:

Sensor interval [cm]:

Sensor numbers at interfaces

Sensor air - snow:

Sensor snow - ice:

Sensor sea surface:

Sensor ice - water:

Additional information (comments, weather, topography, ice floe size, etc.)

good weather with good visibility; deployment of array of eight buoys by helicopter from 3:30 to 5:30 UTC; small floes in ice margin did not allow a regular grid, however, target scales of 15km and 40km were covered; array dimension at deployment: 84km x 32km.

Meteorological conditions at 4 UTC at Polarstern:

air temperature: -1.4°C; water temperature: -1.7°C; pressure: 1013 hPa; humidity: 99%; wind speed 4.9 m/s; wind direction: 178°; visibility 42 km; ceiling 8900 ft

Buoy deployment report



ALFRED-WEGENER-INSTITUT
HELMHOLTZ-ZENTRUM FÜR POLAR-
UND MEERESFORSCHUNG

Buoy information

Buoy name: 2018P78

Modem-ID: 300234011882350

Buoy type: Microstar Drifter

Deployment information

Date and Time (Time zone): 24.09.2018, 04:46 UTC

Position (Lat/Long): 81.939°N/41.400°E

Region: Arctic Ocean, north of Laptev Sea

Name and Institute: owner: AWI; deployment: Gunnar Spreen, University of Bremen

Contact e-mail: gunnar.spreen@uni-bremen.de

Expedition name: Polarstern PS115/2

Means of deployment: Helicopter

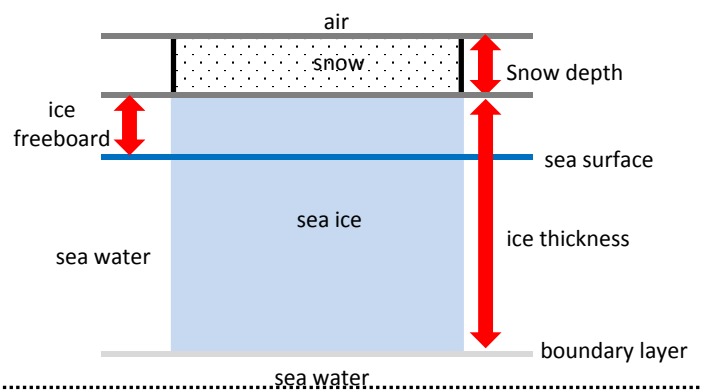
Snow and Ice conditions

Snow depth [m]:

Ice thickness [m]:

Ice Freeboard [m]:

Ice type: **second-year ice**



Required additional information for snow buoys

Snow thickness under sensors [m]: (3 measurements per sensor)

Sensor 1:

Sensor 2:

Sensor 3:

Sensor 4:

Required additional information for IMB (thermistor)

Thermistor chain length [m]:

Sensor interval [cm]:

Sensor numbers at interfaces

Sensor air - snow:

Sensor snow - ice:

Sensor sea surface:

Sensor ice - water:

Additional information (comments, weather, topography, ice floe size, etc.)

good weather with good visibility; deployment of array of eight buoys by helicopter from 3:30 to 5:30 UTC; small floes in ice margin did not allow a regular grid, however, target scales of 15km and 40km were covered; array dimension at deployment: 84km x 32km.

Meteorological conditions at 4 UTC at Polarstern:

air temperature: -1.4°C; water temperature: -1.7°C; pressure: 1013 hPa; humidity: 99%; wind speed 4.9 m/s; wind direction: 178°; visibility 42 km; ceiling 8900 ft

Buoy deployment report



ALFRED-WEGENER-INSTITUT
HELMHOLTZ-ZENTRUM FÜR POLAR-
UND MEERESFORSCHUNG

Buoy information

Buoy name: 2018P83

Modem-ID: 300234011888330

Buoy type: Microstar Drifter

Deployment information

Date and Time (Time zone): 24.09.2018, 05:00 UTC

Position (Lat/Long): 82.146°N/141.126°E

Region: Arctic Ocean, north of Laptev Sea

Name and Institute: owner: AWI; deployment: Gunnar Spreen, University of Bremen

Contact e-mail: gunnar.spreen@uni-bremen.de

Expedition name: Polarstern PS115/2

Means of deployment: Helicopter



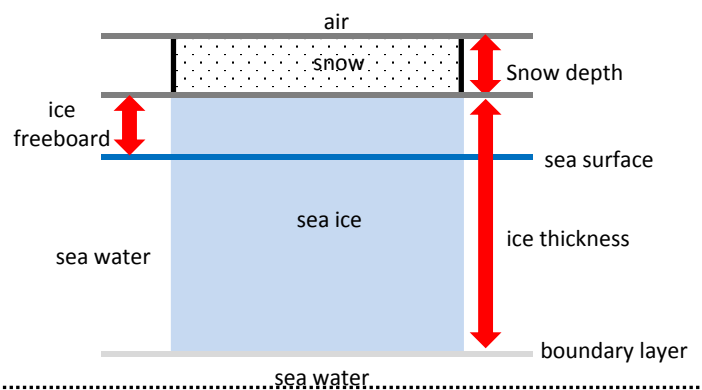
Snow and Ice conditions

Snow depth [m]:

Ice thickness [m]:

Ice Freeboard [m]:

Ice type: **second-year ice**



Required additional information for snow buoys

Snow thickness under sensors [m]: (3 measurements per sensor)

Sensor 1:

Sensor 2:

Sensor 3:

Sensor 4:

Required additional information for IMB (thermistor)

Thermistor chain length [m]:

Sensor interval [cm]:

Sensor numbers at interfaces

Sensor air - snow:

Sensor snow - ice:

Sensor sea surface:

Sensor ice - water:

Additional information (comments, weather, topography, ice floe size, etc.)

good weather with good visibility; deployment of array of eight buoys by helicopter from 3:30 to 5:30 UTC; small floes in ice margin did not allow a regular grid, however, target scales of 15km and 40km were covered; array dimension at deployment: 84km x 32km.

Meteorological conditions at 4 UTC at Polarstern:

air temperature: -1.4°C; water temperature: -1.7°C; pressure: 1013 hPa; humidity: 99%; wind speed 4.9 m/s; wind direction: 178°; visibility 42 km; ceiling 8900 ft

Buoy deployment report



ALFRED-WEGENER-INSTITUT
HELMHOLTZ-ZENTRUM FÜR POLAR-
UND MEERESFORSCHUNG

Buoy information

Buoy name: 2018P82

Modem-ID: 300234011883240

Buoy type: Microstar Drifter

Deployment information

Date and Time (Time zone): 24.09.2018, 06:00 UTC

Position (Lat/Long): 81.944°N/142.191°E

Region: Arctic Ocean, north of Laptev Sea

Name and Institute: owner: AWI; deployment: Gunnar Spreen, University of Bremen

Contact e-mail: gunnar.spreen@uni-bremen.de

Expedition name: Polarstern PS115/2

Means of deployment: Helicopter



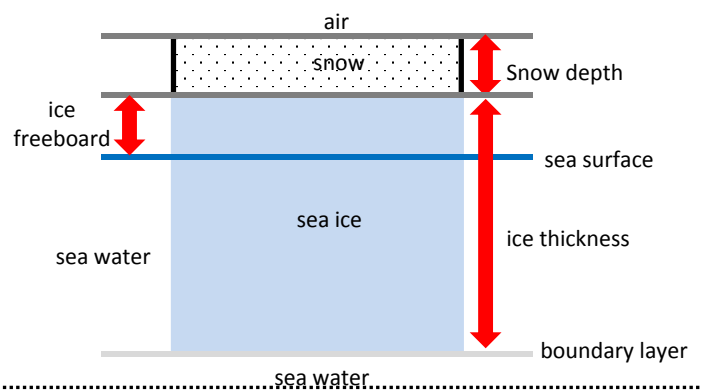
Snow and Ice conditions

Snow depth [m]:

Ice thickness [m]:

Ice Freeboard [m]:

Ice type: **second-year ice**



Required additional information for snow buoys

Snow thickness under sensors [m]: (3 measurements per sensor)

Sensor 1:

Sensor 2:

Sensor 3:

Sensor 4:

Required additional information for IMB (thermistor)

Thermistor chain length [m]:

Sensor interval [cm]:

Sensor numbers at interfaces

Sensor air - snow:

Sensor snow - ice:

Sensor sea surface:

Sensor ice - water:

Additional information (comments, weather, topography, ice floe size, etc.)

good weather with good visibility; deployment of array of eight buoys by helicopter from 3:30 to 5:30 UTC; small floes in ice margin did not allow a regular grid, however, target scales of 15km and 40km were covered; array dimension at deployment: 84km x 32km.

Meteorological conditions at 4 UTC at Polarstern:

air temperature: -1.4°C; water temperature: -1.7°C; pressure: 1013 hPa; humidity: 99%; wind speed 4.9 m/s; wind direction: 178°; visibility 42 km; ceiling 8900 ft

Buoy deployment report



ALFRED-WEGENER-INSTITUT
HELMHOLTZ-ZENTRUM FÜR POLAR-
UND MEERESFORSCHUNG

Buoy information

Buoy name: 2018P76

Modem-ID: 300234011881340

Buoy type: Microstar Drifter

Deployment information

Date and Time (Time zone): 24.09.2018, 05:30 UTC

Position (Lat/Long): 81.801°N/141.988°E

Region: Arctic Ocean, north of Laptev Sea

Name and Institute: owner: AWI; deployment: Gunnar Spreen, University of Bremen

Contact e-mail: gunnar.spreen@uni-bremen.de

Expedition name: Polarstern PS115/2

Means of deployment: Helicopter



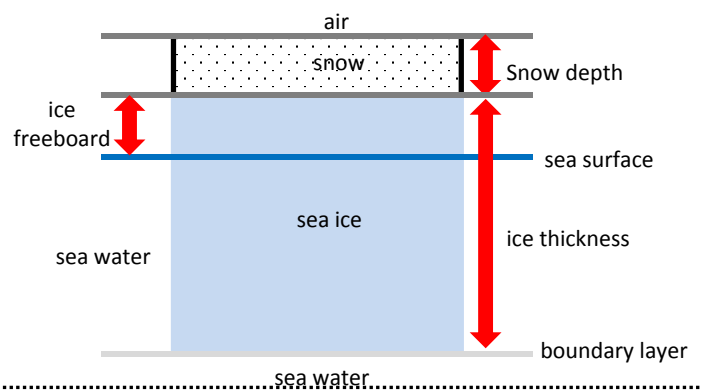
Snow and Ice conditions

Snow depth [m]:

Ice thickness [m]:

Ice Freeboard [m]:

Ice type: **second-year ice**



Required additional information for snow buoys

Snow thickness under sensors [m]: (3 measurements per sensor)

Sensor 1:

Sensor 2:

Sensor 3:

Sensor 4:

Required additional information for IMB (thermistor)

Thermistor chain length [m]:

Sensor interval [cm]:

Sensor numbers at interfaces

Sensor air - snow:

Sensor snow - ice:

Sensor sea surface:

Sensor ice - water:

Additional information (comments, weather, topography, ice floe size, etc.)

good weather with good visibility; deployment of array of eight buoys by helicopter from 3:30 to 5:30 UTC; small floes in ice margin did not allow a regular grid, however, target scales of 15km and 40km were covered; array dimension at deployment: 84km x 32km.

Meteorological conditions at 4 UTC at Polarstern:

air temperature: -1.4°C; water temperature: -1.7°C; pressure: 1013 hPa;

humidity: 99%; wind speed 4.9 m/s; wind direction: 178°; visibility 42 km;

ceiling 8900 ft

Buoy deployment report



ALFRED-WEGENER-INSTITUT
HELMHOLTZ-ZENTRUM FÜR POLAR-
UND MEERESFORSCHUNG

Buoy information

Buoy name: 2018P74

Modem-ID: 300234061872720

Buoy type: Surface Velocity Profiler

Deployment information

Date and Time (Time zone): 28.09.2018, 05:03 UTC

Position (Lat/Long): 82.131°N/148.727°E

Region: Arctic Ocean, north of Laptev Sea

Name and Institute: owner: U. Washington; deployment: Gunnar Spreen, U. Bremen

Contact e-mail: gunnar.spreen@uni-bremen.de

Expedition name: Polarstern PS115/2

Means of deployment: Helicopter

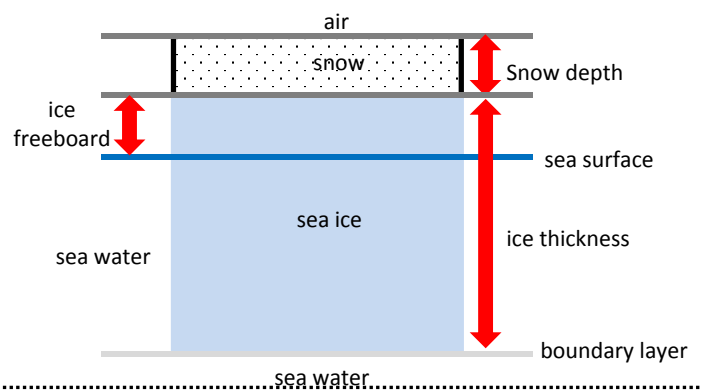
Snow and Ice conditions

Snow depth [m]:

Ice thickness [m]: approx. 1.5 m

Ice Freeboard [m]:

Ice type: second-year ice



Required additional information for snow buoys

Snow thickness under sensors [m]: (3 measurements per sensor)

Sensor 1:

Sensor 2:

Sensor 3:

Sensor 4:

Required additional information for IMB (thermistor)

Thermistor chain length [m]:

Sensor interval [cm]:

Sensor numbers at interfaces

Sensor air - snow:

Sensor snow - ice:

Sensor sea surface:

Sensor ice - water:

Additional information (comments, weather, topography, ice floe size, etc.)

deployment by helicopter but no ice thickness measurements due to swell;
close by melt pond; floe size approx. 100m x 200m; cloudy sky

Buoy deployment report



ALFRED-WEGENER-INSTITUT
HELMHOLTZ-ZENTRUM FÜR POLAR-
UND MEERESFORSCHUNG

Buoy information

Buoy name: 2018P69

Modem-ID: 300234065800040

Buoy type: Surface Velocity Profiler

Deployment information

Date and Time (Time zone): 03.10.2018, 07:50 UTC

Position (Lat/Long): 81.387°N/128.521°E

Region: Arctic Ocean, north of Laptev Sea

Name and Institute: owner: NOAA; deployment: Gunnar Spreen, Univer. of Bremen

Contact e-mail: gunnar.spreen@uni-bremen.de

Expedition name: Polarstern PS115/2

Means of deployment: Mummy Chair from Polarstern



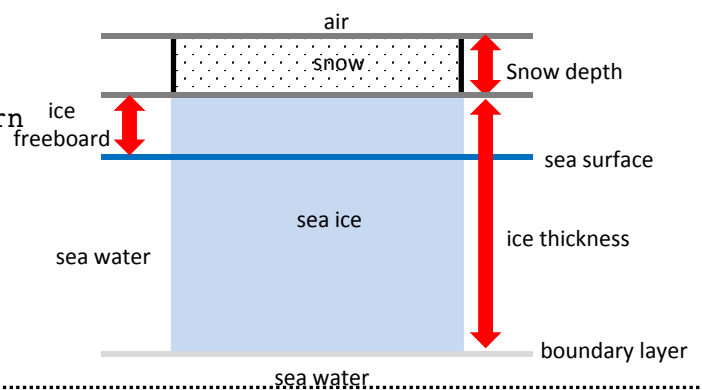
Snow and Ice conditions

Snow depth [m]: 0.0

Ice thickness [m]: 0.05

Ice Freeboard [m]: 0.13

Ice type: **pancake ice**



Required additional information for snow buoys

Snow thickness under sensors [m]: (3 measurements per sensor)

Sensor 1:

Sensor 2:

Sensor 3:

Sensor 4:

Required additional information for IMB (thermistor)

Thermistor chain length [m]:

Sensor interval [cm]:

Sensor numbers at interfaces

Sensor air - snow:

Sensor snow - ice:

Sensor sea surface:

Sensor ice - water:

Additional information (comments, weather, topography, ice floe size, etc.)

on pancake ice; buoy got partly submerged in the water; floe size approx. 2m x 1m;

air temperature: -1.6°C; water temperature: -1.8°C; pressure: 994 hPa;
humidity: 98%; wind speed 8.7 m/s; wind direction: 59°; visibility 1 km;
ceiling 210 ft

Buoy deployment report



ALFRED-WEGENER-INSTITUT
HELMHOLTZ-ZENTRUM FÜR POLAR-
UND MEERESFORSCHUNG

Buoy information

Buoy name: 2018P70

Modem-ID: 300234065801030

Buoy type: Surface Velocity Profiler

Deployment information

Date and Time (Time zone): 04.10.2018, 03:14 UTC

Position (Lat/Long): 81.821°N/119.611°E

Region: Arctic Ocean, north of Laptev Sea

Name and Institute: owner: NOAA; deployment: Gunnar Spreen, Univer. of Bremen

Contact e-mail: gunnar.spreen@uni-bremen.de

Expedition name: Polarstern PS115/2

Means of deployment: Mummy Chair from Polarstern



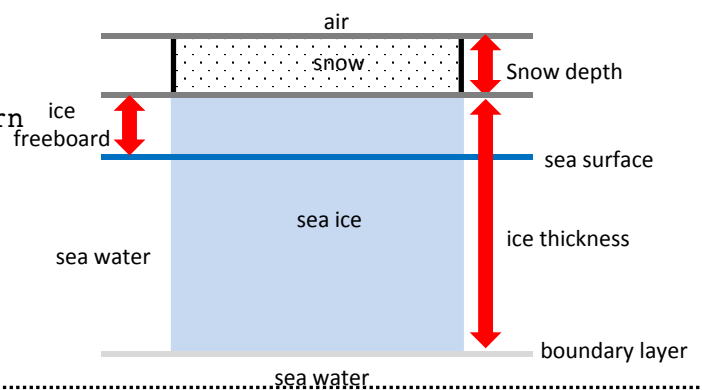
Snow and Ice conditions

Snow depth [m]: 0.03

Ice thickness [m]: 1.92

Ice Freeboard [m]: 0.13

Ice type: pancake ice



Required additional information for snow buoys

Snow thickness under sensors [m]: (3 measurements per sensor)

Sensor 1:

Sensor 2:

Sensor 3:

Sensor 4:

Required additional information for IMB (thermistor)

Thermistor chain length [m]:

Sensor interval [cm]:

Sensor numbers at interfaces

Sensor air - snow:

Sensor snow - ice:

Sensor sea surface:

Sensor ice - water:

Additional information (comments, weather, topography, ice floe size, etc.)

on ice floe next to Polarstern; deployment by mummy chair without ice drilling; floe size approx. 30 m x 10 m; cloudy sky
air temperature: -1.7°C ; water temperature: -1.9°C ; pressure: 992 hPa;
humidity: 98%; wind speed 11.4 m/s; wind direction: 140° ; visibility 10 km; ceiling 300 ft
future of buoy can be considered uncertain :) (Polar Bear visit after deployment)

APPENDIX

A.7 THE “ARCTRAIN FLOATING UNIVERSITY” ONBOARD OF POLARSTERN EXPEDITION PS115/2

A.7	THE “ARCTRAIN FLOATING UNIVERSITY” ONBOARD OF POLARSTERN EXPEDITION PS115/2	
A.7.1	Day to Day Life and Work	
A.7.1.1	Day to Day Duties.....	
A.7.1.2	Experiences from ArcTrain Students.....	
A.7.2	Marine Geology.....	
A.7.2.1	Coring.....	
A.7.2.2	Lab-work.....	
A.7.2.3	Overall – PS115/2 : marine geology work	
A.7.3	Meteorology	
A.7.4	Sea Ice.....	
A.7.4.1	Preliminary Analysis of Data Collected for the Ice Watch Program During Expedition PS115.2.....	
A.7.4.2	Infrared Camera and Thin Ice Thickness.....	
A.7.4.3	Preliminary Analysis of Hyperspectral Images Captured with the SPECIM IQ Camera During PS115/2.....	
A.7.4.4	Ship Radar for Sea Ice Dynamics.....	
A.7.4.5	Sea Ice Buoy Analysis.....	
A.7.4.6	Sea Ice Thickness and Temperature/Salinity Profiles	

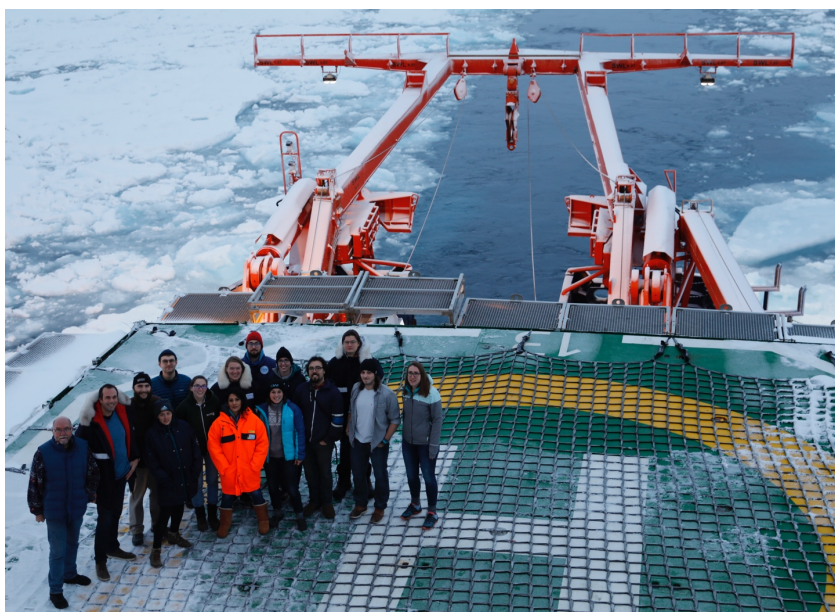


Figure 1: The ArcTrain Team saying farewell to the last sea ice on 6 October 2018.

A.7.1 Day to Day Life and Work

P. Bourgault (McGill), C. Brice (UQAM), C. Brunette (McGill),
M. Caron (UQAR), A. Desmarais (McGill), R. Lenny (UoB-MARUM),
A. Kazlova (UoB-IEP), R. Love (MUoN), D. Murashkin (UoB-IEP),
N. Ridenour (UoAE), D. Ringeisen (AWI), S. Samimi (UoC), A. Vlug (UoB-MARUM)

A.7.1.1 Day to Day Duties

Over the course of expedition PS115/2, the ArcTrain students have taken care of several monitoring programs. The 13 students were an ideal work force for the upkeep of the different watches that took place more or less 24/7 on the ship.

Ice Watch

The Ice Watch is an international project that consists of a database of shipborne observations of sea ice from vessels travelling into polar oceans. Every hour, one of us went to the Bridge (where the navigation operations take place) to have an optimal view of the water and ice surrounding the ship within 1 nautical mile. We recorded some basic information about the ship course (position, speed, direction), about weather (fog, rain, snow, clouds), about fauna if any, and most importantly we provided estimates of the sea ice cover: concentration, thickness, snow cover, topography, melt, and presence of algae or sediments. As a preliminary analysis, we compared our Ice Watch reports to remote sensing data from the AMSR2 satellite (see Appendix A.7.4.1). We performed Ice Watch observations from Sept. 7 until Oct. 6. A total of 329 sea ice observations were realized.



Figure 1 Pictures from the 23.09.2018 - 04:06 UTC Ice Watch report (Pascal Bourgault)

Parasound

We also took turns for the Parasound watch, a responsibility shared with other students taking part in the expedition. The Atlas Parasound is an echosounder instrument that is used by the seismic geology team for retrieving profiles of the sub-bottom ocean (see Cruise Report Section 7.2 for more details). During our 2-hour daily watchkeeping shift (or 4-hour night shifts), we made sure that the instrument is correctly tracking the ocean depth, fine-tuned the amplification of the signal, and we ensured that the profiles displayed and printed properly. All that in real time so that sub-bottom ocean profiles would be ready for operational use: the profiles helped the geologists decide on where to take sediment cores, and also guided the scientific team on what areas were worth exploring further.

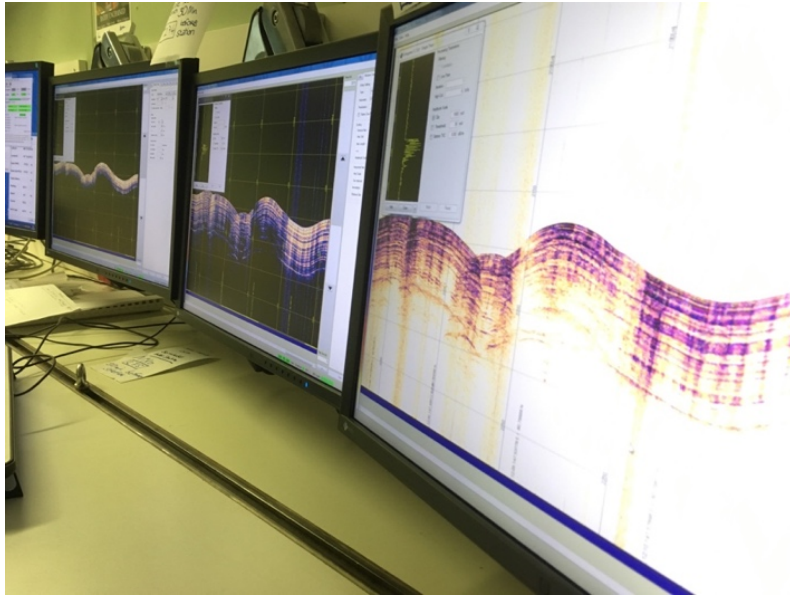


Figure 2. Setup for the Parasound Watch.

Marine Mammal Watch

We were also in charge of the marine mammal watch, in coordination with the geophysics team. Seismic reflection surveys are useful in retrieving the structure of sediments at the bottom of the ocean, but they require the use of air pulsers that emit a sound recognized by marine mammals. Whenever the seismic survey took place, night or day, to avoid perturbing the fauna, we would be taking at the Bridge and reported any mammal sighting to the geophysics team, so they can reduce the intensity of the pulses or stop them to mitigate impact on the wildlife.



Figure 3 Amélie Desmarais watching for marine mammals.

Polar bear watch

During the cruise in addition to shipboard observations fieldwork was done on the sea ice. By going on the sea ice in the Arctic you enter the habitat of the polar bear. In order to work safely on the sea ice you need a polar bear guard. Three of the ArcTrain students participated in the polar bear protection training, which prepared them for being a guard in the field. Once on the

ice as a guard your only task is to look out for polar bears, so others can do their science safely. More information about this training can be found in one of the ArcTrain Blog Posts (<http://arctrain.de/polar-bear-protection-training>). On board of the ship we got a refreshment training. When fieldwork was done next to the ship there would be two people acting as polar bear watch on the ship, in addition to the polar bear guard on the ice. This made the chance of a polar bear encounter even smaller. Once a polar bear would be spotted no one was allowed to go on the ice and everybody on the ice would be informed to immediately come back to the ship. Therefore each time a curious polar bear would come to checkout the ship, everybody would be safely on board.

A.7.1.2 Experiences from ArcTrain Students

Pascal Bourgault: "The Arctic ocean, object of our thesis and dreams, struck us with its wonders. Everything here seems incredible, whether it is polar bears surviving on tiny ice floes or the Kastenlot brining back half-a-million-years old mud. The geology work was non-stop and sleepless, but also joyful and with a strong team spirit. The ice work, well, was full of hope, but when it happened, what a majestic show!"

Charles Brunette: "I got mindblown by something new on every single day of this expedition, whether it was walking on sea ice, watching the Northern Lights, or just knowing that we are steaming over 4000m+ deep waters in the Gakkel Deep region, or learning that the Lomonosov Ridge is actually a piece of the Barents-Kara shelf that started to drift toward the central Arctic millions of years ago. Mind. Blown. To me, Polarstern is a very creative environment, where we all go out of ourselves to find solutions to the challenges that come up. We're making science happen. Kudos to all my friends, it was a fun ride."

Amélie Desmarais: "It's amazing to finally be able to see and do field work on sea ice, the subject of my everyday work. It was a first research cruise experience for me and I am glad to say that discovering the life on board and the people was a highlight of this trip. Well, that and the polar bears!"

Natasha Ridenour: "As part of my first cruise experience, I learned that obtaining observations are way more challenging than I thought. Not only do the weather conditions have to be right, but also ice conditions as well as the ocean conditions. I also got to see sea ice first hand, which was truly an awesome experience (not to mention all the other Arctic experiences we had), as well as useful, coming from a modelling background."

Damien Ringeisen: "When you have been working on sea ice modelling for 2 years, it is a great chance to finally meet sea ice face to face, to look a polar bear in the eyes, to get a change from my daily modelling routine, to gave me a beautiful insight on the human side of Arctic science, as opposition to the data part. It is a beautiful experience to share this ride with so many different people, of different origins, of different background."

Camille Brice: "At first, I was not supposed to be onboard the Floating University, but I got really lucky and ArcTrain offered me a last minute place on the Polarstern. Best news ever! This cruise was not my first one, but no matter how many expeditions I have done, every single one is unique and amazing. And this expedition was crazy! I had the chance to work with an awesome geo-team (night and day!), see polar bears, dolphins, whales, stay outside for hours enjoying the northern lights, and of course meet the most awesome ArcTrain students."

Anouk Vlug: "The expedition was an amazing experience. I very much enjoyed that, as an ArcTrain student, we could join different teams and learn more about the different disciplines. I never had realized before how many types of sea ice there are. The Arctic scenery felt at times surreal, both the constantly changing sea ice around us and the difficulty with finding thick ice flows while being so far up North."

Ryan Love: "I have to admit I have a whole new appreciation for where quite a lot of our understanding of the proxies and the data itself comes from. I knew there was quite a bit of manual work involved but getting to be involved in most all stages of the sampling and a small bit of post-processing has been quite helpful and certainly gives me a better understanding of the uncertainty with respect to some of it. At the least I have also learned that the Arctic has a good number of unique problems from a marine geology perspective (and thus paleoclimate perspective) and the solutions to them, or lack thereof, are interesting. I'd probably have a bit more context for some of it had I had the chance to take a few core geology courses at some point but that's never worked out, perhaps some reading for post-PhD. Luckily, there was also quite a number of students on this cruise. Rüdiger and Michael have been great about answering questions and explaining things to me where the gaps appear for everyone, and unsurprisingly quite often for me."

A.7.2 Marine Geology

Camille Brice (UQAM), Myriam Caron (UQAR), Rémi Ienny (UoB-MARUM),
Ryan Love (MUoN), Anouk Vlug (UoB-MARUM)

The expedition PS115/2 main purpose was to study the southern Lomonosov Ridge, mostly orientated for geoscience (marine geology and geophysics) aspects but also sea-ice observations, drift buoys and meteorology. This expedition was also hosting the second ArcTrain Floating University, for which we are presenting here an overview of our experiences as ArcTrain students. Among the different working groups on board, our little team decided to spend most of our time in the marine geology group. This choice was evident for Camille and Myriam as we are both geologist. Ryan and his passion for photography was ideal, as we needed a photographer in charge of taking pictures of all the cores. Finally, Anouk and Rémi were both very interested to discover more extensively the geology world on a ship, which was definitely an enriching experience.

The two main objectives for the marine geology part:

- 1) High-resolution reconstruction of changes in paleoclimate, paleoceanic circulation, paleoproductivity, and sea-ice distribution during Late Quaternary
- 2) Reconstruction of long-term history of the Mesozoic and Cenozoic Arctic Ocean and its environmental evolution from a warm (Greenhouse) to an ice-covered polar (Icehouse) ocean

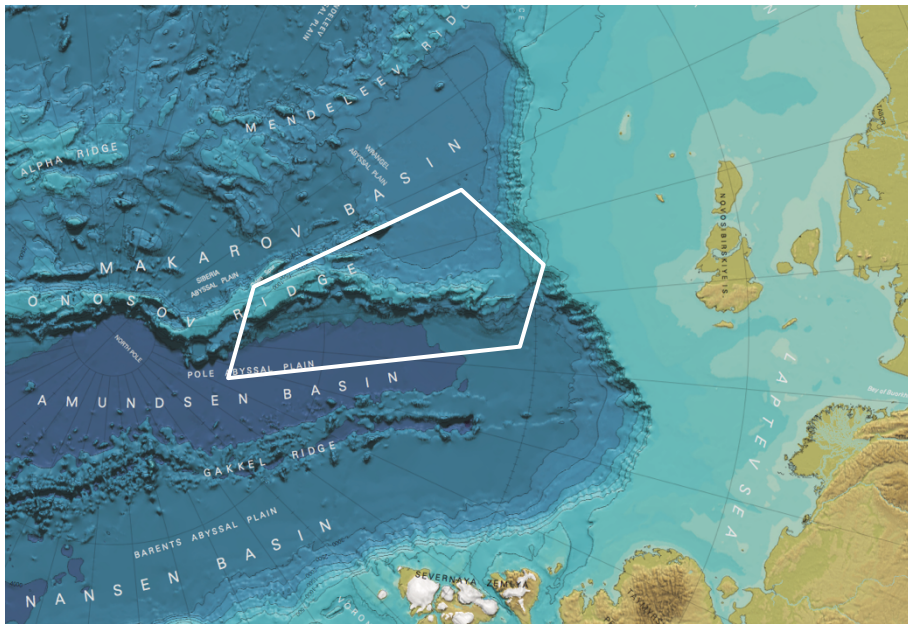


Figure 4: map of the eastern Arctic Ocean with the main work area of PS115/2: the Lomonosov Ridge (map: Rüdiger Stein)

To answer these goals, the plan is to look at the seafloor because marine sediment is recording all of the past oceanographic and climatic changes, which were happening during these periods. Thus, the work of a geologist on board consists mainly of coring the seafloor to get a better idea of those changes, usually associated to geophysical analyses, which will help finding the best locations for these coring.

A.7.2.1 Coring

a) Giant Box Corer (GKG)

Sediment sampling using a Giant Box Corer (GKG) (50 x 50 x 50 cm³) was performed at most stations in order to retrieve the water-sediment interface. The GKG allows to sample undisturbed surface sediments, which further provides information on modern environment at the core site. Once the corer is brought back on the deck, the first step consists of sucking out the water at the surface of the sediment (Figure 2A), which will allow us to get access to the sediment surface (always a pleasure to do this step). Colour images of the surface were then taken immediately once the corer is moved on the side and is ready for sampling. Afterward, multiple subsamplings were made on the GKG. Then, the surface is checked for macro-benthic fauna. Two plastic liners were pushed in the box in order to have the complete stratigraphy record of the GKG. 5 to 6 different surface sediments samples are taken for multiple analysis such as dinocysts or DNA (Figure 2B). Then, the box core is opened by unscrewing one of its side, and after taking some pictures, we are ready to sample two square boxes, X-ray slabs and occasionally discrete samples (Figure 2B). All of these samples need to be properly cleaned, labelled and taped following the sub-sampling, ready to be stored. Finally, the last step consists of throwing the leftover mud back into the sea and clean the box corer, ready for the next round.



Figure 5: A) Sucking the water out of the box corer (Photo: Ryan Love)
B) Box core sub-sampling (Photo: Heike Zimmermann)

b) Multi-Corer (MUC)

The multi-corer (MUC or disguised Octopus, Figure 3A) is composed of 8 tubes of 10 cm diameter lowered to the seafloor to sample the water-sediment interface, similarly to the Box Corer. Once the corer is back onboard, the tricky part is to put caps (Figure 3B) on each of these tubes without losing sediment, so we can then bring them inside.

In order to keep the surface sediment undisturbed, the 8 tubes have to be subsampled within the upcoming days, ideally right after the coring. Subsampling of MUC consists of pushing the sediments out of the tubes and putting them in a labelled bag for every cm. Overall, 5 multicores were entirely subsampled at every cm and the 3 leftovers were only used for the surface sediments.



Figure 6: A) Multi-corer on the deck (Photo: Ryan Love) B) Putting the caps on. (Photo: Gerit Birnbaum)

c) Gravity Corer (SL)

The gravity cores were retrieved with a 5 to 10 meters long gravity corer. Plastic liners with an outer diameter of 11 cm were put into the steel barrel. After retrieval, the plastic liners were cut into sections of approximately 100 cm length with the help of the special “Rudy’s magic meter” (Figure 4). The tubes were then covered with plastic caps, taped and labelled, and subsequently stored at +5°C or frozen.



Figure 7: A) Getting the tubes out of the gravity corer / B) Rudy's magic meter to measure perfect 1-meter sections of the tube (Photos: Ryan Love)

d) Kastenlot (KAL)

The Kastenlot is a massive square corer (two parts 6 meters long and 50 cm wide) which allows minimal sediment disturbance during the coring. With its 3.5 tons weight on top of it, it is lowered to the seafloor by gravity to collect a few more tons of sediment. Once back on board, it is a challenge to bring the two parts of the Kastenlot inside the wet lab (Figure 5A), which takes about 1 hour per part. Indeed, three different cranes and at least 5 persons are needed to get the Kastenlot inside.



Figure 8: A) Getting the Kastenlot inside the wet lab and B) Working on the Kastenlot. (Photo: Gerit Birnbaum)

Once inside, we know that it is going to take at least two days to sample the whole Kastenlot (Figure 5B). Thus, we need to be available and sometimes, it is necessary to wait a couple of days before opening it, as we often have others stations and coring at the same time (GKG, SL or MUC). The opening of the Kastenlot is always a big moment for everyone on the ship, especially for the chief scientist who wants to be called after each opening. However, it is also a challenging step, as we need to be careful to avoid any loss of sediment while opening the boxes. Then, the sampling is organized in three different steps for three different layers of sampling (Figure 6). As the Kastenlot offers a sufficient amount of sediment, it is possible to get samples for several types of analyses including square boxes for physical properties and X-ray slabs (non-destructive) and others geological analyses (destructive), as well as square boxes for archive.

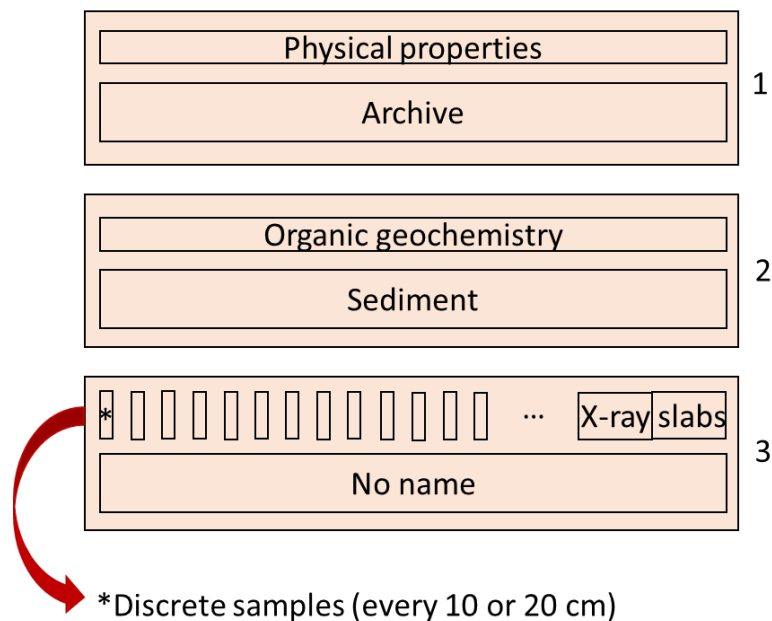


Figure 9: The three layers of sub-sampling of the Kastenlot with the corresponding labels.

e) Dredge

The Dredge consisted of lowering a metallic net to the seafloor while the ship is still moving slowly on a certain distance and hopefully, this net will catch as much rocks as possible (Figure 7). Those rocks can help the geologist to better understand the geological situation of a specific area, as there are either originating from this location, or have been brought by ice-rafted debris. Here, during PS115/2, two dredge have been conducted during the last geological stations and for both of them, similar rocks have been recovered (mix of siltstones and sandstones) more than likely originating from this specific location where they have been taken. As an example of the utility to collect such rocks, some of them had manganese oxidation forming in cracks, which might serve later for dating, and timing of the geological events.

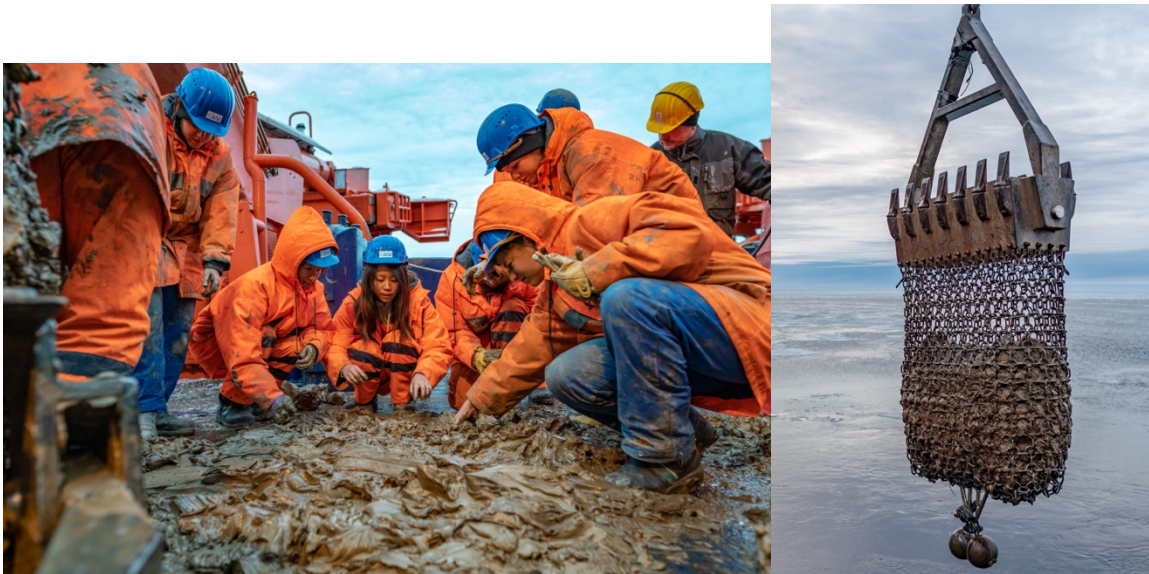


Figure 10: Dredge and the geology team looking for rocks (Photos: Christian Rohleder)

A.7.2.2 Lab-work

a) Sub-sampling (Discrete samples, X-ray slabs)

For each of the cores collected on board, we used different sampling methods in order to divide the sediment towards different type of future analysis. As described above for the GKG, MUC and Kastenlot, those subsampling methods consists mainly of push cores and square boxes, but also with smaller samples such as X-ray slabs and discrete samples. X-ray slabs are very thin (1 cm high) plastic boxes (25 cm long) which were sub-sampled for the full depth of every box core and Kastenlot, and also of the few gravity cores opened on board. The purpose of those X-ray slabs will be to count ice-rafted debris (IRD) based on their size, as the X-ray will highlight those elements based on their higher density.

The sub-sampling of discrete samples consisted of collecting individual samples of sediment at a specific depth interval (e.g. every 10 cm). Once again, the choice between the different recipients used and quantity of material taken depends on the type of analysis, which are going to be used later on. Here for PS115/2, four main types of discrete samples were collected for each of the Kastenlot:

- Every 10 cm (Junjie Wu) in glass vials in order to study biomarkers, organic geochemistry?
- Every 10 cm (Ovie M Benson) in plastic pots in order to study the organic matter content.
- Every 20 cm (Frijhof Lemmel) in plastic bags for sieving and later foraminifera picking.
- Every 20 cm (Max Droellner): syringe for neodymium and plastic bags for mineralogy.

Since the Kastenlot and GKG allows recovering a largely sufficient amount of sediment, the most interesting facies and very often, the coarser layers were also sub-sampled by Max Droellner for Zircon analysis, which requires large quantity of sediment to sieve.

b) Sub-sampling the MUC

Each time the multi-corer (MUC) was used all 8 multicores were sampled in the wet lab on the ship. Four of those cores were cut into 1 cm thick slices. Each slice was packed separately. For three of the four cores these samples ended up in whirlpicks. For the fourth core as much sediment as possible from each slice was put into a glass container, that was then covered with an aluminum foil and closed with a plastic lid. Of the remaining four cores, for three cores only the surface, first centimeter, was sampled. These surfaces were packed in whirlpicks, one bag with one surface and the other with two surfaces. Except for the packaging, the same procedure was used to sample these seven cores.

The two people would place the core on the MUC stand, by removing the bottom plug from the core and putting it on the plug of the stand. Once on the stand the top plug would be removed and the surface water would be extracted with a hosepipe (Figure 8). The tube would be pushed down on the stand until the sediment would reach the top of the tube. Then the rotating disc would be put in place under the tube. Each full turn of the rotating disc on the screw would push sediment 1 cm up. This piece would then be cut off with a knife or a metal plate. In the case of a more fluid sample, a plastic ring would be used to make sure the sample won't drop (Figure 9). For each slice a clean cutting device would be used. Depending on the amount of people available a tasks division would be made for sampling. In all cases there would at least be two people present for sampling: one 'core-cutter' and at least one 'sediment-catcher'. In addition there was sometimes a 'knife-washer'. The 'knife-washer' would clean the cutting devices before each slice in a bucket of water.



Figure 11. Putting the core on the stand and removing the water from the tube. (Photo: Gerit Birnbaum)



Figure 12. Pushing the sediment to the top of the core and subsampling the core.
(Photo: Gerit Birnbaum)

The last core required a different sampling procedure. This core was sampled for DNA analyses of sea ice algae by Heike Zimmermann, from the sea ice group. Sampling for DNA analyses requires a different protocol than sampling for all the other purposes, because you need to avoid contamination with other sediment and your own DNA. Therefore there was a need to work very clean, in comparison with the other sampling in the wet lab. So instead of just washing the knife with water after cutting each sediment slice, the equipment had to be rinsed with DNA exitus, a product that destroys DNA, and then with water to remove the DNA exitus. In addition special suits, a mouth cap, special sleeves and two layers of gloves needed to be worn, to avoid contamination.

c) Sieving

Most of the samples on board were taken to do further analyses back on land. Preliminary analysis of some of the samples was done for the abundance of ice rafted debris (IRD) and foraminifera. These are normally a very small fraction of the total sediment sample. Therefore the samples need to be sieved with a 63 μm sieve, through which you can remove all the silt and clay particles. The sieve needed to be cleaned for each of the samples. This was done rinsing the sieve with water, blowing pressured air against the bottom of the sieve and using an ultra-sonic bath. The sieving of the sample was done with fresh water. The remainder of the sample would be flushed with water into a cup, which would then be put in a dry oven at 60 °C to get rid of all the water. After the water had evaporated, the sample was ready for analysis under the microscope.

d) Opening of cores / photos of the cores

For both the Kastenlot (KAL) and Schwerelot/Gravity-Core (SL) gears, before the cores can be photographically documented and described they must be opened. The procedure for the SL is quite straightforward and for us required only the use of a specialized core cutting rig and an amiable technician to use it. This rig cuts the core liner twice on each side, with a ~1 cm gap between the cuts which run the length of the core. This double cut allows for the working 'half' of the SL core to be sampled with X-Ray slabs (or, if X-Ray slabs are not required, some other method of sampling requiring small volumes of sediment could be implemented), while the archive 'half' needs only cleaning and labelling before being migrated to the photo station.



Figure 13: Niko Wöhljtjen opening a SL core prior to cleaning, documenting, and sampling. (Photo: Ryan Love)

The opening of a KAL core is a more involved process as the equipment is both larger and heavier than that of the SL gear. First and foremost, the casing halves need to be detached from each other, as there are fasteners spread along the length of the casing at ~30cm intervals. Subsequently the uppermost casing can be removed while the lower casing remains in place during the sampling. For the removal of the upper casing, we made use of a winch to lift one end of the KAL casing while manual force was used to lift the other end. While the casing is being lifted, members of the geology team inspect the core and work to ensure that there is clean separation between the casing and the sediment and to assist such a separation if required.



Figure 11: The opening of a KAL core by members of PS115/2 geology. This core featured the 'best case' scenario of a clean separation of the casing from the sediment. (Photo: Gerit Birnbaum)

For each of the 5 KAL cores which were taken a combination of photographic documentation procedures were used. Each KAL, upon initial opening and cleaning of the surface, was photographed in-situ each ~10cm (with a viewing angle permitting about 25cm to each side of the center). This is done as the sampling process naturally distorts and elongates the sediment core and introduces, albeit small, artifacts in the sediment layering with respect to depth. Documenting the cores in-situ without any of these distortions will allow for more exacting description of the cores and easier corrections due to sampling issues later on in the processing of the sediment core. Ideally this further photographic documentation of the Kastenlot cores will help reduce uncertainty in future analysis. Furthermore, after the sampling has been done and the sediment is stored in their archive boxes, these samples are photographed using a small photographic rigging along with accompanying data such as cruise, station and gear numbers as well as the depth range for each section.



Figure 12: Features of a KAL core which would otherwise be difficult to document without the in-situ photography. The top two images are of the same core at the surface, one showing prior to re-enforcement of the core for sampling and one showing the post. The bottom image is the image as produced using the photographic rigging. (Photo: Ryan Love)

Similarly, the gravity cores (SL) are documented using the photographic station in the wet lab. However, due to the nature of the SL there is no opportunity to document the core before it is subdivided into 1m sections. In this case, however, there is minimal distortion in the interior of the sediment core and such issues are generally restricted to the top and bottom of the liners; as such, there are generally only 2, potentially 4 for a 10m core, areas of noticeable disturbance to the sediment in the SL. Both halves of the SL core are photographed for documentation as they may not be entirely symmetric and features such as drop stones may only be present in one of the two halves. Similar to the KAL, these photos also document relevant data such as the depth and station number.

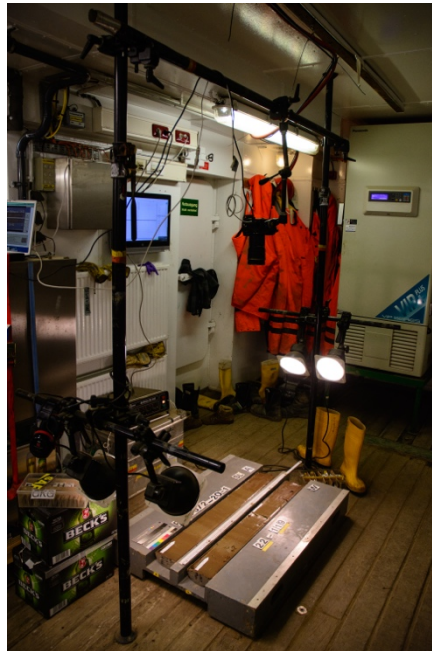


Figure 13: The photographic rigging as used in PS115/2 marine geology lab. (Photo: Ryan Love)

A.7.2.3 Overall – PS115/2 : marine geology work

Overall, 20 Box cores (GKG), 5 Kastenlot (KAL), 31 Gravity cores (SL) and 10 Multi-cores (MUC) were collected during the PS115/2 expedition. For some of these cores, relatively old sediments (Cenozoic: Miocene and Oligocene layers) were identified which is very positive for the goals of the expedition. Also generally, the last glacial cycles were observed in the cores, with for example the well cited (during this cruise) MIS6 glacial period. A proper chronology will have to wait for more dating analyses after the cruise but the Chief Scientist and geologists on board were quite optimistic about the outcomes of these numerous cores collected.

As for us, ArcTrain students, it was without any doubt a very enriching experience to be part of this expedition, as much for every day geologist like Camille and Myriam but also for the non-geologist of our group: Anouk, Rémi and Ryan (Figure 14). As our regular work consists mostly of computer work, it is very satisfying to do some more technical and manual work, especially if this work allows us to have so much great and happy moments because that is what is was mainly a lot of fun!

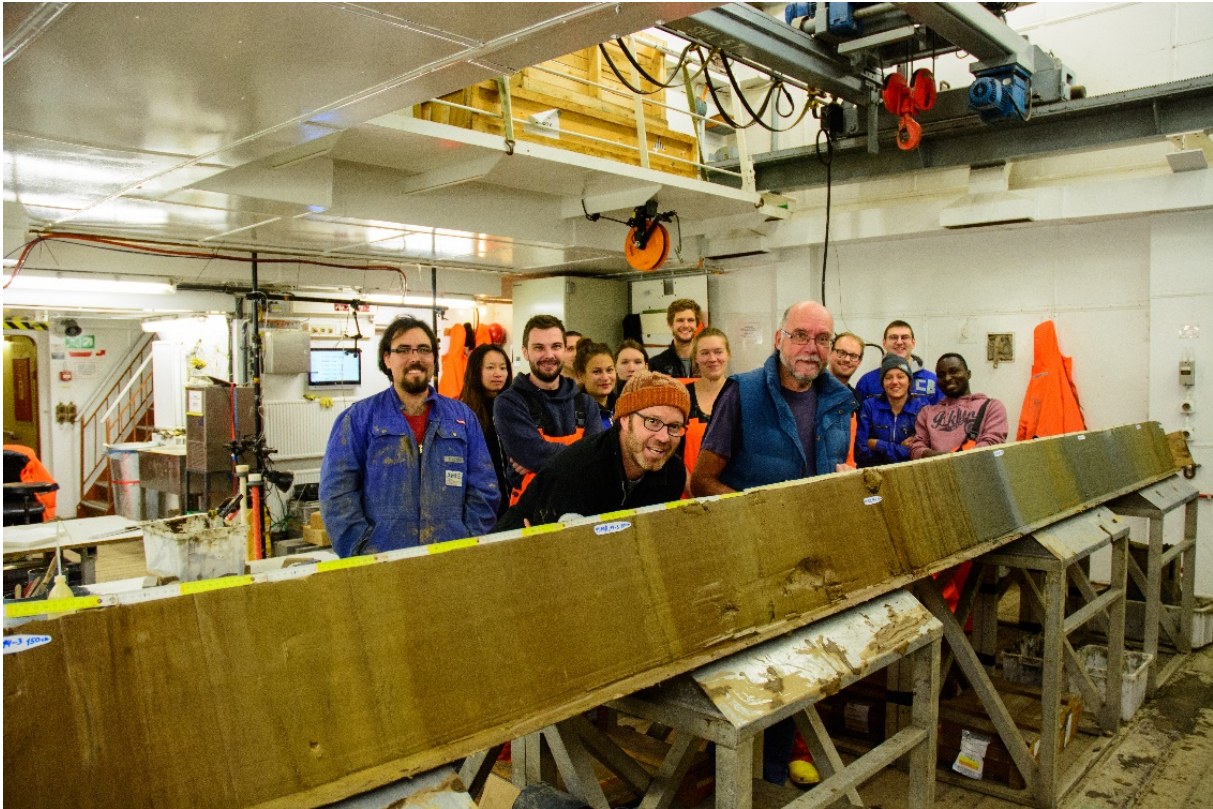


Photo 14: Geology group photo with the Kastenlot. (Photo: Ryan Love)

A.7.3 Meteorology

A. Desmarais (McGill), A. Kazlova (UoB-IEP)

Introduction

Weather prediction is very important on a research vessel in the Arctic, and our meteorologist Max Miller also called “Weather Max” analyzes maps and information that he receives from the main land. In addition, different measurements were also taken onboard. Every day at 11:00UTC, a weather balloon was sent. We were allowed to send this balloon in the Russian EEZ since these measurements are only used for the safety of the vessel. Outside of the Russian EEZ, three more balloons were sent at 5:00UTC, 17:00UTC and 23:00UTC. A cloud camera was also installed on the “Peildeck” and pictures of the clouds were taken every 10 seconds from 8:00 to 23:00. We can extract a lot of information from these pictures as it will be explained in the following sections.

Weather balloon

The launch of weather balloon has to be done at the same time every day. During the whole way through the troposphere and the stratosphere, the radiosonde will take measurements of pressure, temperature humidity and GPS position. The information that we can extract from these measurements can be used for the boat itself (weather prediction, etc.) or for research about Arctic meteorology and climate. To launch the weather balloon, one has to first activate the radiosonde. That means connecting it to the computer via a device furnished by VAISALA™, the brand of the weather balloon equipment. This process takes approximately 8 minutes. After a confirmation that the GPS works, one can start to inflate the balloon with helium, next to the helicopter deck. Once everything is ready, the balloon is launched between 5 to and 5 past the precise time of launching. Figure 14 shows the radiosonde and the balloon being launched.



Figure 14: A picture of the weather radiosonde and the device to attach it to the balloon and a picture of the weather balloon getting launched from the Helicopter deck

Once everything is completed, one needs to fill information about the current weather. The pressure, temperature and humidity profile can be visualised directly. Otherwise, the data can

be accessed later from the PANGAEA database. In addition to pressure temperature and humidity, the wind speed and wind direction is also measured at every height. The temperature profile is usually quite linear through the troposphere while the relative humidity profile shows a bigger variability (Figure 15). Depending on the atmospheric conditions and on the balloon itself, the maximum height of the profile is between 30 and 35km height, in the stratosphere. Since we use the radio sounding for weather purpose, the troposphere is the part that is more interesting for us. Due to uncertain causes, some soundings stop at lower heights. A balloon deficiency could be the cause. Some balloons were also thrown in the ocean and destroyed by strong downward low altitude winds. Overall, most of the weather balloon launchings were a success, which means that we have information through the whole troposphere and beyond.

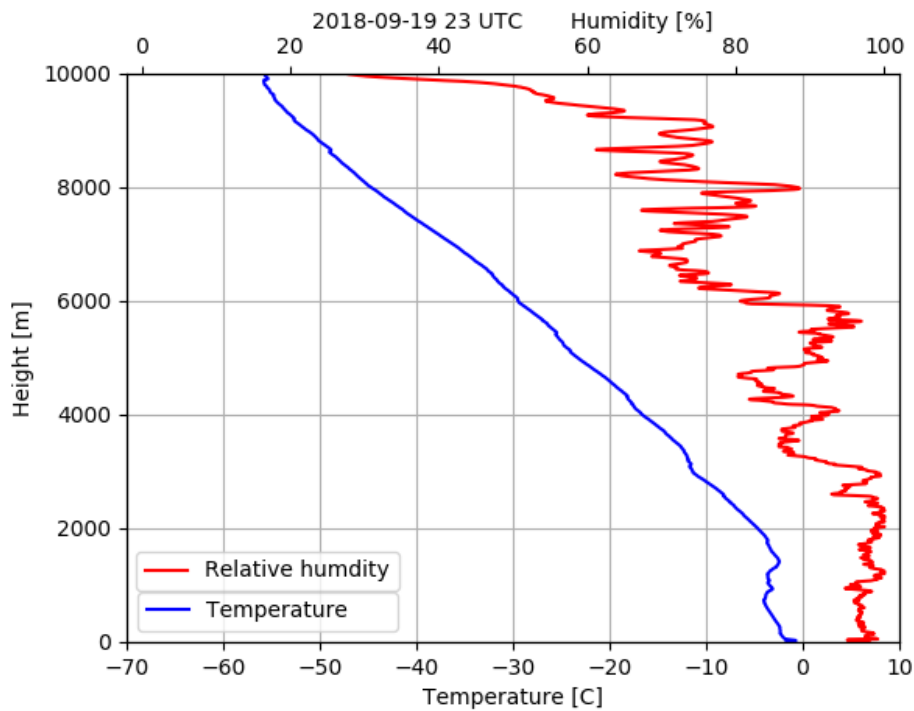


Figure 15 : Typical temperature and relative humidity profiles from Sept. 19, 2018 at 23:00UTC

We can define the lapse rate as $\Gamma = \frac{-dT}{dz}$ where z is the height and T is the temperature. The temperature profile from Figure 15 has an overall positive lapse rate because the temperature diminished with height. Even if the temperature profiles are usually quite straight, we can sometimes observe temperature inversions in the lowest parts of the atmosphere, which means that the lapse rate is negative. These inversions are located under approximately 1500m height and will usually happen during a period of low sun elevation (night time or winter time). In any case, the lapse rate at different height will help us to analyze the cloud camera images.

We can also compute the potential temperature (θ) using the following equation and proceed to an atmospheric stability analysis. R is gaz constant, c_p is the specific heat at constant pressure, T is the temperature, p is the pressure and p_0 is the reference pressure 1000mb.

$$\theta = T \left(\frac{p_0}{p} \right)^{R/c_p}$$

The derivative of the potential temperature according to the height gives a criterion on the stability of the atmosphere: if the derivative is positive, the atmosphere is stable and if it's not,

the atmosphere is unstable. According to our radiosonde profiles, the atmosphere was quite stable for the whole journey in most of the cases. The first few hundred meter of the troposphere sometimes shows some instability due to temperature inversions at this same height. In case of stormy weather conditions, the atmosphere was slightly unstable for the first kilometer since the potential temperature was decreasing with the height.

Cloud camera

The 'Pinocchio' cloud camera system from MPI-M (Figure 16) has been operated during the PS115/2 cruise from 05.09.2018 till 16.10.2018. The system was located above the pile-deck. It consists of two cameras, one is visible with fish-eye lens and another is near-infrared (NIR) camera with field of view 45° . It automatically records images of the sky and clouds every 10 sec. The camera that operates in the visible range is used mainly as a source for a general overview of the sky. It is possible to use the output from this camera only during daylight time. Even though we had a long period of the daylight, we had a lot of foggy days during this cruise. The process of separation of clouds from fog is nearly impossible. The most reliable source in these conditions is the thermal camera. It provides heat-images of the sky. From this dataset it is possible to recover cloud cover and estimate cloud base altitudes. The NIR camera operates in the IR-window ($8.5\text{-}11.0\ \mu\text{m}$), in this case a cloud base altitude can be derived by assuming a close to dry-adiabatic lapse rate with altitude. This assumption fails when water vapor content (as in Arctic) and temperatures increase. In this situation much smaller effective lapse-rates needed to be applied.



Figure 16 : Cloud camera

The impact of water vapor on the background temperatures was considered during previous cruises. In the case of PS 115/2, a new improved algorithm was applied for the data analysis. Additionally, cloud cover at pre-defined altitudes was compared to the dataset derived from the lidar instrument placed on board of *Polarstern*. The result of this calibration can be seen on Figure 17. We can also use the fish eye lens to have another point of view on the clouds as it can be seen on Figure 18.

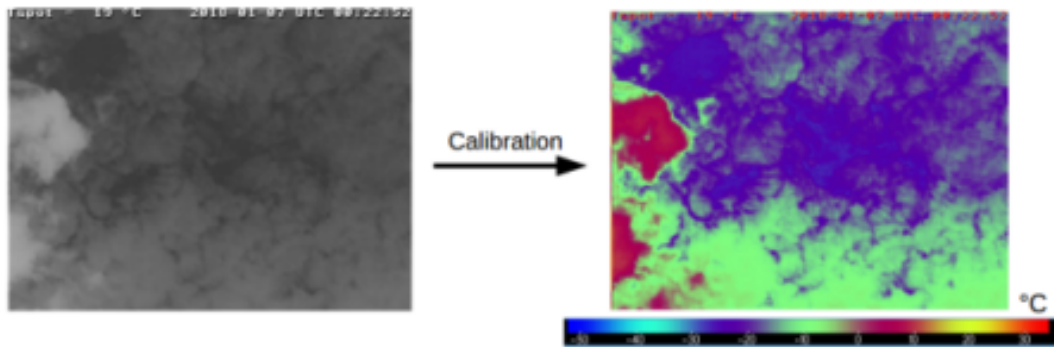


Figure 17 : An example of the 'Pinocchio' cloud camera system. The infrared images before calibration (left) and temperature images after calibration(right).



Figure 18: An example from the fish-eye lens camera

Preliminary results

Using the temperature profile from radiosondes (launched daily from the ship at 11:00 UTC in the Russian EEZ and four times a day at 5:00, 11:00, 17:00 and 23:00 UTC in international waters), the maximum radiative height (or colder temperature) of the sky that can be seen by the camera can be estimated. This provides information about the temperatures in different altitudes. It gives useful information, as this height can also be seen as setting for the upper limit for cloud detection; above it cloud detection cannot be achieved due to the lack of a thermal contrast between the radiative temperatures of the cloud and of the surrounding sky.

From the camera we can get information about the total cloud cover over the whole period of the observations. We also have access onboard to an equipment to measure the aerosol properties and water vapor content of the atmosphere called MICROTOP. This device needs full sunlight to work properly. As it is seen on Figure 19, there was not that many sunny days. In summary we had around 2 weeks of clear sky conditions. This situation did not allow making enough of these MICROTOPS' aerosol properties and water vapor content measurements.

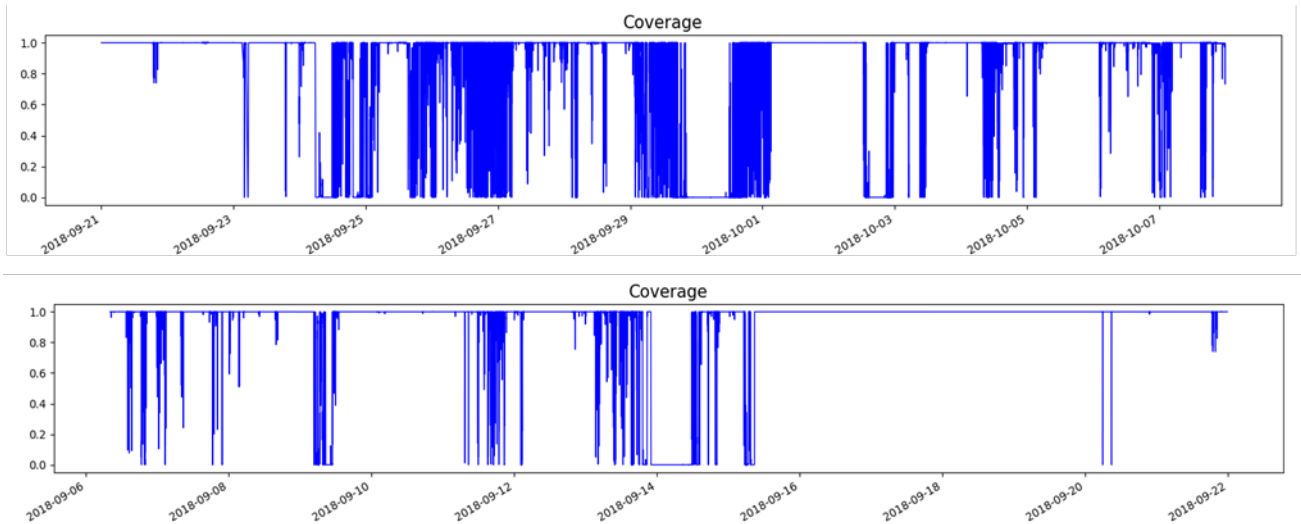


Figure 19: Total cloud coverage during the period of observations from 06.092018 till 07.10.2018.

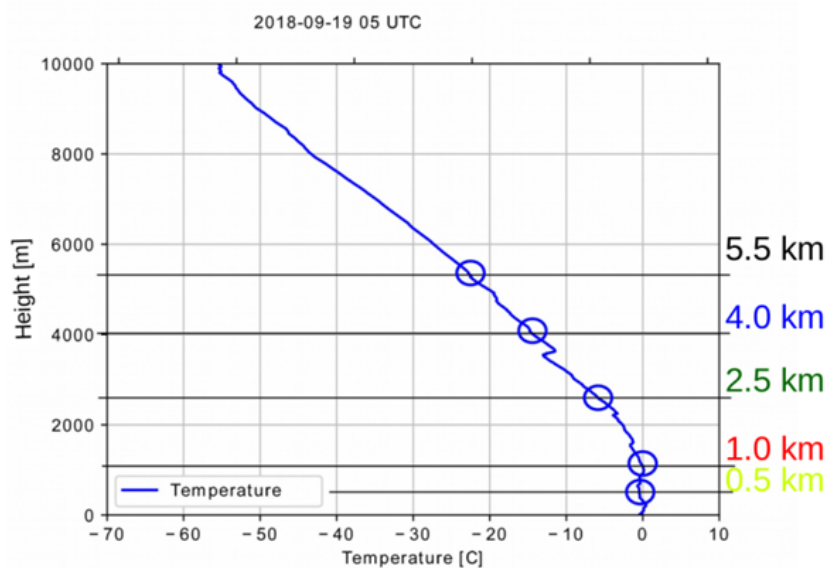


Figure 20: An example of temperature profile from radiosonde

Based on temperature profiles from radiosonde, five different altitudes have been chosen to define five cloud categories: below 0.5 km, 0.5-1.0 km, 1.0-2.5 km, 2.5-4 km and 4.5-5 km. Figure 21 gives us an example of different cloud type distribution over the same day of the 19th of September. During the whole period we have complete coverage with upper altitude clouds (black and blue area on Figure 21, with the black area being hidden behind the blue one). In the morning and evening hours medium altitude clouds (1.0-2.5 km) appears. For a short time period, some low altitude clouds (>0.5 km and 0.5-1 km, respectively yellow and red on Figure 21) appear in the dataset. These clouds overlap each other, which mean that the red curve is behind the yellow one at every moment. They have the same distribution because the temperature is the same at both of these heights as you can see from Figure 20. More accurate data analysis should be introduced during the post processing.

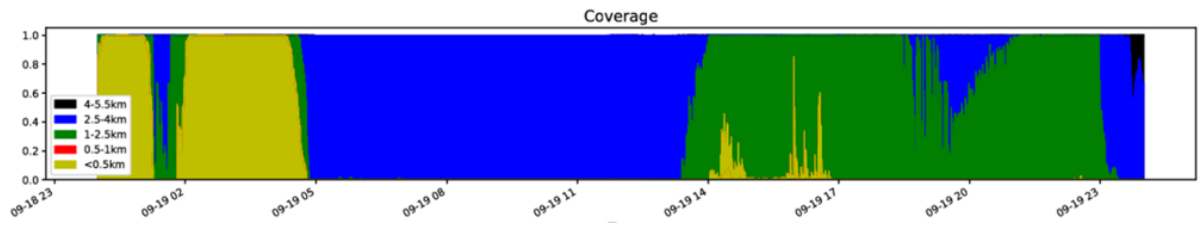


Figure 21: Different type clouds coverage for the 19th of September

A.7.4 Sea Ice

A.7.4.1 Preliminary Analysis of Data Collected for the Ice Watch Program During Expedition PS115.2

C. Brunette (McGill), A. Vlug (UoB-MARUM)
with contributions from all ArcTrain participants

Overview

During this cruise, a collection of observations for the Ice Watch program was performed. A short overview of the Ice Watch work during PS115.2 can be found in Section 4.5 of the cruise report. Here we will add and extend to that with further descriptions and analysis.

Ice Watch is a ship borne sea ice observation program. The ASSIST software was used to perform standardized observations. The Ice Watch Manual (Hutchings et al., 2018) was used as a guide for identifying the different ice and environmental properties that are being reported. The ice observations ran from September 7th to October 6th, during the time that Polarstern was in ice covered regions or had a chance of sea ice occurrence. The Advanced Microwave Scanning Radiometer (AMSR2) retrieved sea ice concentration (SIC) data, available onboard through the DSHIP Mapviewer, was used to decide if we were close enough to the ice edge to start doing observations. During those times, ice observation were performed at every hour of the day from 7:00 to midnight, and every other hour during the night (the night was defined as 01:00 to 06:00 ship time). The observations were done by 15 different people, following an observation schedule. In this schedule, everyone was responsible for one or two observations during the day. For the night watches, turns were taken. When possible night watches were combined with nightly duties for the other disciplines. Information about the objectives and the data storage can be found in section 4.5 of the cruise report: *Ice Watch – Visual Sea Ice Observations from the Bridge*.

Method

Observing the sea ice was a part of the day-to-day duties (Appendix A.7.1.1: *Day to Day Duties*). The sea ice conditions were always observed and recorded at the bridge of the ship. There was an agreement to take three pictures of the sea ice during the observation, starting with port-side, then one picture in the direction of the ship bow and the last on starboard. A valid observation contains at least the following information: the name of the primary observer, the latitude, the longitude, the observed total sea ice concentration and the visibility. However, there are many more details that can be entered in the ASSIST program to provide a fuller picture of the ice situation: information about the ship, the meteorology and details about the sea ice, such as ice type, thickness, presence of algae, etc.

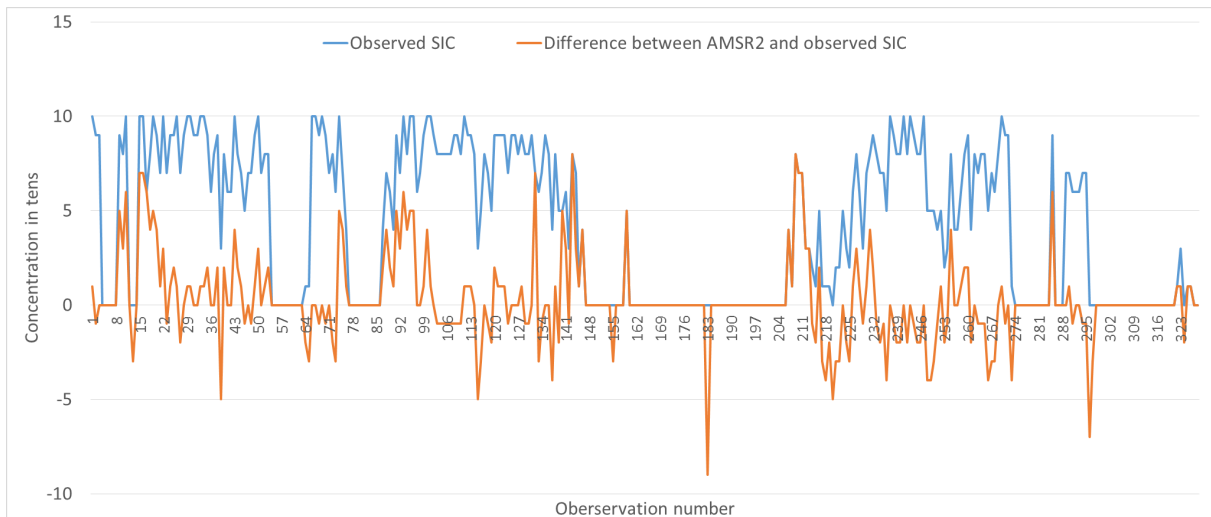


Figure 22. Observed sea ice concentrations and the difference with the AMSR2 data.

Comparison with AMSR2 data

During the cruise a total of 329 valid sea ice observations were recorded. These observations were compared to the sea ice concentration in the AMSR2 dataset (Fig. 1). The AMSR2 SIC are calculated and distributed by the Drift and Noise company following the method from Spreen et al. (2008). The SIC data is updated near-real-time for every satellite overflight and made available on a polar-stereographic grid as geotiff file in the Polarstern intranet. We identified the AMSR2 SIC file that matched the best the time of the Ice Watch observation, and then identified the pixel collocated with our in-situ observation. Of these sea ice concentration pairs, 131 had ice neither in the Ice Watch observations nor in the AMSR2 dataset. The remaining 199 observations have ice either in the AMSR2 and/or in the observations. The sea ice concentration has a similar spread for the observations as the AMSR2 data (Fig. 2. A and B). With a notable difference that there is no concentration of one tenth in the AMSR2 dataset. This is likely due to weather filters applied to passive microwave data as suggested in Spreen et al. (2008). The distribution of ice thickness reported in the Ice Watch observations (Fig. 2. C) is representative of the ice conditions encountered during expedition PS115.2: mostly very thin ice as we sailed through new ice formation regions in the Northern Laptev Sea, a good amount of first/second year of thickness 50-150 cm, and occasionally some thicker floes. Bear in mind that these thickness estimates are very qualitative in nature, since they are estimated from the Bridge by visual inspection. Also, Fig. 2C shows the raw count for each thickness bins. For a more representative picture of the reported thicknesses, they should be weighted by the partial concentration associated to each thickness entry.

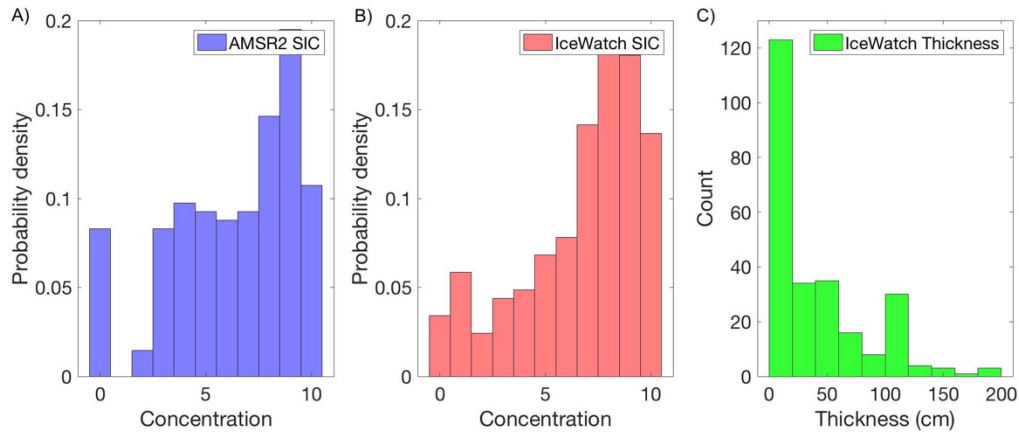


Figure 23. When ice is present either in the Ice Watch observations or the AMSR2 data: A) distribution of binned sea ice concentration in AMSR2, B) distribution of binned sea ice concentration from the Ice Watch observations, C) reported thicknesses in the Ice Watch observations.

In a perfect world, the two data sets would have similar sea ice concentrations, but that is not always the case (Fig. 3). In 31 cases the binned AMSR2 data matches the observation. In 71 cases the binned values are 1 tenth off and 30 cases 2 tenths off. That leave 66 cases (34%) where the AMSR2 concentration is more than 5 tenths off. Taking into account all observations, a Pearson's coefficient of correlation between Ice Watch and AMSR2 SIC carries a value of $r=0.84$ (statistically significant above the 99% level) and the standard deviation of the difference between the two dataset is 2.21 tenths of concentration. When excluding the trivial cases when sea ice is absent from both Ice Watch and AMSR2, the coefficient of correlation is $r=0.53$ (also statistically significant above the 99% level) and the standard deviation of the difference is 2.8 tenths of ice concentration.

As a first attempt to investigate sources of discrepancy between Ice Watch and AMSR2, we looked at partial concentration of thin and thick ice as reported in the Ice Watch observations. Ice types frazil, shuga, grease, slush and nilas were considered as part of the thin ice fraction, and ice types pancakes, young grey, first-year, second-year, multiyear, brash and fast ice were considered as part of the thick ice fraction. Satellite retrieval of sea ice concentration is prone to underestimation of thin ice, as very thin ice such as nilas or wet ice such as slush or shuga can be confused with open water. We therefore expected the partial concentration of thick ice to match better the AMSR2 SIC, however a scatter plot of those two quantities (Fig. 4) shows that comparison with thick ice partial concentration is only marginally better ($r=0.71$, statistically significant to the 99% level; standard deviation of the difference is 2.7 tenths). Yet, when comparing the partial concentration of thin ice in the Ice Watch observations to the difference in concentration between Ice Watch minus AMSR2 SIC, we can see a tendency for the difference to be higher when there is more thin ice in the in-situ observation (Fig. 5). In other words, we get more ice concentration in Ice Watch than in AMSR2 when a larger part of the ice present is of one of the ice types that we qualified as thin ice. When there is low presence of thin ice, the difference between the two datasets tend to agree better but the difference is more scattered.

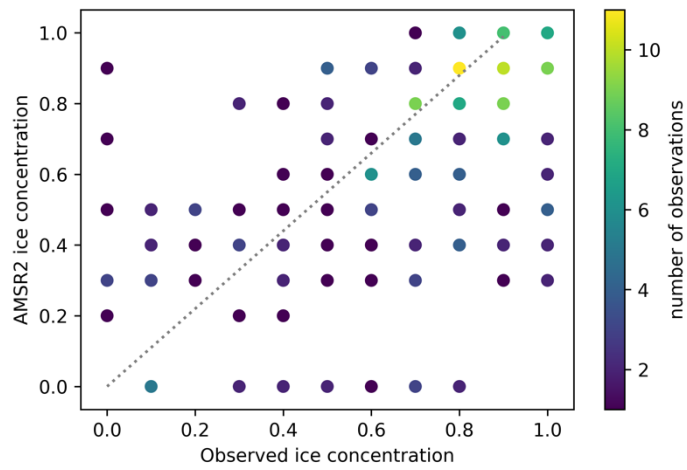


Figure 24. AMSR2 - Ice Watch binned sea ice concentration comparison.

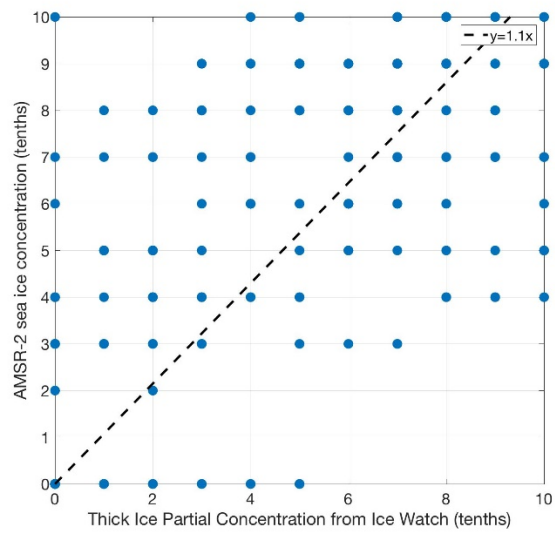


Figure 25. AMSR2 against partial concentration of thick sea ice from the Ice Watch observations

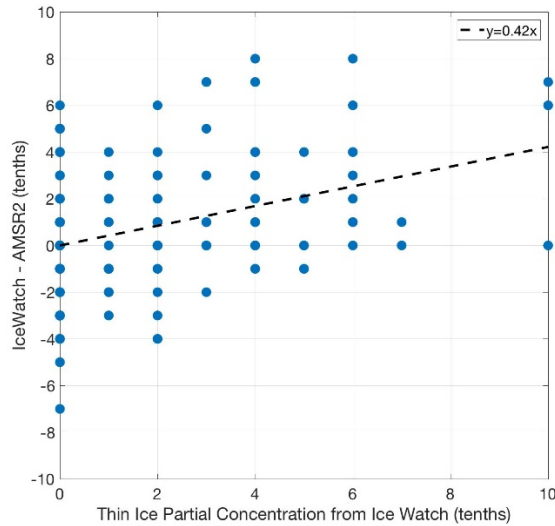


Figure 26. Difference between Ice Watch-AMSR2 against partial concentration of thin sea ice from ICE Watch observations

Case study 1: mismatch between Ice Watch and AMSR2

On September 23rd from 19:15 to 24th 00:50 (UTC), the observed ice concentrations were about twice as high as the AMSR2 ice concentrations for 6 hours in a row (Fig. 6). This difference between the two can have multiple causes. These observations were done by five different people, minimizing the chance of a single observer erroneously identifying this ice concentration. In addition high sea ice concentrations are clearly visible on the pictures that were taken during these observations (Fig. 7 to 12). As mentioned before, some ice types are hard to identify from satellite images. This is especially the case for shuga that is partially submerged in water and wet on top. Also pancake ice, which gets easily flooded, can be hard to identify for the AMSR2. In both cases the AMSR2 radiometer would see a mixture of ice and water, which likely explains a part of the underestimation. The location of the observation were near the ice edge, which could offer explanation for this bias. Another possible but less likely source could be the contribution of atmospheric forcing, with winds and waves breaking up the pack ice in between AMSR2 overflights. A more in-depth analysis of weather conditions at the time of these observations will be required to draw conclusions.

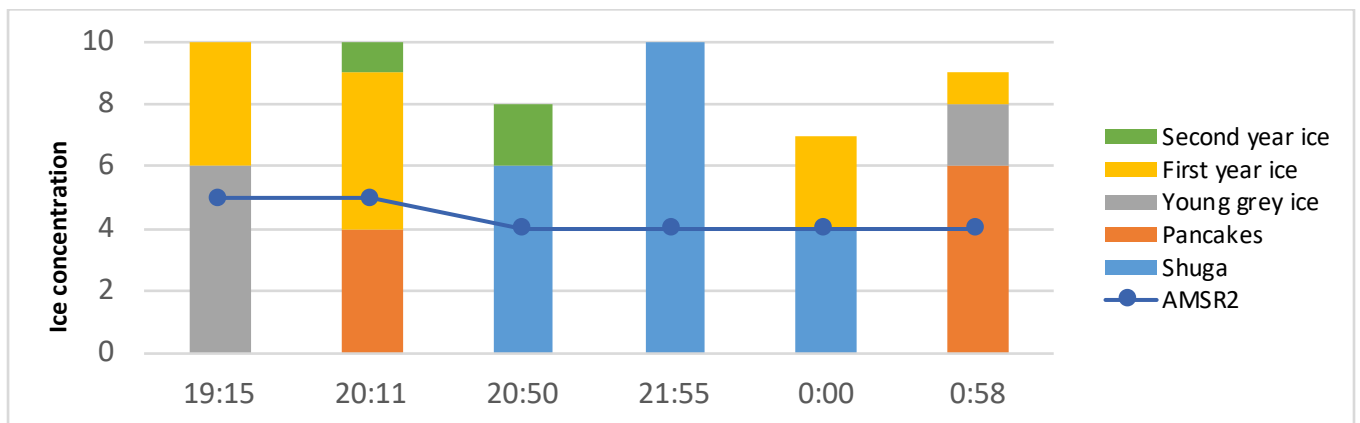


Figure 27. Comparison of AMSR2 data and observed sea ice on September 23 & 24.



Figure 28. The sea ice at September 23th, 19:15. (Photos by Damien Ringeisen)



Figure 29. Sea ice at September 23th, 20:11. (Photos by Remi lenny)



Figure 30. Sea ice at September 23th, 20:50. (Photos by Gunnar Spreen)



Figure 31. Sea ice at September 23th, 21:55. (Photo's by Remi lenny)



Figure 32. Sea ice at September 24th, 00:00. (Photos by Natasha Ridenour)



Figure 33. Sea ice at September 24th, 00:50. (Photos Aliaksandra Kazlova)

Case study 2: Three observers on station

Although according to the Ice Watch guidelines, observations should stop when the ship reaches station, the Ice Watch reports continued during a few stations. These reports turned out useful for getting insights on how different observers perceive a similar scene. Figure 13 presents three observations made during an ice station that took place on September 23. All observers reported the same total concentration (SIC=8 tenths). This is in good agreement with the AMSR2 concentration of 9 tenths. The 3 observers also agreed on the type and shape of open water in the scene, all saying narrow breaks between 50-200m in width. There was more variability regarding the subtypes of ice present. The first observer reported presence of first year ice (70-120cm), young grey ice (15-30cm) and nilas; the second observer reported presence of first year ice (120cm); and the third observer reported presence of second year ice and nilas. We can see a different interpretation of the ice thickness (Observers 2 and 3 reporting thicker ice than Observer 1) and also some differences in definitions (the same ice was reported as thick first year by one observer and as second year by the next observer because we were past mid-September and therefore already into the second year's growth season). In-situ thickness measurements performed during the ice station indicate ice thicknesses of 74, 116 and 144 cm – which covers thickness ranges reported in the three Ice Watch observations described here. This case study illustrates a situation where the Ice Watch and satellite data agree very well to the first order, although there is some variability when looking into a more detailed description of the nature of sea ice around the ship. It remains challenging to produce uniform sea ice observations due to the inhomogeneity of the sea ice cover and also due to the large number of observers involved in the Ice Watch program.



Figure 34. Three Ice Watch reports completed while on station on September 23 at 83.08 N; 142.51 E. A) Pascal Bourgault-04 :06 UTC. B) Charles Brunette-05:05 UTC. C) Gunnar Spreen-05:55 UTC.

A review of potential contributions to the difference between Ice Watch and AMSR2

- Spatial resolution: AMSR2 provides sea ice concentration averaged over 6.25 km grid cells, whereas the Ice Watch report considers ice within 1 nautical mile (~1.8 km) of the ship
- Temporal resolution: a few hours separate the different updates of the AMSR2 SIC maps. Also an individual pixel is not necessarily updated at the exact time of the whole field – it can take some time before a new satellite overflight is available for a specific location. This needs to be kept in mind.
- Subjective interpretation of ice conditions: 15 different ice observers provide a good work force for maintaining hourly watches, but can have slightly different interpretation of an identical scene.
- Misinterpretation of thin ice fraction: As mentioned earlier, thin ice types such as grease ice or wet ice surface can be mixed with open water in satellite imagery, however a ship borne observer can identify this ice category
- Low ice concentration: Due to weather filters on the microwave imagery, concentrations lower than 1 tenth can be lost.
- Traveling the marginal ice zone: As mentioned in Spreen et al. (2008), the agreement between in-situ and satellite observations of SIC is better for 0% and 100% concentration. The difference is larger when the sea ice cover is more variable. We travelled mostly in the marginal ice zone during the PS115/2 expedition.

Suggestions for the Ice Watch program & the ASSIST software

- Comments section:

- When creating a comment the default observer is set to be the very first observer of the Ice Watch campaign rather than the primary observer of the active observation. Setting the primary observer as default comment author would be a good addition.
- Comments cannot be edited, which requires to delete and re-do the comment if an error was made. The option to edit comment would be appreciated.
- First-year ice categories:
 - Pre-defined first year ice categories make it sometime difficult to associate the ice type when thickness of sea ice is not observable. Maybe an open-ended first year ice category could be considered?
- Meteorology:
 - Observers mentioned that the options for meteorology are a somewhat confusing. Maybe streamlining the meteorology categories could be considered.
- Light conditions:
 - A section to describe light conditions would be interesting. A good number of our observations took place during night time and the only place to specify it is in the comment section.
- Camera:
 - We used a small Panasonic Lumix DMC-ZS7 camera for taking pictures of ice conditions around the ship. This camera failed to capture good images at night. A more performing camera would provide better material for further analyses of the Ice Watch observations.

References

- Spreen G., Kaleschke L. and G. Heygster (2008). Sea ice remote sensing using AMSR-E 89-GHz channels Journal of Geophysical Research, 113.
- Hutchings JK, Delamere J, Heil P (2018) The Ice Watch Manual, Draft 2018/06/30 for ASSIST v4.1. Draft Technical Report, University of Alaska Fairbanks, USA. <http://icewatch.gina.alaska.edu/>

A.7.4.2 Infrared Camera and Thin Ice Thickness

P. Bourgault (McGill), D. Murashkin (UoB-IEP), D. Ringeisen (AWI)

Objectives

Sea ice thickness is an important but hard to observe quantity, especially for remote sensing. It is quite easy to measure the sea ice extent from space and it is not surprising that it is the most used indicator of the Arctic sea ice health. However, this is only a part of the picture; the thickness is needed to do a proper analysis of total sea ice volume. Satellite imagery techniques can only go so far, as the atmosphere adds a lot of noise and the electromagnetic frequencies classically used (microwave, infrared and visible) do not penetrate much of the sea ice or the water. Therefore, thickness of thin ice measurements is more reliable. In the current project we apply techniques used for sea ice thickness estimates from infrared satellite images to thermal data taken onboard the ship with an infrared (IR) camera. Also, one goal was to test the method and the equipment in the perspective of the planned "MOSAIC" drift expedition where it could be used in a more systematic way.

Setup

To make shipborne observations of the sea surface and sea ice, the IR camera was installed on the "Peil" deck of the FS Polarstern, approximately 26 m from the surface. Attached to the fence on the portside, the camera was pointed downward in order to be as perpendicular as it could to the water surface. This location was chosen as the setup was not blocking any passages or emergency exits, but also because it allowed for the steepest imaging angles. Two different imaging angles were tested in this configuration: 30° and 40° from the horizontal.

The VarioCam HD camera was solidly fixed on a tripod and connected by an Ethernet cable to a mini PC protected in a waterproof box that also stored the two car batteries providing the needed energy. The camera is able to record images autonomously during approximately one week, after that batteries have to be recharged. The mini PC was accessed wirelessly from another laptop computer to start, stop and transfer recordings. The IRIBIS 3 plus software was used to control the camera and visualize the data. Most of the post-processing was done in Python using exported ASCII files instead of the proprietary binary format used by the software.

In the first outdoor trials, data from the camera showed strange jumps and drifts in temperature. With the help of -Marcus Huntemann (not onboard), we pinpointed the internal Non Uniformity Correction (NUC) as the culprit for those errors. The NUC is an automatic process that resets the shutter of the camera to prevent temperature drifts. A few experiments later, it was found that desynchronizing the NUC with the image capturing solved the problem. However, all this troubleshooting only left us time to capture one full valid sequence, during the night of September 23rd.

Even if the camera in itself is resistant to cold, humidity and wind, we often had to go to the "Peil" deck to wipe the frost off the lens. In humid and windy condition, the whole optics freezes and a thick layer of ice forms during night, making any proper sea surface measurement impossible. Later during the cruise, a simple windscreen was put up but it couldn't completely block the blowing snow from covering the lens. More has to be done if one wants to install this camera in an autonomous mode in an isolated location, like what is planned for the MOSAIC expedition.

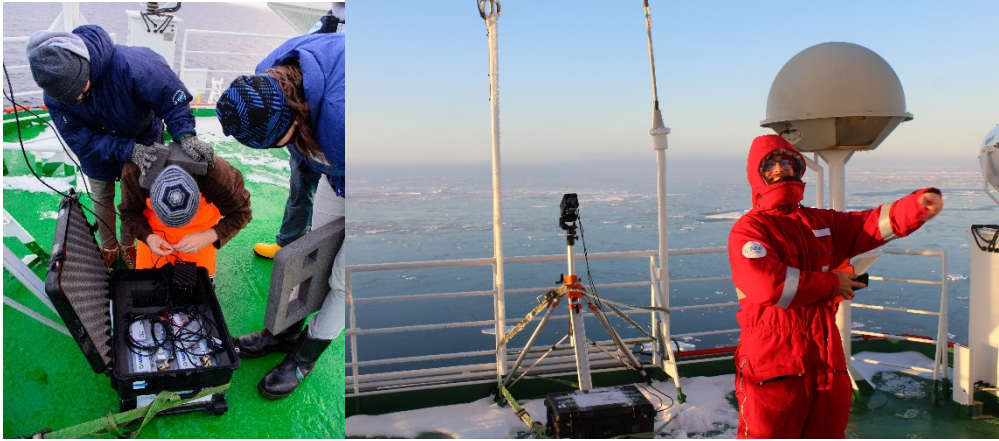


Figure 35 Pictures of the setup on the “Peil” deck.

Left: P. Bourgault tries to fix the mini-pc's power supply cable supervised by D. Murashkin and protected of the chilly wind by M. Caron. Photo: R. Love.

Right: D. Ringeisen dances near the camera. Photo: C. Brunette

Correction

When imaging outside, the received irradiance is highly dependent on both the imaging angle and the downwelling radiation. The brightness temperature seen by the camera is that of a gray body rather than a black one since the emissivity of saline water and sea ice is not 1. Moreover, according to the Fresnel equations, the emissivity varies with the incidence angle, decreasing rapidly for large angles. Reflection from downwelling radiation is more complex to correct since it depends on the cloud cover and the sun's position, thus also changing in time.

After failing to do a theoretical correction, we chose to use some assumptions on the sea surface temperature and compute empirical correction matrices. The principle of the simple correction is the following: knowing the incidence angle of the rays hitting each pixel ($\theta(x, y)$), we use an image of the measured sea surface temperature ($T_{meas}(x, y)$) and assume it is uniform in reality (i.e. $T_{real}(x, y) = T_{ref}$). The ratio of the supposed uniform temperature on the measured temperature of all pixels is compared with the incidence angle and a fitting function $F(\theta)$ is found:

$$\frac{T_{ref}}{T_{meas}(x, y)} \approx F(\theta)$$

Polynomials of the third order were used as fitting functions for this project. Finally, a correction matrix $\epsilon(x, y)$ is computed from the fit and the incidence angles to be used with all other frames with the same imaging angle and downwelling radiation situation by simply calculating:

$$T_{corr} = \epsilon T_{meas}$$

In most cases, T_{meas} was the mean of many similar images in order to get rid of the perturbations made by noise and surface waves. T_{ref} was also found by taking the mean of the pixels of T_{meas} with the lowest incidence angles. This correction and its generation was implemented in Python.

Theory and algorithm

This section describes the algorithm for sea ice thickness estimation based on the previous work of Yu and Rothrock (1996). With the infrared camera the brightness temperature of the

surface of sea ice is measured. The surface temperature depends on the fluxes at play inside and outside the ice floe. Assuming thermodynamic equilibrium, the sum of fluxes is

$$F_{lu} + F_s + F_e + F_{sdn} + F_{ldn} + F_c = F_t + F_c = 0$$

where F_{lu} is the upward longwave radiation, F_s is the sensible heat flux, F_e the latent heat flux, F_{sdn} the absorbed shortwave radiation, F_{ldn} the downward longwave radiation, and F_c the conductive heat flux in the ice and snow. F_c depends on ice thickness with the relationship:

$$F_c = \frac{k_i k_s}{k_s h_i + k_i h_s} (T_w - T_s)$$

with k_s and k_i the snow and ice thermal conductivity, h_i and h_s the ice and snow thickness, T_s the surface temperature, and T_w the water temperature. Therefore, computing all other fluxes, we can invert the relation above and solve for h_i .

To compute this, we thus need to measure the ocean temperature T_w , the downward longwave radiation F_{ldn} , the downward shortwave radiation F_{sdn} , the snow thickness h_s , the air temperature T_a , the relative humidity f , and the wind velocity u . We use the following fluxes computation, with well known constants and parameters (listed in Table 1).

- The upward longwave flux is computed using Stefan-Boltzmann law:

$$F_{lu} = -\varepsilon \sigma T_s^4$$

- The sensible and latent heat flux are computed using the classical equations:

$$F_s = \rho_a c_p C_s u (T_a - T_s)$$

$$F_e = \rho_a L C_e u (f e_{sa} - e_{s0})$$

Where e_{sa} and e_{s0} are calculated using an empirical relationship found in Maykut (1982).

- We compute the absorbed shortwave radiation from the albedo α and the measures downwelling shortwave radiation. We use an estimate of $\alpha = 0.8$, a value inspired by Mäkynen et al. (2013). As the experiments were done under very large sun zenith angles, we also neglect the transmission through ice and snow.

$$F_{sdn} = (1 - \alpha) \Phi_{sdn}$$

- For the absorbed longwave radiation, we use the cloud's brightness temperature T_{atm} , the cloud coverage C and the following atmospheric emissivity parametrization:

$$\varepsilon^* = 0.7855 (1 + 0.2232 C^{2.75})$$

$$F_{ldn} = \varepsilon^* \sigma T_{atm}^4$$

We consider that all the downwelling longwave radiation is absorbed. When the clouds temperatures T_{atm} cannot be measured, the 25-m air temperature T_a , measured on the boat, can be used.

- The thermal conductivity of sea ice is estimated as:

$$k_i = k_0 + \frac{\beta S_i}{T_i - 273}$$

We can now compute an estimated ice thickness:

$$F_c = -F_t$$

$$h_i = k_i \left(\frac{T_s - T_w}{F_t} - \frac{h_s}{k_s} \right)$$

Snow thickness is a quantity hard to observe and measure precisely. We had two ways to estimate its value in our algorithm: visual estimation or parameterizations. The visual estimation was either done from the pictures of the IR camera, other pictures taken at the same time with a regular personal camera or from the ice watch data provided by the ArcTrain students, at an approximately hourly rate. The parameterization is the one from Doronin (1971) used by Yu and Rothrock (1996) and gives a piecewise linear relationship between snow and ice thickness:

$$h_s = \begin{cases} 0 & h_i < 0.05 \\ 0.05h_i & 0.05 \leq h_i \leq 0.2 \\ 0.1h_i & h_i < 0.2 \end{cases}$$

As seen on Table 2, most measurements were taken from the centralized ship database DShip or from Pinocchio, the onboard cloud camera system used by the meteorology team (see Section 3).

Finally, for a better visualisation of the data, images were projected with a simple trigonometric transformation to get a top-down cartesian view. With θ_0 the camera angle from the horizontal, θ_i the pixel's vertical angle relative to θ_0 , ϕ_i the pixel's horizontal angle relative to the center of the image and H the height of the camera above sea surface, we have the projected position X_i, Y_i :

$$X_i = \frac{H}{\cos\left(\frac{\pi}{2} - \theta_0 + \theta\right)} \tan \phi$$

$$Y_i = H \tan\left(\frac{\pi}{2} - \theta_0 + \theta\right)$$

Table 1 Constants and parameters

Constant	Value	Units	Description
σ	5.67×10^{-8}	K	Stefan-Boltzman constant
ε	0.95		Emissivity of ice and snow
k_s	0.3	$\frac{W}{m K}$	Heat conductivity of snow
k_0	2.034	$\frac{W}{m K}$	Heat conductivity of pure ice
ρ_a	1.03	$\frac{kg}{m^3}$	Air density
c_p	1004	$\frac{J}{kg m^3}$	Specific heat of dry air
C_s	0.003		Heat bulk transfer coefficient
C_e	0.003		Evaporation bulk transfer coefficient
L	2.49×10^6	$\frac{J}{kg}$	Latent heat of vaporization
β	0.13	$\frac{W}{m^2 kg}$	Untersteiner (1964)'s salinity parameter
S_i	7.7	$\frac{g}{kg}$	Bulk salinity of sea ice
α	0.8		Approximate albedo of sea ice

Table 2 Observable quantities and data sources

Variable	Units	Data source	Description
T_s	K	IR Camera	Surface temperature (ice or snow)
T_a	K	DShip	Air temperature (25-m used instead of the theoretical 10-m)
T_w	K	DShip	Water temperature
h_s	m	Estimation or parameterization	Snow thickness
u	$\frac{m}{s}$	DShip	Wind speed (25-m instead of 10-m)
f		DShip	Relative humidity
Φ_{sdn}	$\frac{W}{m^2}$	DShip	Downwelling short wave radiation
T_{atm}	K	Pinocchio	Cloud brightness temperature
C		Pinocchio	Cloud coverage

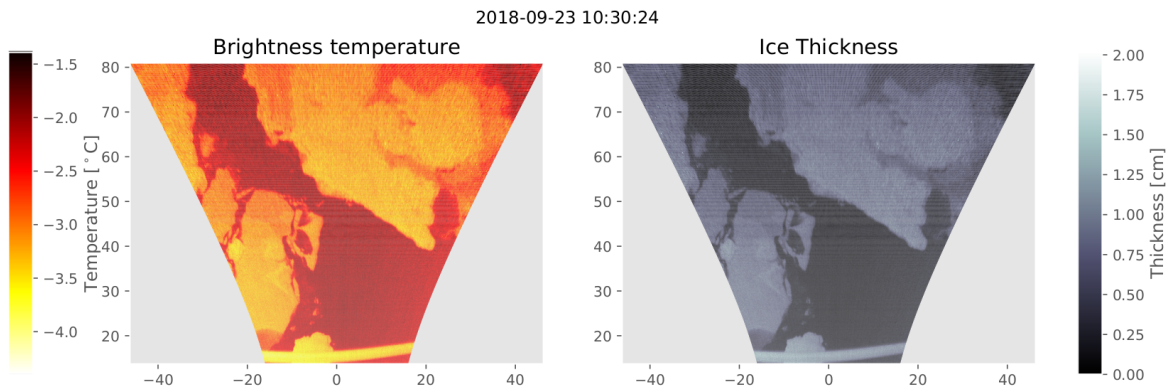


Figure 36 Raw data and computed thickness, first example.

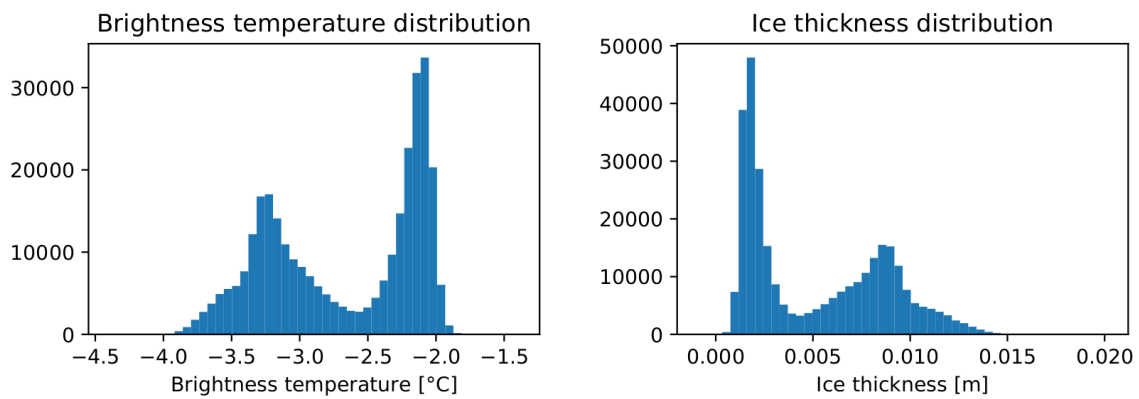


Figure 37 Temperature and thickness distributions of the first example on Figure 2

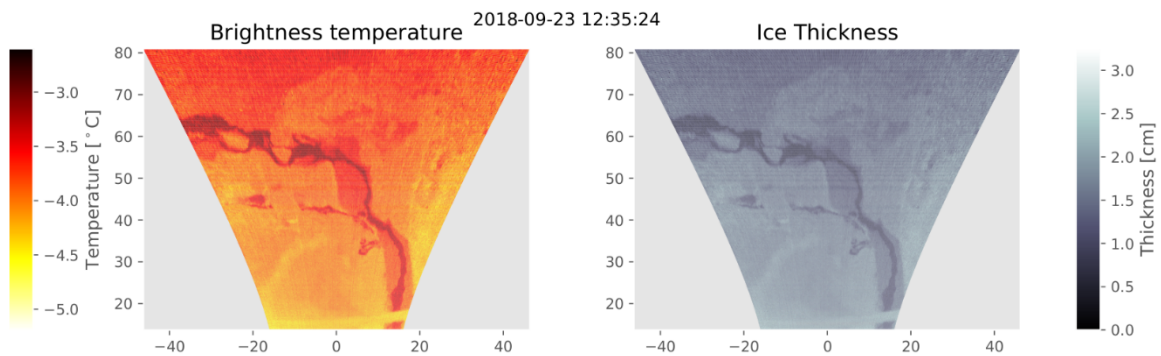


Figure 38 Raw temperature and computed thickness, second example.

Results and discussion

As mentioned in the first section, some problems with the NUC and the freezing of the lens ruined the first captured sequences. Moreover, as the ship spent less time than expected for the expedition in areas with high sea ice concentration, we only got one sequence of 151 images taken each 5 minutes during the night of the 23rd of September. Individual images from first sequences of IR images, taken on the 14th and 16th of October with the same setup, can

also be processed, but no time series can be derived. Figures 2-3 and Figure 4 show two examples of the measured brightness temperature and the computed thickness. Data shown is denoised with the camera's internal algorithm during acquisition, processed and projected in Python.

Figure 3 shows the temperature and ice thickness distributions of data shown in Figure 2. We can see two modes in the distributions. The first one has a peak at -3.3 C and 8 cm thickness corresponds to thicker ice that can be seen in Figure 2 as couple of large ice floes. The second mode at temperatures slightly below -2 C and thicknesses just above 0 cm represents open water areas or very thin ice. It is hard to distinguish between the two having only infrared imagery because their temperatures are quite close together. Similarly, it can be difficult to estimate ice thickness visually from images taken with the IR camera, i.e., we do not know the real ice thickness of these floes. However, from the ice watch observations we assume that the floes are significantly thicker than the 8 cm we derived. To get a better visual estimate of the ice thickness, additional information acquired, for example in the optical part of the spectrum, could be helpful.

Comparing with visual observations of the ice and the climatology, the algorithm produces sea ice thickness values that are lower than expected. There are several reasons that can explain underestimation of sea ice thickness. First, the algorithm is based on the assumption that ice is in thermodynamic equilibrium. During the expedition, air, ice and water temperatures were quite similar, which means that the assumption of linear temperature gradient within an ice flow might not be correct. The articles of Yu and Rothrock and others, on which the algorithm is based, are mainly working in winter conditions when the air is a lot colder than the water and the ice. Second, incoming longwave radiation flux is estimated from cloud temperature. We also tried to use the 25-meter temperature from Dship and found that it varies by several degrees during a day, and these variations cause large discrepancies in sea ice thickness estimation (up to one order of magnitude or even more). Therefore, more work should be done to estimate longwave flux received by the surface. Visual examination of the ice floes provided by ArcTrain's ice watch describes a 90-100% ice concentration dominated by 70-120 cm thick first-year ice. We wouldn't expect to measure such thick ice with infrared radiation alone, but we should measure something around the maximal 50 cm that such a method usually gives. Therefore, we think that the method needs some more tweaking for those summer-autumn conditions.

Acknowledgements

We would like to acknowledge the help of ArcTrain students onboard for the camera installation and Marcus Huntemann (not onboard) for information about the setup and help in troubleshooting issues.

References

- Doronin YP (1971) Thermal interaction of the Atmosphere and the Hydrosphere in the Arctic. Israel Program for Sci. Trans., p. 85.
- Mäkynen M, Cheng B, Similä M (2013) On the accuracy of thin-ice thickness retrieval using MODIS thermal imagery over Arctic first-year ice. *Annals of Glaciology*, 54(62).
- Maykut GA (1982) Large-Scale Heat Exchange and Ice Production in the Central Arctic. *Journal of Geophysical Research*, 87, 7971-7984.
- Rothrock DA, Yu Y (1996) Thin ice thickness from satellite thermal imagery. *Journal of Geophysical Research*, 101, 753-766.

A.7.4.3 Preliminary Analysis of Hyperspectral Images Captured with the SPECIM IQ Camera During PS115.2

C. Brunette (McGill), D. Murashkin (UoB-IEP),
with contributions from M. König (CAS), P. Bourgault (McGill), A. Vlug (UoB-MARUM),
Kazlova (UoB-IEP), A. Desmarais (McGill), D. Ringeisen (AWI),
and G. Spreen (UoB-IEP)

During the expedition PS115.2 to the Arctic Ocean onboard the research vessel Polarstern, we experimented with a portable hyperspectral camera to capture scenes containing sea ice, snow covered ice, melt ponds and algae.

1. Introduction

Remote sensing of sea ice provides useful information for operational and research activities in polar environments. However certain features of the sea ice cover are difficult to observe from satellite imagery. For instance, open melt ponds in summer can easily be confused with open water, refrozen melt pond have similar signatures on optical images as new forming ice. At the same time melt ponds are very important drivers of the thermodynamic budget of sea ice. Also, the presence of algae can provide information about the biological activity in the marginal ice zone, but its detection in ice covered settings remains challenging. Further development of instrumentation and software to detect those features requires a better understanding of the spectral properties of sea ice, snow, melt ponds and algae presence.

Hyperspectral imagery provides a deeper look into the signature of objects in a wide range of electromagnetic spectrum. During the expedition PS115.2, we were equipped with the Specim IQ hyperspectral camera from the Oulu-based Finnish company Specim (Figure 1). Contrarily to a standard red-green-blue (RGB) camera, for every pixel in the picture, the Specim IQ camera records the spectrum in the range from 400 to 1000 nm, with a 7nm spectral resolution. The camera is based on a CMOS sensor and a f/2.2; 21 mm objective. One significant advantage of this specific model is its portability and its ability to take 2D images, while many hyperspectral cameras only provide one dimensional information (in space) and need to be carried across a scene in order to record an image (e.g., airborne measurements, via plane or helicopter).

The Specim IQ camera will be taken onboard during the 2019/2020 MOSAIC expedition. Therefore, an additional objective of experimenting is to learn to operate the camera and to test it in polar environment, in preparation for MOSAIC.

The present report is organized as follows: Section 2 provides a short description on how to operate the camera and also contains description of some test runs we did during transit time. Section 3 is a presentation of hyperspectral images which we successfully captured during three ice stations. Section 4 reviews the main recommendation we provide regarding the use of the camera in polar environment.



Figure 39. The Specim IQ hyperspectral camera (©Specim)

2. Test Run: A Fruit Detector

Taking a good hyperspectral image with the Specim IQ camera requires at least two conditions. Of course, good lighting conditions: sunlight or halogen lights are optimal since they cover most of the spectral range detected by the camera, neon or LED lights are to be avoided since they have narrow spectral bandwidth and do not provide any illumination in the near infrared portion of the EM spectrum. Taking a good picture also requires a still object: the camera scans a scene one vertical line at a time, and the total time required to complete an image ranges between 30 seconds and 3 minutes. In addition, the incidence angle of the camera is important, one should try to minimize direct reflection from the object and maximize scattering (a near-to-nadir view is often a good choice). During transit time it was not possible to take any pictures of sea ice, so we started with a textbook-style example of an apple-orange classification algorithm based on hyperspectral imagery to familiarize ourselves with the camera.



Figure 40. Our setup in Marcel König's lab.

We installed the camera in Marcel König's optical lab (Figure 2) and took pictures of oranges and apples (Figure 3). Taking a picture with the Specim IQ camera requires the following steps:

1. Frame the subject using the RGB camera mounted on the Specim IQ camera.
2. Place the white reference (for the "simultaneous" mode) in the field of view of the camera
3. Half-press the shutter button and release it: the hyperspectral camera displays imaging settings

4. Adjust focus of the hyperspectral camera: an edge-detection feature helps adjusting the focus (tip: maximize the amount of orange points in the hyperspectral camera frame)
5. Accept or adjust the exposition time: a default time is suggested but if the image turns out over- or under-exposed, exposition time can be adjusted manually on the touch-screen.
6. Fully-press the shutter button and release: the hyperspectral capture starts
7. Keep or discard image: the image appears on the screen with some information about quality of exposure and spectral range covered. If declined the camera goes back to step 3.
8. Select white reference (in simultaneous mode only): adjust threshold until the white reference can be isolated and selected. Use the touch screen to selected the white reference and press accept.
9. Normalized reflectance spectra are calculated for every pixel in the frame and can be viewed directly on the camera touch-screen!

The white reference panel should be in the field of view of the camera. The Specim IQ camera offers three modes for taking the white reference into account. One is the “simultaneous” mode when the white reference should be placed within the field of view of the camera, the other two are “custom” and “pre-defined” modes. In these modes the white reference is defined beforehand. The simultaneous white reference has shown to be the most reliable, especially in very variable outdoor light conditions (any change in light conditions in between the shots affects images taken with a pre-defined white reference).

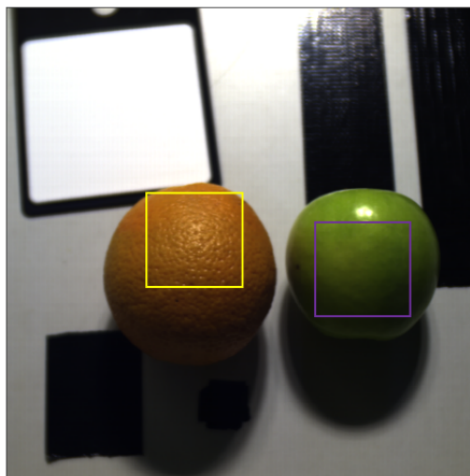


Figure 41 Orange and apple with a box defining the area of interest over each fruit.

We used the software provided with the camera to have a first look at the data and build a classification algorithm. Spectral images can also be accessed from other software as the raw data, white reference and dark reference spectrum and metadata are available in the picture export. Figure 4 presents spectra for a set of pixels within the area of interest defined in Figure 3. Purple curves correspond to the area of interest over the apple, Yellow curves correspond to the orange. A clear difference in the spectra of the two objects can be seen.

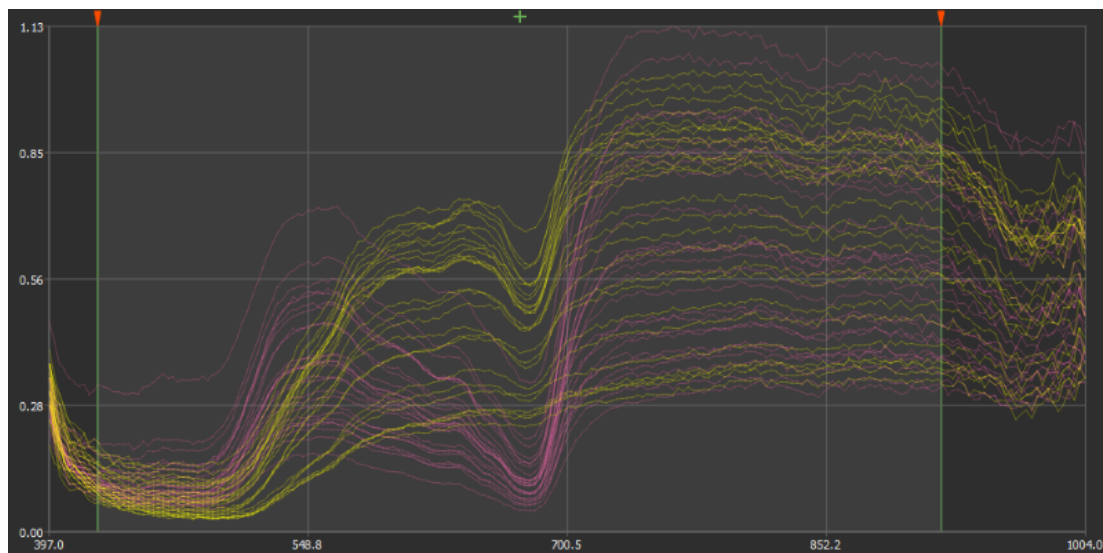


Figure 42. Spectra for different area of interest: apple (purple curves) and orange (yellow curves).

We then select a representative pixel that after re-processing and smoothing becomes the reference spectrum for the respective class of objects (Figure 5). We can see signatures of colours for each fruit (peaks for green around 550 nm and for orange around 600 nm), and also the signature of chlorophyll – more absorption just before 700 nm and then an increase in reflectance starting from around 700 nm.

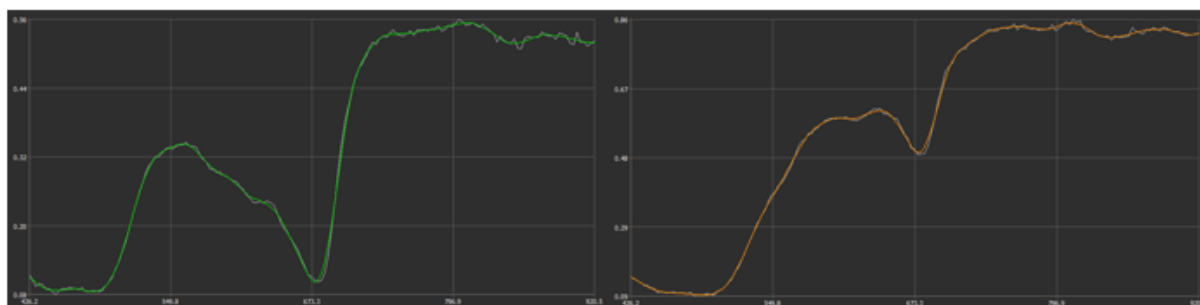


Figure 43. Apple (left) and orange (right) reference spectrum.

The reference spectrum can then be used to make object classification on an image. The user can adjust a tolerance parameter, indicating how much the spectrum from an individual pixel differ from the reference spectrum, in such a way that the object is well defined in the training dataset (area of interest). As a trivial case, the classification can be done on the same image from which the reference spectra were taken (Figure 6), but we also applied the classification tool to scenes that were captured with different illumination conditions. We further tried to 'challenge' the classification application by hiding apples within a scene composed of several other green objects. The classification application was successful in distinguishing the apples (Figure 7).



Figure 44. Classification based on spectral signature, using the Specim software.

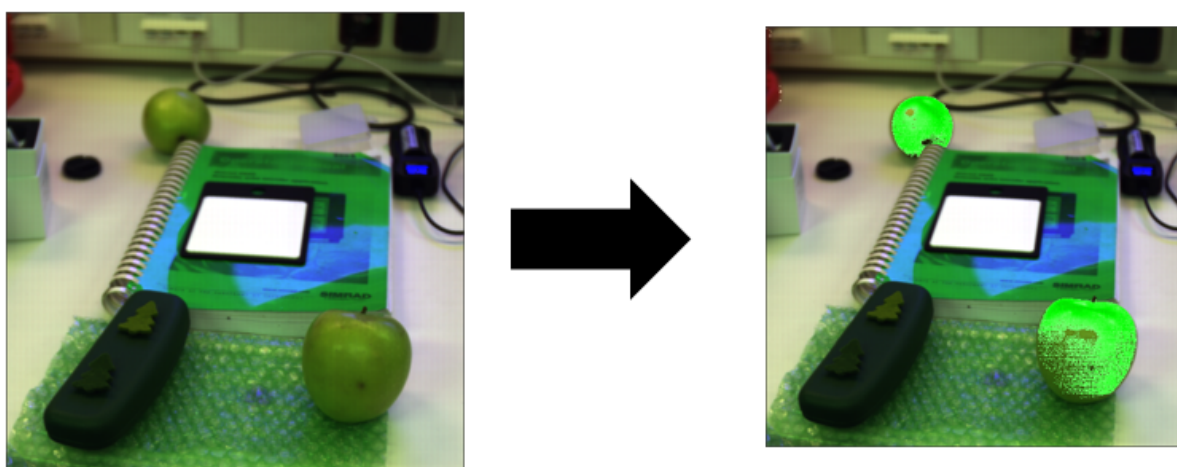


Figure 45. Application of the classification algorithm on a scene of apples hidden among other green objects. The scene was captured under different light conditions.

3. Hyperspectral Pictures of Sea Ice

Seven hyperspectral images of sea ice were taken during the expedition PS115.2. The images are available upon request. A summary of the pictures that were taken can be found in Table 1. More details on acquisition of images are described below.

Picture ID	Time (UTC)	Latitude (°N)	Longitude (°E)	Heading (°;mag) ±10	Incidence Angle (°) ±10
2018-09-21_001	08:22:53	82.182	134.779	N/A	N/A
2018-09-21_003	08:34:24	82.182	134.776	N/A	30
2018-09-21_004	08:37:53	82.182	134.776	N/A	60
2018-09-22_001	06:59:34	82.419	140.096	180	40
2018-09-22_002	07:03:22	82.419	140.094	270	40
2018-09-23_001	05:43:00	83.088	142.521	175	60
2018-09-23_002	05:46:00	83.089	142.522	115	60

Table 1. Hyperspectral images of sea ice taken during PS115/2.

21.09.2018

During an ice station on the 21st of September, Gunnar Spreen, Amelie Desmarais and Charles Brunette took the hyperspectral camera to the observation deck and took 3 pictures of a scene that included snow covered sea ice, underwater sea ice, algae presence, and open water (Figure 8). Unfortunately, the camera failed after the 3rd capture – most likely due to the cold affecting either the sensor or the electromechanic pieces inside of the camera. The RGB camera mounted on the Specim IQ still worked fine, the issue really came up at step 2: upon half-pressing the shutter a black square appeared and no signal was provided by the CMOS sensor. The camera started functioning again several hours later after it was put in warm environments on the ship.

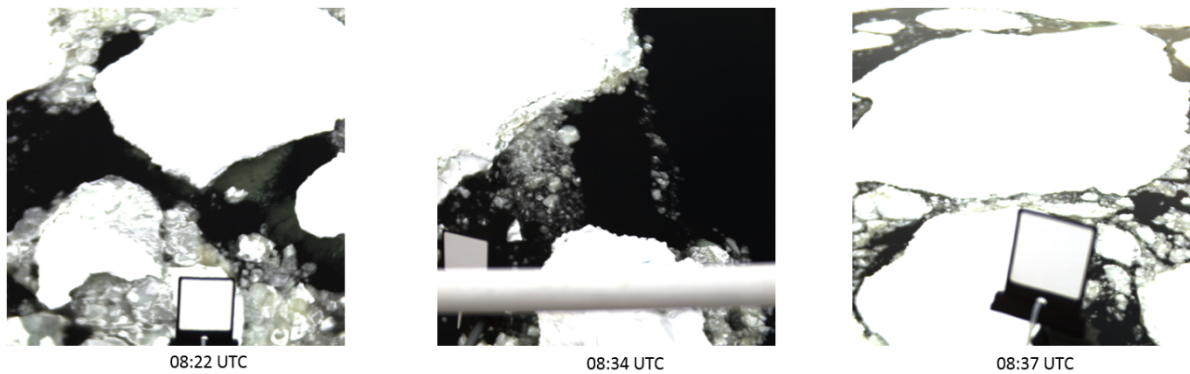


Figure 46. RGB shots of pictures 2018-09-21_001/003/004, respectively.

A quick look at the spectrum of a few points representing different features is presented in Figure 9. The four spectra show different intensities, from really high reflectance for the snow covered surface to much lower values for open water, as expected. The two spectra for sea ice (underwater ice in blue and ice-algae in pink) are representative of a spectrum for sea ice, with slightly higher values in the middle of the visible spectrum, and then a slow decay towards the near infrared. Another interesting detail that can be seen in the spectra of ice-algae, underwater ice and open water is the response of algae in the near infrared (the small peak near 750 nm). An issue is, however, present in the image: the intensity of the spectrum for snow covered ice is way above one, which means the normalization may not have been done correctly. This is likely due to the snow cover being actually more reflective or better illuminated than the white reference. It should be noticed here, that white reference was kept on the ship and not placed in focus on an ice flow. As future work it will be possible to re-process the normalized spectra by using the raw data cube.

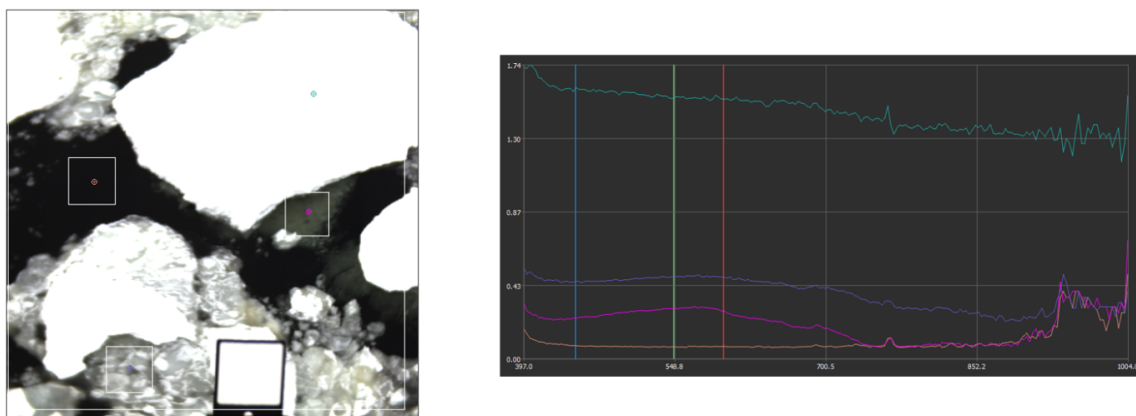


Figure 47. Spectrum of four points representing snow covered ice (dark green), underwater ice (blue), open water (orange), and algae (pink).

22.09.2018

The next day Pascal Bourgault, Aliaksandra Kazlova, Damien Ringeisen and Gunnar Spreen took the camera during an ice station directly on an ice floe and could take two pictures of a melt-pond partly snow covered (Figure 10). Unfortunately, after those two pictures the camera failed again due to the cold.

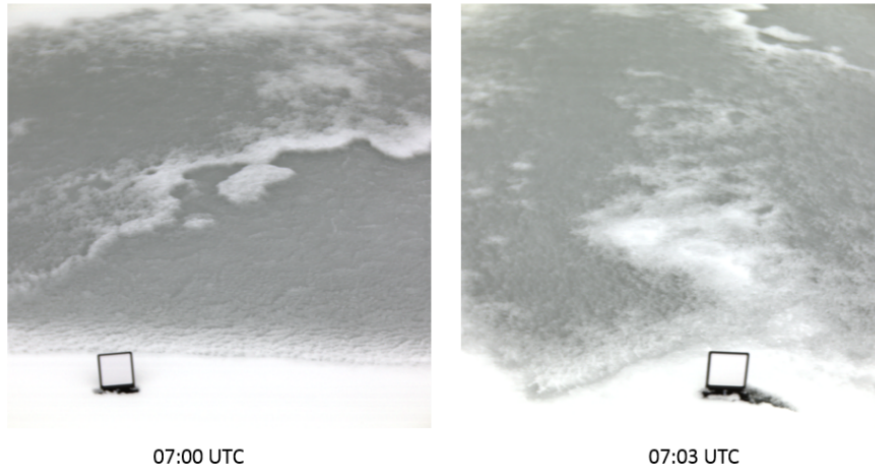


Figure 48. RGB shots of pictures 2018-09-22_001/002, respectively.

23.09.2018

The final set of hyperspectral images was taken on September 23rd (Figure 11). Anouk Vlug and Charles Brunette went to the observation deck and took two pictures of the melt pond on which Marcel König was performing in-situ spectral measurements. We took two more pictures that were overexposed and not usable, after which some snowfall started and had us stop the captures. This time, in addition to the protection case of the camera (the protection case was also on the camera during the previous days), we installed a strap so that the camera can be worn around the neck and hidden under a jacket in between every shot. This makeshift solution worked well as for the short period of time that we spent outside, the camera functioning normally throughout.

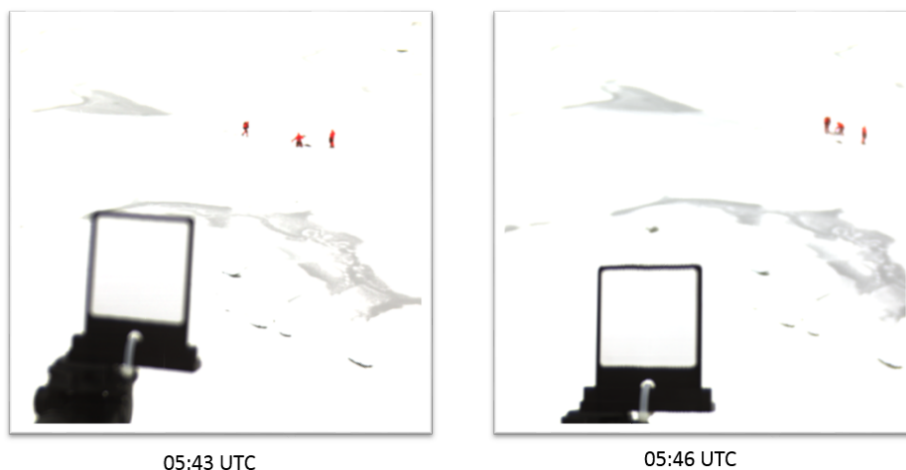


Figure 49. RGB shots of pictures 2018-09-23_001/002, respectively. We can see scientists working on the ice.

First attempt to create and apply a classification algorithm to refrozen melt ponds and snow covered ice gives promising results (Figure 12). We used the image 2018-09-23_001 which show a clear separation between refrozen melt-ponds and snow covered ice to create reference spectra for the two surface types. After that we apply the classification application on the picture 2018-09-22_001 taken the day before. The classification application was able to distinguish between bare refrozen melt-pond and snow covered sea ice. This is encouraging in the sense that even though only several images were taken with the hyperspectral camera during expedition PS115.2, we still were able to perform cross-testing of different classification applications.

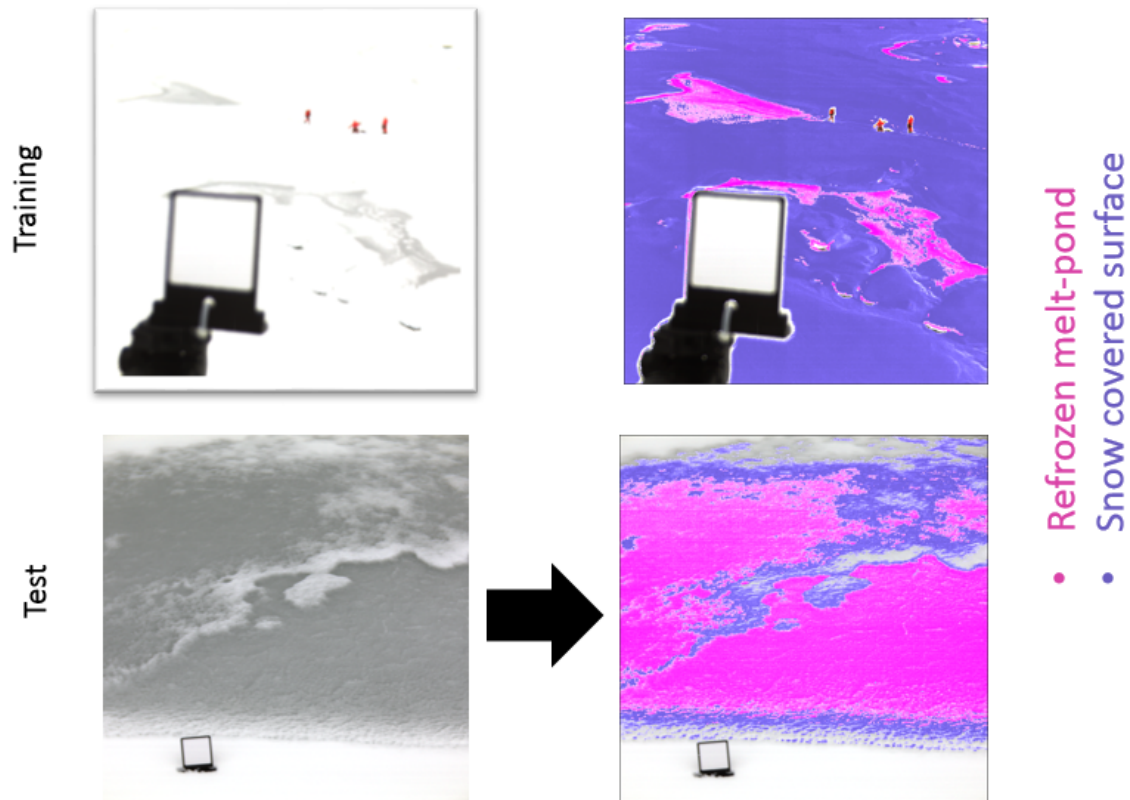


Figure 50. Classification application for refrozen melt-pond and snow covered ice.

4. Outlook

As a final word we wish to provide a few recommendations for future use of the Specim IQ camera in Arctic environment.

- Failure due to cold: To the best of our understanding the hyperspectral sensor failed due to the cold, even though its operating temperature goes down to 0 degree Celsius as indicated by the manufacturer, and even though we did not experience temperatures much colder than -4 C. We conclude that the camera should be kept at temperatures above 0 C to ensure uninterrupted operation. This can be done by keeping the camera underneath a jacket, close to the body, but a device that keeps the camera above the lower temperature required for operation would be an optimal solution and should be considered.
- Orientation and angle of incidence: Some smartphone's compass application that give gyroscopic orientation provide a surprisingly easy and straightforward way of measuring the direction the camera is pointing at. It should be noted, however, that when recording the gyroscopic orientation; to retrieve the orientation of the camera relative to the geographical north one should check the offset between gyroscopic and

geographic orientation at a specific location. This can be done at the Bridge for instance.

- Touch-screen compatible gloves: The Specim IQ camera touch-screen functionalities are very user-friendly but the screen cannot be used with gloves on. Fingers get cold very quickly, and a pair of touch-screen compatible gloves is a nice accessory for the camera.

A.7.4.4 Ship Radar for Sea Ice Dynamics

D. Ringeisen (AWI)

Objectives

The sea ice radars have been used for several years to help navigation in the Arctic and Antarctic Seas. Radar data can be used to investigate the sea ice drift around the ship, and therefore the dynamics of the ice. This can help ship navigation but also would help to design better sea ice models for high resolution. Compared to satellite observation, radar data have a high resolution and a good coverage. Sea ice radar analysis are to be used during the upcoming MOSAiC expedition starting in September 2019 and ending during Summer 2020. RV Polarstern is going to be used as a floating research platform drifting with the ice during a complete year, giving the perfect opportunity to observe the ice at different stages, and through different sea conditions. We are here performing a preliminary analysis of the radar capabilities and give recommendation for the expedition.

Data and methods

Every 5 minutes, radar images are extracted from the ice radar system WAMOS developed by RUTTER. The images are saved on the ship's server dedicated to instruments and accessible to scientists onboard. We choose a radar range of 4 nautical miles, or roughly 7.5 km. The extracted images have dimensions of 1024 by 1024 pixels, giving a spatial resolution of 7 m. The radar is situated on *Polarstern's* mast, on port-side. The ship is shielding the radar returns in direction of the ship's chimney, leaving an empty space of almost 90° on the aft-starboard quadrant of the radar images. The images are recorded in TIFF file format.

The ice movement can be measured only if the ship is moving really slowly or on station. If the ship is in transit, the pieces of ice are going to be on the radar images only for a couple of pictures. As we want to follow the ice deformation, we select only the radar images from stations. The images from stations that feature sea ice in the ship's vicinity are extracted and sorted by station. 10 station have been found to be long enough and with enough sea ice elements to be suitable for an ice drift analysis. These stations are listed in Table 1. A Python algorithm is implemented to analyze the radar images and compute the drift of sea ice, and then compute the sea-ice deformation, shear and divergence. The design of the algorithm is inspired by the previous works of Fowler (1994) and, more recently, Lund et al. (2018).

Name	Date Beginning	Time Beginning	Date End	Date End
Station 1	2018-09-15	07:20	2018-09-15	09:01
Station 2	2018-09-15	10:10	2018-09-15	11:40
Station 3	2018-09-15	12:25	2018-09-15	14:05
Station 4	2018-09-15	19:40	2018-09-15	22 25
Station 5	2018-09-15	22:50	2018-09-16	01:55
Station 6	2018-09-21	08:00	2018-09-21	16:20
Station 7	2018-09-21	17:05	2018-09-21	22:05
Station 8	2018-09-22	06:45	2018-09-22	09:55
Station 9	2018-09-23	08:45	2018-09-23	13:00

Station 10	2018-09-23	04:25	2018-09-23	06:10
------------	------------	-------	------------	-------

Table 3: List of station suitable for ice drift measurement, with their start and end time.

First, the ship's position, heading and speed are extracted from the ship information system (DSHIP). The heading is used to exclude the screened zone from the drift computations. Then, a new grid, the *drift grid*, is laid upon the radar images. The cell size of this *drift grid* can have a size between 5 and 20 pixel of the radar image. The drift grid cells of the first radar image A are extracted to be compared to the second radar image B. The Maximum Cross Correlation (MCC) are used to compare the cell from A and a part of the image B that is plausible for a 5 minutes drift interval. A maximum distance of search of 10 pixels is typical. The place of corresponding pattern in B gives us the drift between two images. There are several methods to compute MCC. Two were implemented here: direct computation and computation using the Fast Fourier Transform (FFT). For the direct method, compute the cross correlation, we use the formula:

$$CC_{direct}(A, B) = \frac{\sum_x \sum_y (A_{xy} - \bar{A})(B_{xy} - \bar{B})}{\sqrt{(\sum_x \sum_y (A_{xy} - \bar{A})^2)(\sum_x \sum_y (B_{xy} - \bar{B})^2)}}$$

where \bar{A} is the average of matrix A. And for the FFT method, the cross correlation is given by

$$CC_{FFT}(A, B) = F^{-1} \left(\frac{\mathcal{F}_A^* \mathcal{F}_B}{|\mathcal{F}_A \mathcal{F}_B|} \right)$$

where F^{-1} is the inverse Fourier transform, F the Fourier transform, and \mathcal{F} the complex conjugate of the Fourier transform. Once the drift velocities are determined by the MCC method, the deformation of the ice can be computed as it is done, e.g., for SAR satellite images (Kowk and Cunningham 2002).

Results

The radar images show the ice movements around the ship and are suitable for ice motion and deformation analysis.

The drift computation algorithm first is tested on simulated drift images, and we compared the difference MCC methods. The direct MCC method appears to be the best method to get reliable results, but is substantially slower. The FFT method is faster but fail in some parts of images, probably because of the interference speckles. Therefore, we only use the direct method below. A patch size of 10 pixels seems a good compromise between resolution and good drift computation. Smaller patch sizes make the reconstruction of the drift difficult and the velocity fields are getting noisier. We can also see that during rough sea with thin ice, the wave crests mask the sea ice cover in the radar images.

The algorithm is tested on a couple of simulated drift images: A radar image is taken and a fake drift is created by moving every pixel a given distance, which means the drift is constant for the whole image and known. The ice drift between the new and original image computed with the different methods to test their efficiency. The MCC method is giving perfect results, while the FFT does not detect the drift for all part of the image.

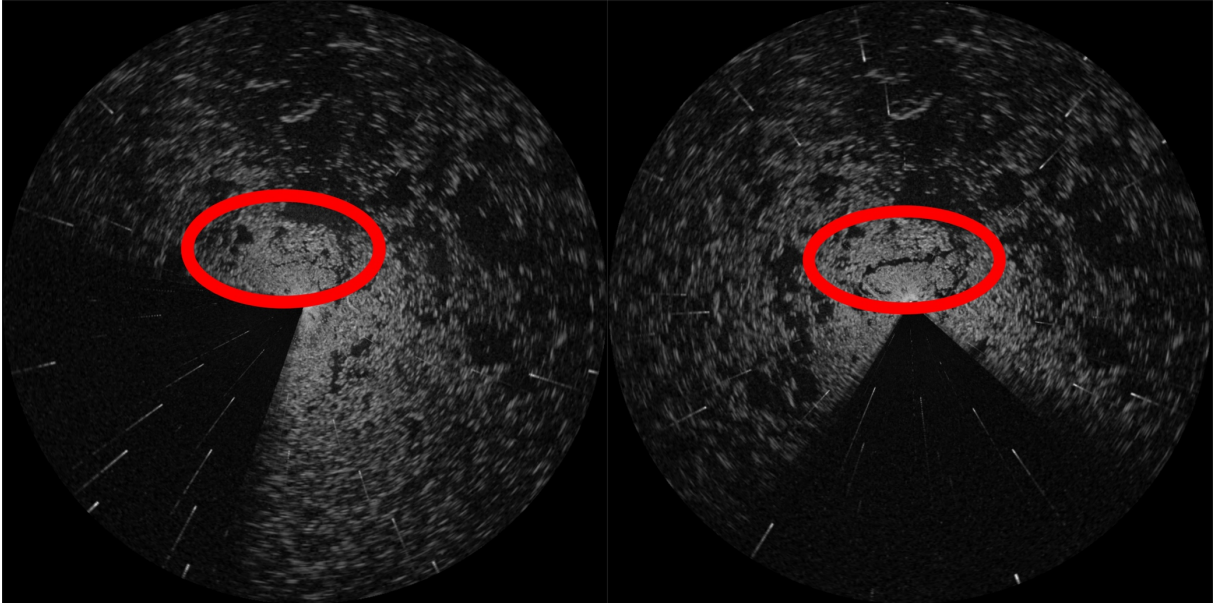


Figure 51: Ice radar images during station 10. Images are North oriented. The ship is in the center of the figure. The images are taken 3 hours apart. The opening of a crack slightly north of the ship can be seen (circled in red on both pictures).

We now focus on station 9 as an example. Figure 1 shows two ice radar images during this station, taken 3 hours apart. We can observe a lead opening north of the ship. This station also features ice motion in the far field, and at the end of the sequence, a strong deformation east of the ship. This station takes place on the 23rd of September, and starts at 8:45 UTC and ends at 13:00 UTC. The set is composed of 51 images.

The algorithm is showing good results in the case of a slow global drift (e.g. when the ship is moving slowly to position for station, or if there is a global drift around the ship). The global drift is clearly visible (figure 2, top right), and there is a bit of noise. In the case of slow movements of only small parts of the image (figure 2, bottom left), the algorithm is less efficient. Some features are recognized, but some are not. More advanced algorithms would be needed to get ice movement with enough precision to compute ice deformations from it. Petrou and Yin Li (2016) described advanced technics that allow for example to improve MCC speed, or get the drift for every pixel in the image.

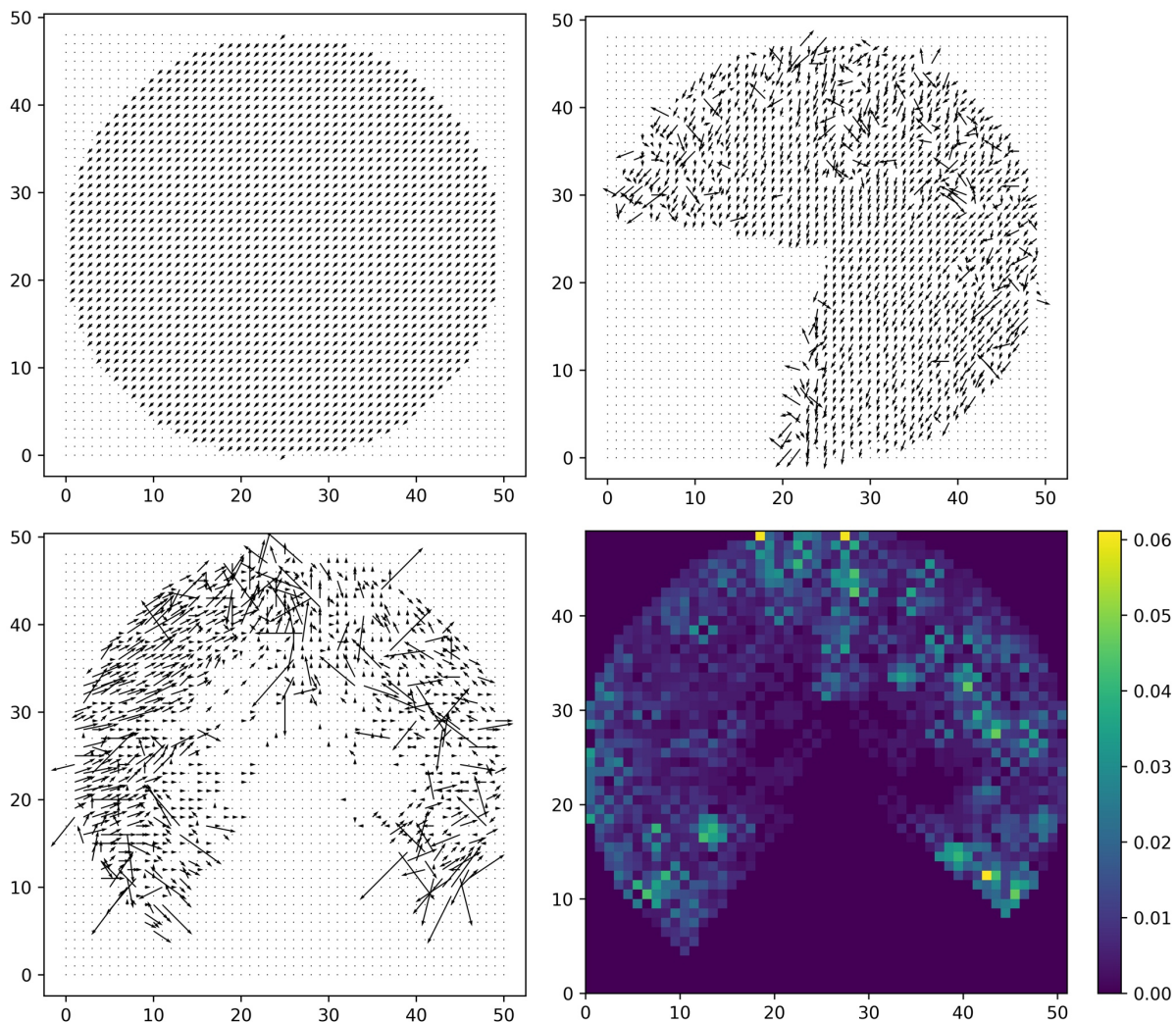


Figure 2: Figures showing the drift vectors measured by the direct MCC algorithm: (top left) for fake drift designed for testing, (top right) for a period of observed uniform drift during station 9, and (bottom left) for a period of small movements during station 9. (Bottom right) Sea ice total deformation computed from drift velocities shown on the bottom left image. We can see that the velocity field is too noisy to be able to compute the deformations. The drift and deformation are given here without units, and should just be compared qualitatively

MOSAiC

From these preliminary results, we can give recommendation for the MOSAiC expedition:

- Two types of artifacts are present in all images and their deletion are not the subject of this work. First, there is some radar interference speckles. These are described and removed from the radar images in Lund et al. (2018). Second, concentric circles appear close to the ship when it is cruising in open-water areas. They may disturb the motion detection algorithm, especially for thin ice.
- In case of high wave events with low sea ice cover, the images are blurred by the waves. Recording images at higher frequency would allow averaging technics to be used (Lund et al, 2018). Every few seconds would be good, every second if possible. Although it may take a lot of disk space for the whole year of MOSAiC drift (1.1 MB per image, 4 GB per hour if 1 image/second).
- The MCC algorithm presented here appear to be robust but is relatively slow and simple. Petrou & Ying Li (2017) present two state-of-the-art algorithms that could be implemented. The first one is an improved MCC algorithm using multi-resolution

cascade of images to compute the drift faster and more precisely. The second one, called Optical Drift give drift information pixel-per-pixel, therefore allows to resolve small scale deformation and yield better recovery of ice drifts.

- A better place for the ice radar, or the use of the navigation radar on top of the mast would avoid losing a quarter of the Field Of View (FOV) because of shadowing from the ship. In case this is not possible, the orientation of the radar has to be taken into account for analysis of ice motion.

Data Management

The images from the radar are stored on the ship servers in TIFF format.

References

- Fowler CW (1994) Ice motion derived from satellite remote sensing with application to ice studies in the Beaufort Sea. PhD Thesis, Department of Aerospace Engineering Science, University of Colorado.
- Kwok, R, Cunningham GF (2002). Seasonal ice area and volume production of the Arctic Ocean: November 1996 through April 1997. *J. Geophys. Res.*, 107, 8038. doi:10.1029/2000JC000469
- Lund B, Graber HC, Persson POG, Smith M, Doble M, Thomson J, (2018) Arctic sea ice drift measured by shipboard marine radar. *Journal of Geophysical Research: Oceans*, 123. doi.org/10.1029/2018JC013769
- Petrou Z, Ying Li T (2017) High-Resolution Sea Ice Motion Estimation With Optical Flow Using Satellite Spectroradiometer Data. *IEEE Transactions On Geoscience And Remote Sensing*, 55(3), March 2017.

A.7.4.5 Sea Ice Buoy Analysis

N. Ridenour (UofAE)

One part of the sea ice work was deploying sea ice buoys on to the ice as part of the MOSAiC and YOPP projects described earlier in the report (Section 4.4). First, the buoys, nine Surface Velocity Profilers (SVPs) and ten Microstar drifters were unpacked and brought to the *Peildeck* (Figure 1A) where the buoys were turned on, so we could see if all buoys were transmitting their locations and working properly. Of those buoys, four Microstar drifters were not working properly, and were taken down to the wet lab to be repaired (Figure 1B). It was determined that two of the Microstars were not able to be repaired, one due to an empty battery, while the other was not transmitting its location. The two remaining buoys were able to be repaired, however after deployment these two buoys stopped working.

The ArcTrain students assisted our ArcTrain PI, Gunnar Spreen, in deploying the buoys, either from the mummy chair, or during ice stations, when the ice conditions allowed for walking on the ice (Figure 1C,D).

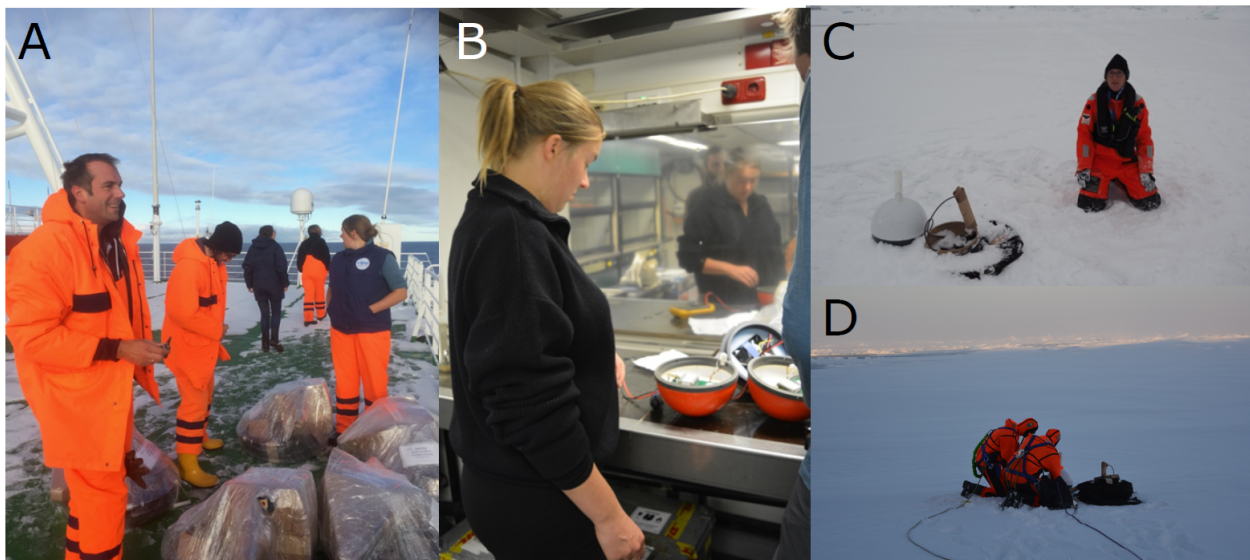


Figure 1: ArcTrain student buoy activities. A) ArcTrain students assisting Gunnar with bringing the buoys to the peildeck. B) Anouk repairing one of the Microstar buoys that was not working. C) Aliaksandra with one of the deployed buoys on one of the helicopter ice stations. D) Gunnar and Charles deploying the first SVP buoy.

Data collected by the SVP buoys consisted of time, location, air pressure, and temperature, while for the Microstar buoys, time and location data was used for the following analysis.

Surface Velocity Drifters

The trajectories of the SVP drifters are towards the north, for the exception of one, which is drifting eastwards, and was the only one deployed in completely open water (Figure 2A,B). Combined with the temperature and pressure time series (Figure 2C,D), we see there was a high pressure system passing over the buoys in early October which also brought colder temperatures, of around -6°C to SVP5 and SVP6. We note that SVPs 2, 3, and 8 are measuring sea surface temperature, as can be seen by the almost constant temperature values between -1.5 to -1.7°C , while SVP 5 and 6 are likely measuring air temperature. The remaining buoys would be measuring the snow surface or air temperature. Air pressures, decrease in the October data, while air temperatures (SVP 5 and 6) remain around -2°C . Buoy drift was also calculated, shown in Figure 3, by using the hourly location and time data transmitted from the

buoy. From the location, we can calculate the distance the buoy had travelled from the previous location and dividing by the change in time from the last location recorded. This calculation gives us a time series of the mean ice drift during one hour (Figure 3A). Note that even during one hour the buoys, in most cases, will not drift linearly and thus the actual distance covered will be longer than the straight line assumed here. Therefore, the instantaneous ice drift speed of the buoys actually is even a bit higher than the hourly ice drift speed recorded here. Oscillations, which are likely inertial but some could also be forced by tides, are clearly seen in the time series. To determine the process behind these oscillations requires a frequency analysis. Using a 48-hour Gaussian smoothing tool, so as to remove the oscillations, we see higher drift speeds at the end of September, and after October 7 (Figure 3B). A storm passed the buoys at the end of September, as can be seen by the decreasing air pressure in the time series. Low pressure systems bring stronger winds, leading to increased ice drift speeds. Increased drift speeds also occur after October 7, which also coincide with decreasing air pressure. The highest correlation coefficients between ice drift speed and air pressure for this data set occur with buoy 2, with an R value of -0.49, buoy 6 with a correlation value of 0.39, and buoy 9 with a value of 0.37. The negative correlation can be explained by low pressure systems with strong winds passing over, while the positive correlations can perhaps be explained by a change in the pressure gradient force induced by high pressure systems, as well as winds. To further this analysis, one could evaluate the relation between the change in pressure and ice drift, as winds would be strongest with larger gradients in pressure. When we correlate the smoothed absolute value change in pressure time series (we used a 48-hour Gaussian window) with the ice drift, correlations are much higher. SVP2 and SVP7 had the highest values of 0.52 and 0.61 respectively. Buoys SVP4, 5, 8, and 9 had lower values of 0.42, 0.49, 0.32, and 0.44 accordingly. The lowest correlation coefficients were associated with SVPs 3 and 6 with R values of 0.19 and -0.08 respectively.

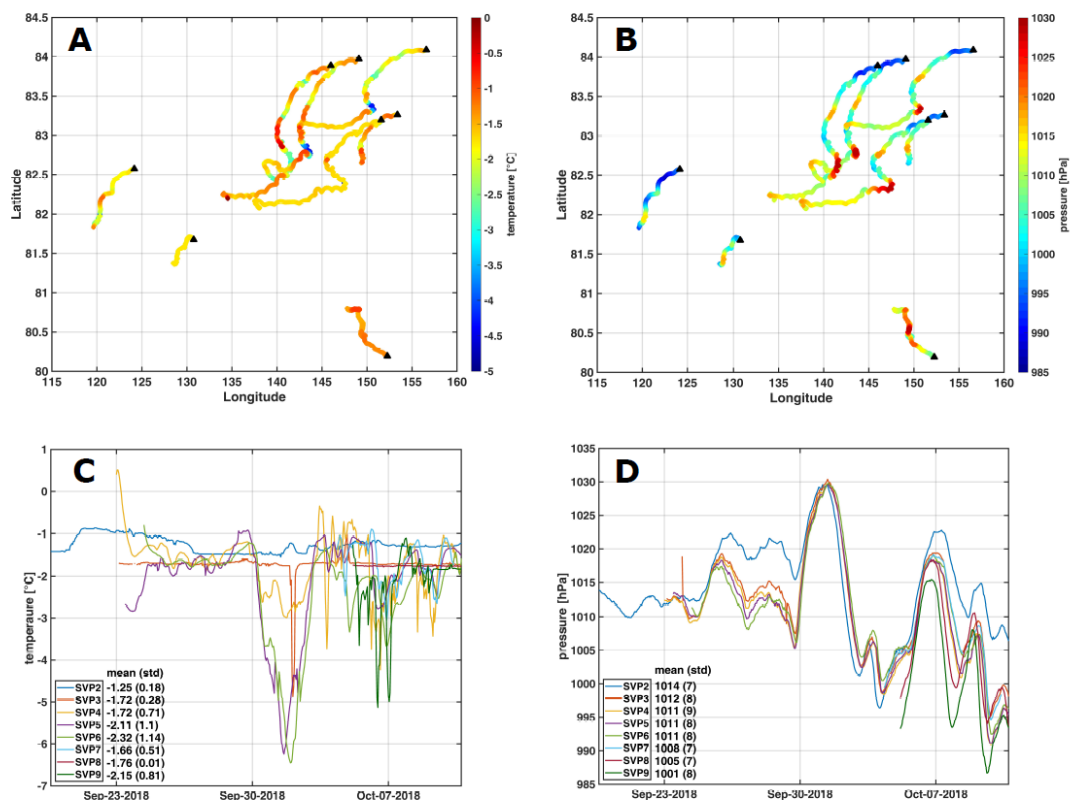


Figure 2: SVP buoy temperature and pressure data. A) Temperature along buoy trajectories with black triangles indicating the most recent position. B) Air pressure along buoy trajectories. Time series of C) temperature and D) pressure for each buoy. Mean and standard deviation for each buoy time series are shown in the bottom left corners.

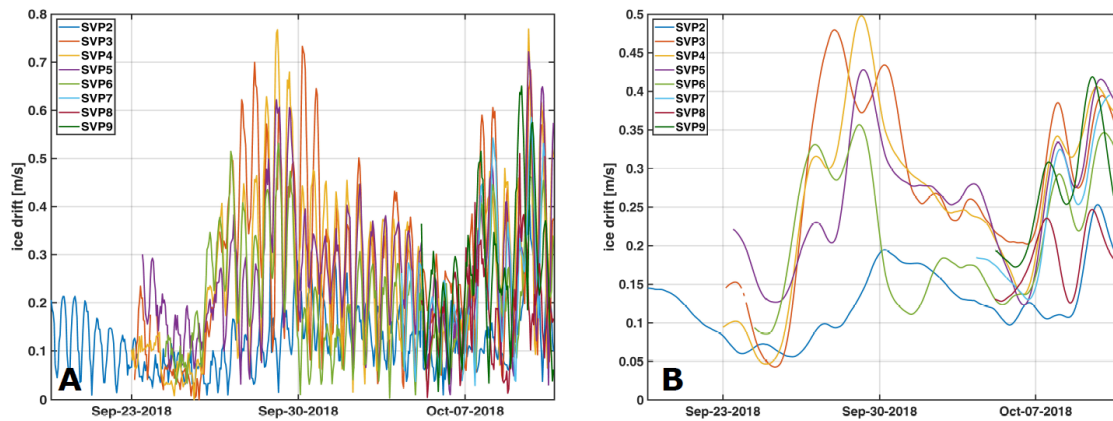


Figure 3: SVP buoy drift. A) Raw ice drift for 8 SVP buoys. B) Smoothed SVP buoy drift using a 48-hour Gaussian smoothing tool.

Microstar drifters

The drift trajectories of the ice show a general northward flow, for the exception of two buoys (numbers 6 and 8), which have mostly eastward trajectories (Figure 4A). The majority of the buoys show inertial or tidal oscillations in their trajectories, similar to the SVP buoys, which is also clearly seen in the drift time series (Figure 4B). The oscillations have a period of almost 12 hours. We used a 48-hour Gaussian smoothing window to remove the effect of the oscillations in the time series, and see the smoothed time series in (Figure 4C). During the first part of the time series, from September 24 to September 29, ice drift speeds were higher than during the data in October thus far. This is in part due to free drift, and higher winds, due to storms passing through the area. To estimate the trajectory of the storm using the ice drift data, we looked at the time of maximum drift speed from September 27-28 (Figure 5). From the ice drift speeds, we estimate that the storm approached the buoys from the north, first passing buoy number 2, before reaching buoy number 8 to the south. Buoy number 3, to the east of buoy 8, had maximum drift following buoy 8, before the storm appeared to turn northward, reaching buoy 1 and 7, followed by buoy 4. This schematic is seen in Figure 5B.

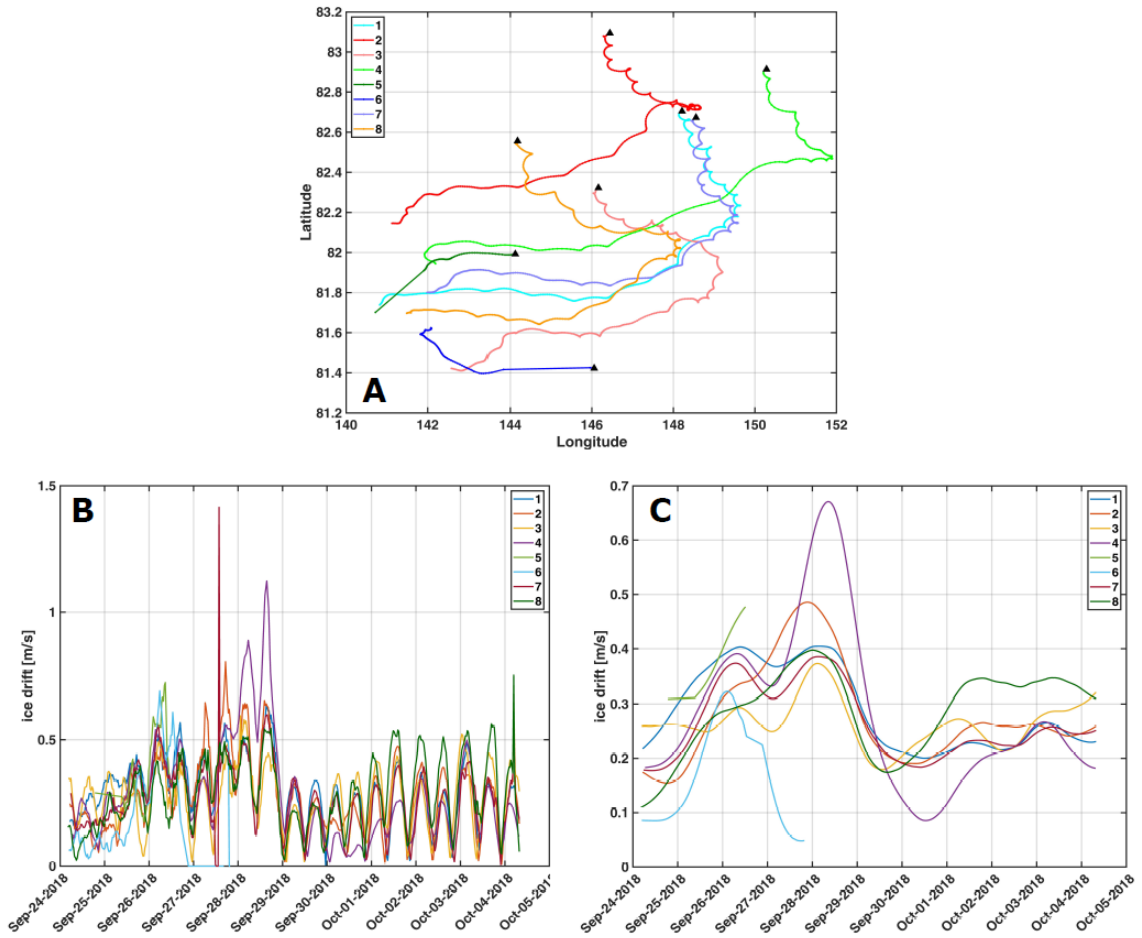


Figure 4: Microstar buoy A) trajectories, B) raw ice drift, and C) smoothed ice drift, using a 48-hour Gaussian smoothing window. Black triangles in panel A shows the most recent position of the buoys.

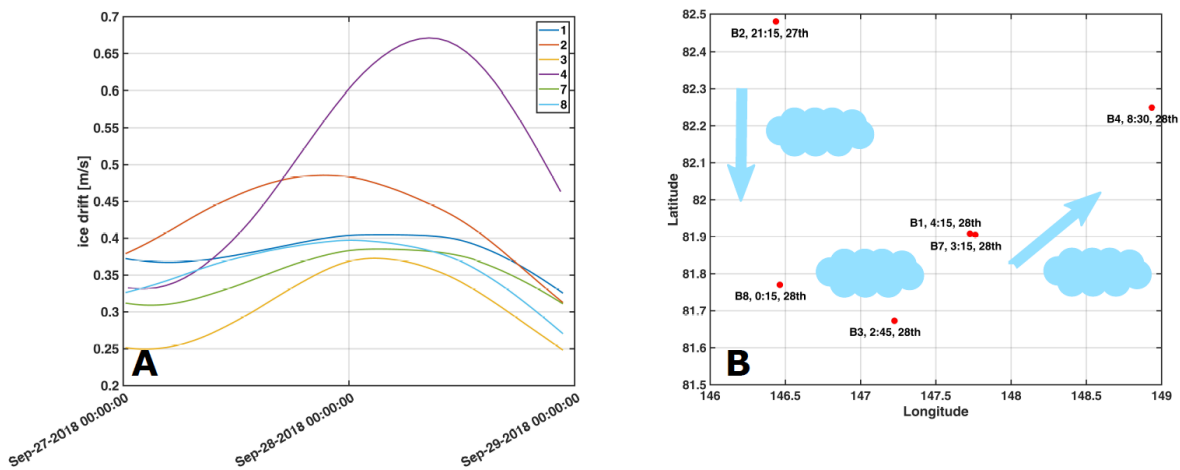


Figure 5: A) Ice drift speeds on September 27-28. B) Times and locations of maximum drift speed during September 27 and 28. Cloud arrows denote the possible track of the storm based on the maximum ice speed.

We also wanted to evaluate the relation between wind and ice, with stronger winds causing faster ice drift, as has been found historically. We compared our smoothed ice drift to model forecast data available onboard, shown in Figure 6 (top panel). We expect during times of high

wind speeds to also have higher ice drift speeds. Unfortunately, we do not see this in Figure 6, which could be due to the fact that the model forecast wind speeds and locations did not match the actual situation. Thus, an atmospheric reanalysis product would likely produce better results than forecast data.

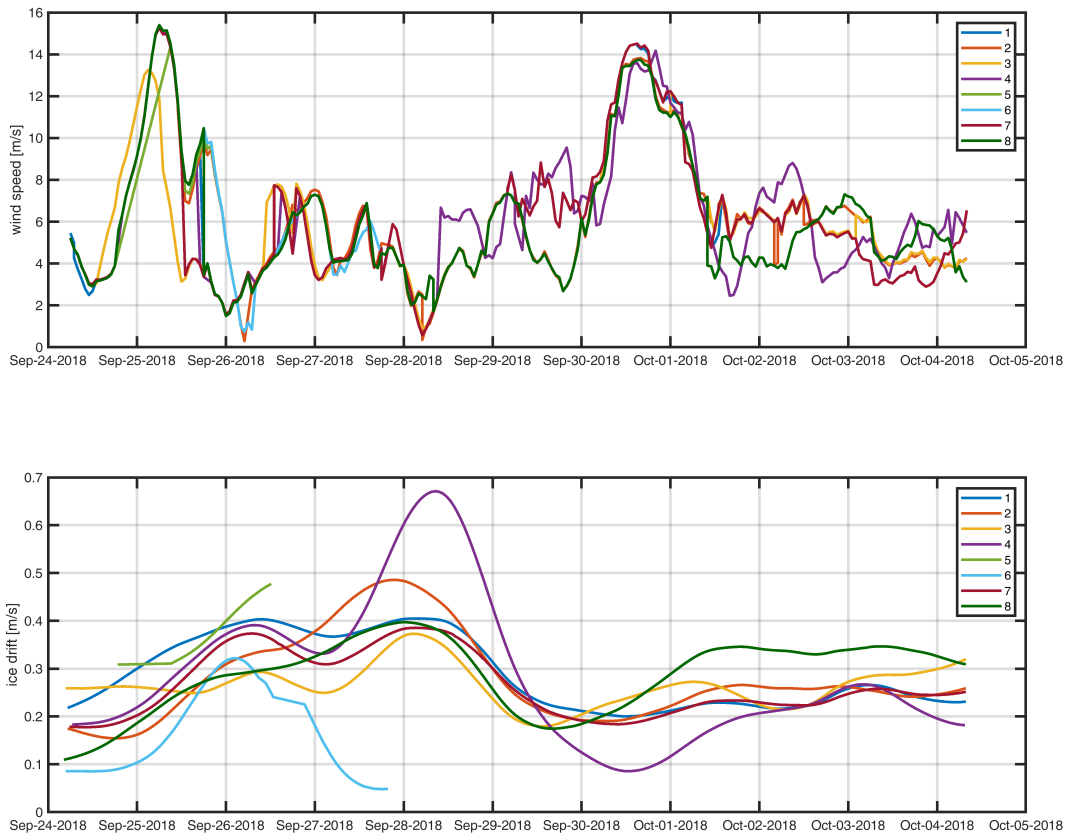


Figure 6: The top panel shows the time series of modelled forecast wind speed, while the bottom panel shows observed ice drift, for each of the 6 Microstar buoys.

A.7.4.6 Sea Ice Thickness and Temperature/Salinity Profiles

Samira Samimi (UoC), A. Kazlova (UoB-IEP), A. Desmarais (McGill)
with contributions from Gerit Birnbaum (AWI), Marcel König (CAU), Niels Fuchs (AWI),
Heike Zimmermann (AWI) and the ArcTrain Team

Objectives

In recent decades, as a result of climate change the Arctic is warming. The summer minimum sea ice extent is decreasing and becoming thinner and younger. The Arctic is now dominated by first-year ice, which is thinner and covered by a larger fraction of melt ponds compared to the older multiyear ice. This leads to an increased absorption of solar radiation in the ice (+18%) and transmission to the ocean (+7%) (Figure 1). The sea ice today is thinner and younger than during previous decades. More in-situ measurements are needed for better understanding of these dramatic changes and to validate the data from remote sensing algorithm with data from ground measurements.

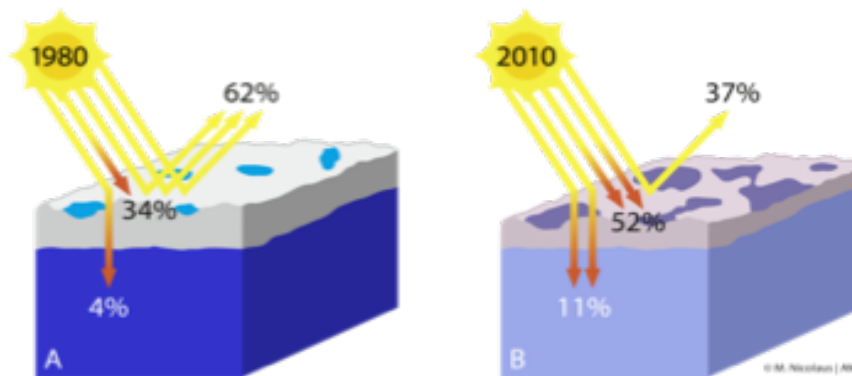


Figure 1. A: multiyear ice B: first-year ice. (Nicolaus et al., 2012).

During the PS115/2 expedition the sea ice team (Gerit Birnbaum, Niels Fuchs, Marcel König, Heike Zimmermann) combined the ground measurements with airborne measurements from helicopter and satellite (see Section 4.2). Their aim is to understand the temporal evolution of melt pond characteristics in different arctic sea ice regimes by producing the link between in-situ observations and the data from airborne and spaceborne measurements.

The sea ice thickness measured from space has large uncertainties. Therefore we measured sea ice thickness in-situ and deployed buoys on different ice floes, which for example can be used to evaluate the data from spaceborne sensors. This measurements are the only in-situ ice thickness measurements that exist in this part of the Arctic during this time of the year.



Figure 2. Preparing for sea ice measurements at Ice station PS115/2_ICE-9.
(Photo: Christian Rohleder)

In-situ ice thickness measurements by drilling and temperature/salinity profiles

Sea ice thickness measurements on the ground were collected during four ice stations:

ICE Station	Location	Date	Time (UTC)	Measurements
PS115/2_ICE-2	82.06° N, 119.27° E	15.09.2018	8:10-8:44	Buoy deployment, Snow/Ice thickness
PS115/2_ICE-6	83.08°N, 142.52°E	21.09.2018	22:15- 13:15	Buoy deployment, Snow/Ice thickness, Ice coring
PS115/2_ICE-8	82.42° N, 140.11° E	22.09.2018	8:29-10:30	Buoy deployment, EMP
PS115/2_ICE-9	83.01° N, 142.31° E	23.09.2018	04:00- 06:00	Buoy deployment, Snow/Ice thickness, Ice coring

Table 1. Ground in-situ sea ice measurements during PS115/2.

Sea ice thickness was measured by drilling and electromagnetic techniques (EMP). Ice sample across the entire depth of an ice floe were collected by coring. At the ice station PS115/2_ICE-2, two holes were drilled 2 meters apart next to the buoy. Only one hole was drilled at Ice station 6 and 8 next to the buoy. Ice station PS115/2_ICE-6 was on the thinner ice flow while PS115/2_ICE-8 was on the more deformed ice. The ice thickness at station 8 was measured at 358 cm thickness, which was very thick and unusual compare to our observation during the sea ice watch. The reason for this diverse thickness was due to the helicopter landing spot which needed to be on the more stable floe. During ice station PS115/2_ICE-9, 3 ice thickness measurements were done: one next to the buoy deployment site on the thinner part of the ice floe, and two each next to the ice coring sites (Table 2). The ice thicknesses between 78 cm and 116 cm observed during ice stations 6 and 9 can be considered more typical for our

working area than the other two stations with thicker ice (see also the estimated ice thickness from the ice watch on the bridge in Section 4.5 and Appendix A.7.4.1).

Preliminary Results

Measurements	Ice thickness (cm)	Snow thickness (cm)	Ice Freeboard (cm)
PS115/2_ICE-2	190	8	13
PS115/2_ICE-2	195	8	13
PS115/2_ICE-6	78	9	6
PS115/2_ICE-8	358	7	63
PS115/2_ICE-9	116	12	11
PS115/2_ICE-9	114	12	7
PS115/2_ICE-9	74	12	2

Table 2. Ice/snow thickness measurements taken during ice stations.

During ice station 6 and 9 ice cores were drilled. The cores were analyzed for temperature profile and salinity. Temperature was measured using a thermistor. Samples were cut in ~10 cm sections (with breaks in some sections) and bagged, melted, bottled and analyzed for salinity profile.



Figure 3. Samples bottled and ready to be analyzed in the lab for salinity.

Temperature/ Salinity profile for ice station PS115/2_ICE-6

Depth (cm)	Temperature (°C)	Salinity depth (cm)	Bulk Salinity
snow	-1.4	5-0	2.137

surface	-1.2	0-10	0.250
10	-0.6	10-35	0.761
20	-0.2	35-45	1.915
30	-0.6	45-55	3.121
40	-0.9		

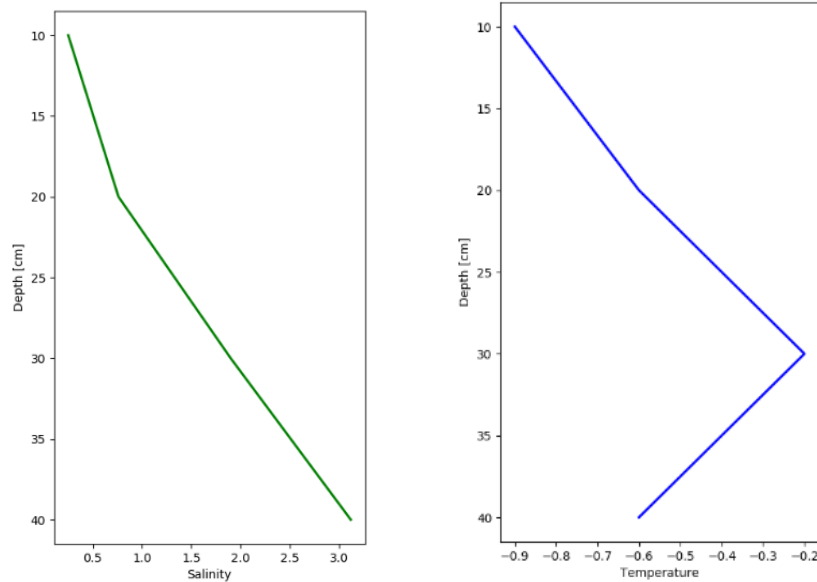


Table 3. Temperature and Salinity profile in the top section of core at PS115/2-6.

The salinity profile was only measured in the upper section of the core. Typically the salinity increase with depth. These values at the station PS115/2-6 were between 2-3 PSU. This is due to the fact that the upper layer of ice is melting during the summer season and the salty brine is propagating down to the lower parts of the ice. These values during the winter are usually higher (about 6-8 psu).

Temperature/ Salinity profile for ice station PS115/2 ICE-9

Depth (cm)	Temperature (°C)	Salinity depth (cm)	Bulk Salinity
Air	-2.2	0-9	2.009
snow	-4.5	9-20	0.730
surface	-2.8	20-30	0.752
2	-2.9	30-40	0.914
5	-1.7	40-53	1.255
15	-1.2	53-63	2.554
20	-1.3		
30	-1.4		
40	-1.1		
50	-1.2		
60	-1.3		
70	-1.4		
80	-1.4		
90	-1.5		

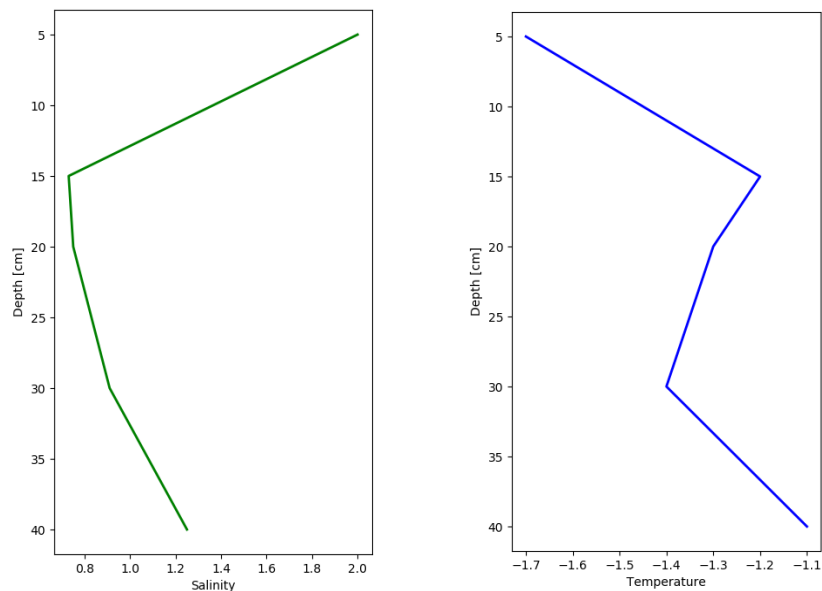


Table 4. Temperature and Salinity profile in the top section of core at PS115/2-9

We can see that the upper layer of the core at the station PS115/2-9 shows higher salinity. This could be due to flooding on the top of the floe.

In conclusion, there were limited amount of ice thickness records and cores collected during this cruise, which thus necessarily do not represent the whole region and cannot give us a complete outlook on the sea ice situation in the eastern Arctic sea.

EMP Ice Thickness Measurements

The Profiler EMP-400 is a digital, portable, multi-frequency electromagnetic induction sensor. With electromagnetic induction (EM) sounding the conductivity of different layers can be measured by actively inducing eddy currents in the layers by means of electromagnetic fields (primary EM field; Figure 4). These eddy currents will induce their own electromagnetic fields (secondary EM field) whose amplitude and phase depend on the electrical conductivity of the respective layers. By measuring the amplitude and phase of the secondary field the conductivity structure of the underground can therefore be observed. The user can collect data at up to three distinct frequencies simultaneously. The system bandwidth extends from 1 kHz to 16 kHz. The systems primary data output is the orthogonal components (Real and Imaginary, or the In phase and Quadrature) of the mutual coupling field ratio (Q) of the transmitted field to the induced field in parts per million (PPM) and apparent conductivity (σA). The In phase and Quadrature components of the induced secondary field, as well as the apparent conductivity are collected and stored for each reading along with a time stamp. GPS data, in the form of a NMEA 0183 GGA string is also recorded if the internal WAAS GPS is enabled or if an external high-resolution GPS system is interfaced with the PDA via its RS-232 serial port. Fig. 4 shows the working principle of the EMP instrument and the equipment itself.

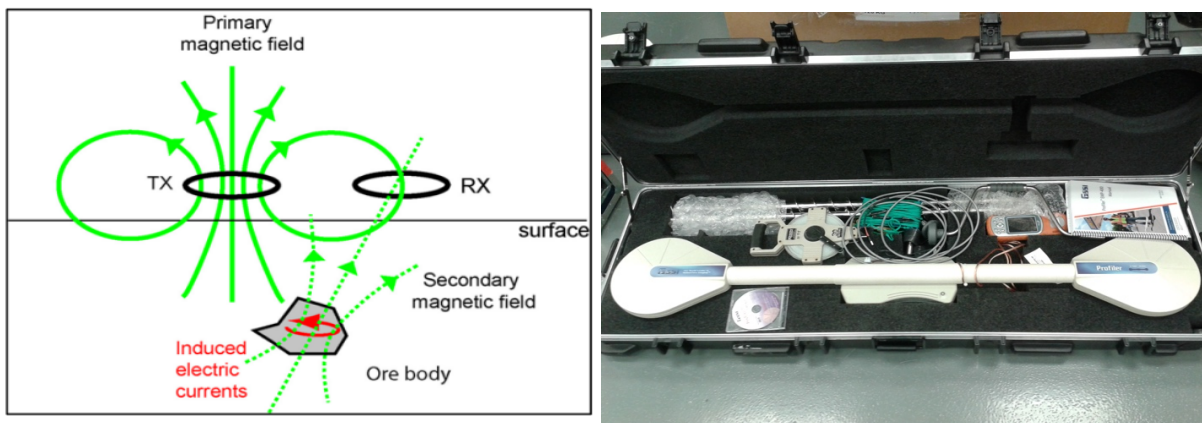


Figure 4. Sketch of the EMP working-principle and photo of the packed EMP instrument.

This instrument find application in different geological and environmental application. These include shallow soil mapping, soil-salinity mapping, ground water investigations etc. It is also widely used for sea ice thickness measurements. This is possible due to the fact that sea ice is resistive compared to the conductive sea ice water. Therefore, the distance to the ice-water interface can be measured by assuming that all changes measured as apparent conductivity are due to changes of the distance of the EMP to the sea water, i.e., by changes in ice thickness.

Sea ice floe station



Figure 5. Sea ice station on 22.09.2018 with Gunnar Spreen, Pascal Bourgault, Aliaksandra Kazlova and Damien Ringeisen working on the sea ice floe (Photo by Lukas Piotrowski).

Sea ice floe description

Ice flow size ~300 m x 200 m. Ice type: second year ice. Location: ~82.42⁰ Lat, ~140.11⁰ Long. Surface area on one side was relatively flat, other side had quite high ridge with height up to 2 m. We have found also couple of refrozen melt ponds covered with a fresh thin snow layer (Figure 6 right). During the work on the surface we detected some deep cracks.



Figure 6. Pictures of the sea ice floe. On the left picture you can see the ridge of the floe (photo: A.Kazlova), on the right picture you can see the melt pond (photo: G.Spreen).

Measurements

During the work on the sea ice flow on the 22nd of September the EMP instrument has been used for measuring the sea ice thickness. EMP is sensitive to the metal around it, that is why during the work we tried to keep it away from the drilling equipment and other metal things. The instrument was installed on the plastic sled (Fig.7). Before we have started EMP measurement, we did a drilling on the sea ice floe to get in-situ ice thickness data that we can relate our EMP measurements to. This one measurement helped us during postprocessing of the collected data. We walked with the sled from one side of the floe to the other and closed the track at the same point we have started our measurements.



Figure 7 Left: EMP installed on the plastic sled. Right: Drilling of the sea ice floe.

EMP Preliminary results

Sea ice thickness was calculated by the eq 1.. This equation was derived on the base of the equation used by Prof. Christian Haas in his work. During the postprocessing we have faced a challenge, because we realized that the original equation is not suitable for the measurements we have collected. The reason was that during the process of getting familiar with the instrument we tried to make some measurements and collebration on the ship environment. This led to the changing of initial settings. On the sea ice floe we did one drill hole measurments. This helped to adjust the original equation. Basically we shifted our sea ice thickness profile on the base of the one drill hole measurment we had. In other words, we found the location of the drill holl measurment in the sea ice thickness profile and shifted the whole profile to this one known value. On the base of our experience we can give couple of recommendations for the future work with EMP-400. First of all, calibration of the EMP400 should be done before measurments in the field, because if calibration is done in other environments (like in our case on the ship with metal around) it is saved in the instrument even after turning it off and can change the measured apparent conductivity to unrealistic values. Secondly, during the work the operator should check if the apparent conductivities are below 1000 mS/m.

$$\text{ThickEM5K} = -1/0.68229 * \ln((\text{AppCond5k}-11303)/1233.1) \quad (\text{eq.1})$$

The sea ice thickness profile calculated by eq.1 from the collected EMP data is shown in Figure 8.

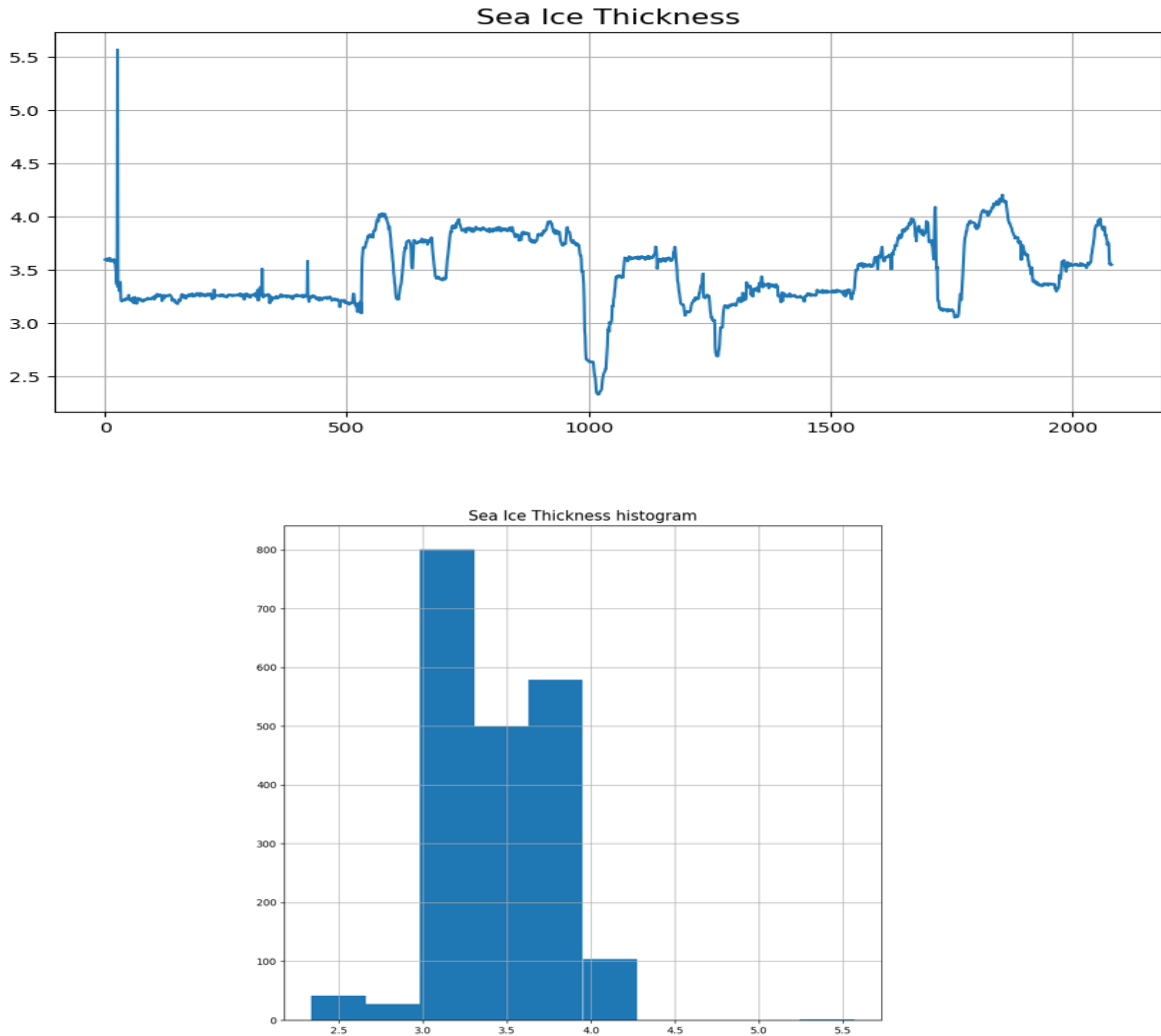


Figure 8. Upper: Sea ice thickness profile from the in-situ data. Down: Sea ice thickness histogram with bin size of 50 cm.

From Fig. 8 we can see that most of the sea ice thickness measurements are distributed between 3 and 4 meters. That means that the ice floe we have been working on likely was deformed second-year ice. When we were searching for the sea ice floe we have noticed that most of the floes are not as thick as the one we have been working on. Thus, this sea ice thickness profile is rather untypical for this time of the year in this region.

The track of the measurements on the sea ice floe is shown on the Fig. 9. Each measurement has latitude and longitude coordinates from the GPS receiver attached. The sea ice floe is not a stable platform, because it moves and rotates forced by wind and ocean currents. That is why first thing to do was to make a correction for the sea ice drift that occurred during our measurement time. We did close our track at the same point on the ice flow. Because of the floe drift GPS coordinates were not the same. We just distributed the difference between start point and end point in this measurements along the track. After the correction the track was closed. To get more precise results it would be nice to have a stationary GPS station on the floe and make positioning measurements in relation to this station, but because of the limited amount of time we could not afford this stationary station on the floe.

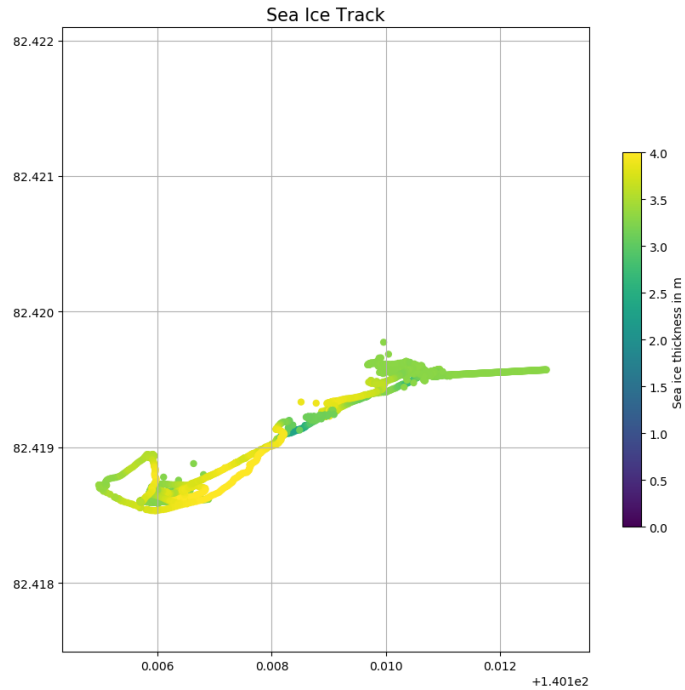


Figure 9. The track of the sled during the measurement campaign.

EM31

In addition to EMP, we also used an instrument called Geonics EM31 to measure the ice thickness. According to its name, the EM31 uses electromagnetic induction to measure the apparent conductivity of a body. When the device is activated, it sends a primary magnetic field that will induce a current in the body. This current will create a secondary magnetic field that we can measure. In our experiment, a signal is sent every second but that can be modified for a different experimental set up. The EM can be mounted on a sledge (Figure 10) that one can pull or attached to a snowmobile. The same type of measurements can also be obtained from an aircraft if in addition the distance between the instrument and the ground is measured by a laser altimeter. Sadly, we haven't been able to use this device in the field.

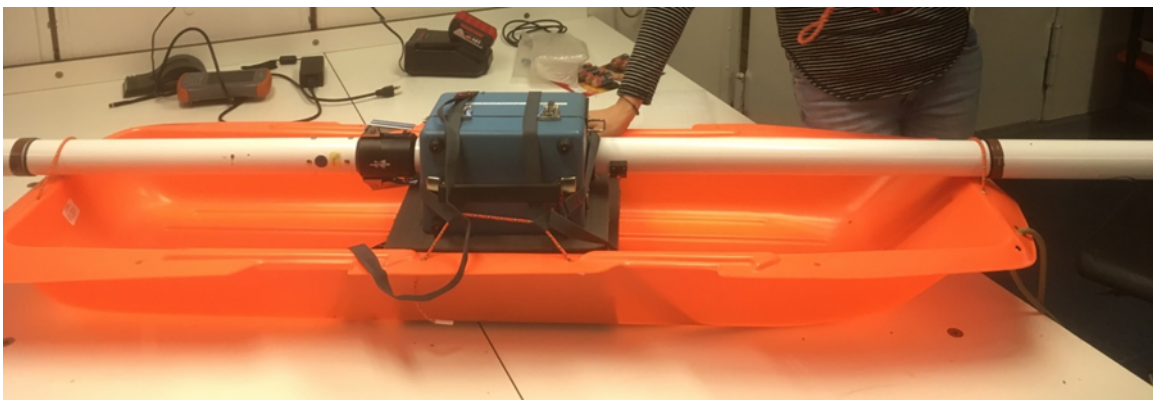


Figure 520. The EM31 mounted on its sledge

The apparent conductivity (C) measured by the EM31 can be related to the total ice and snow thickness (H) over which the device is located. One could use equation 2 from Haas et al. (1997) to derive the ice thickness. Once on the ice, a calibration will still have to be done

because we cannot be sure that our instrument works exactly like the one used in the previous paper.

$$H = 7.81 - \frac{\ln(C-62.5)}{0.915} \quad (\text{Eq. 2})$$

While waiting for an ice station (which never came), one can do a “practice calibration”. This means doing a calibration of the EM31 measured conductivity as a function of the height at which it is held over the deck of the *Polarstern*.



Figure 11. Calibrating the EM31 over the Polarstern deck

These measurements are also a good practice for setting the EM31 and analyzing the data. For this calibration, the device has to be held horizontally (just like in Figure 11) in the horizontal dipole mode configuration (HDM). This mode can be changed in the Archer computer. One will have to lift the EM31 from the ground at different heights (hips, shoulders and over the head height in this case) and note the apparent conductivity. A file can also be created and transferred to a computer using Bluetooth. One then need to convert the file from R31 format to G31 to be able to read the data and proceed to an analysis. Plotting the height (h) as a function of the logarithm of the apparent conductivity (Fig. 12) allows deriving a simple equation which can be seen on the figure. This equation corresponds very well to our measurements with a R^2 coefficient of 0.998. The error bars correspond to the uncertainty on the height at which the EM31 is held and on the conductivity measured many times for every position.

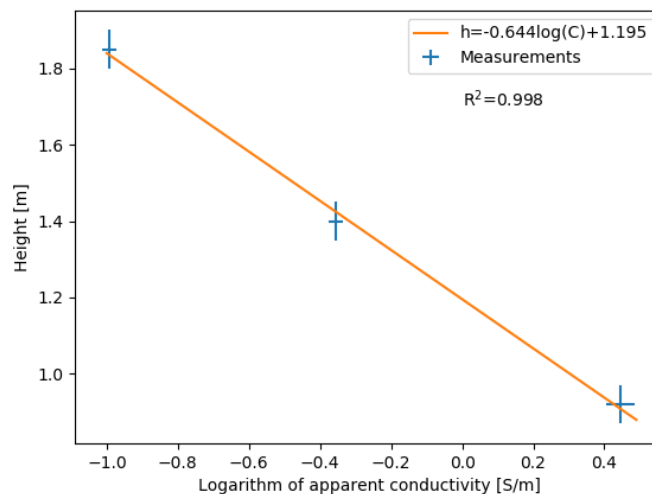


Figure 12. Graph obtained from the calibration

References

- Haas C, Gerland S, Eicken H, Miller H (1997) Comparison of sea-ice thickness measurements under summer and winter conditions in the Arctic using a small electromagnetic induction device. *Geophysics*, 62(3), 749-757. <https://doi.org/10.1190/1.1444184>
- Nicolaus M, Katlein C, Maslanik J, Hendricks S (2012) Changes in Arctic sea ice result in increasing light transmittance and absorption. *Geophysical Research Letters*, 39.
- Profiler EMP-400 User's manual (2006)

Die **Berichte zur Polar- und Meeresforschung** (ISSN 1866-3192) werden beginnend mit dem Band 569 (2008) als Open-Access-Publikation herausgegeben. Ein Verzeichnis aller Bände einschließlich der Druckausgaben (ISSN 1618-3193, Band 377-568, von 2000 bis 2008) sowie der früheren **Berichte zur Polarforschung** (ISSN 0176-5027, Band 1-376, von 1981 bis 2000) befindet sich im electronic Publication Information Center (**ePIC**) des Alfred-Wegener-Instituts, Helmholtz-Zentrum für Polar- und Meeresforschung (AWI); see <http://epic.awi.de>. Durch Auswahl "Reports on Polar- and Marine Research" (via "browse"/"type") wird eine Liste der Publikationen, sortiert nach Bandnummer, innerhalb der absteigenden chronologischen Reihenfolge der Jahrgänge mit Verweis auf das jeweilige pdf-Symbol zum Herunterladen angezeigt.

The **Reports on Polar and Marine Research** (ISSN 1866-3192) are available as open access publications since 2008. A table of all volumes including the printed issues (ISSN 1618-3193, Vol. 377-568, from 2000 until 2008), as well as the earlier **Reports on Polar Research** (ISSN 0176-5027, Vol. 1-376, from 1981 until 2000) is provided by the electronic Publication Information Center (**ePIC**) of the Alfred Wegener Institute, Helmholtz Centre for Polar and Marine Research (AWI); see URL <http://epic.awi.de>. To generate a list of all Reports, use the URL <http://epic.awi.de> and select "browse"/ "type" to browse "Reports on Polar and Marine Research". A chronological list in declining order will be presented, and pdf icons displayed for downloading.

Zuletzt erschienene Ausgaben:

Recently published issues:

728 (2019) The Expedition PS115/2 of the Research Vessel POLARSTERN to the Arctic Ocean in 2018, edited by Ruediger Stein

727 (2019) The Expedition PS115/1 of the Research Vessel POLARSTERN to the Greenland Sea and Wandel Sea in 2018, edited by Volkmar Damm

726 (2019) The Expedition PS108 of the Research Vessel POLARSTERN to the Fram Strait and the AWI-HAUSGARTEN in 2017, edited by Frank Wenzhöfer

725 (2018) Russian-German Cooperation: Expeditions to Siberia in 2017, edited by Jens Strauss, Julia Boike, Dmitry Yu. Bolshiyarov, Mikhail N. Grigoriev, Hassan El-Hajj, Anne Morgenstern, Pier Paul Overduin, Annegret Udke

724 (2018) The Expedition PS113 of the Research Vessel POLARSTERN to the Atlantic Ocean in 2018, edited by Volker Strass

723 (2018) The Expedition PS114 of the Research Vessel POLARSTERN to the Fram Strait in 2018, edited by Wilken-Jon von Appen

722 (2018) The Expedition PS112 of the Research Vessel POLARSTERN to the Antarctic Peninsula Region in 2018, edited by Bettina Meyer and Wiebke Weßels

721 (2018) Alfred Wegener im 1. Weltkrieg. Ein Polarforscher und die „Urkatastrophe des 20. Jahrhunderts“, by Christian R. Salewski

720 (2018) The Expedition PS98 of the Research Vessel POLARSTERN to the Atlantic Ocean in 2016, edited by Bernhard Pospichal

719 (2018) The Expeditions PS106/1 and 2 of the Research Vessel POLARSTERN to the Arctic Ocean in 2017, edited by Andreas Macke and Hauke Flores

718 (2018) The Expedition PS111 of the Research Vessel POLARSTERN to the southern Weddell Sea in 2018, edited by Michael Schröder



ALFRED-WEGENER-INSTITUT
HELMHOLTZ-ZENTRUM FÜR POLAR-
UND MEERESFORSCHUNG

BREMERHAVEN

Am Handelshafen 12
27570 Bremerhaven
Telefon 0471 4831-0
Telefax 0471 4831-1149
www.awi.de

